# RADICAL CHEMISTRY AND MASS SPECTROMETRY FOR ENHANCED BIOMOLECULE ANALYSIS

by

**Sarju Adhikari**

**A Dissertation**

*Submitted to the Faculty of Purdue University*

*In Partial Fulfillment of the Requirements for the degree of*

**Doctor of Philosophy**


Department of Chemistry

West Lafayette, Indiana

May 2019

# THE PURDUE UNIVERSITY GRADUATE SCHOOL
# STATEMENT OF COMMITTEE APPROVAL

Dr. Scott A. McLuckey, Chair
Department of Chemistry
Dr. Hilkka I. Kenttämaa
Department of Chemistry
Dr. Paul Wenthold
Department of Chemistry
Dr. Tong Ren
Department of Chemistry

**Approved by:**

Dr. Christine Hrycyna
Head of the Graduate Program

*ॐ नमः शिवाय*

To My Late Father

Krishna Bahadur Adhikari

# ACKNOWLEDGMENTS

I would like to take this opportunity to acknowledge and show my appreciation to countless professors, researchers, technical experts, and staffs who have contributed to the success and achievement of my education and research at Purdue University.

I would first like to thank my research advisor, Prof. Yu Xia, for her continuous support throughout my graduate career. Prof Xia: I thank you for your immense patience and perseverance in guiding me on a journey so full of curiosity. I would also like to thank my graduate advisor and mentor, Prof. Scott McLuckey, for his support, guidance, and motivation. You have been a huge inspiration and role model to be a good scientist. Although I was in your lab for a "relatively" short period of my graduate career, I have learned and grown so much as a researcher. I feel privileged to have had the opportunity to work with both of them.

I must thank my undergraduate research advisor, Prof. Debra Dolliver, for her support and guidance during my early research career. During my time in her lab, I was inspired to pursue Ph.D. studies. I would also like to thank my dissertation committee member, Prof. Hilkka Kenttämaa, for her insightful suggestion and advice during my seminar, original proposal, and dissertation exam. Prof. Paul Wenthold and Prof. Tong Ren, thank you so much for agreeing to join the dissertation committee at such short notice.

I also thank every member, past and present, of Xia (Purdue and Tsinghua University), Ouyang (Purdue and Tsinghua University), and McLuckey research group; all of whom I have had the good fortune to work, learn and share my graduate life experience. I would like to give special thanks to Dr. Wenpeng Zhang and Tessi Wang for making my visit to Tsinghua University, Beijing, China possible. Words cannot describe my learning experience in Tsinghua. Late night mobike rides on the busy street of Beijing will always be memorable.

To all my collaborators, Prof. Joseph Francisco, Prof. Josep Anglada, Prof. Ramon Crehuet, Prof. Mingji Dai, Prof. Tong Ren, and Dr. Jim Hager, thank you so much for your invaluable inputs on various research topics.

I must acknowledge Purdue University and the Department of Chemistry for providing an exceptional environment for graduate students like me to learn and grow as a professional scientist. I would like to extend warm gratitude to my countless good friends and colleagues in Purdue (and in Southeastern Louisiana University). I would also like to thank all past and present members of the Nepali Student Association at Purdue (NEPSAP). Thank you for being a family away from home.

Finally, thank you to my parents (Krishna Bahadur Adhikari and Sita Adhikari) and my siblings (Prakash Adhikari and Bikash Adhikari) for their unconditional love and support from the very beginning.

# TABLE OF CONTENTS

# LIST OF TABLES

# LIST OF FIGURES

# LIST OF SCHEMES

# LIST OF ABBREVIATIONS

| | |
|---|---|
| CI | Chemical Ionization |
| CID | Collision induced dissociation |
| CEM | Chain Ejection Model |
| CRM | Chain Residual Model |
| Da | Dalton |
| DAG | Diacylglycerol |
| DC | Direct Current |
| DDC | Dipolar Direct Current |
| DMF | Dimethylformamide |
| DMPA | 2,2-dimethoxy-2-phenylacetopheone |
| ECD | Electron Capture Dissociation |
| EI | Electron Ionization |
| ESI | Electrospray ionization |
| ETD | Electron Transfer Dissociation |
| eV | Electron-volt |
| GC | Gas Chromatography |
| HPLC | High Pressure Liquid Chromatography |
| IEM | Ion Evaporation Model |
| LC | Liquid Chromatography |
| LIT | Linear Ion Trap |
| LOD | Limit of detection |
| LTP | Low Temperature Plasma |
| MALDI | Matrix-assisted Laser Desorption Ionization |
| MS | Mass Spectrometry |
| MS/MS | Tandem Mass Spectrometry |
| MW | Molecular Weight |
| *m/z* | mass-to-charge ratio |
| NanoESI | Nanoelectrospray Ionization |
| NLS | Neutral Loss Scan |

| | |
|---|---|
| PIS | Precursor Ion Scan |
| PTM | Post-translational Modification |
| QqQ | Triple Quadrupole Analyzer |
| RF | Radio Frequency |
| S/N | Signal to Noise Ratio |
| TAG | Triacylglycerol |
| TGA | Thioglycolic acid |
| TOF | Time of Flight |
| SRM | Selected Reaction Monitoring |
| UV | Ultraviolet |
| v/v | volume/volume |
| XIC | Extracted Ion Chromatogram |

# ABSTRACT

Author: Adhikari, Sarju. PhD
Institution: Purdue University
Degree Received: May 2019
Title: Radical Chemistry and Mass Spectrometry for Enhanced Biomolecule Analysis
Committee Chair: Scott A. McLuckey

Electrospray ionization-tandem mass spectrometry (ESI-MS/MS) has been established as a powerful tool for qualitative and quantitative analysis of biomolecules. However, mass spectrometric analysis of biomolecules is often limited by poor ionization efficiency of analyte for sensitive detection and limited fragmentation for structural characterization. Over the years, various solution phase as well as gas-phase derivatization techniques, have been coupled with MS to increase the ionization efficiency and facilitate the formation of structural informative fragment ions. The research presented in this dissertation falls into two major parts; focusing on method development and application of radical chemistry for enhanced biomolecule analysis on an ESI-MS/MS platform. In the first part, a method of rapid charge tagging of neutral lipids (e.g. sterols, glycerides) with a thiol radical-based charge tag is developed, followed by comprehensive analysis via ESI-MS/MS without the use of a chromatographic separation (shotgun lipidomics). This charge tagging is performed in an easily constructible fused silica capillary-based microflow photo-reactor which is relatively low in cost and requires no instrument modifications. This method significantly enhances the ionization efficiency of the neutral lipids for sensitive MS detection (pM range). This method can be applied to the small volume of biological complex samples (e.g. 1 µL plasma) and doesn't require extensive sample pretreatment procedure (analysis time of 2 min vs. traditional >60 min on GC-MS and HPLC-MS systems). Furthermore, the derivatized neutral lipids can also be fragmented via soft collision-induced dissociation to obtain fatty acyl chain

composition of the neutral lipids (sterol esters, diacylglycerols, triacylglycerols, etc.) for structural characterization. This can especially be useful for determination for fatty acyl compositional isomers in neutral lipids for analysis related to biomarker detection. The characteristic fragmentation pattern of tagged neutral lipids has also been utilized for quantitation of lipids from biological mixture samples. Initial application of this method has shown alteration in the concentration of diacylglycerol lipid species in clinical samples of Type 2 Diabetes Mellitus patients, suggesting the potential of understanding the biological roles of such lipids in insulin resistance.

In the second part, a unique approach of radical-induced disulfide bond cleavage in peptides and proteins is demonstrated. Using 254 nm UV emission, acetone was used as a photoinitiator to initiate secondary radical formation i.e. hydroxyalkyl radical, from alcohol co-solvents used for electrospray. These radicals can then be used to efficiently cleave the disulfide bonds (R-S-S-R) in peptide/proteins to give reduced reaction products (RSH) at the cleavage site. Upon soft collision-induced dissociation, the reduced product gave abundant *b*- and *y*- type fragment ions for complete or enhanced sequence coverage as compared to intact disulfide-linked peptides and proteins. With the use of a simple microflow photo-reactor, this radical based approach can also be coupled with infusion ESI-MS/MS for a rapid online-based peptide and protein analysis. The yield for disulfide bond reduction was almost 100% within less than 5 s of UV irradiation. Furthermore, by adjusting the UV irradiance time, different degrees of partial reduction could be achieved, which greatly facilitated the disulfide linkage mapping in peptides and proteins with multiple disulfide bonds. This method has been incorporated with both bottom-up and top-down approach for protein analysis for unraveling the molecular complexity, quantifying and deep sequencing of disulfide-linked proteins.

# CHAPTER 1. INTRODUCTION

## 1.1 Overview

In the recent decade, radical chemistry has emerged as one of the popular areas in mass spectrometry (MS) development and application to bioanalysis.[1] Radicals are atoms, molecules, or ions that contain one or more unpaired electrons. They are, generally, highly reactive. Such reactive species can usually be formed in three distinct ways: by the loss of an electron, by the gain of an electron, or by homolytic bond cleavage where each species retains a single electron.[2] In biosystems, radicals can serve as an active intermediate in several enzyme species which is critical for normal functioning of body.[3-4] They are also involved in various cell signaling processes.[5-6] However, highly reactive and uncontrolled nature of these radicals can also catalyze oxidative modification of macromolecules such as proteins, lipids, and DNA.[7-9] This type of radical-initiated damage or modification has been associated with Parkinson's disease, Alzheimer's disease, the aging process, and various other neurodegenerative diseases and disorders.[10-11] Fundamental understanding of radical chemistry is critical for understanding the principle of various biochemical processes, such as radical generation, transfer, reactivity, and termination. However, the study of such reactive radical intermediate remains significantly under-explored.

The development of gas phase MS analysis can serve as a suitable platform to investigate the intrinsic property of radical species. On the other hand, the highly reactive property of radical species can also add a new tool for MS to tackle traditionally challenging problems for biomolecule analysis. Over the years, radical chemistry has found many applications in conjunction with mass spectrometry. It is widely used in fundamental ion chemistry as well as in method and instrument development. During the late 1990s, it was first demonstrated that the surface of proteins could be probed after their limited exposure to hydroxyl radicals.[12-13] Over the years, this radical probe mass

spectrometry has proven itself to be a powerful method for footprinting protein structures, studying the dynamics of single proteins and larger assemblies, and unraveling the onset of protein oxidative damage, at both local and global level.[14] Similarly, development of electron capture/transfer dissociation (ECD/ETD) has also helped to recognize the importance of radical chemistry for biomolecule analysis via MS.[15-16] Electron is captured by the isolated ions in MS, forming a radical cation, which can spontaneously initiate radical-driven fragmentation pathways. These fragmentations can produce rich extensive sequence information for biomolecule analysis that complements the information obtained from collision-induced dissociation (CID).[17] Furthermore, ECD/ETD often retain the labile post-translation modifications (PTMs) during backbone fragmentation, thus, substantially improving the protein identification and characterization process.[17-18] Various derivatization techniques have also been developed utilizing radical-driven fragmentation behavior or facilitate spectral interpretation as a complementary alternative to traditional mass spectrometric techniques for biomolecule analysis.[19-20]

This review is structured around the mechanism used to create radical species and its application as a MS-based bioanalysis tool to tackle traditionally challenging problems for structural characterization of biomolecules. The ideal criteria used for application of radical based reactions for biomolecule analysis were: fast reaction kinetics, quantitative yields, minimal byproducts, and strong potential for coupling with MS. Application of such reactive species for biomolecule analysis will primarily involve peptides, proteins, and lipids. Most reactions in this review are performed using photo-induced or dielectric barrier discharge induced radical reactions in conjunction with MS; therefore, important aspects of photochemistry, electric discharge, and mass spectrometry will also be discussed in the following section. The reader is referred to chapters

and subsequent references to understand more about radical chemistry as an increasingly important area of MS development and its application to biomolecule analysis.

## 1.2 Photochemistry

### 1.2.1 Photophysical processes

Photochemistry is used to describe a chemical reaction caused by molecular absorption of ultraviolet (UV, $\lambda$ = 100-400 nm), visible light (VIS, $\lambda$ = 400-750 nm) or infrared radiation ($\lambda$ = 750-2500 nm). Often, photochemistry leads to intramolecular chemical bond rearrangements or chemical bond dissociation. A simplified Jablonski diagram can be used as a model in illustrating the electronic states of a molecule after excitation, and the radiative and non-radiative transitions between them, which return the molecule to its electronic ground state.[21-22] The absorbing molecule is initially in the ground electronic state (the parallel bars labeled $S_0$) and upon excitation can undergo a vibronic (electronic and vibration) transition to its excited singlet state ($S_1$); sometimes to a second electronic excited state ($S_2$). At each energy level, the molecule can exist in a number of vibrational energy levels (represented by multiple lines in each electronic state). Once excited to higher vibrational energy level the molecule will quickly relax to the lowest vibrational level of $S_1$, before rapidly relaxing to the lowest energy level. The transition from upper to lower bars in $S_1$ is termed as internal conversion ($> 10^{12}$ $s^{-1}$). At the lowest vibrational level of $S_1$, the species will undergo radiative energy release (fluorescence; orange; $10^{6}$-$10^{9}$ $s^{-1}$) or perform an intersystem crossing to a vibronic excited triplet state ($T_1$) and rapidly relax to the lowest vibrational energy level (non-radiative energy transfer). In the triplet excited state, the molecule can then emit energy as a photon (phosphorescence; blue line; $10^{-2}$-$10^{2}$ $s^{-1}$) to return to the ground electronic state of the molecule. Alternatively, in the excited state, the molecule may undergo intramolecular or intermolecular chemical reactions. For the photo-initiation purpose, the desired

reaction is cleavage at the excited triplet state to generate initiating radicals. These physical processes are not limited to photon absorption and, for example, may also result from inelastic collisions with electrons as a result of electric discharge (as discussed in subsequent sections of this dissertation).

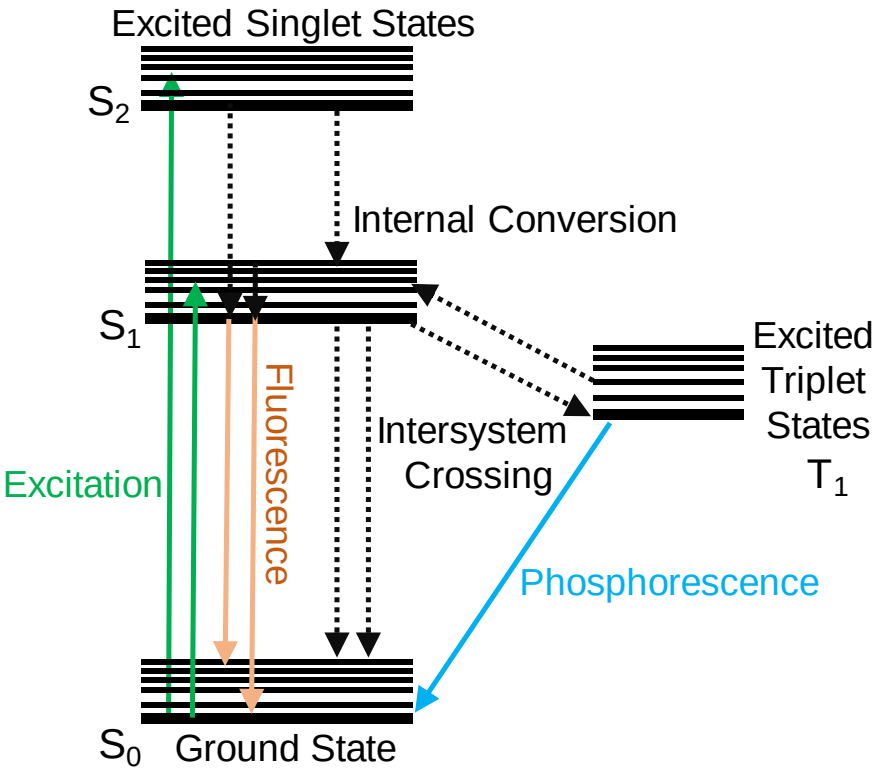


Figure 1-1 Jablonski Diagram depicting various photophysical pathways that a molecule can take from ground state to the excited state, and back.[22]

### 1.2.2 Photoinitiators

A photoinitiator (PI) is a molecule that converts absorbed light energy, UV or visible light, into chemical energy in the form of reactive species viz. free radicals, cations or anions. These reactive species can now promote other reactions. To proceed efficiently, the absorption bands of photoinitiator must overlap with the emission spectrum of the light source. Also, there must be

minimal competition for light absorption by other species (such as solvents) at the wavelengths corresponding to photoinitiator's excitation. Photoinitiators can be generally divided into two classes based on the mechanism by which initiating radicals are formed.

### 1.2.2.1 Type I photoinitiators

Type I photoinitiator absorbs a photon, transforms into an excited state and then undergoes a homolytic cleavage to yield free radicals or other reactive species. These free radicals or reactive species then initiate further reactions. 2,2-dimethoxy-2-phenylacetopheone (DMPA) is a common commercial type I photo-initiator, which decomposes *via* α-cleavage from the triplet state by a Norrish Type I mechanism to give benzoyl radical and dimethoxybenzoyl radical (Scheme 1-1).[23-24] The dimethoxylbenzoyl radical can further decompose to give a more stable methyl benzoate and a methyl radical.

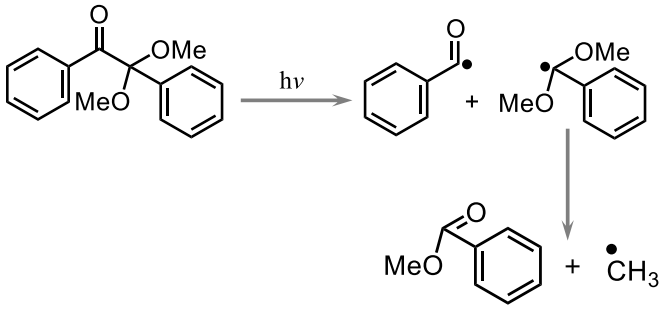


Scheme 1-1 Photochemical decomposition of 2,2-dimethoxy-2-phenylacetophenone (DMPA) under UV irradiation.

### 1.2.2.2 Type II photoinitiators

They undergo a bimolecular reaction where the excited state of the photoinitiator interacts with a second molecule (a co-initiator) to generate free radicals. These radicals then initiate further reactions. Benzophenone is one of the common commercial type II photoinitiators. Photolysis of

benzophenone in the presence of a hydrogen donor leads to the formation of a ketyl radical and a radical derived from the hydrogen donor (Scheme 1-2).

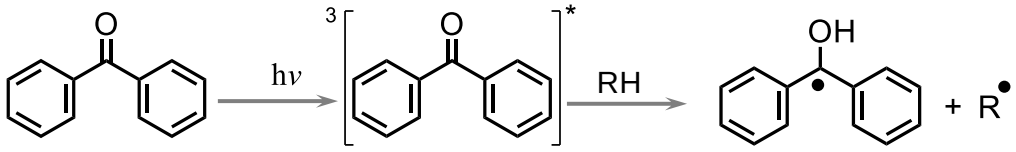


Scheme 1-2 Photoinitiation mechanism with benzophenone and hydrogen donor under UV irradiation.

### 1.2.3 Light Sources

Mercury and xenon lamps are the most widely used sources of UV-VIS light for continuous irradiation in the laboratory. Deuterium and tungsten lamps are utilized for spectrophotometers. For their relevance in photochemical studies in this dissertation, it is of interest to concentrate some additional attention to mercury lamps. The spectral irradiance of the mercury lamp is strongly dependent upon the mercury vapor pressure. *Low-pressure* mercury lamp (vapor pressure of mercury is about ~$10^{-3}$ mbar) emits primarily two bands of radiation centered at 253.7 nm and 184.9 nm, due to Hg ($^3P_1$) and Hg ($^3P_1$) de-excitation, respectively. The short-wavelength of the lamp can be partially filtered out with a quartz envelope. The excited atoms in *medium-pressure* mercury lamp (vapor pressure of mercury is about ~1 bar) can undergo more frequent collisions with an electron, resulting in excitation to higher states. This results in more emission lines such as 313.9 or 365.4 nm. These mercury lamps have a longer lifetime and provide efficient input power. Often, the lamp envelope's temperature can reach a higher temperature due to continuous irradiation, producing a considerable amount of heat and infrared heat. In such a scenario, cooling-water circulation or water cuvette filters can be used to prevent the system from becoming heated.

For most experiments in this dissertation, commercially available mercury lamps with primary emission at ~254 nm and ~351 nm were used.

Lasers are an alternative light source, that emits light through a process of optical implication based on the stimulated emission of electromagnetic radiation.[25] A laser consists of a gain medium, a mechanism to energize it and something to provide an optical feedback. The material property of the gain medium amplifies the light by way of stimulated emission. Commonly used lasers (and their common wavelengths) include $N_2$ (337.1 nm), KrF (excimer) (248 nm), frequency quadrupled Nd YAG (266 nm), and $F_2$ (157 nm).[26] Lasers can produce highly intense, strongly monochromatic and parallel beams. Both continuous and pulsed lasers have been developed and are commercially available. However, lasers are considerably expensive compared to mercury or xenon lamps.

### 1.2.4 Photochemistry in Flow

Batch reactor systems have been an excellent device to carry out photochemistry on scales of milligrams up to a few grams. The reaction set-up is often simple and less expensive. Despite numerous successful applications of traditional reactors (batch reactors) in photochemistry, they have, at times, been limiting. One of the key issues in a batch reactor is that the longer path length reduces the efficiency with increase in distance from the lamp. Even distances as short as 1 mm can result in a reduction up to 20% of the incident light as described by using Beer-Lambert law.[28-29] This can cause an increase in reaction times, which can often lead to decomposition or increased formation of undesired side products and photopolymers. Microflow reactor can overcome many of the problems associated with traditional batch reactors as they allow exquisite control over reaction conditions. Small characteristics dimension of microflow reactors ensures uniform light irradiation over the entire reaction medium, resulting in higher reaction selectivity, accelerated

reaction times, and lower catalyst loading.[27-29] Other advantages of microflow include enhanced heat and mass transfer rates, reduced safety hazards and ease of increasing throughput by numbering-up, etc.[29] Over the years, there have been many developments in the technology for photochemical reaction in flow, ranging from simple tubing based reactors to complex microfluidic devices. For most of the photochemical experiments in this dissertation, a simple fused silica capillary-based microflow photo-reactor was built and used. A comparison of reaction efficiency of performing the reaction in microflow photo-reactor versus in batch reactor (borosilicate glass vial and nanoESI borosilicate glass tip) are discussed in subsequent chapters.

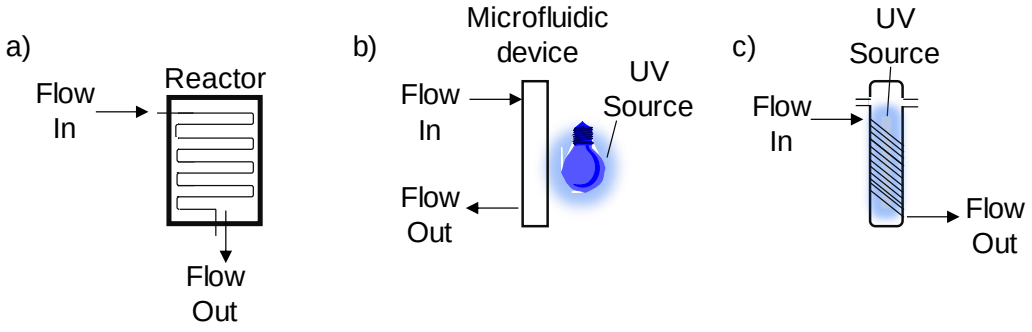


Figure 1-2 Common flow reactor designs. Adapted from Beeler and Corning (2015).[27]

## 1.3 Electric Discharge Reactions

When an applied potential between two conducting electrodes and a low conducting medium (neutral gas eg. He) results in an electric current via an inelastic collision between high energy electrons and neutral species, electric discharge is produced. Various factors affect the nature of discharge which includes the content of the gas, electrode geometry, and material, distance of electrode, pressure, and mechanism of the applied potential.[30] The relatively inexpensive and versatile method of forming energetic species for subsequent reaction by electric discharge reactions has been found application in a wide range of fields. Low-temperature plasma

(LTP) dielectric-barrier discharge[31] was used during the study of the dissertation and is described below.

### 1.3.1 Dielectric-barrier discharge

Dielectric barrier discharge (DBD) is usually driven by AC voltage between two spaced electrodes coupled outside an insulating dielectric barrier.[32] Historically, it was originally called the silent discharge.[31] Previously, Xia *et al*. have reported a method for generation of radical ions for peptides/protein analysis using a low-temperature helium plasma dielectric barrier discharge in a nanoESI plume.[33-34] The nanoESI emitter is positioned coaxially and downstream from with the DBD in a T-shape glass tube. A piece of copper tape is wrapped around the exterior of the tube as the high voltage electrode. A low-temperature helium plasma (LTP) can be initiated using AC while concurrently flowing helium through the vessel, to generate reactive species at atmospheric pressure. Reactive species such as OH radicals can be generated from the water molecules present in the air.[33] A rubber stopper is placed at the back of the tube to help position the nanoESI spray tip, which is kept at a distance of 5-10 nm from the MS inlet. The nanoESI plume interacts with the plasma and the products formed in situ were analyzed on-line by MS. Scheme 1-3 shows the apparatus used for the formation of radicals using an LTP.

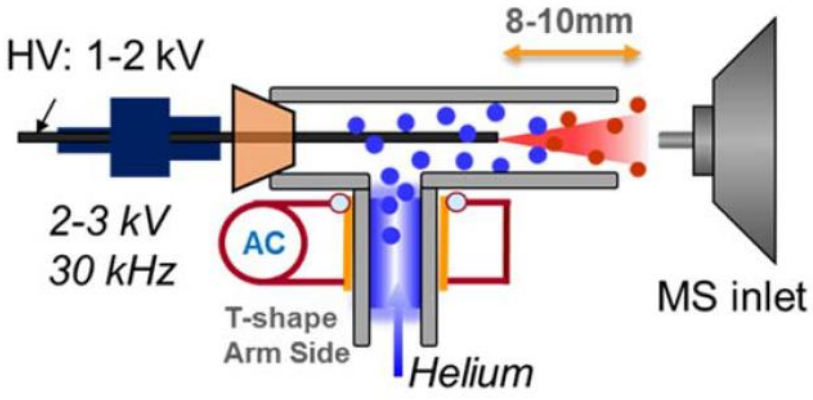


Scheme 1-3 Schematic of atmospheric low-temperature helium plasma source.[35]

## 1.4 Mass Spectrometry

In simple words, mass spectrometry (MS) is an analytical technique that measures ions based on their mass-to-charge ratio (*m/z*). As such, it is a subject of enormous scope. Since its inception by W. Wien[36] and J.J.Thompson[37], MS has become one of the most popular and powerful analytical tools to study the complexities of elemental and molecular processes in nature. A simple mass spectrometer is usually composed of three main components: an ion source, where ions are generated, a mass analyzer, which separates ions based on their *m/z*, and a detector, where the ions are detected. Each of these components is briefly described below.

### 1.4.1 Ionization Source

The ion source is the part of MS that ionizes material under analysis. Techniques for ionization have been key to determining what types of sample can be analyzed by MS. Ionization techniques can be broadly categorized into soft and hard ionization. Soft ionization exhibits little or no fragmentation while hard ionization techniques result in significant fragmentation. Electron ionization (EI) is a hard ionization technique, in which analyte interacts with an accelerated beam of the electron emitted from a heated metallic filament (e.g. tungsten, rhenium ), energy is imparted to the analyte causing ejection of an electron and the formation of a positively charged radical ion (Equation 1.1).[38-39] EI is widely coupled with gas chromatography (GC) which is especially suitable for volatile and thermally stable compounds. EI also has efficient ionization yield, is universal, and highly reproducible. However, EI can lead to excessive fragmentation of analyte, resulting in a highly complicated spectrum to decipher.[40]

Equation 1.1 $$M + e^- \rightarrow M^{\bullet +} + 2e^-$$

Chemical ionization (CI) is a soft ionization technique usually coupled with GC.[41] In CI, reagent gas molecules such as methane, isobutane are ionized by energetic electrons, which subsequently reacts with the analyte molecules in the gas phase in order to achieve ionization (Equation 1.2).[39] CI is a low energy ionization technique and thus may be used to generate abundant $[M+H]^+$ ions which can be used to determine the molecular mass of the analyte.

Equation 1.2

$$CH_4 + e^- \rightarrow CH_4^{\bullet +} + 2e^- \quad \text{(Primary ion formation)}$$

$$CH_4^{\bullet +} + CH_4 \rightarrow CH_5^+ + {}^{\bullet}CH_3 \quad \text{(Secondary reagent ions)}$$

$$M + CH_5^+ \rightarrow [M+H]^+ + CH_4 \quad \text{(Product ion formation)}$$

In recent years, Electrospray ionization (ESI),[42-43] matrix-assisted laser desorption ionization (MALDI),[44] and desorption electrospray ionization (DESI)[45] have become more widely used soft ionization techniques, which facilitate the generation of charged species of several different classes of analytes (i.e. peptides, proteins, lipids, polymers, etc.) for analysis by MS. This dissertation employs the use of ESI, more especially nano-ESI, the facets of which are discussed below.

#### 1.4.1.1 Electrospray ionization

The first application of ESI was demonstrated by Dole and co-workers in 1968, where they ionized polymer molecules and detected by using a Faraday cup.[46] Nearly 20 years later, Fenn further improved Dole's work and developed ESI as it is used today. Fenn demonstrated that the use of a nitrogen gas counterflow to Dole's interface condition efficiently evaporate the solvent from the electrospray droplet, thus improving technique by providing cleaner mass spectra.[42-43] Fenn *et al.* showed that ESI-MS produced charged ions from proteins which allowed calculation

of protein's molecular weight.[43] Since these pioneering experiments, ESI has become one of the most widely utilized ionization technique for analysis of biomolecules including proteins, lipids, biopolymers, etc. Furthermore, the interface of ESI can also be coupled with pre-MS separation methods, such as high-performance liquid chromatography (HPLC), for a direct online analysis of components in a mixture. A general set-up for ESI is summarized in Figure 1-3.

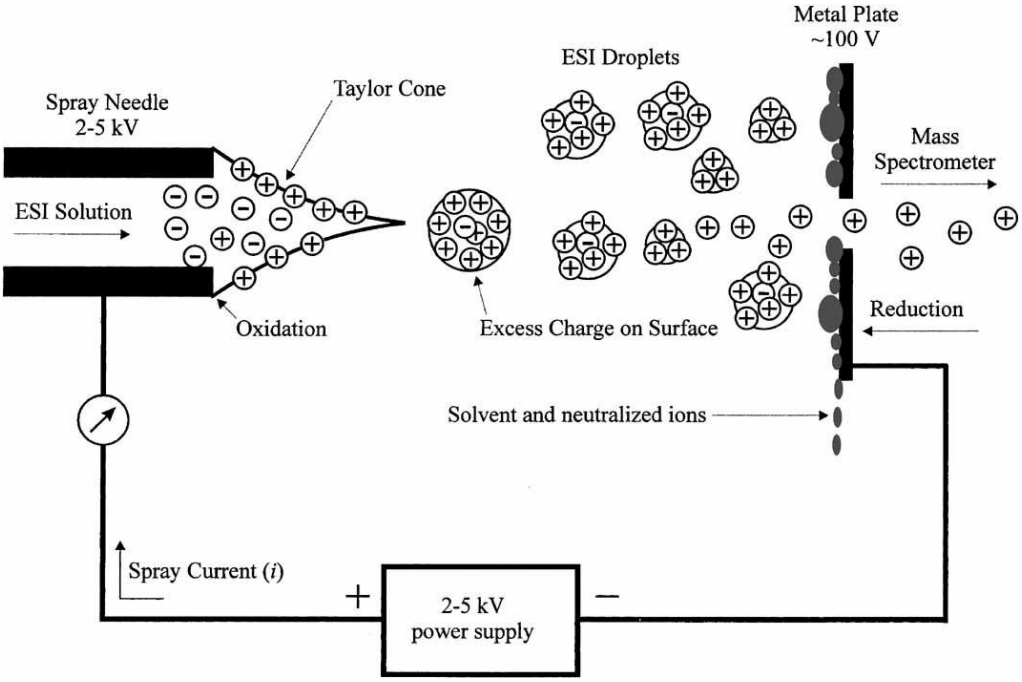


Figure 1-3 Schematic of the electrospray ionization. Adapted from Cech and Enke (2001).[47]

Electrospray ionization produces ion using an electrospray in which a high voltage is applied to the liquid to create an aerosol. Usually, a sheath gas (commonly nitrogen) is used to aid in nebulization in addition to the high temperature of ESI source. A solution is infused through a narrow capillary to which a voltage is applied. This causes the solution inside the capillary to move forward to form a cone or elongated droplet at the tip of the capillary. As the voltage exceeds the

force from the surface tension (threshold voltage), a Taylor cone is formed from which a spray of highly charged droplets are ejected.[48] Higher the surface tension, higher the voltage is needed to produce this spray. The droplets are typically on the order of micrometers in size. The polarity of the generated droplets is determined by the polarity of applied potential relative to the ground. The solvent from the charged droplets evaporates until it becomes unstable reaching its Rayleigh limit, given by equation 1.3.[49-50]

Equation 1.3 $$q^2 = 64\pi^2\varepsilon\sigma r^3$$

where q is the charge of the droplet, ε the permittivity of free space, σ is the surface tension, and r is the radius of the spherical droplet. As the Rayleigh limit is approached, the coulombic repulsion will increase relative to the surface tension and the droplet will undergo fission. This process of solvent evaporation and droplet fission will continue to create even smaller highly charged droplets until pseudomolecular gas phase ions are produced and introduced into the mass spectrometer. However, the exact mechanism for the formation of the charged ion via ESI is still of some debate. There are three main proposed models to explain this mechanism by which ions in solution become bare ions that enter a mass spectrometer, each of which is discussed in more detail below.

#### 1.4.1.1.1 Ion Evaporation Model

The ion evaporation model (IEM) was proposed by Iribarne and Thomson in 1976.[51] As droplet dissolvate, the charge in droplet overcomes the surface tension. The charged analytes are ejected from the surface of the droplet. This mechanism is widely accepted for smaller analytes.

1.4.1.1.2 Chain Residue Model

The chain residue model (CRM) was first introduced by Dole *et al.* in 1968.[46] This model is widely accepted mechanism for generating ions from large, globular shaped analytes and macromolecules (e.g. native conformation proteins). When the analyte is too big to be ejected from the droplet, the droplet evaporates, leaving the charge in solution to remain with the now gaseous analyte. Molecular dynamic studies have supported this mechanism as it shows that large analytes tend to locate in the center of the droplet.[52-53]

1.4.1.1.3 Chain Ejection Model

The chain ejection model (CEM) was proposed by Konermann *et al.* in 2013 for the ionization of elongated or disordered polymers and (denatured or linear) proteins from charged droplets.[54] The largely hydrophobic nature of denatured proteins results in migration of the ions away from the center of the droplet towards the droplet surface. The analyte then undergoes gradual ejection via "tadpole-like" structures where the droplet carries an extended analyte tail until all the analyte has entered the gas-phase.

1.4.1.2 Nano-Electrospray ionization

Nano-electrospray ionization (nanoESI or nESI) is an alternative approach to conventional electrospray ionization, developed by Wilm and Mann.[55-56] They demonstrated that a capillary flow at ~25 nL/min could sustain an electrospray at the tip of emitters fabricated from glass capillaries, pulled to a few micrometers.[55] The use of low flow rate generates much smaller initial droplets as compared to conventional ESI (~200 nm droplet size for nanoESI as compared to ~1-2 μm for conventional ESI).[56-57] Solvent evaporation in smaller droplets are more efficient resulting in an overall increase in sensitivity for nanoESI.[57] The usage of low flow rate also greatly

decreases the amount of sample consumed as compared to conventional ESI.[56] NanoESI is also less susceptible to non-volatile salt effects (ion suppression) as compared to ESI.[58]

### 1.4.2 Mass Analyzer

Once the analyte ions are formed, mass analyzer is used to separate ions according to their *m/z*. Often, a combination of different mass analyzers is used to form hybrid mass spectrometers. In this dissertation, majority of the experiments were carried out using ESI (including nanoESI) on two hybrid mass spectrometers: hybrid triple quadrupole/linear ion trap mass spectrometer and quadrupole time of flight mass spectrometer. These are described in the following sections.

#### 1.4.2.1 Quadrupole

Quadrupole ion traps are the most commonly used mass analyzer which can have the configuration of a linear ion trap (LIT), also termed as a 2D ion trap,[59] or a Paul trap, also termed as 3D ion trap[60-61]. For the majority of experiments in this dissertation, mass analysis was performed using a LIT mass spectrometer and thus will be the only the trap discussed. LIT consists of four cylindrical rods, set parallel to each other. Each opposing rod pair is connected and held at sample polarity. A radio frequency (RF) and a direct current (DC) offset voltage is applied between one pair of rods and the other. Ions from the ion source travel down the quadrupole between the rods towards the detector. Only ions of certain *m/z* will reach the detector for a given U (magnitude of the DC potential) and V (magnitude of the RF signal), given a constant AC frequency. Other ions that have unstable trajectories will collide with the rods. By continuously varying the applied voltage, it is also possible to scan for a range of values. This process can be modeled with the use of the Mathieu differential equation.[62] LITs have higher injection efficiencies and has more than 10-fold higher storage capacities, increasing both the sensitivity and dynamic range of the instrument.[63] Quadrupole mass analyzer is capable of high-throughput analyses because of their

relatively fast and simple operation. However, they are only capable of low (unit) resolution and the mass range is generally limited below to ions below *m/z* 4000.

Triple quadrupole mass spectrometer is one of the widely used quadrupole set-ups in MS. It consists of a linear series of three quadrupoles (QqQ or $Q_1q_2Q_3$). Generally, the first ($Q_1$) and third ($Q_3$) quadrupole act as a mass filter and the second ($q_2$) quadrupole is employed as a collision cell. $Q_1$ is set to filter or allow selection of precursor ions and transmit them to $q_2$. In collision cell ($q_2$), the precursor ions go under collision with an inert gas such as Ar, He or $N_2$ gas, producing fragment ions. This process is known as collision-induced dissociation (CID). The resulting fragment ions are passed through Q3, where they may be filtered or fully scanned.[64-65] The third quadrupole in SCIEX triple quadrupole system (4000 and 4500 QTRAP system) can also be used as linear ion trap (LIT) which significantly enhances ion trap performance by increasing the ion capacity, improving injection and trapping efficiencies, and increasing duty cycle.[66] Ions are expelled by an axial ejection for mass analysis. The current arrangement of triple quadrupole also allows to perform different scan functions, which are briefly described below.

#### 1.4.2.1.1 Product Ion Scan

In product ion scan, $Q_1$ is set to a fixed mass and $Q_3$ sweeps over a mass range. This scan will search for all of the product of particular precursor ion fragmenting in $q_2$.

#### 1.4.2.1.2 Precursor Ion Scan

Precursor ion scan scans for an ion of a specific *m/z* that is generating from specific product ions. The $Q_3$ is set to a fixed mass, while the $Q_1$ sweeps a mass range.

1.4.2.1.3 Neutral Loss Scan (NLS)

In a neutral loss scan, both $Q_1$ and $Q_3$ sweeps over a mass range using a fixed mass difference between them. The *m/z* for the ion will be observed if the ion chosen by the first analyzer fragments by losing or gaining the mass difference or neutral loss specified.

1.4.2.1.4 Selected reaction monitoring (SRM)

In selected reaction monitoring, both $Q_1$ and $Q_3$ are fixed over a fixed mass, allowing only a distinct fragment ion from a certain precursor ion to be detected. If $Q_1$ and $Q_3$ are set to more than a single mass, this configuration is called multiple reaction monitoring (MRM). This scan function is used for analysis of a very specific target compound.

1.4.2.2 Time of Flight Mass Spectrometry (TOF MS)

Time of flight mass spectrometry (TOF MS) is a method of mass spectrometry that separate and detect ions via a time of flight measurement, first described by Stephens *et al*.[67-68] TOF MS contains an acceleration region, a field-free region, and a detector. Ions are accelerated by an electric field. As the ions accelerate through the flight tube, they are separated based on their *m/z* (lighter ions travel faster than heavy ions given the same initial kinetic energy). The *m/z* determination is dependent on the time the ions spends traveling through the field free region, also known as drift time (t) (Equation 1.4):

Equation 1.4 $$m/z = \left(\frac{2eV_S}{L^2}\right) t^2$$

where e is the elementary charge of a proton, $V_S$ is the amplitude of the acceleration potential, and *L* is the length of the flight tube. TOF MS is widely used due to their relatively high mass resolution (Sciex TripleTOF ~ 32,000 m/Δm), quick analysis time (μs time scale), high

transmission efficiency (i.e. good sensitivity), and can easily be coupled to other analyzers. The resolution can be further increased by adding a reflectron.[69] Reflectron effectively functions as an ion mirror to compensate for the spread in kinetic energy. A mass selecting quadrupole and collision quadruple in conjunction with the time of flight device is known as quadrupole time of flight mass spectrometer (QTOF MS). QTOF instruments were first developed in the mid-1990s and originally applied for sequencing of peptide species.[70-71] They have the advantage of improved sensitivity, mass accuracy and can be used for analysis of the large biomolecular sample.[72]

### 1.4.3 Dissociation Techniques

Gas-phase fragmentation remains very important and widely used in modern mass spectrometry. It has proven to be very useful for the identification and structural characterization of ions. Throughout the experiments presented, various fragmentation techniques were utilized to facilitate the formation of the desired product and fragmentation ions.

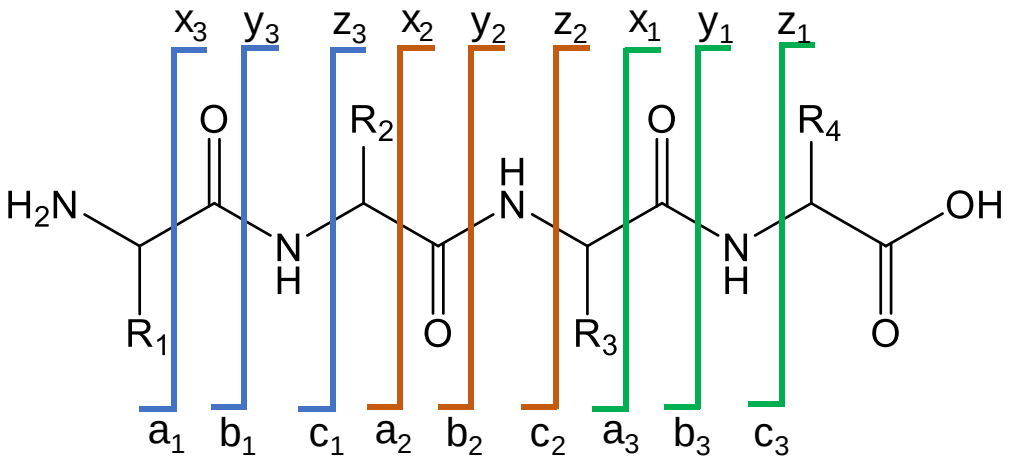


Scheme 1-4 Schematic showing nomenclature for common peptide backbone fragmentation pathways as proposed by Roespstorff and Fohlman.[73] $C_\alpha$-C bond cleavage generates *a/x* ions; C-N bond cleavage generates *b/y* ions; N-$C_\alpha$ bond cleavage generates *c/z* ions.

#### 1.4.3.1 Collision-Induced Dissociation

Collision-induced dissociation (CID), also referred to as collisionally activated dissociation (CAD), is one of the most widely used dissociation methods in tandem MS to obtain structural information.

##### 1.4.3.1.1 Ion-Trap CID

Ion trap CID is a slow heating dissociation method. In Ion-Trap CID, a dipolar excitation (AF2) was used for on-resonance collisional activation in Q3 linear ion trap (low-pressure cell, $10^{-5}$ torr) in a triple quadrupole/linear ion trap MS instrument. Activation amplitudes used were in the range of 20-100 mV, with an activation time of 200 ms. In triple / TOF hybrid instruments, ion-trap CID take place in the high-pressure cell ($10^{-3}$ torr). The AC waveform amplitude is generally higher in the high-pressure cell to surpass collisional cooling that can occur due to the bath gas. For peptides and proteins, the lowest energy pathway tends to fragment via N-$C_O$ bond cleavage, production *b*- and *y*-type fragment ions, as shown in Scheme 1-6.[73]

##### 1.4.3.1.2 Beam-Type CID

In beam-type CID, the precursor ions are isolated by Q1 and accelerated to q2 (collision cell). The ions collide with the neutral bath gas in q2 resulting fragmentation. This is considered a broadband excitation method as any ion with appropriate polarity and *m/z* to traverse the region will experience an energetic collision, resulting in collisional activation. The fragmentation pattern observed are largely dependent on the collision energy used. Collision energy (CE) is defined by the direct current (DC) potential difference between the quadrupolar cells. They can be in either high (keV/charge) or low energy regimes (10-200 eV/charge). Beam type CIDs are much more rapid and energetic than ion trap CID, allowing for different fragmentation patterns are observed.

1.4.3.1.3 Dipolar Direct Current CID

Dipolar Direct Current CID is a broadband excitation technique that is implemented via application of equal but opposite voltages to two of the four quadruple rods, while the remaining two rods are grounded. Ions are displaced from the center of the trap towards the rods, causing an increase in RF heating.[74-75] This causes more energetic collisions with the background to effect dissociation. DDC CID is a slow heating dissociation method. All the DDC experiments presented in this dissertation are performed on a modified QqTOF MS.

1.4.3.2 Electron Capture Dissociation

In 1998, McLafferty and co-worker introduced electron capture dissociation (ECD), a new fragmentation technique which induces radical chemistry through the interaction of the low-energy electron with polycations.[15] ECD is widely used in peptide and protein sequencing and characterization, especially in top-down sequencing approaches and PTM identification and location. ECD involves a multiply protonated molecule M interacting with a free electron to form an odd-electron ion. Liberation of the electron potential energy results in fragmentation of product ions (Equation 1.5).

Equation 1.5 $[M+nH]^{n+} + e^- \rightarrow [\,[M+nH]^{(n-1)+}\,]^{\bullet} \rightarrow$ fragments

The major product observed from the electron capture is typically the charge reduced species $[M+nH]^{(n-1)+\bullet}$ (i.e. the precursor ion has captured an electron but not undergone dissociation). The can be accompanied by hydrogen radical loss species, $[M + (n-1)H]^{(n-1)+}$.[76] For peptides and proteins, fragmentation pathways occur via N-$C_\alpha$ backbone cleavage resulting in either c'-/z$^{\bullet}$- or c$^{\bullet}$-z'- type ions (" ' " denotes a hydrogen addition and a " $^{\bullet}$ " denotes a radical). The

mechanism for initial electron capture and radical hydrogen transfer is still not fully understood. There are currently two mechanisms proposed: the Cornell mechanism[15] and the Utah-Washington mechanism[77]. ECD is used exclusively with Fourier transfer ion cyclotron resonance mass spectrometer (FTICR MS), as ECD requires a large amount of near thermal electron (<0.2 eV).

#### 1.4.3.3 Electron Transfer Dissociation

Electron transfer dissociation (ETD) was introduced by Hunt and coworkers.[16] It is a method of fragmenting multiply-charged cations by transferring electrons from a radical reagent anion, e.g. azobenzene, fluoranthene.[78] Transferring an electron creates an open-shell radical cation, which subsequently fragments to produce *c*- and *z*- type sequence ions from backbone N-$C_\alpha$ bond dissociation of peptides and proteins, similar to that observed in ECD (Equation 1.6).

Equation 1.6 $$[M+nH]^{n+} + A^{-\bullet} \rightarrow [\,[M+nH]^{(n-1)+}\,]^{\bullet} + A^{-} \rightarrow \text{fragments}$$

ETD offers a more robust method to characterize post-translational modification (PTMs), which are often labile under traditional CID conditions. Unlike ECD, ETD can be performed in less costly MS instruments such as quadrupole ion trap (QIT), quadrupole time of flight (QTOF), hybrid linear ion trap-orbitrap, etc. Studies have shown that the efficiency of electron transfer is greater than electron capture; however, the fragmentation efficiency is lower in ETD than for ECD.[16]

### 1.4.4 Detector

After an ion exits the mass analyzer, it hits the detector in the mass spectrometer generating a representative electric signal. This signal is picked up by a computer (with a dedicated software) capable of plotting intensity of the signal against it *m/z* value, called a spectrum. Typically, electron

multipliers are used which multiplies incident charge. Electron multipliers can be of a continuous-dynode type or can have discrete dynodes as in a photomultiplier.

## 1.5 Conclusions

Utilization of radical chemistry in conjunction with MS studies have arisen, not only due to its biological significance but also because of its potential for enhanced structural characterization. The following chapters describe in detail the development and application of new approaches to radical chemistry for enhanced structural elucidation with ESI MS/MS. In the first part of the dissertation research (**Chapter 2** and **3**), we utilized photo-induced thiyl radicals for charge tagging of neutral lipids (cholesterol, diacylglycerol, etc.) in microflow photo-reactors. These radical tagged lipids showed enhanced ionization efficiency and allowed structural characterization of the neutral lipids for analysis via ESI-MS/MS. In **Chapter 4**, the reactivity of cysteine disulfide towards hydroxyl radical (•OH) attack was studied. A low-temperature plasma from a dielectric barrier discharge was used to generate the •OH and was allowed to interact with cysteine disulfide bond in a nanoESI plume region. A systematic study on the reactivity of hydroxyl radical attack based on the electronic properties of substituents in the cysteine disulfide was also performed. In **Chapter 5**, an acetone/isopropanol-based photoinitiating system was used to perform radical induced disulfide cleavage and disulfide mapping in peptides/proteins. In comparison to conventional multistep approach for characterizing peptides with disulfide bonds, this online reaction approach is fast (<5 s), efficient (100% yield), and can also be coupled with high throughput proteomics workflows. Future studies should pursue the issue of structural characterization of biomolecules by coupling these techniques (Chapter 2, 3, and 5) with LC-MS/MS to further expand its capability for online analysis workflows.

## 1.6 Reference


1. Tureček, F.; Julian, R. R., Peptide Radicals and Cation Radicals in the Gas Phase. *Chem. Rev.* **2013,** *113* (8), 6691-6733.

2. Cheeseman, K. H.; Slater, T. F., An Introduction to Free Radical Biochemistry. *Brit. Med. bull*: 1993, 49 (3), 481-493.

3. Bollinger, J.; Edmondson, D.; Huynh, B.; Filley, J.; Norton; Stubbe, J., Mechanism of assembly of the tyrosyl radical-dinuclear iron cluster cofactor of ribonucleotide reductase. *Science* **1991,** *253* (5017), 292-298.

4. Shisler, K. A.; Broderick, J. B., Glycyl radical activating enzymes: Structure, mechanism, and substrate interactions. *Arch. Biochem. Biophys.* **2014,** *546*, 64-71.

5. Hancock, J. T.; Desikan, R.; Neill, S. J., Role of reactive oxygen species in cell signaling pathways. *Biochem. Soc. Trans.* **2001,** *29* (2), 345-349.

6. Pacher, P.; Beckman, J. S.; Liaudet, L., Nitric Oxide and Peroxynitrite in Health and Disease. *Psychol. Rev.* **2007,** *87* (1), 315-424.

7. Girotti, A. W., Lipid hydroperoxide generation, turnover, and effector action in biological systems. *J. Lipid Res.* **1998,** *39* (8), 1529-1542.

8. Davies, M., The oxidative environment and protein damage. *BBA-Proteins Proteomics*, 2005; Vol. 1703, pp 93-109.

9. Rastogi, R. P.; Richa, A.; Kumar, M. B.; Tyagi, R. P.; Sinha, R. P., Molecular Mechanisms of Ultraviolet Radiation-Induced DNA Damage and Repair. *J Nucleic Acids* **2010,** *2010* (2010).

10. Stadtman, E., Protein oxidation and aging. *Science* **1992,** *257* (5074), 1220-1224.

11. Klaunig, J. E. E. m. j. i. e.; Wang, Z.; Pu, X.; Zhou, S., Oxidative stress and oxidative damage in chemical carcinogenesis. *Toxicol. Appl. Pharmacol.* **2011,** *254* (2).

12. Maleknia, S. D.; Brenowitz, M.; Chance, M. R., Millisecond Radiolytic Modification of Peptides by Synchrotron X-rays Identified by Mass Spectrometry. *Anal. Chem.* **1999,** *71* (18), 3965-3973.

13. Maleknia, S. D.; Chance, M. R.; Downard, K. M., Electrospray-assisted modification of proteins: a radical probe of protein structure. *Rapid Commun. Mass Spectrom.* **1999,** *13* (23), 2352-2358.

14. Maleknia, S. D.; Downard, K. M., Advances in radical probe mass spectrometry for protein footprinting in chemical biology applications. *Chem. Soc. Rev.* **2014,** *43* (10), 3244-3258.

15. Zubarev, R. A.; Kelleher, N. L.; McLafferty, F. W., Electron Capture Dissociation of Multiply Charged Protein Cations. A Nonergodic Process. *J. Am. Chem. Soc.* **1998,** *120* (13), 3265-3266.

16. Syka, J. E. P.; Coon, J. J.; Schroeder, M. J.; Shabanowitz, J.; Hunt, D. F., Peptide and protein sequence analysis by electron transfer dissociation mass spectrometry. *Proc. Natl. Acad. Sci. U.S.A.* **2004,** *101* (26), 9528-9533.

17. Lin, C.; O'Connor, P., Ion Activation and Mass Analysis in Protein Mass Spectrometry. In *Protein and Peptide Mass Spectrometry in Drug Discovery*, Gross, M. L.; Guodong, C.; Pramanik, B. N., Eds. John Wiley & Sons, Inc.: Hoboken, New Jersey, 2012; pp 55-59.

18. Cui, W.; Rohrs, H. W.; Gross, M. L., Top-down mass spectrometry: Recent developments, applications, and perspectives. *Analyst* **2011,** *136* (19), 3854-3864.

19. Oh, H. B.; Moon, B., Radical-driven peptide backbone dissociation tandem mass spectrometry. *Mass Spectrom. Rev.* **2015,** *34* (2), 116-132.

20. Gao, J.; Thomas, D. A.; Sohn, C. H.; Beauchamp, J. L., Biomimetic Reagents for the Selective Free Radical and Acid–Base Chemistry of Glycans: Application to Glycan Structure Determination by Mass Spectrometry. *J. Am. Chem. Soc.* **2013,** *135* (29), 10684-10692.

21. Klán, P., *Photochemistry of organic compounds from concepts to practice*. Chichester, U.K. : Wiley: Chichester, U.K., 2009.

22. Jabłoński, A., Über den Mechanismus der Photolumineszenz von Farbstoffphosphoren. *Zeitschrift für Physik* **1935,** *94* (1), 38-46.

23. Norrish, R. G. W.; Kirkbride, F. W., 204. Primary photochemical processes. Part I. The decomposition of formaldehyde. *J. Chem. Soc.* **1932,** (0), 1518-1530.

24. Norrish, R. G. W.; Crone, H. G.; Saltmarsh, O. D., 318. Primary photochemical reactions. Part V. The spectroscopy and photochemical decomposition of acetone. *J. Chem. Soc.* **1934,** (0), 1456-1464.

25. Siegman, A. E.; Scully, M. O., Lasers. *Phys. Today* **1987,** *40* (12), 89-90.

26. Montalti, M., *Handbook of photochemistry*. 3rd ed.; CRC/Taylor & Francis: Boca Raton, 2006.

27. Beeler, A. B.; Corning, S. R., Photochemistry in flow. *Photochemistry* The Royal Society of Chemistry: 2016; Vol. 43, pp 173-190.

28. Jonathan, P. K.; Luke, D. E.; Kevin, I. B.-M., Flow photochemistry: Old light through new windows. *Beilstein J. Org. Chem.* **2012,** *8* (1), 2025-2052.

29. Su, Y.; Straathof, N. J. W.; Hessel, V.; Noël, T., Photochemical Transformations Accelerated in Continuous-Flow Reactors: Basic Concepts and Applications. Weinheim, 2014; Vol. 20, pp 10562-10589.

30. Raizer, Y. P., Gas Discharge Physics, Springer-Verlag Berlin, 1991.

31. Kogelschatz, U., Dielectric-Barrier Discharges: Their History, Discharge Physics, and Industrial Applications. *Plasma Chem. Plasma P.* **2003,** *23* (1), 1-46.

32. Kogelschatz, U.; Eliasson, B.; Egli, W., From ozone generators to flat television screens: History and future potential of dielectric-barrier discharges. *Pure Appl. Chem.* **1999,** *71* (10), 1819-1828.

33. Xia, Y.; Cooks, R. G., Plasma Induced Oxidative Cleavage of Disulfide Bonds in Polypeptides during Nanoelectrospray Ionization. *Anal. Chem.* **2010,** *82* (7), 2856-2864.

34. Tan, L.; Xia, Y., Gas-Phase Peptide Sulfinyl Radical Ions: Formation and Unimolecular Dissociation. *J. Am. Soc. Mass. Spectrom.* **2012,** *23* (11), 2011-2019.

35. Tan, L.; Xia, Y., Gas-Phase Reactivity of Peptide Thiyl (RS•), Perthiyl (RSS•), and Sulfinyl (RSO•) Radical Ions Formed from Atmospheric Pressure Ion/Radical Reactions. *J. Am. Soc. Mass. Spectrom.* **2013,** *24* (4), 534-542.

36. Wien, W., Untersuchungen über die electrische Entladung in verdünnten Gasen. *Annalen der Physik* **1898,** *301* (6), 440-452.

37. Thomson, J. J., LXIV. On the emission of negative corpuscles by the alkali metals. *Phil. Mag.* **1905,** *10* (59), 584-590.

38. Dempster, A. J., A new Method of Positive Ray Analysis. *Phys. Rev.* **1918,** *11* (4), 316-325.

39. Hoffmann, E. d., *Mass spectrometry: principles and applications*. 3rd ed.; Chichester, West Sussex, England; Hoboken, N.J. : John Wiley: 2007.

40. Biemann, K., The Application of Mass Spectrometry in Organic Chemistry: Determination of the Structure of Natural Products. *Angew. Chem. Int. Ed. Engl.* **1962,** *1* (2), 98-111.

41. Munson, M. S. B.; Field, F. H., Chemical Ionization Mass Spectrometry. I. General Introduction. *J. Am. Chem. Soc.* **1966,** *88* (12), 2621-2630.

42. Fenn, J.; Mann, M.; Meng, C.; Wong, S.; Whitehouse, C., Electrospray ionization for mass spectrometry of large biomolecules. *Science* **1989,** *246* (4926), 64-71.

43. Fenn, J. B.; Mann, M.; Meng, C. K.; Wong, S. F.; Whitehouse, C. M., Electrospray ionization–principles and practice. *Mass Spectrom. Rev.* **1990,** *9* (1), 37-70.

44. Karas, M.; Bachmann, D.; Bahr, U.; Hillenkamp, F., Matrix-assisted ultraviolet laser desorption of non-volatile compounds. *Int. J. Mass Spectrom. Ion Processes* **1987,** *78*, 53-68.

45. Takáts, Z.; Wiseman, J. M.; Gologan, B.; Cooks, R. G., Mass Spectrometry Sampling Under Ambient Conditions with Desorption Electrospray Ionization. *Science* **2004,** *306* (5695), 471-473.

46. Dole, M.; Mack, L. L.; Hines, R. L.; Mobley, R. C.; Ferguson, L. D.; Alice, M. B., Molecular Beams of Macroions. *J. Chem. Phys.* **1968,** *49* (5), 2240-2249.

47. Cech, N. B.; Enke, C. G., Practical implications of some recent studies in electrospray ionization fundamentals. *Mass Spectrom. Rev.* **2001,** *20* (6), 362-387.

48. Tang, L.; Kebarle, P., Dependence of ion intensity in electrospray mass spectrometry on the concentration of the analytes in the electrosprayed solution. *Anal. Chem.* **1993,** *65* (24), 3654-3668.

49. Rayleigh, L., XX. On the equilibrium of liquid conducting masses charged with electricity. *The London, Edinburgh, and Dublin Philosophical Magazine and Journal of Science* **1882,** *14* (87), 184-186.

50. Kebarle, P., A brief overview of the present status of the mechanisms involved in electrospray mass spectrometry. *J. Mass Spectrom.* **2000,** *35* (7), 804-817.

51. Iribarne, J. V.; Thomson, B. A., On the evaporation of small ions from charged droplets. *J. Chem. Phys.* **1976,** *64* (6), 2287-2294.

52. Fernandez de la Mora, J., Electrospray ionization of large multiply charged species proceeds via Dole's charged residue mechanism. *Anal. Chim. Acta* **2000,** *406* (1), 93-104.

53. McAllister, R. G.; Metwally, H.; Sun, Y.; Konermann, L., Release of Native-like Gaseous Proteins from Electrospray Droplets via the Charged Residue Mechanism: Insights from Molecular Dynamics Simulations. *J. Am. Chem. Soc.* **2015,** *137* (39), 12667-12676.

54. Konermann, L.; Ahadi, E.; Rodriguez, A. D.; Vahidi, S., Unraveling the Mechanism of Electrospray Ionization. *Anal. Chem.* **2013,** *85* (1), 2-9.

55. Wilm, M. S.; Mann, M., Electrospray and Taylor-Cone theory, Dole's beam of macromolecules at last? *Int. J. Mass Spectrom. Ion Processes* **1994,** *136* (2), 167-180.

56. Wilm, M.; Mann, M., Analytical Properties of the Nanoelectrospray Ion Source. *Anal. Chem.* **1996,** *68* (1), 1-8.

57. Gibson, G. T. T.; Mugo, S. M.; Oleschuk, R. D., Nanoelectrospray emitters: Trends and perspective. *Mass Spectrom. Rev.* **2009,** *28* (6), 918-936.

58. Schmidt, A.; Karas, M.; Dülcks, T., Effect of different solution flow rates on analyte ion signals in nano-ESI MS, or: when does ESI turn into nano-ESI? *J. Am. Soc. Mass. Spectrom.* **2003,** *14* (5), 492-500.

59. Prestage, J. D.; Dick, G. J.; Maleki, L., New ion trap for frequency standard applications. *J. Appl. Phys.* **1989,** *66* (3), 1013-1017.

60. Paul, W.; Steinwedel, H., Notizen: Ein neues Massenspektrometer ohne Magnetfeld. In *Zeitschrift für Naturforschung A*, 1953; Vol. 8, p 448.

61. Paul, W., Electromagnetic Traps for Charged and Neutral Particles (Nobel Lecture). *Angew. Chem. Int. Ed. Engl.* **1990,** *29* (7), 739-748.

62. McLachlan, N. W., *Theory and application of Mathieu functions*. Oxford, Clarendon Press: Oxford, 1947.

63. Douglas, D. J.; Frank, A. J.; Mao, D., Linear ion traps in mass spectrometry. *Mass Spectrom. Rev.* **2005,** *24* (1), 1-29.

64. Yost, R. A.; Enke, C. G., Selected Ion Fragmentation with a Tandem Quadrupole Mass Spectrometer. *J. Am. Chem. Soc.* **1978,** *100* (7), 2274-2275.

65. Yost, R. A.; Enke, C. G., Triple quadrupole mass spectrometry for direct mixture analysis and structure elucidation. *Anal. Chem.* **1979,** *51* (12), 1251.

66. Hager, J. W., A new linear ion trap mass spectrometer. *Rapid Commun. Mass Spectrom.* **2002,** *16* (6), 512-526.

67. Wolff, M. M.; Stephens, W. E., A Pulsed Mass Spectrometer with Time Dispersion. *Rev. Sci. Instrum.* **1953,** *24* (8), 616-617.

68. Boesl, U., Time-of-flight mass spectrometry: Introduction to the basics. *Mass Spectrom. Rev.* **2017,** *36* (1), 86-109.

69. Mamyrin, B. A.; Karataev, V. I.; Shmikk, D. V.; Zagulin, V. A., Mass reflection: a new nonmagnetic time-of-flight high-resolution mass- spectrometer. *Zh. Eksp. Teor. Fiz. 64: No. 1, 82-89.* **1973**.

70. Morris, H. R.; Paxton, T.; Dell, A.; Langhorne, J.; Berg, M.; Bordoli, R. S.; Hoyes, J.; Bateman, R. H., High Sensitivity Collisionally-activated Decomposition Tandem Mass Spectrometry on a Novel Quadrupole/Orthogonal-acceleration Time-of-flight Mass Spectrometer. *Rapid Commun. Mass Spectrom.* **1996,** *10* (8), 889-896.

71. Shevchenko, A.; Chernushevich, I.; Ens, W.; Standing, K.; Thomson, B.; Wilm, M.; Mann, M., Rapid 'de novo' peptide sequencing by a combination of nanoelectrospray, isotopic labeling and a quadrupole/time-of-flight mass spectrometer. *Rapid Commun. Mass Spectrom.* **1997,** *11* (9), 1015-1024.

72. Steen, H.; Küster, B.; Mann, M., Quadrupole time-of-flight versus triple-quadrupole mass spectrometry for the determination of phosphopeptides by precursor ion scanning. *J. Mass Spectrom.* **2001,** *36* (7), 782-790.

73. Roepstorff, P.; Fohlman, J., Proposal for a common nomenclature for sequence ions in mass spectra of peptides. *Biomed. Mass Spectrom.* **1984,** *11* (11), 601.

74. Tolmachev, A. V.; Vilkov, A. N.; Bogdanov, B.; PĂsa-Tolić, L.; Masselon, C. D.; Smith, R. D., Collisional activation of ions in RF ion traps and ion guides: The effective ion temperature treatment. *J. Am. Soc. Mass. Spectrom.* **2004,** *15* (11), 1616-1628.

75. Webb, I. K.; Londry, F. A.; McLuckey, S. A., Implementation of dipolar direct current (DDC) collision-induced dissociation in storage and transmission modes on a quadrupole/time-of-flight tandem mass spectrometer. *Rapid Commun. Mass Spectrom.* **2011,** *25* (17), 2500-2510.

76. Breuker, K.; Oh, H.; Cerda, B. A.; Horn, D. M.; McLafferty, F. W., Hydrogen Atom Loss in Electron-Capture Dissociation: A Fourier Transform-Ion Cyclotron Resonance Study with Single Isotopomeric Ubiquitin Ions. *Eur. J. Mass Spectrom.* **2002,** *8* (2), 177-180.

77. Syrstad, E.; Turecček, F., Toward a general mechanism of electron capture dissociation. *J. Am. Soc. Mass. Spectrom.* **2005,** *16* (2), 208-224.

78. Coon, J. J.; Schroeder, M. J.; Shabanowitz, J.; Hunt, D. F.; McLafferty, F. W., Peptide and Protein Sequence Analysis by Electron Transfer Dissociation Mass Spectrometry. *Proc. Natl. Acad. Sci. U.S.A.* **2004,** *101* (26), 9528-9533.

# CHAPTER 2. THIYL RADICAL-BASED CHARGE TAGGING ENABLES RAPID STEROL QUANTITATION VIA MASS SPECTROMETRY

(Adapted from publication in Analytical Chemistry)

## 2.1 Introduction

Sterols are naturally occurring and essential lipid molecules for animals (zoosterols), plants (phytosterols), and fungi. They commonly contain an unsaturated four-ring core structure (A, B, C, D rings), a 3β-hydroxyl (OH) group, and an aliphatic side chain attached to C17 (demonstrative structures shown in Scheme 1a). The major biological functions of sterols include regulating membrane fluidity and serving as precursors of steroids, vitamin D, hormones, and many other important mediator molecules.[1] Gas chromatography-mass spectrometry (GC-MS) and liquid chromatography-mass spectrometry (LC-MS) are the primary methods for the analysis of sterols from complex mixtures.[2-3] Since GC-MS suffers from lower sensitivity and throughput,[4] more recent development focuses on enhancing separation and throughput using high-performance liquid chromatography (HPLC)-MS platform, which typically employs electrospray ionization (ESI)-MS interface.[5] Given the nonpolar nature of sterols, charge derivatization is a necessary and effective strategy to enhance the response of sterols via ESI. Established derivatization methods either target the hydroxyl function group via forming an ester bond with a charge tag (e.g. sulfate,[6] phosphonium,[7] picolinyl esters[8]) or convert the hydroxyl to ketone first and then use carbonyl chemistry to link a charge tag to sterols (e.g. forming Girard P hydrazones).[9-10] These methods significantly improved sterol analysis via ESI with the limit of detection (LOD) achieved at nM to sub-nM concentration.[6-10] The derivatization reactions typically require several hours or even days to accomplish. Several derivatization reagents need to be synthesized in-house, further curbing wide accessibility to these methods.

Radical reactions, due to their fast reaction kinetics, are attractive candidates for chemical derivatization. Although only marginally explored, some notable examples of derivatization via radical chemistry include protein surface mapping via radical modification[11-12] and carbon-carbon double location determination in lipids via the Paternò–Büchi reactions.[13-14] Thiyl radicals are known to exhibit high reactivity toward alkenes, which has been harnessed as a type of "click chemistry" for forming a carbon-sulfur bond.[15-16] Inspired by the reactions of thiyl radicals toward alkenes, we aim to tailor thiyl radical chemistry into a highly efficient charge derivatization strategy to enhance the analysis of nonpolar molecules, which are poorly detected by ESI-MS. In this report, we choose sterols as the first-time demonstration of this concept.

## 2.2 Materials and Methods

### 2.2.1.1 Materials

All the reagents and solvents were purchased from commercial sources and were used without further purification. Cholesterol standard (purity ≥99%) was purchased from Nu-Chek Prep, Inc. (Elysian, MN, USA). Campesterol (purity >99%), and cholesterol-25,26,26,26,27,27,27-$d_7$ (purity >99%) were purchased from Avanti Lipids Polar, Inc. (Alabaster, AL, USA). β-sitosterol (purity >95%), stigmasterol (purity ~95%), brassicasterol (purity >98%), cycloartenol (purity ≥90%), *N*,*O*-bis-trimethylsilyltrifluoroacetamide (BSTFA) with 1% of trimethylchlorosilane (TMCS), *N*,*N*-dimethylformamide (DMF), cysteamine hydrochloride, Sodium 2-mercaptoethanesulfonate (MESNA), thioglycolic acid (TGA), 2,2-dimethoxy-2-phenylacetophenone (DMPA), sodium hydroxide (NaOH), ethanol, potassium hydroxide (KOH), *n*-hexane, diethyl ether, chloroform and ethyl acetate were purchased from Sigma-Aldrich (St. Louis, MO, USA). Deionized water was obtained from a purification system at 0.03 μS·cm (model: Micropure UV; Thermo Scientific; San Jose, CA, USA). Pooled human plasma (Li Heparin used

as anticoagulant) was purchased from Innovative Research (Novi, MI, USA). Vegetable oil (soybean oil) was bought from a supermarket and then stored at -20$^{o}$C until analysis.

### 2.2.2 Extraction protocols for sterol analysis from oil and plasma

#### 2.2.2.1 Total sterols in human plasma

The extraction procedure is derived as previously described by Yang et al.[17] An aliquot of human plasma (30 µL, spiked with 100 µL of cholesterol-$d_7$, 394 µg/mL in chloroform) and then saponified in 2 mL of 2 M KOH ethanol/water (8:2, v/v) at 80$^{o}$C for 1 h. Saponification is performed to convert sterol esters to free sterols, and also to remove other lipids (fatty acids and glycerin) from the extract before sterol analysis. After cooling, 2 mL of deionized water was added, followed by 3 mL of *n*-hexane. The mixture was vortexed for 1 min and then, centrifuged for 5 minutes at 3000 x g. The upper hexane layer was collected, and the extraction procedure was repeated twice with *n*-hexane. The hexane extracts were combined and evaporated to dryness, dissolved in 1 mL chloroform and stored until the derivatization process for analysis.

#### 2.2.2.2 Esterified and free sterols in human plasma

Separation of esterified and free sterols in human plasma was determined following the method developed by Lund et al.[18] An aliquot of human plasma (30 µL, spiked with 100 µL of cholesterol-$d_7$, 394 µg/mL in chloroform) was subjected to Bligh/Dyer extraction, dried under nitrogen, and reconstituted in 1 mL toluene. The lipid extract was loaded onto a 100-mg Isolute silica cartridge (Biotage, Charlotte, NC) previously conditioned with 2 mL of *n*-hexane. Esterified sterols were eluted first with 2 mL of *n*-hexane, while free sterols eluted next with 8mL of 30% isopropanol in *n*-hexane. Both fractions of sterols were separately subjected to saponification, and extraction according to the procedures described for the total sterol analysis.

2.2.2.3 Total sterols in vegetable oil

The procedure is derived from the extraction protocol as reported by Bedner et al.[19] 30 mg of the vegetable oil was spiked with 100 µL of internal standard (cholesterol-$d_7$, 394 µg/mL in chloroform) was subjected directly to saponification, and extraction according to the procedures for total sterol analysis for human plasma.

2.2.2.4 Esterified and free sterol in vegetable oil

Separation of esterified and free sterols in vegetable oil was determined following the extraction procedure previously reported by Olivera et. al.[20] 30 mg of the vegetable oil (spiked with 100 µL of cholesterol-$d_7$, 394 µg/mL in chloroform) was diluted with 1 mL of *n*-hexane and was loaded onto a 300-mg SPE silica cartridge (Biotage, Charlotte, NC) previously conditioned with 5 mL of *n*-hexane. Esterified sterols were eluted first with 10 ml of *n*-hexane/diethyl ether (95:5, v/v), while the more polar free sterols were extracted next using 10 mL of *n*-hexane/diethyl ether/ethanol (25:25:50, v/v/v). Both fractions of sterols were separately subjected to saponification, and extraction according to the procedures described for the total sterol analysis.

2.2.2.5 Derivatization of sterols in bulk processes

A mixture of sterol (0.1-200µM range), thiol reagent (100 mM), and DMPA (photo-initiator) (1 mM) was dissolved in DMF in a borosilicate scintillation glass vial. The content of the vial were mixed thoroughly to ensure uniformity and were degassed with nitrogen gas for 5 minutes. The mixture was then irradiated using a low-pressure mercury (LP-Hg) lamp with an emission band at 351nm (model number: 80-1057-01/351; BHK, Inc.; Ontario, CA, USA) for 15-20 minutes at room temperature. This set-up, both the light source and the vial, was covered with aluminum foil, in order to increase the light intensity by reflecting UV light. All reactions were carried out at ambient temperature. The reaction progress can be monitored by MS. The reaction

solution was then dissolved in ~0.1 N sodium hydroxide aqueous solution and was extracted with ethyl acetate (x 2) to remove the excess thioglycolic acid.

### 2.2.3 Derivatization of sterols in a photochemical microreactor

A schematic overview of the photochemical microreactor setup is shown in figure 1 (c). The flow reactor capillary (fused silica capillary tubing (100 µm i.d., 375 µm o.d.)) is passed through a small cardboard box (reaction chamber), without coiling. The overall length of the tube inside the chamber is 10 cm. The LP-Hg (emission band at 351 nm) is placed next to capillary tube (at a distance of 0.5 cm) inside the box. All the reactant with the optimized reaction concentration from the bulk processes were premixed and degassed prior to introduction into the chamber and were irradiated in one-layer continuous flow format (µL/min rate). The total residence time for the reaction was calculated by the total reactor volume exposed to the UV irradiation by the sample flow rate. It is worth mentioning that the overall set-up of the photo-microreactor itself is quite general and can be readily applied or optimized for other photochemical applications.

### 2.2.4 Mass spectrometry

All mass analysis of derivatized sterols were performed using nano-electrospray ionization (nanoESI)-MS. NanoESI tips (~10 µm o.d.) were made from borosilicate glass capillary tips (1.5 mm o.d. and 0.86 mm i.d.) using a micropipette puller (P-1000 Flaming/Brown; Sutter Instrument, Novato, CA, USA). Data collection were done on a 4000 QTRAP (triple quadrupole/linear ion trap (LIT)) mass spectrometer. Analyst software 1.6.2 (Applied Biosystems / Sciex) was used for instrument control and data processing. $MS^1$ mass analysis were performed in LIT mode in Q3 by the mass selective axial scan.[21] Typical MS parameters during the study were: nanoESI spray voltage, - (1500-1800) V; curtain gas, 10 psi; declustering potential, -20V; scan rate, 1000 Da/s unless otherwise specified. Two modes of Collision-induced dissociation (CID) were performed:

beam type CID and ion trap CID. For neutral loss scan (NLS), collision energy (CE) optimized at 32 V was used.

### 2.2.5 Derivatization yield for cholesterol

GC-MS analysis of sterols was performed to estimate the yield of derivatization since sterols are not typically detected using ESI. Cholesterol was derivatized using BSTFA+1%TMCS as the silylating reagent and was operated in the SIM mode. Analysis was carried out with a Shimadzu QP-2010 GC-MS system (70 eV, electron ionization mode), equipped with DB-5MS (20.0 m X 0.18 mm I.D., 0.18 µm film thickness) column. Helium was used as the carrier gas, at a flow rate of 1.0 mL/min. Samples were introduced in split-injection mode (1:20). The column oven temperature was set initially at 70.0 ºC (3 min) and then programmed to rise to 325.0 ºC (3 min) at a rate of 13 ºC/min. The mass range scanned was 50-800. The yield was determined based on the loss of the silylated cholesterol peak following the photochemical derivatization reaction.

## 2.3 Results and Discussions

### 2.3.1 Charge tagging of cholesterol

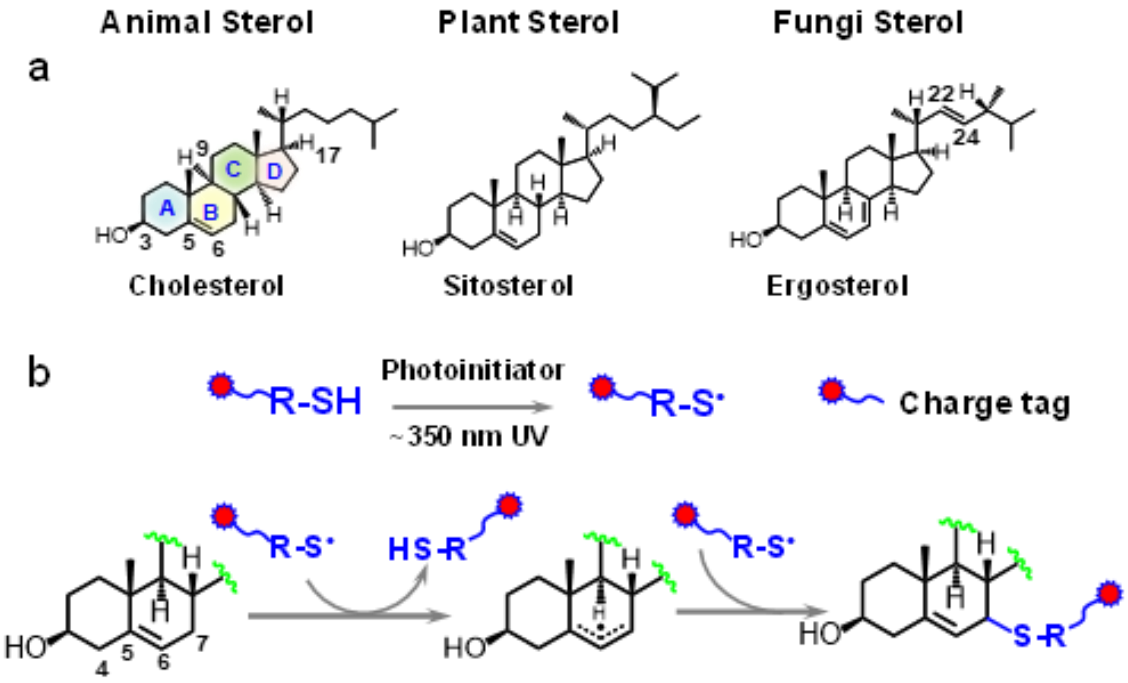


Scheme 2-1 (a) Chemical structures of representative sterols in animals, plants, and fungi. (b) Proposed reaction pathways for thiyl radical-based charge tagging of sterols. Tagging can happen at C7 and C5 (structure not shown).

The C5-C6 double bond in the B ring of sterols makes them susceptible to thiyl radical tagging (Scheme 1b). In the survey studies, cholesterol was used as a model compound to react with a series of thiol reagents each consisting of a readily-charged functional group via ESI (cysteamine, thioglycolic acid (TGA), and sodium 2-mercaptoethanesulfonate). Based on the reaction conditions reported in thiol-ene coupling,[22] the thiol reagent (100 mM) and cholesterol (5 µM) were co-dissolved in dimethylformamide (DMF) with 1 mM 2,2-dimethoxy-2-phenylacetophenone (DMPA) added as a photoinitiator to effect thiyl radical formation. The reaction mixture was placed in a borosilicate glass vial and irradiated by a low-pressure mercury lamp with emission centered at 351 nm. After the completion of the reaction, 1 ml of sodium

hydroxide (NaOH) solution (0.1 M) was added to the reaction mixture and the reaction product was extracted with ethyl acetate. The above procedure effectively removed remaining high concentration TGA, which could cause signal suppression upon subsequent nanoESI-MS analysis.

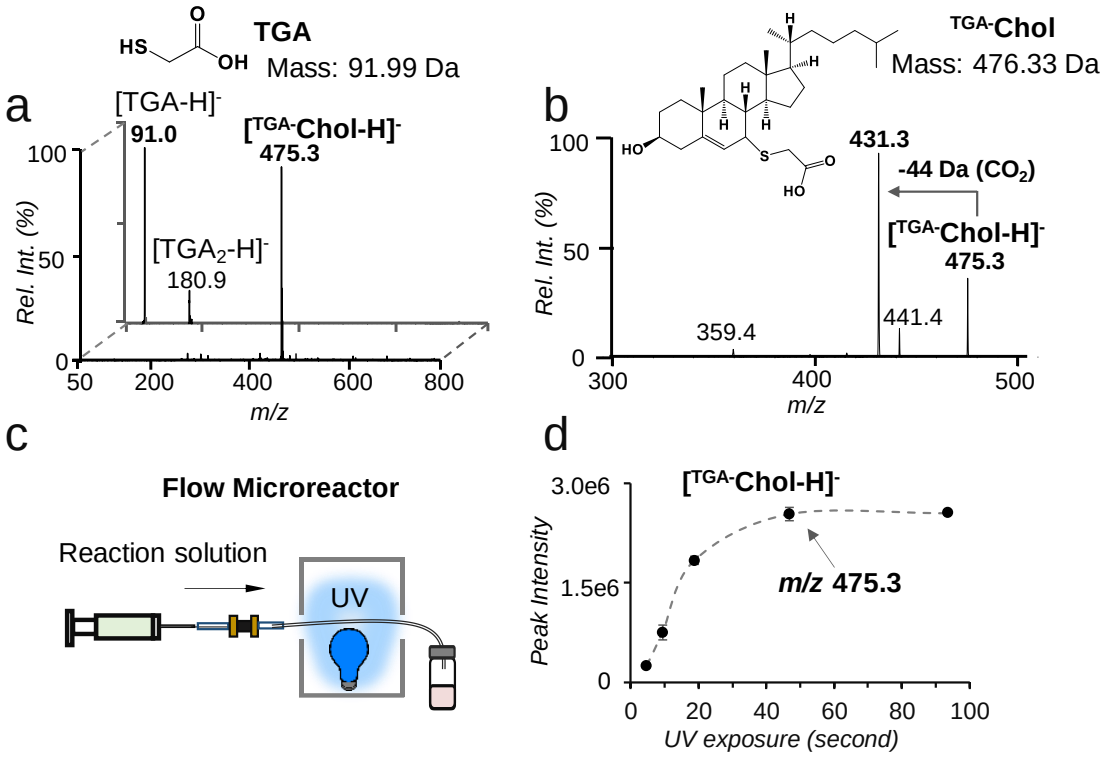


Figure 2-1(a) Negative ion mode nanoESI MS spectra of cholesterol (5 µM) and TGA before reaction (back panel) and after reaction (front panel). TGA-tagged cholesterol appears at *m/z* 475.3 ([TGA-Chol-H]-). (b) MS2 CID of [TGA-Chol-H]-. (c) Schematic for a flow microreactor. (d) Plot of the peak intensity of [TGA-Chol-H]- as a function of UV exposure time using the flow microreactor setup.

Figure 1a compares nanoESI MS spectra of cholesterol before and after TGA tagging in the negative ion mode. Before reaction, only deprotonated TGA, $[TGA\text{-}H]^-$ (*m/z* 91.0) and a small amount of its oxidized product, $[O\text{-}TGA_2\text{-}H]^-$ (*m/z* 180.9), were observed. As a big contrast, the post-reaction spectrum is dominated by a single peak at *m/z* 457.3 (front panel of Figure 1a). Accurate mass measurement proved that this product (*m/z* 457.3253) had a mass increase of 89.9776 Da relative to cholesterol, corresponding to a net addition of $C_2H_2O_2S$, the elemental

composition of deprotonated TGA (spectrum not shown). Collision-induced dissociation (CID) of the product ($[^{TGA}$-Chol-H$]^-$) produced a prominent loss of 44 Da ($CO_2$) from the carboxylic acid group of the TGA moiety (Figure 1b). The above data all supported that TGA addition to cholesterol was successful.

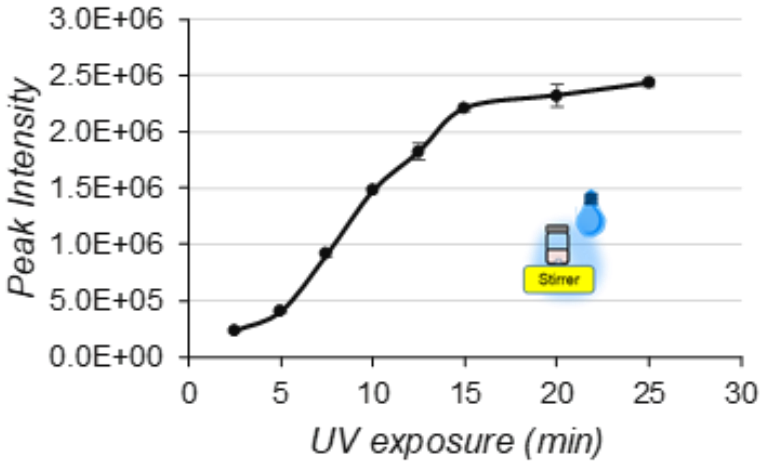


Figure 2-2 Reaction kinetics for TGA derivatization of cholesterol using batch processes plotted over UV exposure. The inset shows schematics for bulk reaction.

Photochemical reactions in flow microreactors (micrometer (μm)-size inner dimensions) have been demonstrated to proceed more rapidly due to higher photon absorption efficiency.[23] To speed up TGA derivatization and make this reaction compatible with small sample size handling which is typically encountered in bioanalysis, a flow microreactor employing a fused silica capillary (100 μm i.d., 375 μm o.d.) has been developed (Figure 1c). The reaction kinetic curve was obtained by monitoring the ion intensity of $[^{TGA}$-Chol-H$]^-$ (Figure 1d). Clearly, the reaction proceeded to a steady state within 50 seconds. The reaction progress was also monitored by bulk processes as shown in figure 2.2, which showed a rapid increase in the first 15 minutes and a plateau afterward. The vastly accelerated reaction rate in the flow microreactor can be attributed

to the large surface area to volume ratio of the microreactor, allowing maximal light transmission and thus significantly improving irradiation efficiency of the reaction mixture.

a

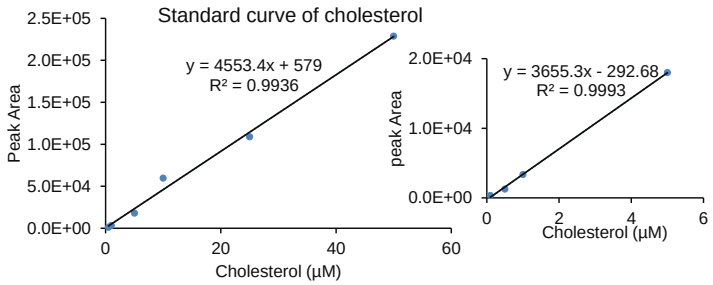


b

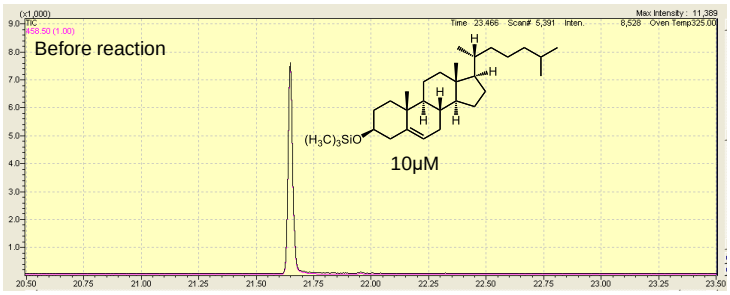


c

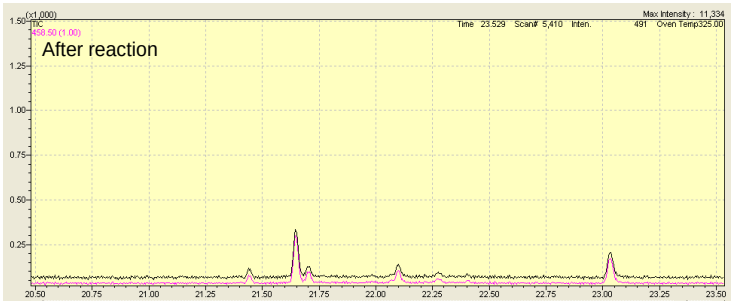


Figure 2-3 (a) GC/MS standard curve used for determination of the derivatization yield of Cholesterol. GC/MS chromatograms of silylated cholesterol (retention time 21.65 min) (b) before reaction (c) after reaction.

Quantitative analysis of cholesterol via GC-MS showed that the derivatization yield was above 90% after 20-minute UV exposure (Figure 2.3). TGA outperformed the rest thiol reagents

tested in this study in terms of speed of reaction, product yield, and the easiness of sample cleanup for MS analysis; therefore, it was chosen for further method development.

Initially, we expected to detect the thiol-ene coupling product, resulting from thiyl radical addition to the C5-C6 double bond followed by H atom abstraction from another thiol. This product should appear at *m/z* 477.3; however, the observed product (peak at *m/z* 475.3) is two Da less than the thiol-ene coupling product, suggesting the preservation of the C=C. This result can be rationalized from the reverse nature of thiyl radical addition to a C=C and the structure of cholesterol. The rate of thiyl radical addition to a ring C=C is several orders of magnitude smaller than the product dissociation rate,[24] leading to ineffective thiol-ene coupling. This explains why the thiol-ene coupling product was not observed for cholesterol. On the other hand, although alkyl thiyl radicals cannot abstract alkyl hydrogen due to the relatively small S-H bond dissociation energies (BDEs, ~87 kcal/mol),[25] they can abstract the allylic hydrogen at the C7 position (C7-H BDE=83.2 kcal/mol).[26] We hypothesize that the TGA thiyl radical abstracts the C7-H, forming a delocalized three-carbon allylic radical intermediate, which recombines with another thiyl radical at either C5 or C7 position, leading to the observed TGA-tagged cholesterol. The proposed reaction pathway is shown in Scheme 2.1b. It is worth noting that TGA thiyl radical is unlikely to abstract C4-H, the BDE of which is 89.0 kcal/mol,[26] higher than the BDE of the alkyl thiol reagent. The proposed reaction pathway (Scheme 1b), however, needs to be further verified, e.g., using C7-D cholesterol, to provide more evidence on the C7-H abstraction process.

Established derivatization techniques target the free -OH functionality of sterols and thus have a limitation in analyzing the esterified form of sterols. As a contrast, the TGA tagging method can be readily applied to cholesterol ester (CE) analysis. Figure 2.4a shows the post-tagging spectrum using cholesterol acetate ($[^{TGA-}$Ac-Chol-H$]^-$, *m/z* 517.2) as a demonstration. $MS^2$ CID of

the tagged product (Figure 2.4b) produced 44 Da loss and 86 Da loss. The latter fragment resulted from sequential losses of $CO_2$ (from TGA) and $CH_2CO$ (from the acetyl moiety).

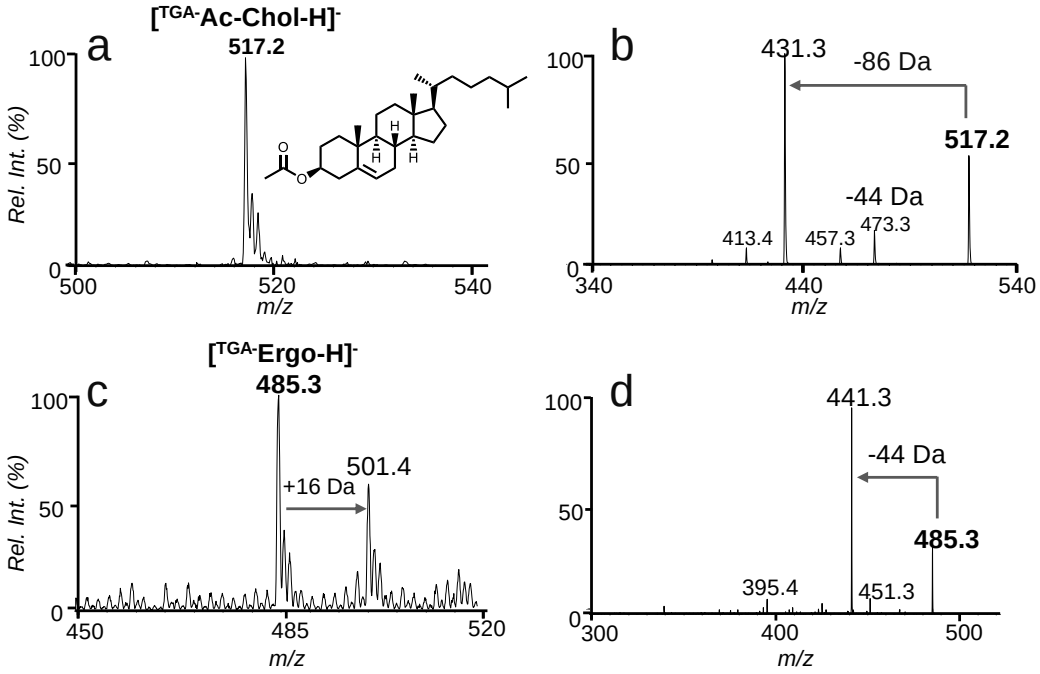


Figure 2-4 Negative ion mode nanoESI-MS of TGA derivatized (a) cholesterol acetate (1 μM, m/z 517.2), and (b) MS2 CID of [TGA-Ac-Chol-H]-, (c) ergosterol (1 μM, m/z 485.3), and (d) MS2 CID of [TGA-Ergo-H]-.

Ergosterol serves as a structural component of fungi cell membrane and thus it is a frequently used target for developing antifungal drugs.[27] Ergosterol consists of three C=Cs, the diene structure in the B ring and a C22-C23 double bond in the aliphatic chain (structure shown in Scheme 2.1a). Since the aliphatic allylic hydrogen has a higher BDE than that of C9-H (about 10 kcal/mol higher),[25] we expect that TGA tagging would be more competitive at the B ring. Indeed, only one TGA tagging product (the peak at *m/z* 485.3, Figure 2.4c) was observed from the reaction of TGA and ergosterol for an extended reaction period and no competing thiol-ene coupling product was observed (should appear at *m/z* 487.5, if formed). $MS^2$ CID of tagged product produced abundant 44 Da loss (Figure 2.4d), characteristic to the TGA tag. Due to the presence of

diene in the B ring, minor sequential oxidation of the TGA-tagged ergosterol was detected (the peak at *m/z* 501.4 in Figure 4c).

We further applied the TGA tagging to several other frequently encountered sterols from mammalian cells and plants (e.g. 7-dehydrocholesterol, Figure 2.5). We found that that efficient and single TGA tagging could be achieved for sterols consisting of at least one C=C in the B ring. TGA tagging, however, was not successful for steroids having a conjugated enone structure (e.g. progesterone) due to competitive photochemical rearrangement reactions.[28] These results demonstrate that thiyl radical tagging of sterols exhibits selectivity to unsaturated B ring, which is an attractive feature for mixture analysis.

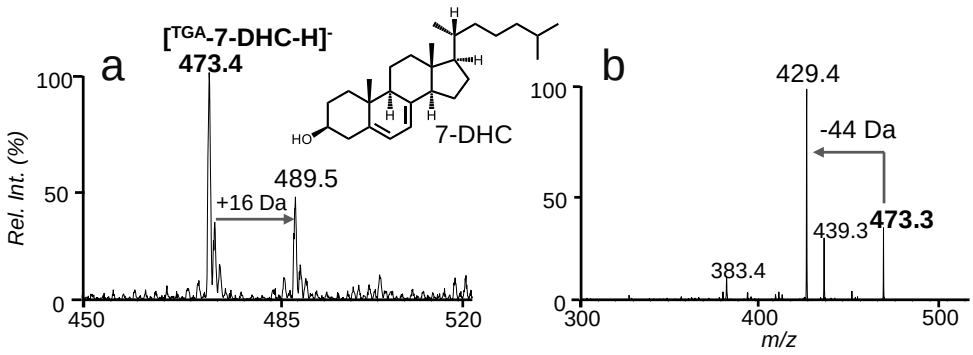


Figure 2-5 NanoESI-MS of TGA derivatized (a) 7-dehydrocholesterol (1 µM, detected at m/z 473.3, negative ion mode), (b) $MS^2$ CID of $[^{TGA}$-7-DHC-H$]^-$.

Tandem mass spectrometry (MS/MS) analysis of TGA-tagged sterols all showed abundant loss of $CO_2$, due to the presence of deprotonated carboxylic acid moiety. Based on this characteristic fragmentation channel, 44 Da neutral loss scan (NLS) was evaluated for the quantitation of TGA-tagged sterols. Figure 2.6 (a) shows a representative 44 Da NLS spectrum of 1 µM cholesterol with 5 µM cholesterol-$d_7$ (Chol-$d_7$) added as an internal standard (IS). The calibration curve obtained by plotting the peak area ratios of $[^{TGA}$-Chol-H$]^-$ and $[^{TGA}$-IS-H$]^-$ against cholesterol concentration showed good linear regression ($R^2$ =0.9968). LOD was achieved at 0.5

nM (S/N ratio >3), comparable to those reported by other charge derivatization approaches, such as sulfation (0.2 nM),[6] phosphonium labelling (0.05 nM),[7] *N*-alkyl pyridinium quaternization (54 nM),[29] and Girard P reagent (0.1 nM).[10] Most importantly, the whole process of TGA tagging and subsequent MS analysis is significantly shortened to less than 2 min per run. Although the $CO_2$ loss is a facile fragmentation channel for unsaturated fatty acids, their potential interference for sterol analysis via 44 Da NLS should be limited due to their appearance at lower *m/z* range than the commonly observed sterols.

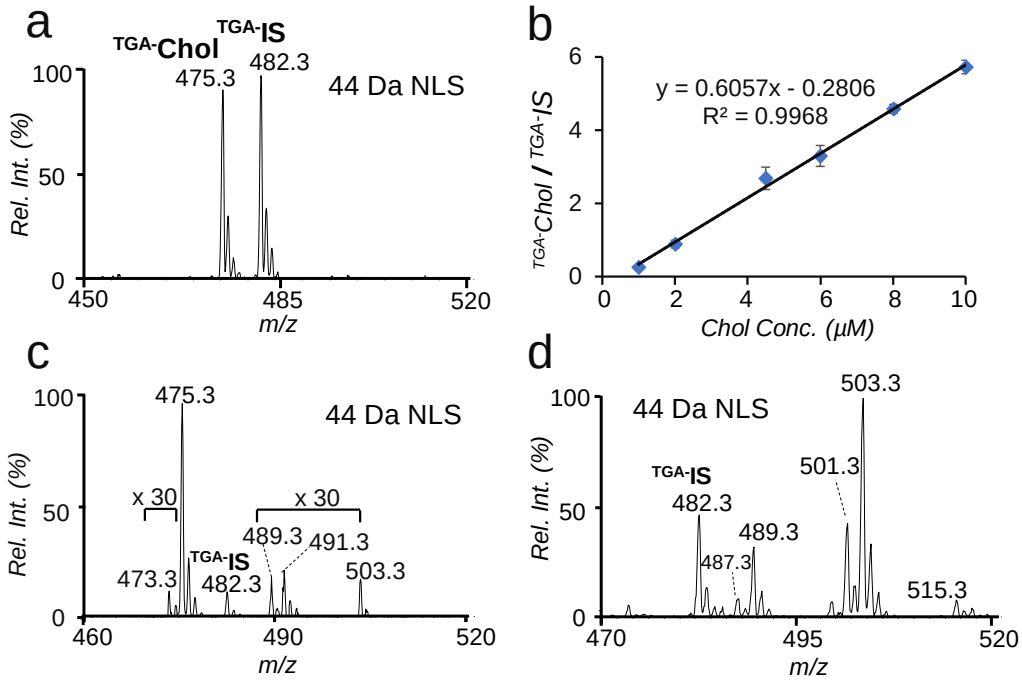


Figure 2-6 (a) 44 Da NLS of TGA tagged cholesterol (1μM) and Cholesterol-$d_7$ (IS, 5 μM). (b) Calibration curve obtained for cholesterol based on 44 Da NLS. 44 Da NLS profile of TGA tagged sterols from (c) 20 μL human plasma and (d) soybean oil.

Because of the selectivity and sensitivity of TGA tagging toward sterols, this method is well suited for small sample volume analysis without a prior lipid extraction. As a demonstration, 20 μL of human plasma was dissolved in DMF at a final volume of 200 μL for TGA derivatization (1-minute UV irradiation). Figure 2.6c shows the 44 Da NLS spectrum. Besides the TGA-tagged

cholesterol peak (*m/z* 475.4), less abundant sterols such as dehydrocholesterol (*m/z* 473.4, intact mass: 384.6 Da), campesterol (*m/z* 489.3, intact mass: 400.37 Da), and sitosterol (*m/z* 503.3, intact mass: 414.4 Da) were also detected. The peak at *m/z* 491.4 corresponds to hydroxycholesterols (intact mass: 402.6 Da), which have been reported to be a mixture of multiple structural isomers in human plasma.[30] Calibration curve for cholesterol was constructed based on NLS of 44 Da, using 5μM of cholesterol-d7 as internal standard (Table 1). The concentration of free cholesterol was found to be 1.4 ± 0.3 μmol/mL, while the concentrations of total and esterified cholesterol were 3.1 ± 0.1 μmol/mL and 2.0 ± 0.1 μmol/mL, respectively. These values fall within the range of reported cholesterol levels from human plasma using GC/LC-MS methods.[30]

Table 2-1 Calibration curve equations for TGA derivatized sterol standards based on 44 Da NLS using cholesterol-$d_7$ as the internal standard.

| Sterols | Calibration curve equation | $R^2$ |
|---|---|---|
| Cholesterol | $y = 0.6057x - 0.2806$ | 0.9968 |
| Brassicasterol | $y = 0.2481x - 0.0120$ | 0.9959 |
| Campesterol | $y = 0.3275x - 0.0701$ | 0.9943 |
| Stigmasterol | $y = 0.2576x - 0.0114$ | 0.9993 |
| β-Sitosterol | $y = 0.3544x - 0.0667$ | 0.9991 |

Phytosterols typically exist at low concentrations (ppm) in vegetable oil and their quantitation demands laborious sample processing. To test the applicability the TGA tagging method, we performed a quantitative analysis of phytosterols in soybean oil purchased from a local grocery store. A variety of TGA derived sterols including brassicasterol (*m/z* 487.3), campesterol (*m/z* 489.3), stigmasterol (*m/z* 501.3), β-sitosterol (*m/z* 503.3), and cycloartenol (*m/z* 515.3) were clearly observed from 44 Da NLS spectrum (Figure 2.6 (d)). Calibration curve for brassicasterol,

campesterol, stigmasterol, and sitosterol were constructed based on NLS of 44 Da, using 5μM of cholesterol-d7 as internal standard (Table 2.1). Table 2.2 summarizes the quantitative information of the free, esterified, and total phytosterols, expressed in mg/100g of soybean oil. A significant portion of the sterols existed in their free form rather than in esterified form. β-Sitosterol was found to be the most abundant species in all sterol fraction (both free and esterified form) followed by stigmasterol and campesterol.

Table 2-2 Free, esterified, and total (free and esterified) sterols from commercially bought soybean oil (using $^{TGA}$-Chol-$d_7$ as IS).

| Sterol | MW | Detection | Concentration [mg/100g] | | |
|---|---|---|---|---|---|
| | Da | *m/z* | Free | Esterified | Total |
| Brassicasterol | 398.67 | 487.3 | 0.52 ± 0.07 | 0.41 ± 0.01 | 1.4 ± 0.1 |
| Campesterol | 400.69 | 489.3 | 64 ± 5 | 17 ± 0.3 | 75 ± 4 |
| Stigmasterol | 412.70 | 501.3 | 69 ± 8 | 23 ± 0.3 | 84 ± 5 |
| β-Sitosterol | 414.70 | 503.3 | 135 ±1 | 67 ± 1 | 190 ± 6 |

## 2.4 Conclusions

In summary, a rapid and simple charge derivatization method via thiyl radical tagging was developed for quantitative analysis of sterols from complex mixtures. The reaction allows linking the charged thiol group to the allylic position of the double bond in B ring of a sterol. Thioglycolic acid (TGA), a commercially available compound, stands out as a highly efficient reagent. The carboxylic acid group in TGA allows tagged sterols to be detected by negative ion mode nanoESI-MS with high sensitivity. The deployment of a flow microreactor setup for this photochemical reaction further shortens the reaction time to less than 1 min with a yield higher than 90%, a significant improvement over conventional tagging methods which require several hours or even

days to accomplish. Taking advantage of the dominant $CO_2$ loss from CID of TGA-tagged sterols, 44 Da NLS has been established as a sensitive and quantitative method for sterol analysis from mixtures (e.g. total, free, and esterified sterols in human plasma and vegetable oil). Due to the fast reaction stemmed from radical chemistry, the TGA derivatization method shows potential to be incorporated into high throughput workflows for applications in lipidomics and biomedical research. In this study, we noticed that structural isomers of several oxysterols cannot be distinguished using thiyl radical tagging. The same issue also exists for other conventional charge derivatization methods and has been resolved by adding an LC separation component in the workflow. In future studies, we plan to couple thiyl radical tagging with HPLC-MS/MS to further expand its capability in mixture analysis.

## 2.5 References


1. Bloch, K., Chapter 12 Cholesterol: evolution of structure and function. *New Compr. Biochem.* **1991,** *20*, 363-381.

2. McDonald, J. G.; Smith, D. D.; Stiles, A. R.; Russell, D. W., A comprehensive method for extraction and quantitative analysis of sterols and secosteroids from human plasma. *J. Lipid Res.* **2012,** *53* (7), 1399.

3. Murphy, R. C., *Tandem Mass Spectrometry of Lipids Molecular analysis of complex lipids*. Cambridge : RSC: Cambridge, 2014.

4. Hübschmann, H.-J., Fundamentals. In *Handbook of GC/MS*, Wiley-VCH Verlag GmbH & Co. KGaA: 2008; pp 7-292.

5. Liebisch, G.; Binder, M.; Schifferer, R.; Langmann, T.; Schulz, B.; Schmitz, G., High throughput quantification of cholesterol and cholesteryl ester by electrospray ionization tandem mass spectrometry (ESI-MS/MS). *Biochim. Biophys. Acta* **2006,** *1761* (1), 121-128.

6. Chatman, K.; Hollenbeck, T.; Hagey, L.; Vallee, M.; Purdy, R.; Weiss, F.; Siuzdak, G., Nanoelectrospray mass spectrometry and precursor ion monitoring for quantitative steroid analysis and attomole sensitivity. *Anal. Chem.* **1999,** *71* (13), 2358-2363.

7. Woo, H. K.; Go, E. P.; Hoang, L.; Trauger, S. A.; Bowen, B.; Siuzdak, G.; Northen, T. R., Phosphonium labeling for increasing metabolomic coverage of neutral lipids using electrospray ionization mass spectrometry. *Rapid Commun. Mass Spectrom.* **2009,** *23* (12), 1849-55.

8. Honda, A.; Miyazaki, T.; Ikegami, T.; Iwamoto, J.; Yamashita, K.; Numazawa, M.; Matsuzaki, Y., Highly sensitive and specific analysis of sterol profiles in biological samples by HPLC–ESI–MS/MS. *J. Steroid Biochem.* **2010,** *121* (3), 556-564.

9. Griffiths, W.; Wang, Y.; Alvelius, G.; Liu, S.; Bodin, K.; Sjövall, J., Analysis of oxysterols by electrospray tandem mass spectrometry. *J. Am. Soc. Mass. Spectrom.* **2006,** *17* (3), 341-362.

10. Crick, P. J.; William Bentley, T.; Abdel-Khalik, J.; Matthews, I.; Clayton, P. T.; Morris, A. A.; Bigger, B. W.; Zerbinati, C.; Tritapepe, L.; Iuliano, L.; Wang, Y.; Griffiths, W. J., Quantitative Charge-Tags for Sterol and Oxysterol Analysis. *Clin. Chem.* **2015,** *61* (2), 400-411.

11. Hambly, D. M.; Gross, M. L., Laser flash photolysis of hydrogen peroxide to oxidize protein solvent-accessible residues on the microsecond timescale. *J. Am. Soc. Mass. Spectrom.* **2005,** *16* (12), 2057-2063.

12. Chen, J.; Rempel, D. L.; Gau, B. C.; Gross, M. L., Fast photochemical oxidation of proteins and mass spectrometry follow submillisecond protein folding at the amino-acid level. *J. Am. Chem. Soc.* **2012,** *134* (45), 18724-18731.

13. Ma, X.; Xia, Y., Pinpointing Double Bonds in Lipids by Paternò-Büchi Reactions and Mass Spectrometry. *Angew. Chem. Int. Ed.* **2014,** *53* (10), 2592-2596.

14. Ma, X.; Chong, L.; Tian, R.; Shi, R.; Hu, T. Y.; Ouyang, Z.; Xia, Y., Identification and quantitation of lipid C=C location isomers: A shotgun lipidomics approach enabled by photochemical reaction. *Proc. Natl. Acad. Sci. U.S.A.* **2016,** *113* (10), 2573-2578.

15. Tasdelen, M. A.; Yagci, Y., Light-Induced Click Reactions. *Angew. Chem. Int. Ed.* **2013,** *52* (23), 5930-5938.

16. Dénès, F.; Pichowicz, M.; Povie, G.; Renaud, P., Thiyl radicals in organic synthesis. *Chem. Rev.* **2014,** *114* (5), 2587-2693.

17. Yang, C.; McDonald, J. G.; Patel, A.; Zhang, Y.; Umetani, M.; Xu, F.; Westover, E. J.; Covey, D. F.; Mangelsdorf, D. J.; Cohen, J. C., Sterol intermediates from cholesterol biosynthetic pathway as liver X receptor ligands. *J. Biol. Chem.* **2006,** *281* (38), 27816-27826.

18. Lund, E. G.; Diczfalusy, U., Quantitation of receptor ligands by mass spectrometry. *Methods Enzymol.* **2003,** *364*, 24-37.

19. Bedner, M.; Schantz, M. M.; Sander, L. C.; Sharpless, K. E., Development of liquid chromatographic methods for the determination of phytosterols in Standard Reference Materials containing saw palmetto. *J. Chromatogr. A.* **2008,** *1192* (1), 74-80.

20. Cunha, S. S.; Fernandes, J. O.; Oliveira, M. B. P., Quantification of free and esterified sterols in Portuguese olive oils by solid-phase extraction and gas chromatography–mass spectrometry. *J. Chromatogr. A.* **2006,** *1128* (1), 220-227.

21. Hager, J. W., A new linear ion trap mass spectrometer. *Rapid Commun. Mass Spectrom.* **2002,** *16* (6), 512-526.

22. Jackson, J. A.; Turner, J. D.; Rentoul, L.; Faulkner, H.; Behnke, J. M.; Hoyle, M.; Grencis, R. K.; Else, K. J.; Kamgno, J.; Bradley, J. E.; Boussinesq, M., Cytokine response profiles predict species-specific infection patterns in human GI nematodes. *Int J Parasitol* **2004,** *34* (11), 1237-44.

23. Su, Y.; Straathof, N. J. W.; Hessel, V.; Noël, T., Photochemical Transformations Accelerated in Continuous-Flow Reactors: Basic Concepts and Applications. *Chem. Eur. J.* **2014,** *20* (34), 10562-10589.

24. Chatgilialoglu, C.; Ferreri, C., Trans Lipids: The Free Radical Path. *Acc. Chem. Res.* **2005,** *38* (6), 441-448.

25. Luo, Y.-R., *Handbook of bond dissociation energies in organic compounds*. CRC Press: Boca Raton, FL, 2003.

26. Zielinski, Z. A.; Pratt, D. A., Cholesterol Autoxidation Revisited: Debunking the Dogma Associated with the Most Vilified of Lipids. *J. Am. Chem. Soc.* **2016,** *138* (22), 6932-6935.

27. Muller, C.; Binder, U.; Bracher, F.; Giera, M., Antifungal drug testing by combining minimal inhibitory concentration testing with target identification by gas chromatography-mass spectrometry. *Nat. Protoc.* **2017,** *12* (5), 947-963.

28. Asher, J. D. M.; Sim, G. A., 302. Sesquiterpenoids. Part II. The stereochemistry of isophotosantonic lactone: X-ray analysis of 2-bromodihydroisophoto-[small alpha]-santonic lactone acetate. *J. Chem. Soc.* **1965,** (0), 1584-1594.

29. Wang, H.; Wang, H.; Zhang, L.; Zhang, J.; Leng, J.; Cai, T.; Guo, Y., N-alkylpyridinium quaternization for assisting electrospray ionization of sterols in oil by quadrupole-time of flight mass spectrometry. *J. Mass Spectrom.* **2013,** *48* (10), 1101-1108.

30. Quehenberger, O.; Armando, A. M.; Brown, A. H.; Milne, S. B.; Myers, D. S.; Merrill, A. H.; Bandyopadhyay, S.; Jones, K. N.; Kelly, S.; Shaner, R. L.; Sullards, C. M.; Wang, E.; Murphy, R. C.; Barkley, R. M.; Leiker, T. J.; Raetz, C. R.; Guan, Z.; Laird, G. M.; Six, D. A.; Russell, D. W.; McDonald, J. G.; Subramaniam, S.; Fahy, E.; Dennis, E. A., Lipidomics reveals a remarkable diversity of lipids in human plasma. *J. Lipid Res.* **2010,** *51* (11), 3299-305.

# CHAPTER 3. SHOTGUN ANALYSIS OF DIACYLGLYCEROLS ENABLED BY THIOL-ENE CHEMISTRY

(Adapted from publication in Analytical Chemistry)

## 3.1 Introduction

Neutral lipids, including sterol lipids and glycerol lipids, are important components of cellular lipidomes, performing distinct biological functions as compared to polar lipids. As a subclass of glycerol lipids, diacylglycerols (DAGs) share a generic structure, in which two hydroxyl groups in the glycerol backbone are substituted by fatty acyls through ester bonds. DAGs play a variety of roles inside cells; they are produced as metabolites of triacylglycerols (TAGs), while they can be precursors or intermediates in the biosynthesis of TAGs, glycerophospholipids, and glyceroglycolipids.[1] DAGs also serve as signaling molecules.[2] For example, DAG accumulation is associated with activation of protein kinase C in skeletal muscle and liver cells, which ultimately influences downstream insulin signaling.[3] Abnormal accumulation of DAGs has been reported in disease states associated with insulin resistance, such as cardiac hypertrophy,[4] diabetes,[5] and cardiac lipotoxicity.[6] Recently, plasma DAG composition has been used as a biomarker of metabolic syndrome onset in rhesus monkeys.[7]

In terms of DAG profiling, gas chromatography-mass spectrometry (GC-MS) is a traditionally used technique.[8] In this workflow, DAGs need to be separated from other lipid classes and subsequently derivatized (e.g., trimethylsilyl ethers) to increase their volatility.[9] The overall process requires a relatively large sample amount and long analysis time. More recently, high-performance liquid chromatography (HPLC)-MS has been increasingly applied to DAG analysis. DAGs together with other neutral lipids can be well-separated on the column, allowing

quantitation of 1,2-DAG and 1,3-DAG *sn*-isomers from complex mixtures.[10] The advancement of electrospray ionization-tandem mass spectrometry (ESI-MS/MS) of lipids has facilitated global lipid analysis without the need of a prior lipid class separation, coined as "shotgun lipid analysis" by Han and Gross.[11] Shotgun analysis has the advantages of fast analysis speed and the capability of detecting a broad range of lipid classes, which has found increasing applications in biomedical discoveries.[12] Per the non-polar nature, DAGs are detected as adduct ions, viz. $[DAG + X]^+$ (X = $Li^+$, $Na^+$, $NH_4^+$) by ESI.[13-14] Collision-induced dissociation (CID) of the ammonium adduct ions forms abundant fatty acyl specific fragment ions (as combined loss of $NH_3$ and free fatty acid), allowing the assignment of DAG structures.[13] An obvious drawback of using adduct ion formation in DAG analysis is that the ionization efficiency is not high, which also varies according to the fatty acyl chain lengths and the degree of unsaturation.[15-16] These variations require the use of multiple DAG internal standards for quantitation.[13]

Charge derivatization is an effective approach to boost ionization efficiency of neutral lipids via ESI-MS.[17] Established derivatization methods target the free hydroxyl group in DAGs through ester bond formation with a charge reagent. This strategy also blocks potential fatty acyl migration in DAGs.[18] *N*-Chlorobetainyl chloride,[19] *N*,*N*-dimethylglycine (DMG),[18] and DMG imidazolide[20] have been demonstrated as efficient charge derivatization reagents, enhancing the ion signal of DAGs by at least two orders of magnitude than forming their adduct ions.[19] CID of charge derivatized DAGs typically produces tag specific fragment in high abundance, facilitating the development of MS/MS transitions for sensitive quantitation (limit of quantitation (LOQ), 100 pM via DMG derivitization).[18] Because fatty acyl chain specific fragment ions are absent from direct CID of the charge tagged DAGs, adduct formation of the derivatized DAGs with $Li^+$ or $NH_4^+$ is still needed for structural elucidation. This approach although requires the addition of salt

into ESI solution, the Han group demonstrated that it provided a distinct benefit of quantifying the *sn*-1,2- and 1,3- isomers based on CID of lithiated DMG-DAG ions.[18]

In biological systems, a substantial proportion of DAGs consists of unsaturated fatty acyls. As an example, the concentration of unsaturated DAGs was found to be ~0.81 μM out of ~0.88 μM, the total DAG concentration in human plasma; that is, 92% of DAGs are unsaturated.[21] Given the prevalence of unsaturated DAGs in lipidomes, we are interested in exploring alternative charge derivatization methods that target the carbon-carbon double bond (C=C) as a site for the introduction of a charge tag. Recently, we have demonstrated thiyl radical tagging for sterol lipid analysis by linking an ionizable thiol reagent (thioglycolic acid, TGA) to the unsaturated B ring in sterols.[22] This derivatization, when coupled with ESI-MS/MS via low energy CID, provided rapid (in minutes) and sensitive quantitation (limit of detection (LOD) in nM) of sterols from complex mixtures.

Thiol-ene coupling reaction, involving thiyl radical addition to an alkene function group, is a widely adopted methodology for the formation of carbon-sulfur bonds.[23] It fulfills the "click-chemistry" paradigm of high reaction rates, quantitative conversion in mild condition, and simple work-up procedures (i.e. removal of byproducts by nonchromatographic methods).[24] Thiol-ene chemistry has found broad applications in polymer and material synthesis,[25] surface functionalization,[26] and drug delivery.[27] Taking advantage of its high specificity for C=C transformation, herein we explored a charge derivatization strategy based on thiol-ene chemistry to tag the C=C in unsaturated DAGs. The success of the tagging would allow enhanced sensitivity of the DAGs via ESI-MS. Moreover, the newly formed C-S bond in the derivatized DAG species is less likely to be a facile dissociation site under charge driven fragmentation conditions due to the relatively non-polar nature of the C-S bond. This property should facilitate the formation of

structural informative fragment ions, i.e., fatty acyl chain related fragments. In this work, synthetic DAG standards with varying chain lengths and degrees of unsaturation were used for method development, including optimizing reaction conditions, screening for suitable thiol compounds as charge tags, and developing MS/MS methods for identification and quantitation. The analytical capability of the established method was demonstrated by performing analysis of DAGs from human plasma samples of type 2 diabetes mellitus (DM) patients using a shotgun lipidomic approach.

## 3.2 Materials and Methods

### 3.2.1 Lipid Nomenclature

Shorthand notations for glycerolipids are based on the guidelines provided by LIPID MAPS.[28] For synthetic lipid standards with known *sn* positions, "/" separator is used such as in DAG 16:0/18:1/0:0 to represent DAG consisting of C16 and C18 fatty acyls at *sn*-1 and *sn*-2 positions, respectively. DAG 16:0/0:0/18:1 stands for a DAG with C16 and C18 fatty acyls at *sn*-1 and *sn*-3 positions, respectively. 0:0 represents no fatty acyl chain is linked. The "0" and "1" after the carbon number represents the degree of unsaturation. The interchangeable "_" notation, such as in DAG 16:0_18:1, is adopted for DAG with unidentified *sn* positions.

### 3.2.2 Materials

All the chemical reagents and solvents were purchased from commercial sources and were used without further purification. DAG lipid standards 16:0/18:1(9Z)/0:0, 18:0/20:4(5Z,8Z,11Z,14Z)/0:0, 15:0/18:1-$d_7$(9Z)/0:0, 18:1(9Z)/18:1(9Z)/0:0, and 18:1(9Z)/0:0/18:1(9Z) were purchased from Avanti Polar Lipids Inc. (Alabaster, AL, USA). DAG lipid standards 14:1(9Z)/14:1(9Z)/0:0, 16:1(9Z)/16:1(9Z)/0:0, 17:1(9Z)/17:1(9Z)/0:0,

18:1(6Z)/18:1(6Z)/0:0, 18:2(9Z,12Z)/18:2(9Z,12Z)/0:0, 18:3(9Z,12Z,15Z)/18:3(9Z,12Z,15Z)/0:0, 20:1(9Z)/20:1(9Z)/0:0, 22:1(9Z)/22:1(9Z)/0:0, and 24:1(9Z)/24:1(9Z)/0:0 were purchased from Nu-Check Prep, Inc. (Elysian, MN, USA). Thioglycolic acid (TGA), sodium-2-mercaptoethanesulfonate (MESNA), cysteamine hydrochloride (CA), dimethylformamide (DMF), 2,2-dimethoxy-2-phenylacetophenone (DMPA), hydrochloric acid (HCl), and ethyl acetate were purchased from Sigma-Aldrich (St. Louis, MO, USA). Deionized water was obtained from a purification system at 0.03 μS·cm (model: Micropure UV; Thermo Scientific; San Jose, CA, USA). Pooled human plasma (Li Heparin used as anticoagulant) was purchased from Innovative Research (Novi, MI, USA).

### 3.2.3 Human Plasma Sample Collection

Six human plasma samples, including 3 healthy normal controls and 3 Type 2 DM patients were collected from Affiliated Dongfeng Hospital, Hubei University of Medicine (Shyian, Hubei Province, China).

### 3.2.4 Lipid Extraction

The procedure for total lipid extraction from plasma was based on established protocols.[29,30] Briefly, 50 μL of plasma, 0.3 mL of 0.67 M phosphate buffer solution, and 2.0 mL of chloroform-methanol (3:1, v/v) were combined in 100 mm x 13 mm glass test tubes. The mixture was vortex-mixed for 2 min and then was centrifuged at 1200 g for 5 min for phase separation. The aqueous layer was removed using a glass Pasteur pipette, while the remaining organic layer was transferred to another glass test tube and was dried under a stream of nitrogen gas. For quantitative analysis, DAGs were fractioned from other classes of lipids. The residues resulting from total lipid extraction from plasma (50 μL) were extracted twice with 0.5 mL of isooctane-ethyl acetate (80:1, v/v). The lipid extract was loaded onto a 100-mg Isolute silica

cartridge (Biotage, Charlotte, NC) previously conditioned with 4 mL of isooctane-ethyl acetate (80:1, v/v). Esterified sterols were eluted first with 4.5 mL of isooctane-ethyl acetate (80:1, v/v) (fraction 1), triglycerides were then eluted next by 5 mL of isooctane-ethyl acetate (20:1, v/v) (fraction 2). Diglycerols were eluted with 4.5 mL of isooctane-ethyl acetate (75:25, v/v) (fraction 3). Collected lipid fractions were evaporated to dryness under a gentle stream of nitrogen and dissolved in a small volume (10-250 μL) of chloroform and stored at -20$^{o}$C in 2 mL amber glass vial, until derivatization process for analysis.

### 3.2.5 Derivatization of DAG standards, plasma lipid extract, and plasma

DAG (0.01-200 μM), thiol reagent (100 mM), and DMPA (photo-initiator, 0.5 mM), were dissolved in DMF and degassed with nitrogen gas before photochemical reactions. The solution was pumped through a flow microreactor (in μL/min flow rate range), made from UV transparently coated fused silica capillary (100 μm i.d., 375 μm o.d.; Polymicro Technologies; Phoenix, AZ, USA). A low-pressure mercury lamp with an emission band at 351 nm (model number: 80-1057-01/351; BHK, Inc; Ontario, CA, USA) was placed in parallel to the capillary at a distance of 0.5 cm. This whole set-up was enclosed in a cardboard box to prevent stray light. At the exit of the microflow reactor, the reaction solution (100 μL) was collected in a glass vial and added with ethyl acetate (200 μL). The mixture was washed twice with 0.1 M aq. HCl (400 μL) to remove excess thiol reagent (e.g., CA) before MS analysis. The same procedure was applied to direct derivatization of lipids in plasma (1-20 μL) without a prior lipid extraction step.

### 3.2.6 MS analysis of neutral lipid standards and lipid extracts

MS analysis of charge derivatized DAG standards and lipid extracts were performed on a 4000 QTRAP and a 4500 QTRAP mass spectrometer (SCIEX, Toronto, ON, CA) equipped with

a home-built nanoESI source (pulled borosilicate glass emitters). Optimized MS parameters were as follows: nanoESI spray voltage: ± (1400-1800) V; curtain gas: 10 psi; declustering potential: ± 20 V; a scan rate of 1000 Da/s for 4000 QTRAP and 10,000 Da/s for 4500 QTRAP. The instrument was used in a linear ion trap MS analysis mode or in triple quadrupole linked scan mode (precursor ion scan (PIS) or neutral loss scan (NLS)).[31]

## 3.3 Results and Discussions

### 3.3.1 Charge Tagging via Thiol-Ene Chemistry

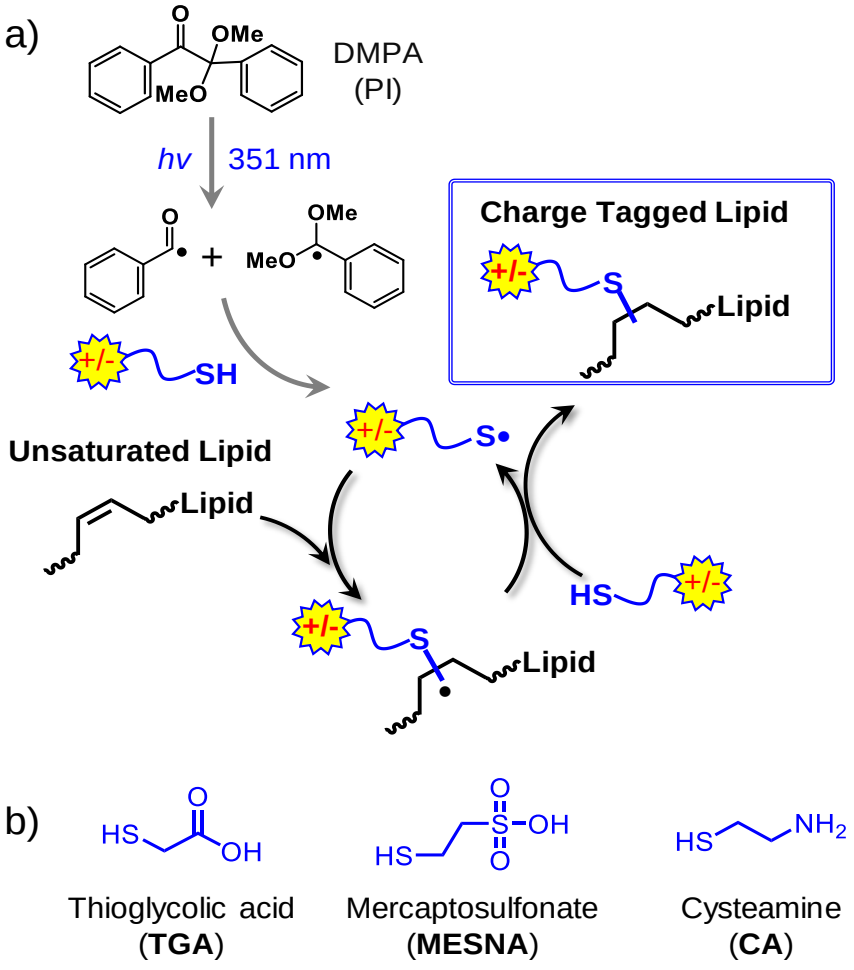


Scheme 3-1 (a) Charge tagging of unsaturated lipid via thiol-ene click chemistry. DMPA is a commonly used photoinitiator (PI) for thiyl radical formation upon 351 nm wavelength UV irradiation. (b) Chemical structures of the three thiol reagents tested.

Scheme 3.1a shows a classic view of thiol-ene reaction with an unsaturated lipid depicted for the conventional alkene.[24] Briefly, upon exposure to 351 nm UV irradiation, DMPA (the photoinitiator, PI) undergoes Norrish Type I cleavage to generate benzoyl radical and 1,1-dimethoxy-1-phenylmethyl radical. These carbon-centered radicals abstract the sulfur-hydrogen in the thiol reagent, forming alkylthiyl radical. The thiyl radical then adds to the C=C to form a carbon-centered radical, which subsequently abstracts a hydrogen atom from another thiol molecule to produce the derivatized product, while the newly formed thiyl radical propagates in the radical chain process. Thiol-ene reactions are not regioselective for internal double bonds; so two regioisomers resulting from the addition to either carbon in the original C=C are formed.[32]

Using DAG 16:0/18:1/0:0 as a model compound, three thiol reagents, TGA, MESNA, and CA (structures are shown in Scheme 3.1(b)), were tested for thiol-ene charge tagging. These thiols were selected based on the presence of readily ionizable functional group either for protonation or deprotonation under typical ESI conditions, reasonable solubility, and commercial availability. Moreover, it was preferred that the charge tagged DAG ions could generate structurally informative fragment ions upon CID. DMPA, a commonly used photoinitiator for thiol-ene reactions was adopted here, while DMF was used as the reaction solvent.[23] Prior to MS analysis, a simple wash procedure was performed to reduce signal suppression from remaining thiol reagent. The reaction progress was monitored through the intensity of tagged DAG ions via nanoESI-MS.

Figure 3.1(a-c) summarize the post-reaction nanoESI-MS spectra of DAG 16:0/18:1/0:0 (1 μM) resulting from three individual thiol reagents after reaching equilibrium. A single reaction product was detected at high ion intensities (counts per second, cps) from each reagent, i.e., *m/z* 685.5 ($[^{TGA}$DAG - H$]^-$, *m/z* 735.4 ($[^{MESNA}$DAG - H$]^-$), *m/z* 672.5 ($[^{CA}$DAG + H$]^+$) from TGA and MESNA in negative ion mode, and CA in positive ion mode, respectively. The mass differences

(insets in Figure 3.1) between the detected products and the DAG molecule (594.2 Da) match well with the mass of the corresponding thiol reagent, suggesting successful thiol-ene coupling. Moreover, all three thiol reagents significantly improved ionization of DAG in nanoESI.

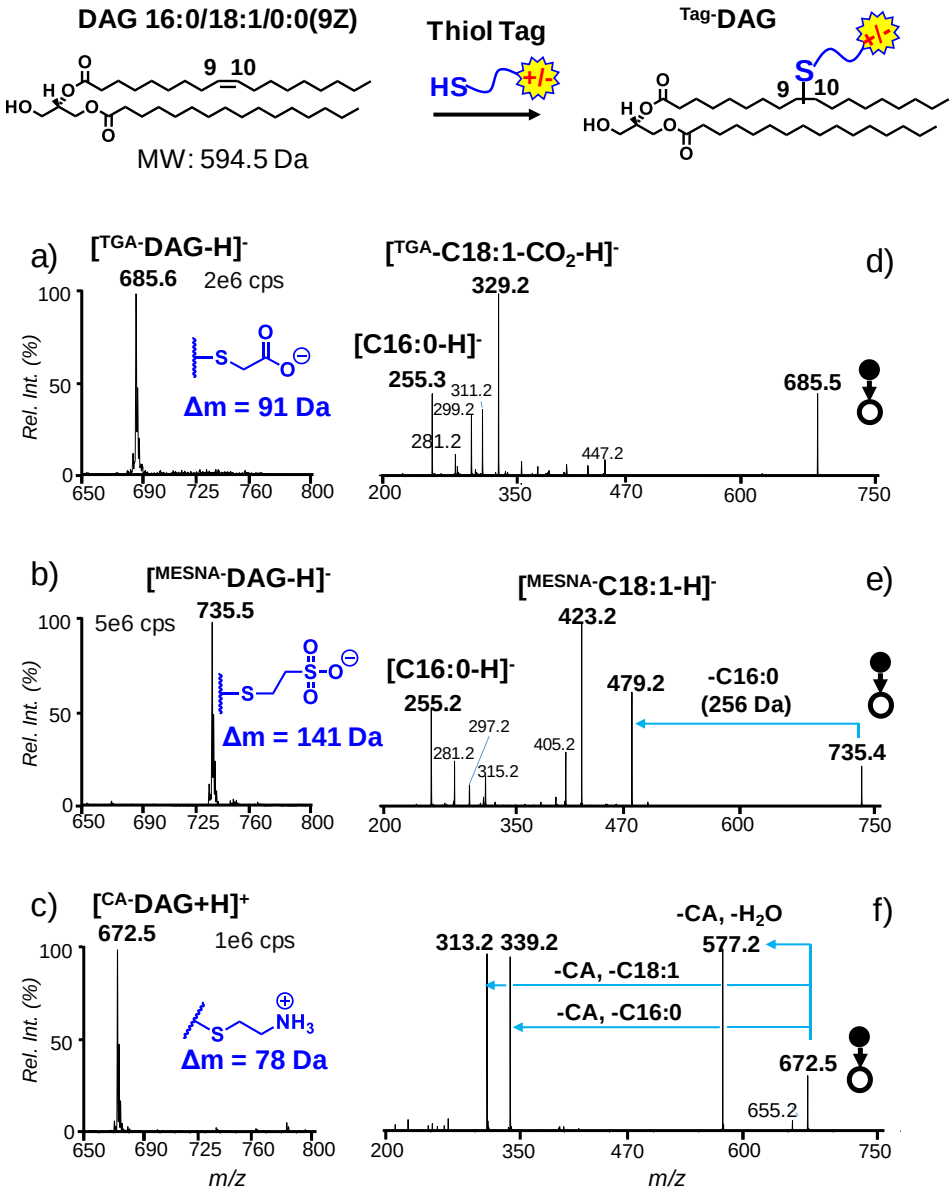


Figure 3-1 Charge tagging of DAG 16:0/18:1(9Z)/0:0 (1 µM) using thiol-ene chemistry. The inset at the top shows a generic reaction scheme for charge tagging. Post reaction nanoESI MS spectra after derivatization with (a) TGA and (b) MESNA in negative ion mode, and (c) CA in positive ion mode. MS2 beam-type CID of (d) TGA-DAG at m/z 685.5 (CE = 35 V) in negative ion mode, (e) MESNA-DAG at m/z 735.4 (CE = 60 V) in negative ion mode, and (f) CA-DAG at m/z 672.5 (CE = 32 V) in positive ion mode.

The data in Figure 3.1d represent typical $MS^2$ beam-type CID (CE = 35 V) of TGA derivatized DAG anions (*m/z* 685.5) in negative ion mode. Different from CID of TGA derivatized sterols,[22] 44 Da loss ($-CO_2$) from TGA carboxylic group was not observed; neither was the tag loss. Instead, the fatty acyl anions, including $[C16:0\text{-}H]^-$ (*m/z* 255.3) and $[^{TGA}\text{-}C18:1\text{-}CO_2\text{-}H]^-$ (*m/z* 329.2, a sequential loss of $CO_2$ from the TGA tag) were quite abundant. Beam-type CID of MESNA derivatized DAG anions (CE = 60 eV, Figure 3.1e) produced three major fragments, neutral loss of C16:0 (*m/z* 479.2), thiol tagged C18:1 anions ($[^{MESNA}\text{-}C18:1\text{-}CO_2\text{-}H]^-$, *m/z* 423.2), and $[C16:0\text{-}H]^-$ (*m/z* 255.3). Clearly, CID of TGA and MESNA tagged DAG anions readily allow identification of fatty acyl composition in DAG.

Beam-type CID spectrum of protonated $^{CA}$-DAG (Figure 3.1f, CE = 32 V) is rather simple with three fragment peaks produced present at almost equal abundance. The fragment peak at *m/z* 577.5 resulted from the sequential loss of CA tag (77 Da) and $H_2O$ (18 Da), leading to a characteristic neutral loss of 95 Da. The fragment ions at *m/z* 339.5 and 313.5 derived from the sequential loss of CA tag and the fatty acyl chains, C18:1 and C16:0, respectively. The above sequences of fragmentation were supported by accurate mass measurement and $MS^3$ CID experiments (data not shown).

Although the three thiol reagents all delivered improved ionization and useful structural information (fatty acyl chain composition) upon CID, we decided to choose CA for further method development. This is because, besides the fatty acyl information, the distinct 95 Da neutral loss associated with the CA tag facilitates the development of NLS for detection and quantitation of DAGs from mixtures.

### 3.3.2 Optimization of CA Thiol-Ene Coupling

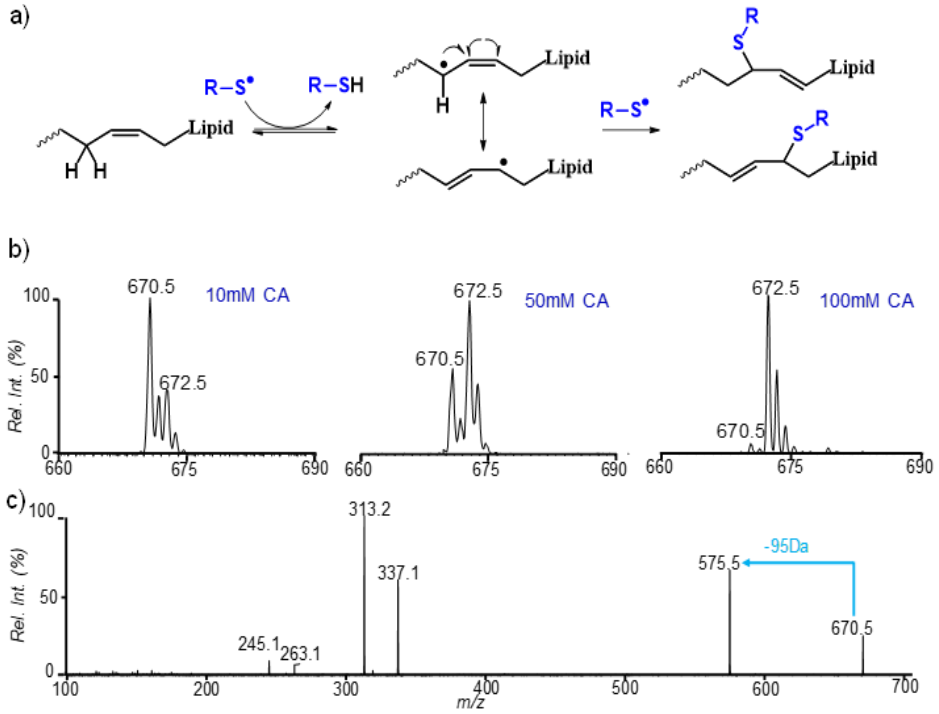


Figure 3-2 (a) Proposed mechanism for thiyl addition and a double bond migration within the chain. (b) NanoESI reaction spectrum for the thiol-ene reaction of DAG 16:0/18:1/0:0 under different concentration of cysteamine (CA). (c) $MS^2$ beam type CID of *m/z* 670.5.

In synthetic settings, the thiol reagent is typically placed in stoichiometric relationship to the alkenes in thiol-ene reactions.[23] Although the concentrations of DAGs in biological samples are typically at sub-µM level or lower, it is necessary to use high concentrations of PI and thiol reagent (both in mM) to maintain adequate steady-state concentrations of the thiyl radical so as to sustain radical chain reactions depicted in Scheme 3.1(a). For instance, reactions involving 10 mM CA, 0.5 mM DMPA, and 5 µM DAG 16:0/18:1/0:0 produced a major product at *m/z* 670.5, two Da less than the expected thiol-ene coupling product (Figure 3.2 (b)). Beam-type CID spectrum of the product at *m/z* 670.5 gave product peak at *m/z* 337.5 from sequential loss of CA tag and C16:0 (Figure 3.2 (c)), instead of *m/z* 339.5 (Figure 3.1 (c), revealing the presence of unsaturation in

C18:1 chain from double bond migration (Figure 3.2 (a)). This type of product has been observed in polymer synthesis and identified by NMR to have a shifted C=C in the structure.[33] By increasing the concentration of CA to 100 mM or higher, this side product could be effectively reduced to less than 2% of the thiol-ene coupling product. Although higher concentrations of CA led to faster and cleaner reactions, there was no significant benefit to increase CA concentrations over 100 mM.

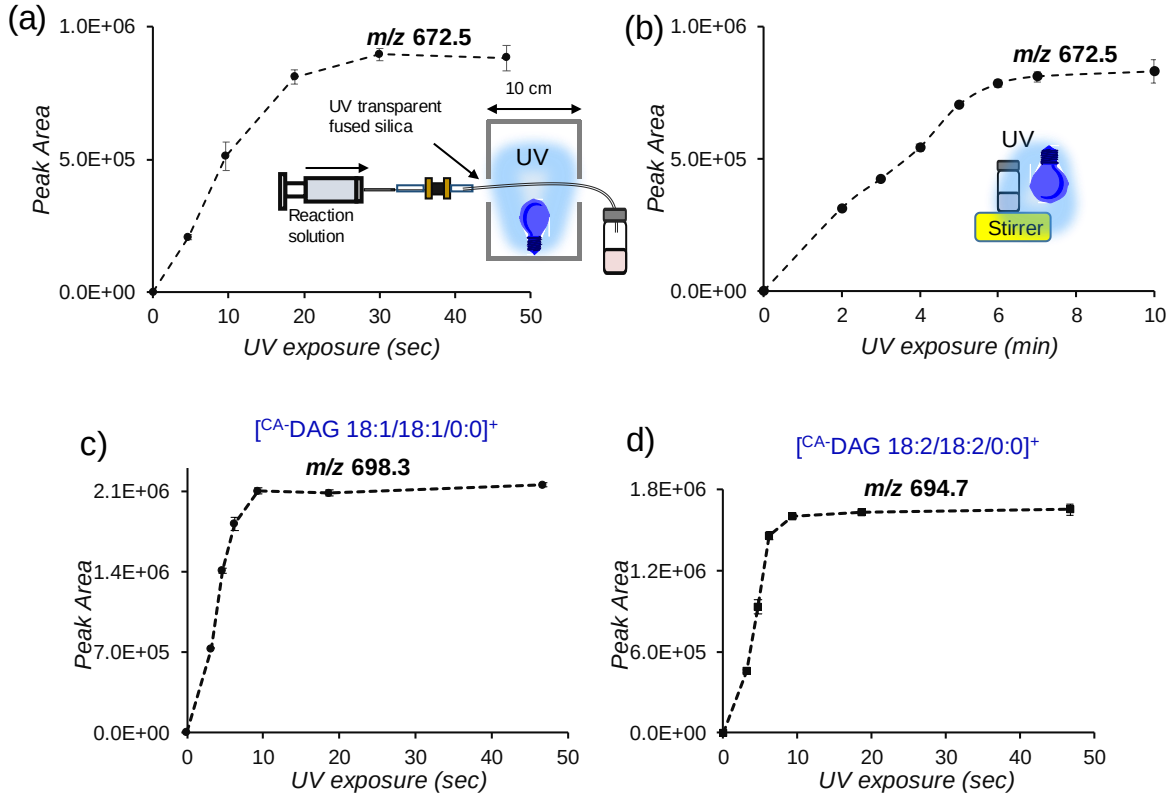


Figure 3-3 The plot of peak intensity of [$^{CA}$-DAG 16:0/18:1/0:0 +H] $^{+}$ over UV exposure time using (c) flow microreactor set up (d) bulk processes. Insets show schematics for conducting radical charge tagging in flow microreactor and in bulk processes. Error bars represent standard deviation; n=3. The plot of peak intensity of (a) [$^{CA}$-DAG 18:1/18:1/0:0+H]$^{+}$ and (b) [$^{CA}$-DAG 18:2/18:2/0:0+H]$^{+}$, over UV exposure time using flow microreactor set up.

The effect of UV exposure on the efficiency of reaction time was also investigated to optimize the derivatization of DAG species. The total irradiation time for the reaction mixture in the micro flow reactor was calculated by the total volume of the fused silica capillary exposed to

UV divided by the sample flow rate. For this study, the irradiation time was modulated by controlling the flow rate of the reaction mixture. The UV exposed reaction mixtures at different flow rates were analyzed by MS using the 95 Da NLS. A plot of reaction product intensity as a function of UV exposure time is shown in figure 3.3. The signal intensity of the derivatized product reached a plateau within 50 sec of UV exposure (Figure 3.3 (a)). A comparative study was also done with a batch reaction set-up (Figure 3.3 (b)). A borosilicate glass vial (5 mL) containing the optimized reaction solution was $N_2$ purged, capped, and was continuously stirred with a magnetic stir bar. The 351 nm UV lamp was kept at a distance of ~0.5 cm from the glass vial. The overall set-up was covered with aluminum foil. After the UV is turned on, the reaction solution was sampled and analyzed by MS at different intervals. The overall reaction intensity of the derivatized product reached a similar plateau at 8 minutes of UV irradiation as compared to the microreactor. These results show microreactor have a significant advantage over batch setup in terms of reaction time and sample volume consumption. This can be contributed to significant irradiation efficiency of the reaction mixture in silica tubing of a microflow reactor due to the large surface area to volume ratio of silica capillary tubing, allowing maximal light transmission. With the use of a flow microreactor, CA tagging could also be accomplished within 40 s for a variety of DAGs consisting of different lengths of fatty acyls and different numbers of C=Cs. The representative kinetic curves for DAG 18:1/18:1/0:0 and DAG 18:2/18:2/0:0 are shown in figure 3.3 (c) and (d), respectively.

### 3.3.3 Polyunsaturated DAGs

For DAGs consisting of polyunsaturated fatty acyls, we wondered if multiple tagging could happen. Figure 3.4 summarizes the post-reaction spectra of DAG 15:0/18:1-$d_7$/0:0, DAG 18:3/18:3/0:0 and DAG 18:0/20:4/0:0, which were derivatized separately but under identical reaction conditions using the flow microreactor setup. The production of mono-CA tagging

products reached steady state within 1 min of UV exposure. Despite the presence of multiple C=Cs in the latter two DAGs, only single CA tagging products were observed (*m/z* 690.3 and 722.3), same as the tagging of DAG 15:0/18:1-$d_7$ /0:0 (*m/z* 665.3), which has one C=C in the molecule. It is worth noting that no doubly charged ions corresponding to sequential tagging were present in the lower mass range. Irradiation of reaction mixture with UV for 1 h in bulk processes, led to <10% of 2$^{nd}$ tagging (Figure 3.5). Under the same reaction condition, derivatization using TGA produced >35% of second tagging products of DAG 18:1/18:1/0:0 (Figure 3.6). Such difference can be attributed to the higher reactivity of TGA than CA.[34] Although the preferred formation of mono-CA tagging products in the polyunsaturated system is not fully understood at this moment, the phenomenon nonetheless is advantageous for sensitive detection and quantitation in subsequent MS/MS experiments.

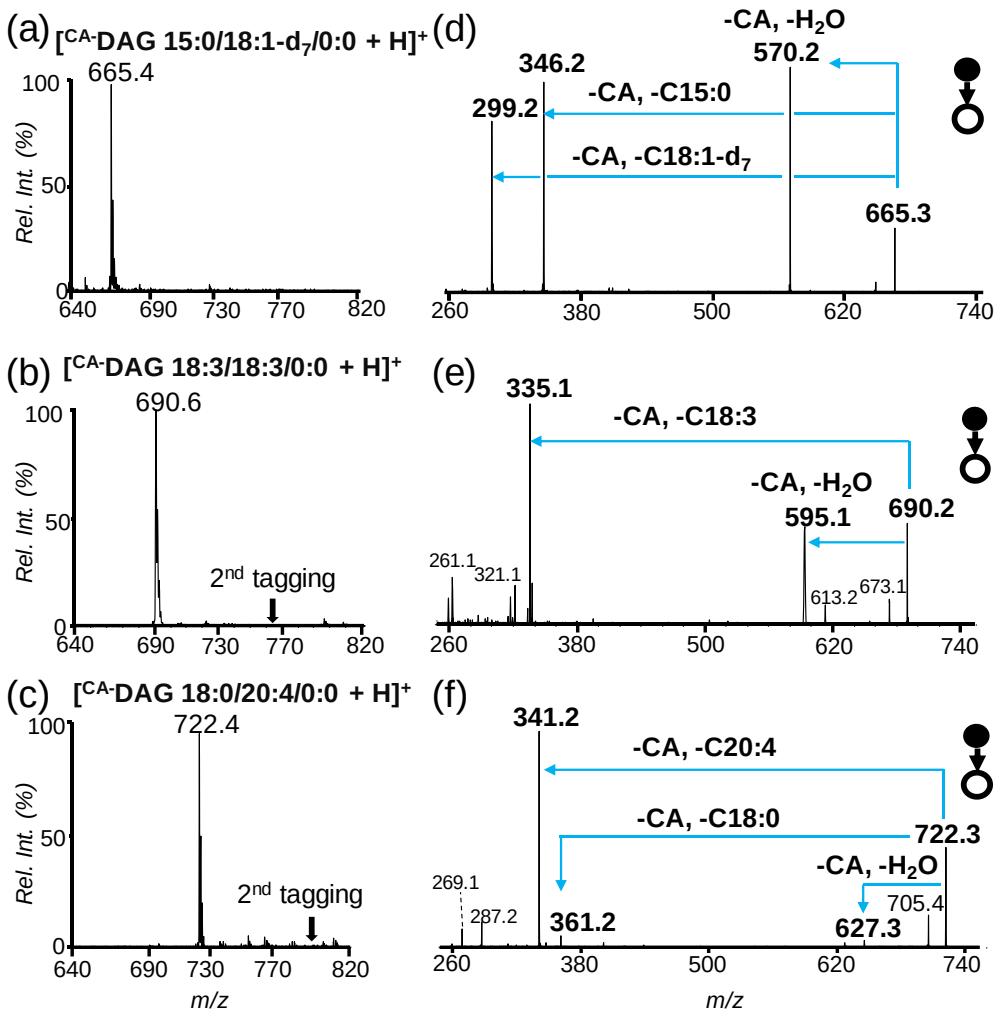


Figure 3-4 Post-CA tagging nanoESI MS spectra of (a) DAG 15:0/18:1-d7/0:0, (b) DAG 18:3/18:3/0:0, (c) DAG 18:0/20:4/0:0. $MS^2$ beam type CID (CE 32V) of (d) CA-DAG 15:0/18:1-d7/0:0 (*m/z* 665.3) (e) CA-DAG 18:3/18:3/0:0 (*m/z* 690.2) (f) CA-DAG 18:0/20:4/0:0 (*m/z* 722.3).

The CA derivatized DAG species was further analyzed by MS/MS via beam-type CID (Figure 3.4(d-f)). Upon CID (CE = 32 V), fragments corresponding to sequential loss of CA and fatty acyl chains are consistently observed with high intensities. However, the relative intensity of the 95 Da loss (the combined loss of CA and $H_2O$) decreases as the degree of unsaturation in a fatty acyl chain increases, e.g., C20:4 < C18:3 < C18:2 < C18:1. This aspect suggests that the application of 95 Da NLS to the polyunsaturated system may have a lower sensitivity than the ones

consisting lower degree of unsaturation in the fatty acyl chains. In this case, NLS targeted for a specific polyunsaturated fatty acyl chain, e.g. 381 Da NLS for the combined losses of CA (77 Da) and C20:4 (304 Da), can be used to get around this problem and achieve sensitive detection. Table 3.1 and 3.2 summarizes the combined loss of CA and various fatty acyl chains present in DAGs.

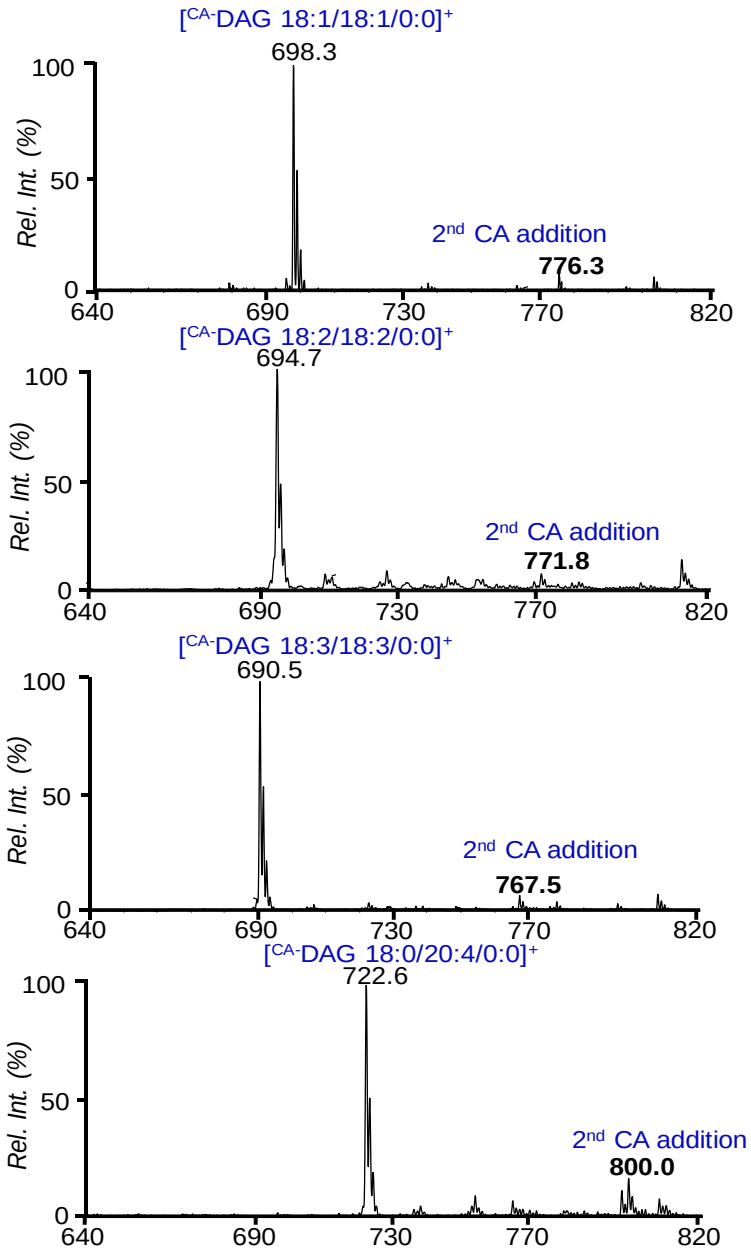


Figure 3-5 NanoESI $MS^1$ spectra of cysteamine derivatized (a) DAG 18:1/18:1/0:0, (b) DAG 18:2/18:2/0:0, (c) DAG 18:3/18:3/0:0, and (d) DAG 18:0/20:4/0:0, in bulk processes for UV irradiation period of 1 hour.

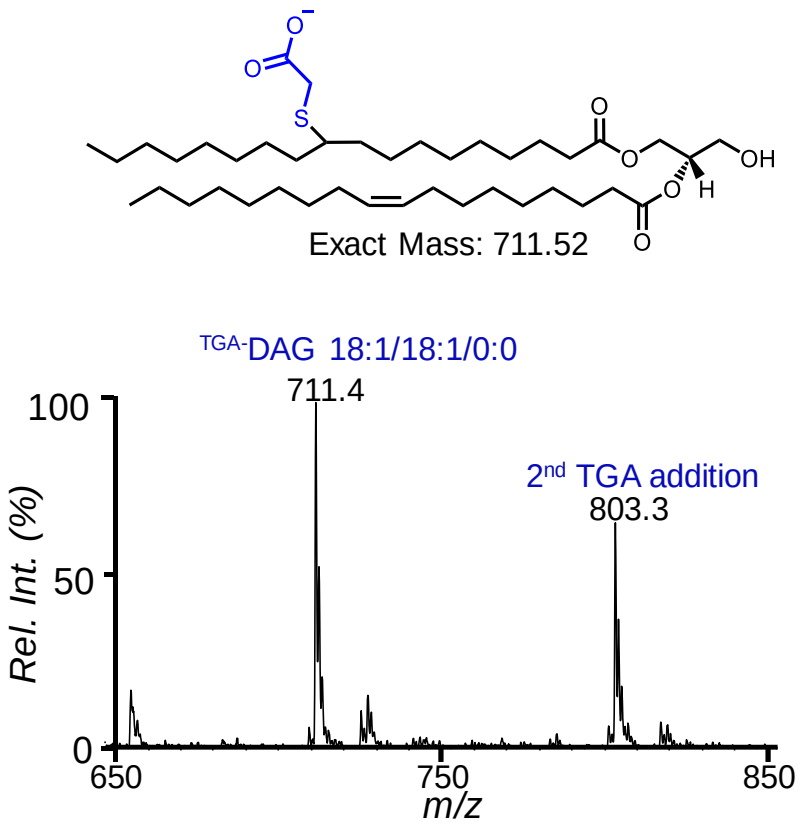


Figure 3-6 Thiol-based radical charge tagging of DAG 18:1/18:1/0:0 using thioglycolic acid as the derivatizing reagent in bulk processes for UV irradiation period of 1 hour.

Table 3-1 Neutral loss mass corresponding to common fatty acyl groups esterified to DAGs

| DAG Fatty acyl | Neutral Loss (Da) CA + RCOOH | DAG Fatty acyl | Neutral Loss (Da) CA + RCOOH |
|---|---|---|---|
| C14:1 | 303 | C18:2 | 357 |
| C14:0 | 305 | C18:1 | 359 |
| C15:1 | 317 | C18:0 | 361 |
| C15:0 | 319 | C20:5 | 379 |
| C16:1 | 331 | C20:4 | 381 |
| C16:0 | 333 | C20:2 | 385 |
| C17:1 | 345 | C20:1 | 387 |
| C17:0 | 347 | C20:0 | 389 |
| C18:3 | 355 | C22:6 | 405 |

Table 3-2 Product ions corresponding to common fatty acyl groups esterified to DAGs

| DAG Fatty acyl | Precursor Ion (Da) | DAG Fatty acyl | Precursor Ions (Da) |
|---|---|---|---|
| C14:1 | 283 | C18:2 | 337 |
| C14:0 | 285 | C18:1 | 339 |
| C15:1 | 297 | C18:0 | 341 |
| C15:0 | 299 | C20:5 | 359 |
| C16:1 | 311 | C20:4 | 361 |
| C16:0 | 313 | C20:2 | 365 |
| C17:1 | 325 | C20:1 | 367 |
| C17:0 | 327 | C20:0 | 369 |
| C18:3 | 335 | C22:6 | 385 |

### 3.3.4 DAG *sn*- and C=C Positional Isomers

We also explored the potential of differentiating *sn*- and C=C positional isomers of DAGs via CA tagging and subsequent CID. For instance, *sn*-1,2- and 1,3-DAG 18:1(9Z)/18:1(9Z) were derivatized by CA and analyzed. Unfortunately, the MS/MS spectra for the two *sn*-isomers were identical and thus, did not provide any distinction (Figure 3.7). CID of CA tagged DAG 18:1(6Z)/18:1(6Z)/0:0 showed similar fragmentation pattern to DAG 18:1(9Z)/18:1(9Z)/0:0 (data not shown). Therefore, no distinction on the C=C location was achieved from CA tagging and CID.

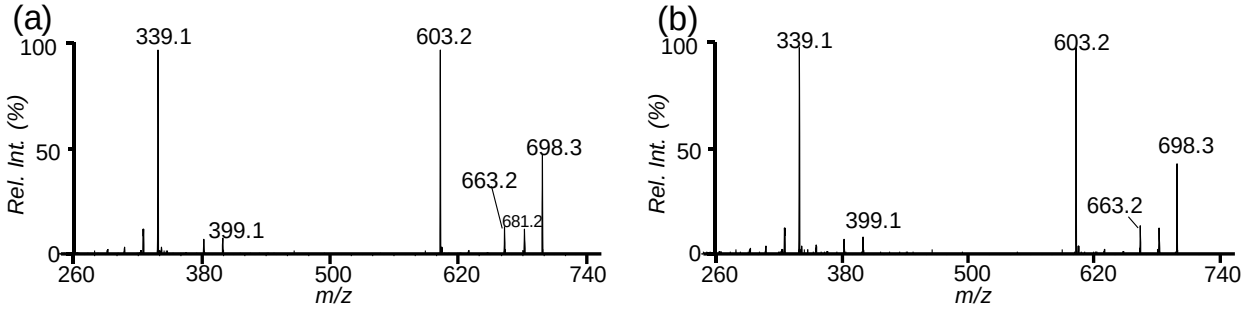


Figure 3-7 $MS^2$ CID of the (a) *sn*-1,2-$^{CA}$-DAG 18:1/18:1, and (a) *sn*-1,3-$^{CA}$-DAG 18:1/18:1.

### 3.3.5 Quantitative Analysis

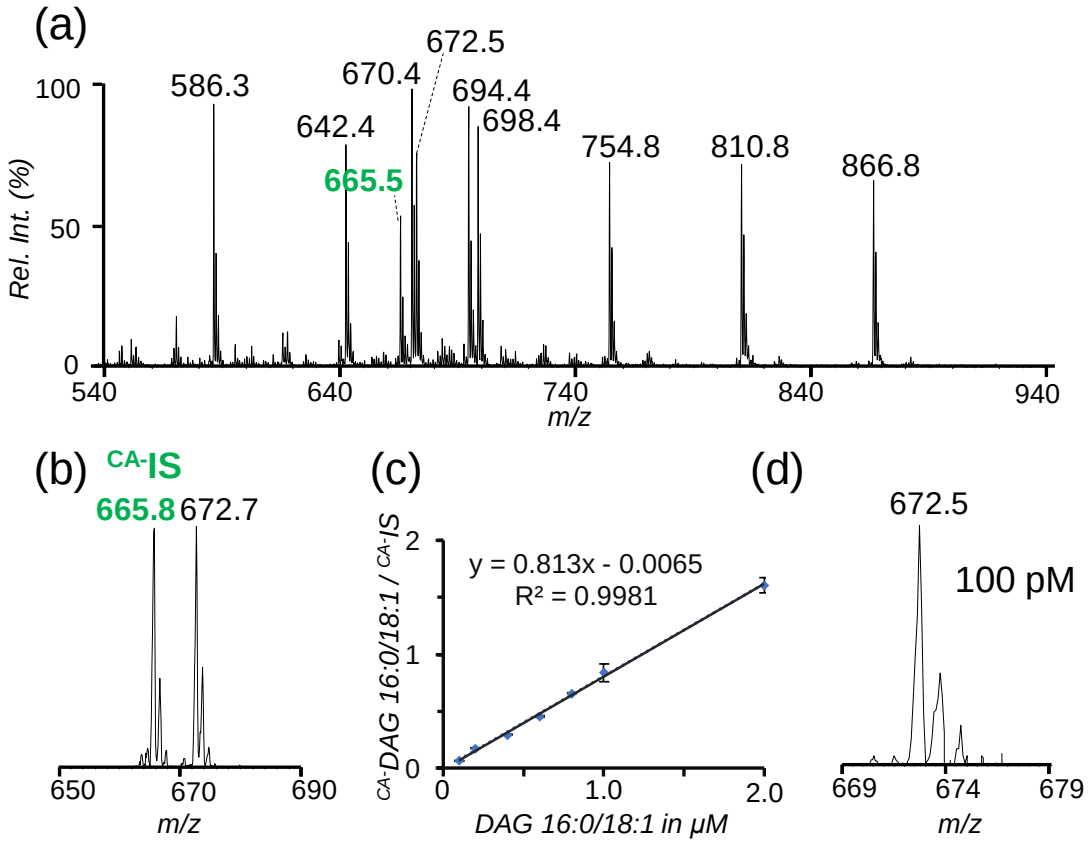


Figure 3-8 (a) Post-CA tagging nanoESI MS spectrum of equimolar (1 µM each) mixture of DAG 14:1/14:1/0:0 (*m/z* 586.3), 16:1/16:1/0:0 (*m/z* 642.4), 17:1/17:1/0:0 (*m/z* 670.4), 16:0/18:1/0:0 (*m/z* 672.5), 18:2/18:2/0:0 (*m/z* 694.4), 18:1/18:1/0:0 (*m/z* 698.4), 20:1/20:1/0:0 (*m/z* 754.8), 22:1/22:1/0:0 (*m/z* 810.8), and 24:1/24:1/0:0 (*m/z* 866.8), with 0.5 µM of IS (15:0/18:1-$d_7$/0:0, *m/z* 665.5). (b) 95 Da NLS of $^{CA}$-DAG 16:0/18:1/0:0 (1µM) and IS (1µM). (c) A linear plot resulted from 95 NLS for DAG 16:0/18:1/0:0 ($R^2$ = 0.9981). Error bars represent standard deviation; n = 3. (d) 95 Da NLS of 100 pM DAG 16:0/18:1/0:0 after CA tagging.

It has been shown that the ionization response of DAGs in alkali metal adduct forms are highly dependent on chain lengths and the degrees of unsaturation of fatty acyls.[13] Here we examined if such bias also existed for DAGs after CA tagging. Nine unsaturated DAGs (equal molar, 1 µM each) with fatty acyls varying from C28 to C48 and degrees of unsaturation in the range of 1 to 4 were mixed together, while 0.5 µM DAG 15:0/18:1-$d_7$/0:0 was added as the internal standard (IS). This mixture was then subjected to CA derivatization for 1 min using the flow

microreactor setup. Figure 3.8 (a) shows the post-reaction nanoESI-MS spectrum. The derivatized DAG species yielded similar ion response regardless of the change of fatty acyl chain length and unsaturation. The relative standard deviation (16%, n=3) of the DAG signals are within the expected errors arising from sample handling. The above results suggest that CA tagging can successfully minimize ionization bias for DAGs in ESI due to variations in fatty acyl composition. Moreover, signal suppression among DAGs during mixture analysis is very limited.

Table 3-3 Calibration curve equations for cysteamine (CA) derivatized DAG standards based on 95 Da NLS using DAG 15:0/18:1-$d_7$/0:0 (1 μM) as the internal standard.

| **DAGs** | **Calibration curve equation** | **$R^2$** |
|---|---|---|
| 14:1/14:1$_{/0:0}$ | $y = 0.7366x + 0.0762$ | 0.9917 |
| 16:0/18:1$_{/0:0}$ | $y = 0.8130x - 0.0065$ | 0.9981 |
| 18:1/18:1$_{/0:0}$ | $y = 0.8991x - 0.1714$ | 0.9924 |
| 18:2/18:2$_{/0:0}$ | $y = 0.7901x - 0.2197$ | 0.9923 |

We further assessed the performance of 95 Da NLS for DAG quantitation. A good linear correlation ($R^2$= 0.9981) was achieved between MS response and concentration (DAG 16:0/18:1/0:0, 0.1-2 μM) by employing 1.0 μM DAG 15:0/18:1-$d_7$/0:0 as IS (Figure 8 (b) and (c)). Since mono-tagging was dominant for DAGs consisting of multiple C=Cs, 95 Da NLS also provided good linear correlations for their quantitation (Table 3). The LOD for DAG 16:0/18:1/0:0 could be achieved at 100 pM from 95 Da NLS (S/N 3:1). Such level of LOD is comparable to values reported from other charge derivatization approaches, e.g. LOQ of 100 pM using DMG via ESI-MS/MS[18] and LOD of 10 nM using *N*-chlorobetainyl chloride via ESI-MS.[19] Overall, CA

tagging of DAG followed by ESI-MS/MS enjoys the benefits of fast analysis (less than 2 min per run) and sensitive detection.

Calibration curves for the DAG standards were also constructed based on NLS of 95 Da, using 1 μM of DAG 15:0/18:1-$d_7$/0:0 as the internal standard. The cysteamine derivatized DAGs gave excellent correlation coefficient ($R^2$) as shown in Table 3.3.

### 3.3.6 Analysis of DAGs from Human Plasma

The analysis of DAGs from the crude mixture is often hindered from their relatively low abundance (~0.88 μM) and ion suppression from other neutral lipids, such as CEs (~3.5 mM) and TAGs (~1.0 mM).[21] Conventional analytical methods typically involve multistep liquid-liquid extraction, enrichment and/or chromatographic separation before MS. Herein, we tried to achieve rapid and sensitive analysis of DAGs by thiol-ene derivatization without resorting to chromatographic separation on clinical human plasma samples. As a demonstration, 1 μL of human plasma was directly subjected to CA derivatization (1 μM of DAG 15:0/18:1-$d_7$/0:0 added as IS). Figure 3.9 (a) shows the post-reaction nanoESI-MS spectrum. Three classes of neutral lipids were detected, representing CA tagged CEs, DAGs, and TAGs. These assignments were based on the detected monoisotopic *m/z* values and corresponding MS/MS data. For instance, the peak at *m/z* 726.9 was identified as $^{CA}$-CE 18:2. CID of this peak produced a dominant fragment peak at *m/z* 369 (cholestene cations) due to sequential loss of CA and C18:2 from the tagged CE (Figure 3.9(b)). Similarly, ions at *m/z* 962.8 were identified as $^{CA}$-TAG 18:1/18:1/18:1 based on the detection of sequential loss of CA and C18:1(Figure 3.9(c)).

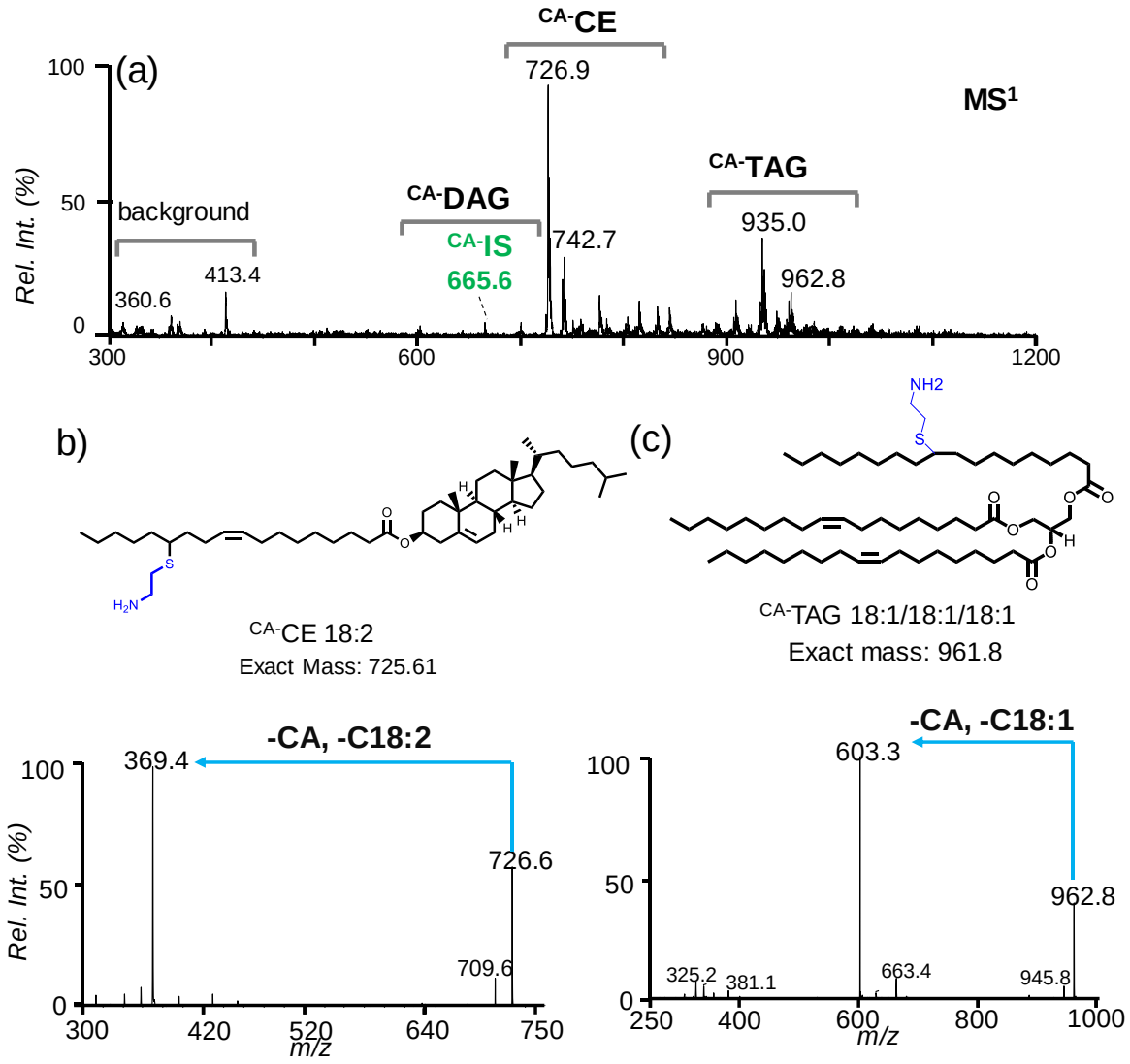


Figure 3-9 (a) NanoESI-MS[1] from 1 µL of unprocessed human plasma subjected to photochemical charge tagging. The *m/z* regions correspond to tagged neutral lipid classes are indicated. MS[2] beam type CID of (b) [CA-]CE 18:2 detected at *m/z* 726.6 (c) [CA-]TAG 18:1_18:1_18:1 detected at *m/z* 962.8.

As expected, CA tagged DAGs were detected at low intensities as compared to CEs and DAGs in the MS[1] spectrum (Figure 3.9(a)). However, by using 95 Da NLS, 7 distinct DAG molecular species were observed as shown in figure 3.10. The above data clearly demonstrate the capability of CA tagging followed by 95 Da NLS for selective detection of DAGs even at the presence of other more abundant neutral lipids.

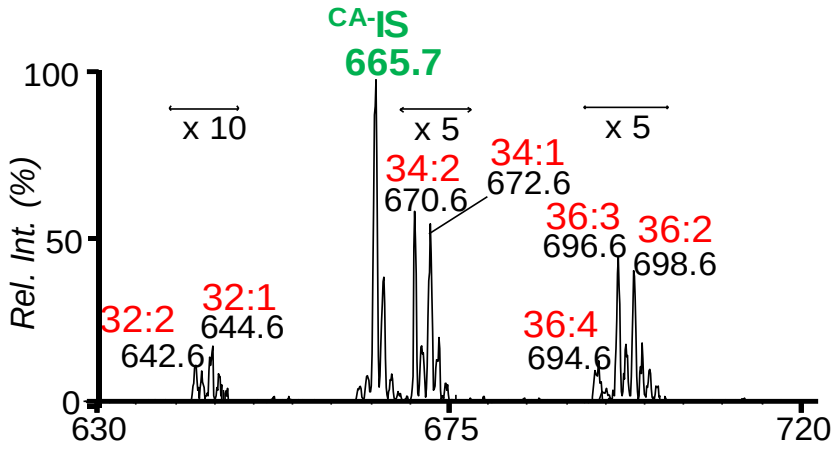


Figure 3-10 NLS of 95 Da for unsaturated DAGs from 1µL of pooled human plasma, subjected to photochemical charge tagging with cysteamine (with 1µM $^{CA}$-DAG 15:0/18:1-d$_7$/0:0 as the IS).

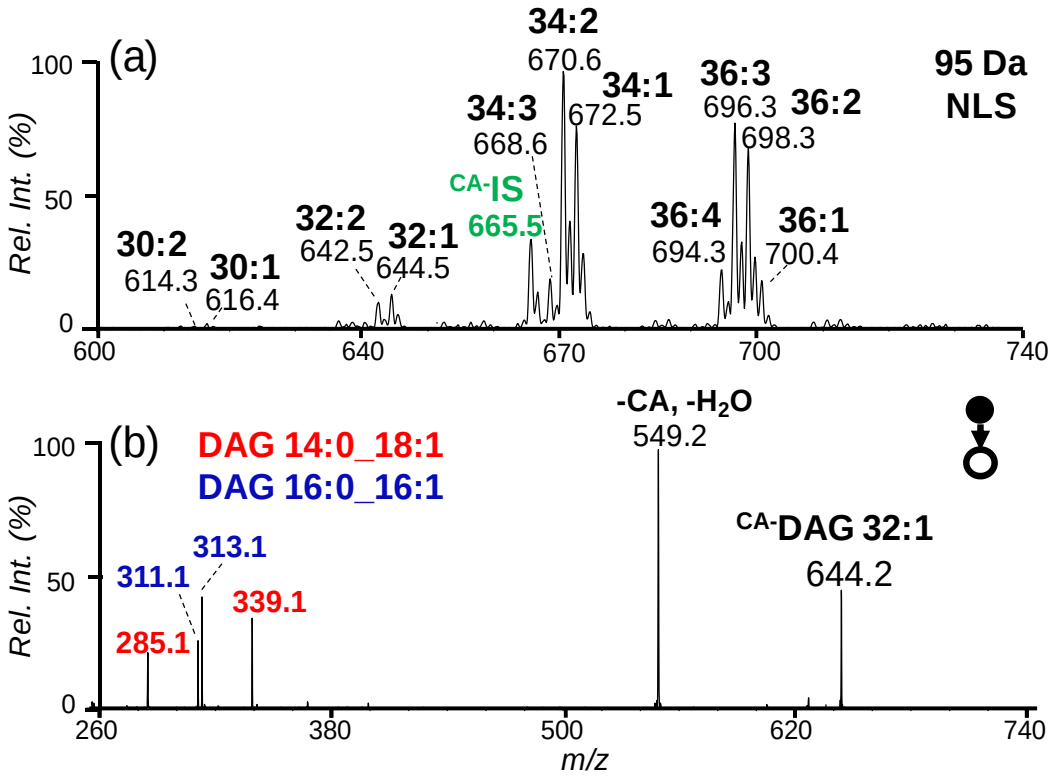


Figure 3-11 Post-CA tagging nanoESI mass spectrum of pooled human plasma with 1 µM DAG 15:0/18:1-d$_7$/0:0 added as the IS. (a) 95 Da NLS for unsaturated DAGs (mass range *m/z* 600-740). (b) MS$^2$ CID of *m/z* 644.2 ([$^{CA}$-DAG 32:1+H]$^+$) reveals two fatty acyl composition isomers, DAG 14:0_18:1 and DAG 16:0_16:1

For quantitative analysis, DAGs were extracted and purified from 50 µL of human plasma (recovery rate: 94 ± 3 %). Eleven peaks of $^{CA-}$DAGs were detected from 95Da NLS (Figure 3.11). MS/MS analysis proved that many DAGs consisted of fatty acyl compositional isomers. For example, CID of ions at *m/z* 644.2, $^{CA-}$DAG 32:1, showed abundant losses of 359 Da (CA + C18:1), 333 Da (CA + C16:0), 331 (CA + C16:1), and 305 Da (CA + C14:0), corresponding to product ions at *m/*z 285, 311, 313, and 339, respectively (Figure 3.11 (b)). Based on the number of fatty acyl carbon atoms and double bonds, DAG 32:1 was assigned to contain two fatty acyl compositional isomers: DAG 14:0_18:1 and DAG 16:0_16:1. Similarly, DAG 34:2 (the peak at *m/z* 670.2 in Figure 3.10 (a)) contained DAG 16:1_18:1 and DAG 16:0_18:2 (data now shown). In order to assess the relative change of the distinct DAG species within the parent ion, fatty acyl chain specific NLS and PIS can also be employed (Table 3.4-3.5). PIS of 339 and 337 Da revealed the existence of DAGs containing C18:1 and C18:2, respectively. Overall, 18 distinct DAG species were identified to the level of fatty acyl composition as summarized in Table 3.4. Quantitative analysis of DAGs from the pooled human plasma was performed using 95 Da NLS. Calibration curves for each individual DAG species were obtained using DAG 15:0/18:1-$d_7$/0:0 (1 µM) as IS (Table 3.3). These values fall within the range of reported unsaturated DAGs measured from human plasma using HPLC-MS/MS.[21] However, since CA tagging is specific for unsaturated DAGs, saturated DAGs (e.g., DAG 16:0/16:0) could not be detected. Besides, CA tagging followed by CID cannot differentiate *sn*-isomers. This problem could potentially be resolved by coupling an LC separation before or after CA derivatization in the workflow.

Table 3-4 Identified DAG species in pooled human plasma.

| DAG | MW (Da) | Detection (*m/z*) | Acyl Chain Composition | Conc. (µM) |
|---|---|---|---|---|
| 30:1 | 538.5 | 616.4 | 14:0_16:1 | 0.1 ± 0.01 |
| 30:2 | 536.5 | 614.3 | 14:1_16:1 | 0.08 ± 0.01 |
| 32:1 | 566.5 | 644.5 | 16:0_16:1/14:0_18:1 | 1.1 ± 0.1 |
| 32:2 | 564.5 | 642.5 | 16:1_16:1/14:0_18:2 | 0.7 ± 0.2 |
| 34:1 | 594.5 | 672.5 | 16:0_18:1/16:1_18:0 | 6.4 ± 1.0 |
| 34:2 | 592.5 | 670.6 | 16:0_18:2/ 16:1_18:1 | 7.7 ± 1.1 |
| 34:3 | 590.5 | 668.6 | 16:1_18:2/ 16:0_18:3 | 1.4 ± 0.3 |
| 36:1 | 622.5 | 700.4 | 18:0_18:1 | 1.3 ± 0.4 |
| 36:2 | 620.5 | 698.3 | 18:1_18:1/ 18:0_18:2 | 5.3 ± 0.6 |
| 36:3 | 618.5 | 696.3 | 18:1_18:2 | 6.0 ±1.0 |
| 36:4 | 616.5 | 694.3 | 18:2_18:2/ 18:1_18:3 | 1.6 ± 0.6 |

### 3.3.7 DAG Analysis of Type 2 Diabetes Mellitus Human Plasma

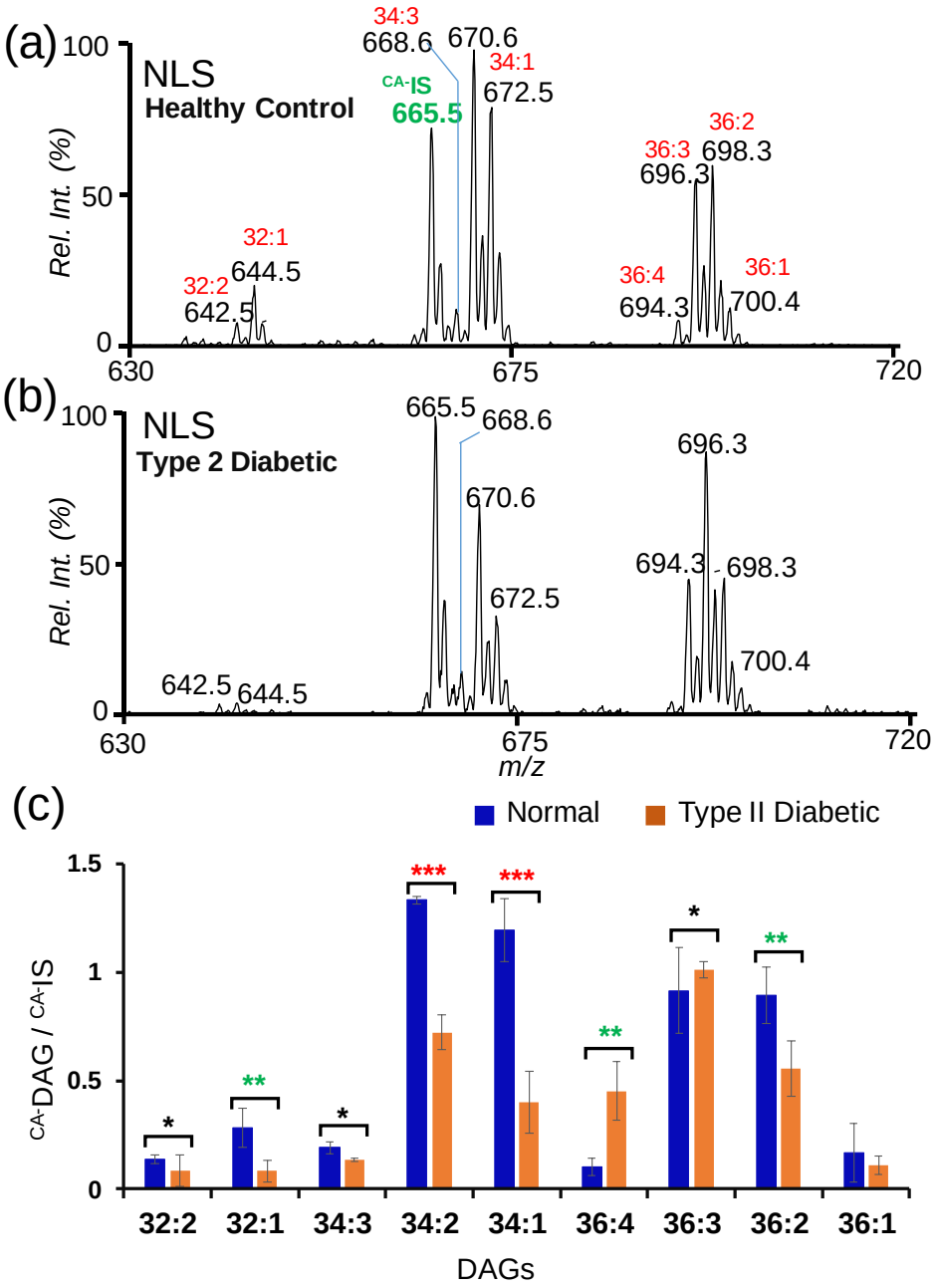


Figure 3-12 NLS of 95 Da for unsaturated DAGs from human plasma sample for (a) healthy control and (b) type 2 DM patient, subjected to photochemical charge tagging with cysteamine (c) Comparison of the relative amount of major unsaturated DAGs in human plasma samples from normal control and type 2 DM patient. 1 µM of the internal standard (CA-DAG 15:0/18:1-d7/0:0) was added before the derivatization step. Error bars represent standard deviation; n=3, *p<0.05, **p<0.01, ***p<0.001 (t-test).

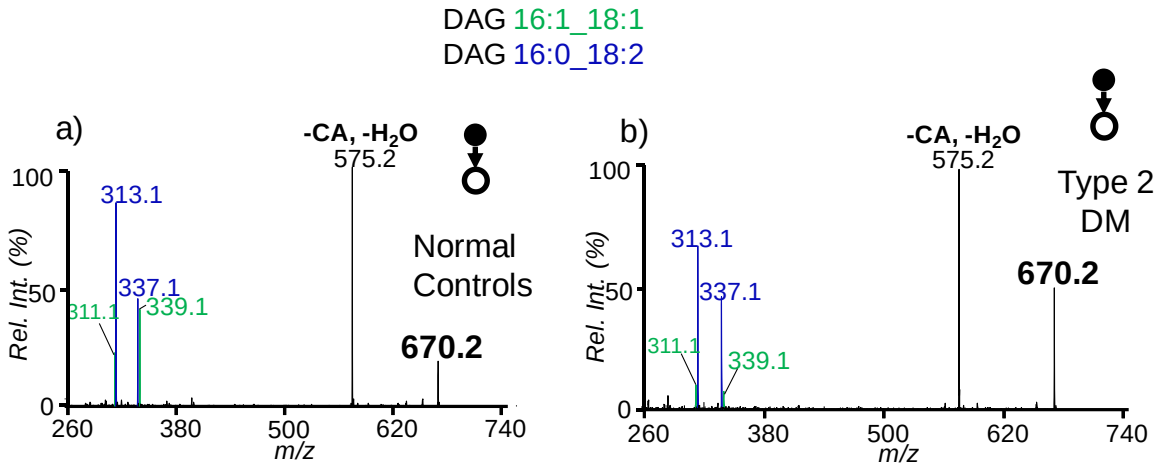


Figure 3-13 DAG 34:2 in plasma samples of normal and type 2 DM patients is a mixture of DAG 16:0_18:2 and DAG 16:1_18:1 isomer. CID of DAG 34:2 in (a) healthy normal control and (b) type 2 DM patients. (CE energy: 32 V). Diagnostics ions at m/z 311.1 and 339.1 are unique to DAG 16:1_18:1 species, while diagnostic ions at *m/z* 313.1 and 337.1 are unique to DAG 16:0_18:2.

Various studies have shown the correlation of increased intracellular DAG content in liver and muscle in type 2 DM.[35] Recently, Shaw et al. have demonstrated aberration of plasma lipidome occurs prior to the onset of type 2 DM.[36] We were interested to test if CA tagging followed by 95 Da NLS was capable in providing quick profiling of DAGs in plasma for type 2 DM patients. Figure 12 (a-b) shows the representative 95 NLS for unsaturated DAGs from human plasma sample for healthy control and type 2 DM patient. Figure 12 (c) summarizes the relative intensity changes of unsaturated DAGs relative to IS (DAG 15:0/18:1-$d_7$/0:0, 1 µM) from two sets of samples (Normal controls: N = 3, DM Patients: N = 3). The major DAG species include DAG 34:2, 34:1, 36:3, and 36:2. The relative intensities of DAG 34:2, 34:1, and 36:2 decreased by 2.5 ± 0.7, 2.8 ± 1.1, and 1.6 ± 0.4 times in DM patients as compared to the control, respectively. However, DAG 36:4 in the DM patients increased by 5 ± 2 times relative to the control. In terms of the change of fatty acyl compositional isomers, CID of $^{CA}$-DAG 36:2 revealed a reduction of DAG

16:0_18:1 relative to isomer DAG 16:0_18:2 in DM patients (Figure 13). The above data are suggestive of large variations in the metabolic pathways involving DAGs in DM patients. Further studies are required with the use of larger sampling size and controlled medication of the type 2 DM patients.

## 3.4 Conclusions

In this study, we have utilized thiol-ene click chemistry as an effective charge derivatization method to enable fast analysis of unsaturated DAGs by nanoESI-MS. Cysteamine (CA) was identified as a proper derivatization reagent, which allowed fast charge tagging (in 1 minute) and enhanced ionization (by 10 times) of a variety of unsaturated DAGs as compared to conventional adduct ion formation. Low energy CID of CA tagged DAGs led to simple product ion spectrum, yet rich in structural information. Specifically, the combined neutral loss of the tag (CA) and fatty acyls (RCOOH) readily allowed the assignment of fatty acyl chains, leading to the confident identification of multiple fatty acyl compositional isomer of DAGs in biological samples. The other major fragmentation channel was the combined loss of CA and $H_2O$ (95 Da). Based on this characteristic loss, 95 Da NLS was established as a sensitive means for detection (LOD of 100 pM) and quantitation of unsaturated DAGs. The above method was further applied to DAG analysis of pooled human plasma and plasma samples from type 2 DM patients. Significant alteration in concentrations was found for several unsaturated DAG species, suggesting the potential of CA tagging in biomedical applications. In comparison with methods based on GC-MS and HPLC-MS for DAG analysis, CA tagging followed by ESI-MS/MS has several advantages, such as fast analysis speed (2 min vs. up to 60 min for analysis) and the potential of direct analysis of small quantity of clinical sample (e.g. 1 μL plasma). In terms of limitations, this method cannot analyze saturated DAGs and it is not capable to provide *sn*-position information. Preliminary LC-

MS data showed multiple or broadened elution peaks resulting from mono-CA tagging of DAGs having more than one C=C, likely due to the formation of multiple regio-isomers. This phenomenon suggests that CA tagging could increase the complexity of mixture analysis when coupled with LC-MS. CA tagging for DAG analysis is just one example of applying thiol-ene click chemistry to solve a specific analytical problem, viz. DAG analysis. As shown in the example of direct analysis of human plasma, other classes of unsaturated neutral lipids (CEs and TAGs) were also detected. In future studies, we plan to expand the thiol-ene derivatization toolbox and develop methods to enhance analysis of other important neutral lipids.

## 3.5 References


1. Goñi, F. M.; Alonso, A., Structure and functional properties of diacylglycerols in membranes1. *Prog. Lipid Res.* **1999,** *38* (1), 1-48.

2. Colón-González, F.; Kazanietz, M. G., C1 domains exposed: from diacylglycerol binding to protein-protein interactions. *Biochim. Biophys. Acta* **2006,** *1761* (8), 827-837.

3. Erion, D. M.; Shulman, G. I., Diacylglycerol-mediated insulin resistance. *Nature medicine* **2010,** *16* (4), 400-402.

4. Arimoto, T.; Takeishi, Y.; Takahashi, H.; Shishido, T.; Niizeki, T.; Koyama, Y.; Shiga, R.; Nozaki, N.; Nakajima, O.; Nishimaru, K., Cardiac-specific overexpression of diacylglycerol kinase ζ prevents Gq protein-coupled receptor agonist-induced cardiac hypertrophy in transgenic mice. *Circulation* **2006,** *113* (1), 60-66.

5. Eichmann, T. O.; Lass, A., DAG tales: the multiple faces of diacylglycerol--stereochemistry, metabolism, and signaling. *Cell Mol Life Sci* **2015,** *72* (20), 3931-3952.

6. Drosatos, K.; Schulze, P. C., Cardiac lipotoxicity: molecular pathways and therapeutic implications. *Current heart failure reports* **2013,** *10* (2), 109-121.

7. Polewski, M. A.; Burhans, M. S.; Zhao, M.; Colman, R. J.; Shanmuganayagam, D.; Lindstrom, M. J.; Ntambi, J. M.; Anderson, R. M., Plasma diacylglycerol composition is a biomarker of metabolic syndrome onset in rhesus monkeys. *J. Lipid Res.* **2015,** *56* (8), 1461-1470.

8. Murphy, R. C.; Fiedler, J.; Hevko, J., Analysis of Nonvolatile Lipids by Mass Spectrometry. *Chem. Rev.* **2001,** *101* (2), 479-526.

9. Tserng, K.-Y.; Griffin, R., Quantitation and molecular species determination of diacylglycerols, phosphatidylcholines, ceramides, and sphingomyelins with gas chromatography. *Anal. Biochem.* **2003,** *323* (1), 84-93.

10. Leiker, T. J.; Barkley, R. M.; Murphy, R. C., Analysis of diacylglycerol molecular species in cellular lipid extracts by normal-phase LC-electrospray mass spectrometry. *Int. J. Mass spectrom.* **2011,** *305* (2), 103-108.

11. Han, X., *Lipidomics Comprehensive Mass Spectrometry of Lipids*. : Wiley: 2016.

12. Han, X., Lipidomics for precision medicine and metabolism: A personal view. *Biochim. Biophys. Acta* **2017,** *1862* (8), 804-807.

13. Murphy, R. C.; James, P. F.; McAnoy, A. M.; Krank, J.; Duchoslav, E.; Barkley, R. M., Detection of the Abundance of Diacylglycerol and Triacylglycerol Molecular Species in Cells Using Neutral Loss Mass Spectrometry. *Anal. Biochem.* **2007,** *366* (1), 59-70.

14. Bowden, J. A.; Albert, C. J.; Barnaby, O. S.; Ford, D. A., Analysis of Cholesteryl Esters and Diacylglycerols using Lithiated Adducts and Electrospray Ionization Tandem Mass Spectrometry. *Anal. Biochem.* **2011,** *417* (2), 202-210.

15. Li, X.; Evans, J. J., Examining the collision-induced decomposition spectra of ammoniated triglycerides as a function of fatty acid chain length and degree of unsaturation. I. The OXO/YOY series. *Rapid Commun. Mass Spectrom.* **2005,** *19* (18), 2528-2538.

16. Li, X.; Collins, E. J.; Evans, J. J., Examining the collision-induced decomposition spectra of ammoniated triglycerides as a function of fatty acid chain length and degree of unsaturation. II. The PXP/YPY series. *Rapid Commun. Mass Spectrom.* **2006,** *20* (2), 171-177.

17. Wang, M.; Wang, C.; Han, R. H.; Han, X., Novel advances in shotgun lipidomics for biology and medicine. *Prog. Lipid Res.* **2016,** *61* (Supplement C), 83-108.

18. Wang, M.; Hayakawa, J.; Yang, K.; Han, X., Characterization, and quantification of diacylglycerol species in biological extracts after one-step derivatization: a shotgun lipidomics approach. *Anal. Chem.* **2014,** *86* (4), 2146-2155.

19. Li, Y. L.; Su, X.; Stahl, P. D.; Gross, M. L., Quantification of diacylglycerol molecular species in biological samples by electrospray ionization mass spectrometry after one-step derivatization. *Anal. Chem.* **2007,** *79* (4), 1569-1574.

20. Johnson, D. W., Analysis of alcohols, as dimethylglycine esters, by electrospray ionization tandem mass spectrometry. *J. Mass Spectrom.* **2001,** *36* (3), 277-283.

21. Quehenberger, O.; Armando, A. M.; Brown, A. H.; Milne, S. B.; Myers, D. S.; Merrill, A. H.; Bandyopadhyay, S.; Jones, K. N.; Kelly, S.; Shaner, R. L.; Sullards, C. M.; Wang, E.; Murphy, R. C.; Barkley, R. M.; Leiker, T. J.; Raetz, C. R.; Guan, Z.; Laird, G. M.; Six, D. A.; Russell, D. W.; McDonald, J. G.; Subramaniam, S.; Fahy, E.; Dennis, E. A., Lipidomics reveals a remarkable diversity of lipids in human plasma. *J. Lipid Res.* **2010,** *51* (11), 3299-305.

22. Adhikari, S.; Xia, Y., Thiyl Radical-Based Charge Tagging Enables Sterol Quantitation via Mass Spectrometry. *Anal. Chem.* **2017,** *89* (23), 12631-12635.

23. Hoyle, C. E.; Bowman, C. N., Thiol–Ene Click Chemistry. *Angew. Chem. Int. Ed.* **2010,** *49* (9), 1540-1573.

24. Hoyle, C. E.; Lee, T. Y.; Roper, T., Thiol–enes: Chemistry of the past with promise for the future. *J. Polym. Sci., Part A: Polym. Chem.* **2004,** *42* (21), 5301-5338.

25. Lowe, A. B., Thiol-ene "click" reactions and recent applications in polymer and materials synthesis: a first update. *Polym. Chem.* **2014,** *5* (17), 4820-4870.

26. Resetco, C.; Hendriks, B.; Badi, N.; Du Prez, F., Thiol-ene chemistry for polymer coatings and surface modification - building in sustainability and performance. *Mater. Horiz.* **2017,** *4* (6), 1041-1053.

27. Meghani, N. M.; Amin, H. H.; Lee, B.-J., Mechanistic applications of click chemistry for pharmaceutical drug discovery and drug delivery. *Drug Discov. Today* **2017**.

28. Liebisch, G.; Vizcaíno, J. A.; Köfeler, H.; Trötzmüller, M.; Griffiths, W. J.; Schmitz, G.; Spener, F.; Wakelam, M. J. O., Shorthand notation for lipid structures derived from mass spectrometry. *J. Lipid Res.* **2013,** *54* (6), 1523-1530.

29. Folch, J.; Lees, M.; Stanley, G. H. S., A simple method for the isolation and purification ot total lipids from animal tissues. *J. Biol. Chem.* **1957,** *226* (1), 497-509.

30. Ingalls, S. T.; Kriaris, M. S.; Xu, Y.; Dewulf, D. W.; Tserng, K. Y.; Hoppel, C. L., Method for isolation of non-esterified fatty acids and several other classes of plasma lipids by column chromatography on silica gel. *J. Chromatogr.* **1993,** *619* (1), 9.

31. Hager, J. W., A new linear ion trap mass spectrometer. *Rapid Commun. Mass Spectrom.* **2002,** *16* (6), 512-526.

32. Turunc, O.; Firdaus, M.; Klein, G.; Meier, M. A. R., Fatty acid derived renewable polyamides via thiol-ene additions. *Green Chem.* **2012,** *14* (9), 2577-2583.

33. Mutlu, H.; Parvulescu, A. N.; Bruijnincx, P. C. A.; Weckhuysen, B. M.; Meier, M. A. R., On the Polymerization Behavior of Telomers: Metathesis versus Thiol−Ene Chemistry. *Macromolecules* **2012,** *45* (4), 1866-9297.

34. Hong, M., Application of thiol-ene click chemistry to preparation of functional polyethylene with high molecular weight and high polar group content: Influence of thiol structure and vinyl type on reactivity. *Journal of Polymer Science Part A: Polymer Chemistry* **2012,** *50* (12), 2499-2507.

35. Szendroedi, J.; Yoshimura, T.; Phielix, E.; Koliaki, C.; Marcucci, M.; Zhang, D.; Jelenik, T.; Müller, J.; Herder, C.; Nowotny, P.; Shulman, G. I.; Roden, M., Role of diacylglycerol activation of PKCθ in lipid-induced muscle insulin resistance in humans. *Proc. Natl. Acad. Sci. U.S.A* **2014,** *111* (26), 9597-9602.

36. Meikle, P. J.; Wong, G.; Barlow, C. K.; Weir, J. M.; Greeve, M. A.; MacIntosh, G. L.; Almasy, L.; Comuzzie, A. G.; Mahaney, M. C.; Kowalczyk, A.; Haviv, I.; Grantham, N.; Magliano, D. J.; Jowett, J. B. M.; Zimmet, P.; Curran, J. E.; Blangero, J.; Shaw, J., Plasma Lipid Profiling Shows Similar Associations with Prediabetes and Type 2 Diabetes. *PLoS ONE* **2013,** *8* (9), e74341.

# CHAPTER 4. TUNING THE REACTIVITY OF CYSTEINE DISULFIDES TOWARDS OH RADICAL ATTACK

## 4.1 Introduction

The formation of disulfide bridges involving cysteine amino acid residue is a high-frequency post-translational modification that helps proteins fold and execute proper biological functions.[1-2] Cysteine disulfide linkage is also a widely-employed strategy in the synthesis of peptide mimics, antibiotics, and antibody-drug conjugates (ADCs).[3-6] Disulfide bonds readily undergo substitution reactions with nucleophilic reagents such as thiolate under physiological conditions, which have profound importance in redox homeostasis, enzyme catalysis, and regulations of biological activity.[7-8] Besides the thiol-disulfide interexchange reactions, disulfides are also known to be highly reactive toward reactive oxidative species (ROS), including radicals.[9-10] Hydroxyl radicals ($^{\bullet}$OH) are among the most oxidative species produced in aerobic systems, causing undesirable chemical modifications of biomolecules and irreversible cell damage and cell death once the degree of the modifications is above a critical level.[11] Endogenous cysteine disulfides, such as oxidized glutathione, often serve in cells as sacrificing reagents due to their high reactivity and large cellular concentrations to shield other biomolecules from direct free radical attack.[12-13] The cysteine disulfide functionality has also been purposely incorporated into the design of many powerful antioxidants even though the mechanistic detail of the reaction itself has not been fully characterized.

The mechanistic picture of $^{\bullet}$OH attack to a disulfide bond has been mainly acquired from experimental and theoretical studies using organic disulfides, most frequently with dimethyl disulfide (DMDS, $CH_3SSCH_3$), in solution or in the gas phase. In solution, two major processes compete: 1) electron transfer from DMDS to $^{\bullet}$OH to form $[CH_3SSCH_3]^{\bullet+}$ and $OH^-$ and 2)

dissociative addition of •OH to the disulfide bond, resulting in $CH_3SOH$ and $CH_3S^{\bullet}$.[14] The fate of $[CH_3SSCH_3]^{\bullet+}$ has been speculated with different pathways proposed; however, there are limited experimental evidence supporting detailed chemical changes. Gas-phase studies on the reactions of DMDS with •OH demonstrate that the dissociative addition of •OH to the disulfide bond is the only dominant process both experimentally and computationally, as compared to possible H abstraction or C-S bond cleavage.[15] The early view of the mechanism describes a relatively simple picture: •OH adds onto the disulfide bond in R-S-S-R to form an adduct, followed by a rapid scission of the disulfide bond to form RS• and RSOH. This mechanistic picture, however, is not adequate to explain the detection of $CH_3SH/CH_3SO^{\bullet}$ product pair as a more favorable process to $CH_3S^{\bullet}$ and $CH_3SOH$ formation in the reaction of DMDS and •OH, as reported by Butkovskaya et al.[16] More recently, Bil et al. proposed a more complex multistep mechanism to rationalize the formation of product pair $CH_3SO^{\bullet}$ /$CH_3SH$.[17] Their ab initio/quantum chemical topology data support H atom transfer in the hydrogen-bonded product complex $[CH_3SOH\text{---}^{\bullet}SCH_3]$ after •OH addition, which produces the $[CH_3SO^{\bullet}\text{---}HSCH_3]$ complex before final product separation. In the accompanying experimental study of DMDS reaction with •OH in the presence of NO•, the detection of *cis*-$CH_3SONO$ provides indirect evidence for the formation of $CH_3SO^{\bullet}$. Curiously, the previously reported minor product pair: RS• and RSOH, was not detected with their study and thus the corresponding reaction channel was ruled out in the mechanistic studies.

It is clear that the identification of the unstable reaction products resulting from radical reactions is key in mechanistic illustration. Due to the lasting difficulty in the detection and characterization of biomolecules consisting of radical site, due to their structural complexity and short lifetime, the mechanism of •OH attack cysteine disulfide bonds in proteins and peptides mostly stays at the stage of speculations. Recently, our group has developed a mass spectrometry-

based method to enable *in situ* detection and characterization of a series of bio-radical species resulting from radical reactions.[18-21] The method is based on performing radical reactions between the plume region of a nanoelectrospray ionization (nanoESI) source and the sampling interface of a mass spectrometer. Such a setup provides short sampling time (sub *ms* to *ms*) so that reactive intermediates, such as bio-radicals, can be effectively detected and analyzed by MS. As an example, •OH are produced by discharge in air in the vicinity of the nanoESI source and then react with disulfide-linked peptide (pep-S-S-pep) in the nanoESI plume.[18-19] Two pairs of reaction products, pep-S• /pep-SOH and pep-SH /pep-SO• resulting from disulfide bond cleavage are detected and structurally characterized by mass spectrometry (MS). These data corroborate with the formation of two pairs of products upon disulfide bond cleavage reported from the gas-phase reactions of •OH with DMDS; they also demonstrate the effectiveness of MS as a tool for identifying reactive intermediates. Base on this method, we aim to obtain detail knowledge on the reaction of •OH and the cysteine disulfide bond using a combined experimental and theoretical approach. A model system composed of a series of simple cysteine disulfide derivatives (Cy-S-S-R, structures shown in Scheme 1) is employed in this study, with the electronic property of the R group being varied from electron donating to electron withdrawing. Such a system allows the impact of the electron richness of a disulfide upon OH attack to be investigated, including changes in the reactivity, the selectivity of •OH toward a certain sulfur atom in an asymmetric disulfide bond, and the competitions of different channels. This type of information will not only provide direct evidence in understanding the mechanism but also provide guidance on tuning the reactivity of cysteine disulfide bond in biomolecules to meeting their desirable roles.

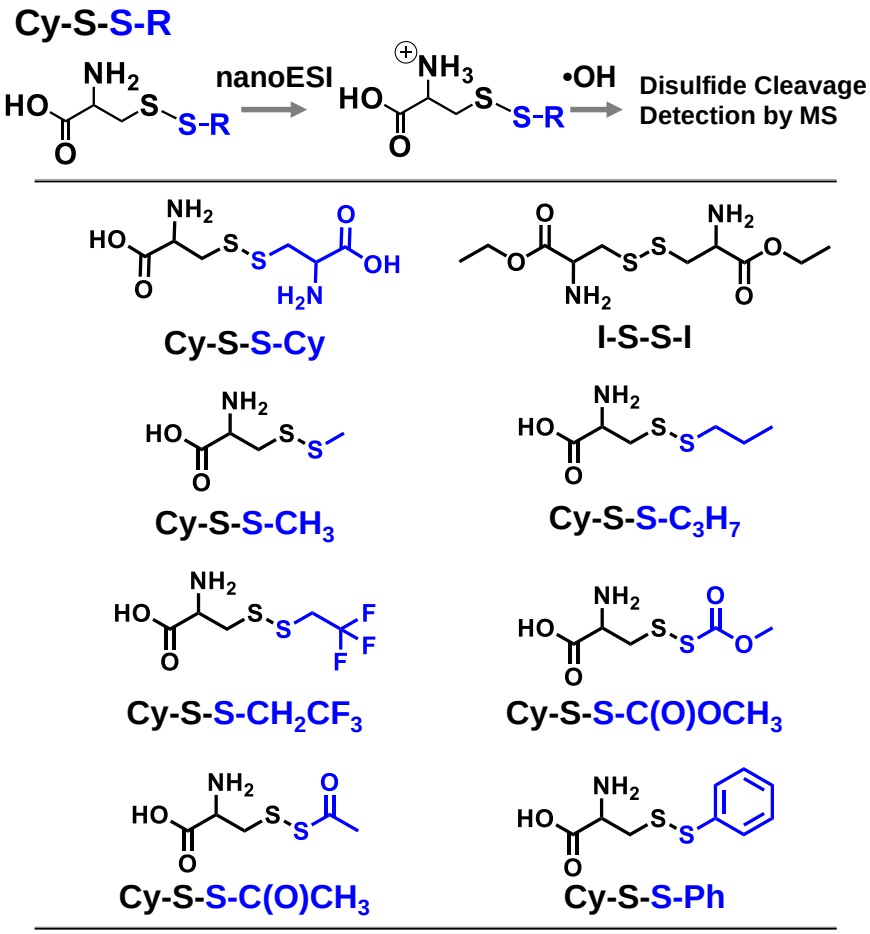


Scheme 4-1 A series of cysteinyl disulfides with varying electron property of the R group (Cy-S-S-R). O-ethylated cystine was used as an internal standard (I-S-S-I). Reactions of Cy-S-S-R and I-S-S-I with OH radicals were facilitated at the nanoESI-MS interface and detected by online MS in the positive ion mode.

## 4.2 Materials and Methods

### 4.2.1 Materials

All the reagents and solvents were purchased from commercial sources and were used without further purification. S-methyl methanethiosulfonate (MMTS), L-cysteine, DL-cysteine, thioacetic acid, methoxycarbonyl chloride, benzyl mercaptan, 1-propantethiol, 2, 2, 2-trifluoroethanethiol, acetyl chloride, ethanol, anhydrous methanol, trimethylamine were purchased from Sigma-Aldrich (MO, USA). Ethyl ester of cysteine was synthesized and used as an internal

standard to keep a relatively constant reaction rate among different cysteine disulfide derivatives. Working solution for positive nanoESI were prepared in deionized $H_2O$ (ultrapure purification system at 0.03 µS cm). The degree of reaction (product/unreacted starting material ratio) was monitored by mass spectrometric analysis.

### 4.2.2 Synthesis of cysteinyl disulfide derivatives

Synthesis of cysteine disulfide derivatives (CySSR) were performed, following the procedures previously described in the literature.[13-15]

**_S_-(methylthio)cysteine (2)**[22]

L-cysteine (60mg, 0.5 mmol) was dissolved in deionized $H_2O$ (0.25 mL) and cooled at 0$^o$C. MMTS (73 mg, 0.6 mmol) in ethanol (0.1 mL) was added in dropwise fashion to the reaction vial, forming a white precipitate. The reaction was stirred for 10 mins. The reaction solution was then washed with cold ethanol (2 mL) twice and then with cold water (2 mL). It was purified by reverse phase-high performance liquid chromatography (RP-HPLC) (Agilent 1200 series, Agilent Technologies, Santa Carla, CA). The collected eluent was vacuum dried using a centrivap concentrator (Labconco, Kansas City, MO).

**_S_-((methoxycarbonyl(thio)cysteine (3)**[22]

Methoxycarbonylsulfenic chloride (0.1 mL, 1.1 mmol) in methanol (1 mL) was added to a solution of cysteine hydrochloride (89 mg, 0.56 mmol) in methanol-HCl (2 mL, 1.25 M). The solution was stirred at 0$^o$ C for 30 minutes. The resulting solution was vacuum dried to remove excess reagent and methanol. The dried sample was purified by RP-HPLC.

**_S_-(propylthio)cysteine (4)**[22-23]

To a solution of 1-propanethiol (1mL, 11 mmol), *S*-((methoxycarbonyl(thio)cysteine **3** (112 mg, 0.56 mmol) in anhydrous methanol (5mL) was added dropwise with stirring. Few drops

of trimethylamine were added to the reaction vial. The reaction was stirred for 24 hours, then the resulting solution was vacuum dried. The dried sample was purified by RP-HPLC.

***S*-((2, 2, 2-trifluoroethyl)thio)cysteine (5)[22]**

To a solution of 2,2, 2-trifluoroethanethiol (50µL, 0.35 mmol), *S*-((methoxycarbonyl(thio)cysteine **3** (40 mg, 0.2 mmol) in anhydrous methanol (3mL) was added dropwise with stirring. Few drops of trimethylamine were added to the reaction vial. The reaction was stirred for 24 hours, then the resulting solution was vacuum dried. The dried sample was purified by RP-HPLC.

***S*-(acetylthio)cysteine (6)[22]**

To a solution of thioacetic acid (55 µL, 0.35 mmol), *S*-((methoxycarbonyl(thio)cysteine **3** (40 mg, 0.2 mmol) in anhydrous methanol (3mL) was added dropwise with stirring. Few drops of trimethylamine were added to the reaction vial. The reaction was stirred for 24 hours, then the resulting solution was vacuum dried and subjected to RP-HPLC separation.

***S*-(phenylthio)cysteine (7)[22]**

To a solution of benzyl mercaptan (40µL, 0.35 mmol), *S*-((methoxycarbonyl(thio)cysteine **3** (40 mg, 0.2 mmol) in anhydrous methanol (3mL) was added dropwise with stirring. Few drops of trimethylamine were added to the reaction vial. The reaction was stirred for 24 hours, then the resulting solution was vacuum dried and purified by RP-HPLC.

**Ethyl ester of cystine (Internal standard, IS)[24]**

DL-cystine (30mg, 0.25mmol) was dissolved in ethanol (3mL). Acetyl chloride (1 mL, 0.012mmol) was added to the solution in a drop-wise manner. The reaction was monitored for 3 days at room temperature by mass spectrometry. The resulting solution was vacuum dried and purified by RP-HPLC.

### 4.2.3 Mass spectrometry

All the MS data collection were done on a 4000 QTRAP (triple quadrupole/linear ion trap (LIT)) mass spectrometer through nano-electrospray ionization (nanoESI).[25] Analyst software 1.6.2 software was used for data acquisition, processing, and instrument control. Typical MS parameters during the study were: spray voltage, ± 1500-1800 V; curtain gas, 10 psi; declustering potential, ±20V; scan rate, 1000 Da/s. $MS^1$ mass analysis was performed in LIT mode in Q3. Collision-induced dissociation (CID) were performed in both modes: beam type and ion trap CID. Beam-type CID was performed by precursor ion selection in Q1, ion acceleration into q2 collision cell, and followed by product analysis in Q3 linear ion trap. Ion-trap CID consisted of precursor ion selection in Q1, ion transfer through q2 to Q3 with a minimum activation energy, followed by re-isolation, accumulation, and application of dipolar excitation to effect CID in Q3. NanoESI plume of disulfide was allowed to interact with the oxidative radical (•OH) in the afterglow region of an atmospheric pressure helium low-temperature plasma (LTP) enabled in a T-shaped glass tube placed in front of the entrance of the mass spectrometer (Figure 2 ).[26]

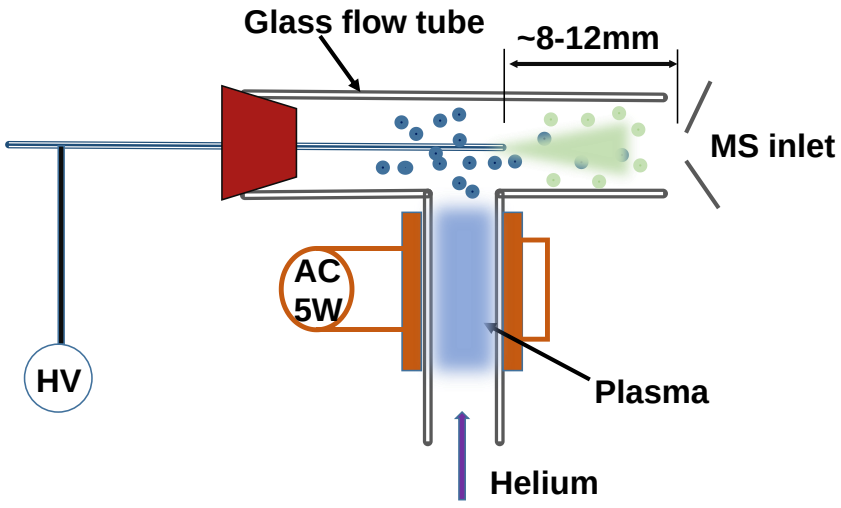


Scheme 4-2 Experimental Setup for the reaction of CySSR with •OH.

## 4.3 Results and discussion

### 4.3.1 Reaction phenomena of •OH and Cy-S-S-R

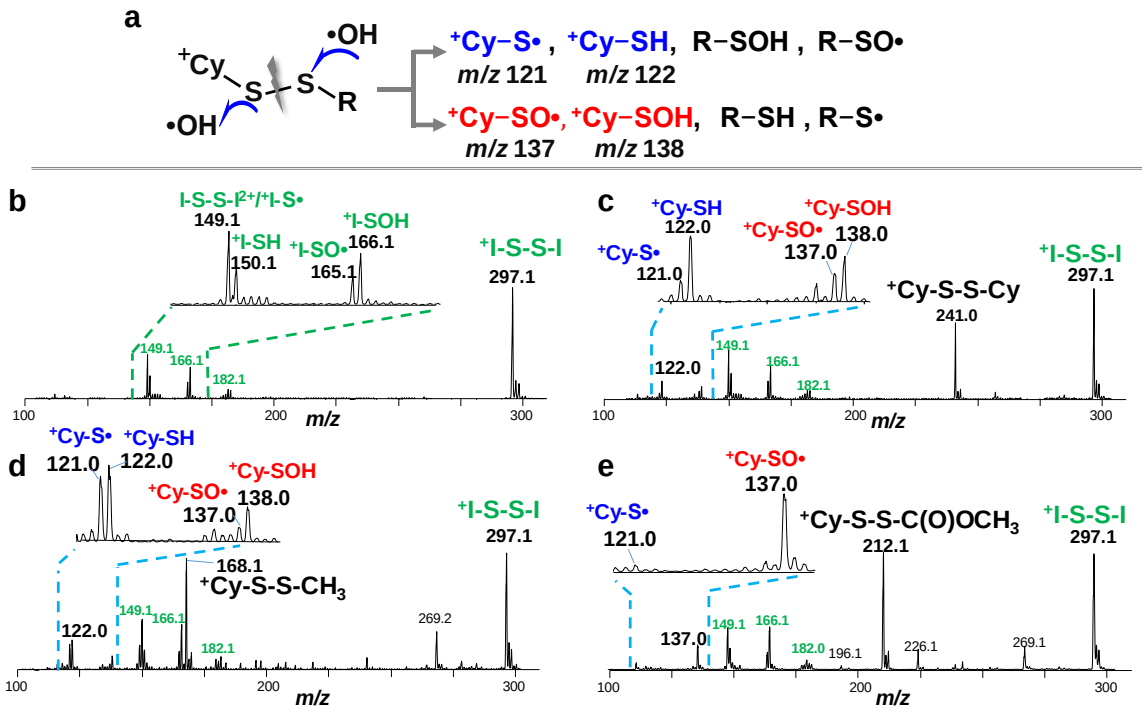


Figure 4-1 On-line MS monitoring of reactions of OH• and cysteinyl disulfides. A) Four charged products are formed from OH attack to a disulfide bond in Cy-S-S-R: $^{+}$Cy-S• (*m/z* 121), $^{+}$Cy-SH (*m/z* 122), $^{+}$Cy-SO• (*m/z* 137), and $^{+}$Cy-SOH (*m/z* 138), while the other four neutral products (R-S•, R-SH, R-SO•, R-SOH) not detected by MS. Reaction MS spectra of B) I-S-S-I, C) Cy-S-S-Cy, D) Cy-S-S-$CH_3$, and E) Cy-S-S-C(O)$OCH_3$. Insets show the zoom-in region of the first-generation of the reaction products.

A series of cysteine disulfide derivatives (Cy-S-S-R) (Scheme 1) was synthesized with the substituent group (R) at the disulfide bond being either an electron withdrawing group (EWG) or electron donating group (EDG). The reactions between each cysteine disulfide model compound and •OH were conducted at the sampling interface region of a mass spectrometer and monitored by MS analysis (Figure 1). In brief, cysteine disulfide (10 μM in deionized water) was ionized by nanoESI and subjected to the reaction with •OH produced by dielectric barrier discharge of helium in air. The reactions were monitored in the positive ion mode, leading to the detection of intact

cysteine disulfide derivatives and their reaction products in the protonated form (at the amine site, Scheme 1).

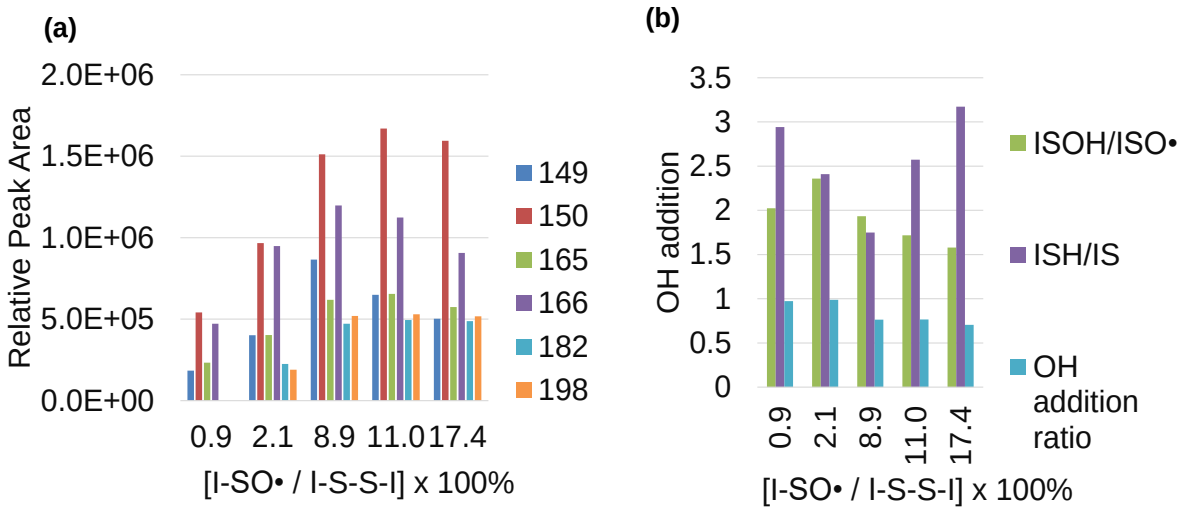


Figure 4-2 Ion intensity with the degree of reaction of ISSI with •OH (a) Kinetic of I-S-S-I with •OH in the formation of I-SO• (b) •OH addition to IS-SI.

To facilitate cross-comparisons on the reactivity of Cy-S-S-R toward •OH, an internal standard, O-ethylated cystine (I-S-S-I), was employed. Four products (Figure 1 (a)) due to •OH addition and disulfide bond cleavage were detected and verified by MS/MS: $^{+}$I-S• (*m/z* 149), $^{+}$I-SH (*m/z* 150), $^{+}$I-SO• (*m/z* 165), and $^{+}$I-SOH (*m/z* 166). Possible reaction products involving C-S bond cleavage or H abstraction were not detected above the noise level. Due to an overlap to the doubly protonated I-S-S-I (*m/z* 149.1), the actual intensity of $^{+}$I-S• (*m/z* 149.1) should be lower than that shown in the spectrum. The formation of the $^{+}$I-SOH/$^{+}$I-S• pair may result from hydroxyl radical addition to one of the sulfur atom and subsequent cleavage of the disulfide bond. The formation of $^{+}$I-SH and $^{+}$I-SO• products, however, suggests H transfer during the reaction. By varying the helium gas flow in the discharge area and the relative position of the nanoESI tip to the discharge area, different degrees of the reaction of I-S-S-I with OH radicals were achieved

(Figure 2). The kinetic data suggested that by keeping the formation of $^{+}$I-SO• at ~10% relative ion intensity relative to the remaining I-S-S-I ions (*m/z* 297, Figure 2), the first-generation reaction products dominated while the sequential reaction products contributed to a relatively small extent (i.e. I-$SO_2$H at *m/z* 182.1, Figure 2). The 10% relative intensity of $^{+}$I-SO• was kept constant to ensure that the same reaction conditions were reproducible for each individual cysteine disulfide derivatives (Cy-S-S-R) even though the actual number density of OH radicals and the reaction time cannot be precisely controlled using our current experimental methods.

Seven Cy-S-S-R compounds were each subjected to the reactions with OH radicals with equal molar of I-S-S-I added as an internal standard. It is worth noting that because the R groups (except for cysteine) do not contain basic functional groups for protonation, the reaction products involving R side, viz. R-S•, R-SH, R-SO•, and R-SOH, cannot be detected by MS. For this reason, only four products are expected to be detected regardless of the change of R substituent in Cy-S-S-R (Figure 1 (a)); these include the protonated cysteine thiyl radical ($^{+}$Cy-S$^{\bullet}$, *m/z* 121), cysteine ($^{+}$Cy-SH, *m/z* 122), cysteine sulfinyl radical ($^{+}$Cy-SO$^{\bullet}$, *m/z* 137), and cysteine sulfinic acid ($^{+}$Cy-SOH, *m/z* 138). Their identities were confirmed by tandem mass spectrometry. Among these four products, $^{+}$Cy-S$^{\bullet}$ and $^{+}$Cy-SH result from OH attack to the sulfur atom connected to the R group, while $^{+}$Cy-SO$^{\bullet}$ and $^{+}$Cy-SOH derive from OH attack to the cysteine sulfur. The reaction spectra of Cy-S-S-Cy, Cy-S-S-$CH_3$, and Cy-S-S-C(O)-$OCH_3$ are used as examples to demonstrate the reaction phenomena of a symmetric disulfide bond and an asymmetric disulfide bond connected to an EDG and EWG, respectively. For Cy-S-S-Cy, the four expected reaction products due to OH cleavage of the disulfide bond are clearly detected showing patterns similar to that of the internal standard (Figure 1(c)). The reaction of OH with Cy-S-S-$CH_3$ (Figure 1(d)), however,

produces higher intensities of $^{+}$Cy-S• and $^{+}$Cy-SH than $^{+}$Cy-SO• and $^{+}$Cy-SOH. This result suggests that OH radical has a preference for reacting at the S-$CH_3$ than the S-Cy side. The reaction

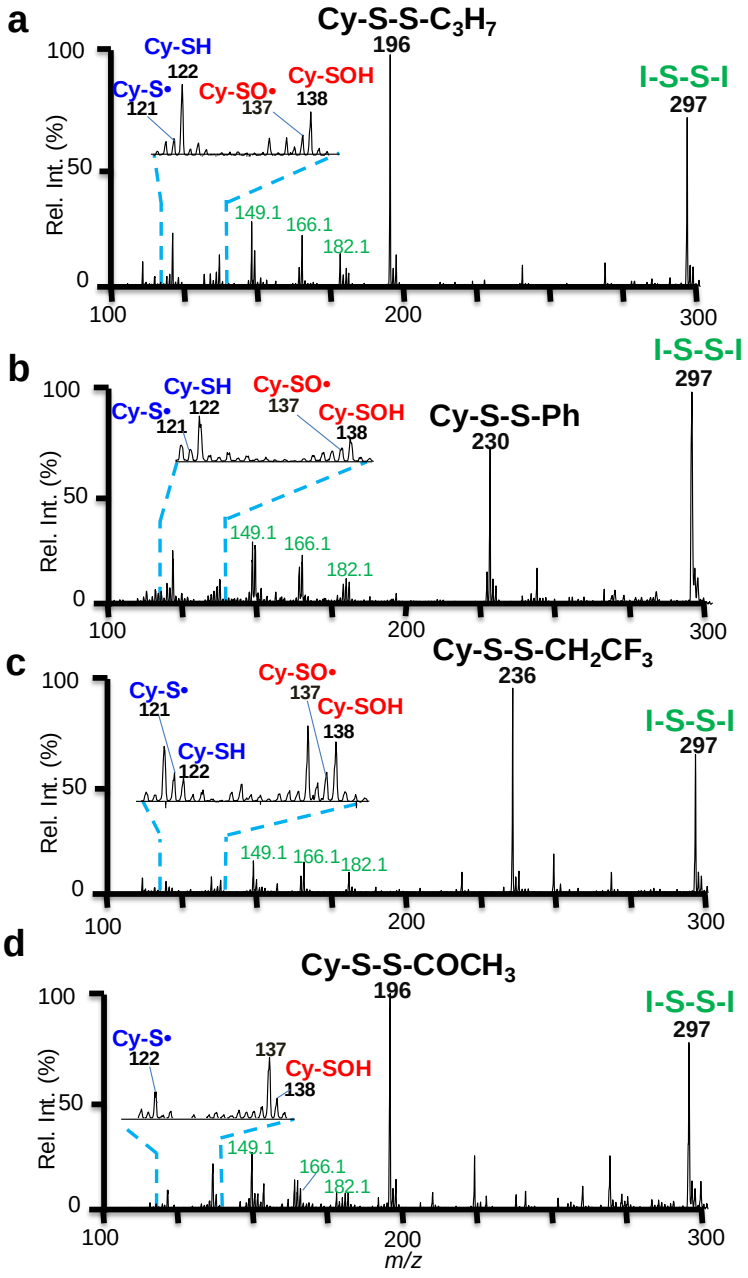


Figure 4-3 On-line MS monitoring of reactions of OH• and cysteinyl disulfides. Reaction MS spectra of a) Cy-S-S-$C_3H_7$, b) Cy-S-S-Ph, c) Cy-S-S-$CH_2CF_3$, and d) Cy-S-S-$COCH_3$. I-S-S-I ($^{+}$I-SO• at ~10% relative ion intensity relative to the remaining I-S-S-I ions) is used as the internal standard. Insets show the zoom-in region of the first-generation of the reaction products.

spectrum of Cy-S-S-C(O)$OCH_3$ (Figure 1(e)), where the disulfide bond is connected to an EWG, shows drastically different fractioning of reaction products as compared to the previous two cysteine disulfides. Only dominant $^{+}CySO^{\bullet}$ was detected as the reaction product, while the other three products cannot be confidently differentiated from background noise. The reaction spectra of the other Cy-S-S-R compounds can be found in Figure 3. In summary, online monitoring of the reactions of Cy-S-S-R and OH shows that the electronic property of the substituent group holds a strong impact on the reaction phenomena.

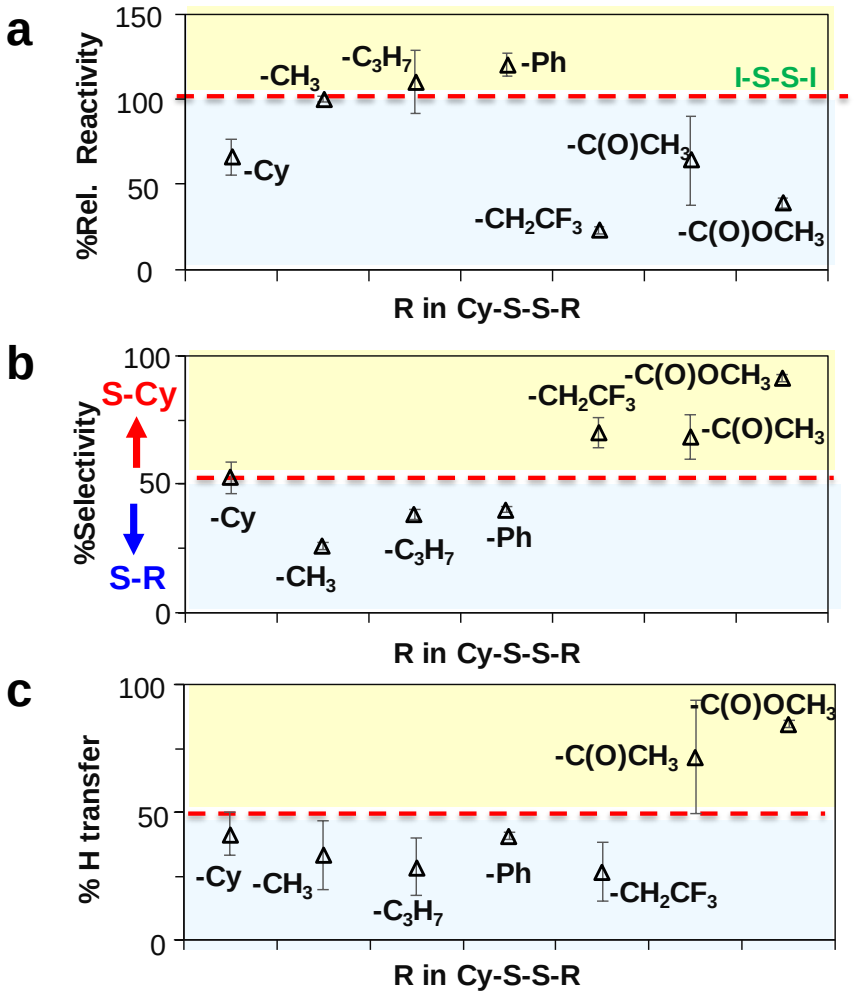


Figure 4-4 a) *% Relative reactivity* of Cy-S-S-R toward OH, normalized to I-S-S-I. The Cy-S-S-R compound exhibits a higher reactivity with -R being an EDG. b) *% Selectivity* of OH attack to the Cy-S sulfur atom relative to S-R within Cy-S-S-R. A 50% selectivity is obtained for a compound containing symmetric disulfide bond, Cy-S-S-Cy. The plot suggests OH prefers to react at the more electron rich sulfur atom within a disulfide bond. c) *% H transfer* leading to the formation of Cy-SO•. Dominant H transfer was observed when R is -C(O)$CH_3$ and -C(O)$OCH_3$.

The relative reactivity of various cysteine disulfides can be readily compared with the use of the internal standard. First, the *%reaction* of each Cy-S-S-R is calculated by dividing the sum of the peak areas of all first-generation reaction products by the peak area of the remaining $^{+}$Cy-S-S-R ions. This *%reaction* is further normalized to the *%reaction* of I-S-S-I to provide *%rel. reactivity* of each Cy-S-S-R compound. The *%rel. reactivity* data in Figure 4 (a) show that for an asymmetric disulfide bond, Cy-S-S-R shows a higher reactivity toward OH• when R is an EDG, i.e., -$CH_3$ (100 ± 2%), -$C_3H_7$ (110 ± 17%), -Ph (120 ± 6%), as compared to R being an EWG, i.e., -$CH_2CF_3$ (23 ± 10%), -$C(O)CH_3$ (64 ± 40%), -$C(O)OCH_3$ (39 ± 7%). Interestingly, Cy-S-S-Cy shows a slightly lower reactivity (66 ± 16%) than the internal standard (100%), while the two compounds only differ in the modification of the ethyl ester at the carboxylic group. Overall, these data suggest that the disulfide bond reacts faster when connected to an electron-rich substituent.

Since $^{\bullet}$OH can attack either sulfur atom within a disulfide bond, the preference of attack (*%Selectivity*) is evaluated by calculating the fraction of products resulting from OH attack to the cysteine residue, forming Cy-SO• and Cy-SOH, from all first-generation products. A value of 50% selectivity suggests that OH radical has an equal probability of attacking either sulfur atoms in the disulfide bond, which in fact is the case for cysteine (53 ± 12%). A value of selectivity larger than 50% indicates that OH radical prefers reaction at the cysteinyl sulfur (Cy-S), while a value smaller than 50% suggests a preference at the S-R moiety. As plotted in Figure 4 (b), the *%selectivity* values of the Cy-S-S-R compounds are clearly clustered into two groups based on R being an EWG or EDG. That is, OH radical shows a high preference to attack the cysteinyl sulfur atom when R is an EWG, with the *% Selectivity* values at 70 ± 9% (-$CH_2CF_3$), 68 ± 13% (-$C(O)CH_3$), and 91 ± 1% (-$C(O)OCH_3$). When R is an EDG, the *% selectivity* values are all smaller than 50%,

viz. 26 ± 5% for -$CH_3$, 38 ± 5% for -$C_3H_7$, and 40 ± 3% for -Ph. These data clearly suggest that $^{\bullet}$OH has a preference to react with the electron-rich sulfur within a disulfide bond.

One of the most interesting phenomena of the reactions between Cy-S-S-R and OH is the observation of $^{+}$Cy-SO$^{\bullet}$. This product is likely produced from H transfer from Cy-SOH to $^{\bullet}$S-R, accompanying the formation of the other product R-SH. The *%H transfer* value is calculated from the intensity of $^{+}$Cy-SO$^{\bullet}$ divided by the summed intensity of $^{+}$Cy-SOH and $^{+}$Cy-SO$^{\bullet}$. Figure 4 (c) summarizes a plot of *%H transfer* for all seven Cy-S-S-R compounds. Only two Cy-S-S-R compounds, R= -C(O)$CH_3$ and C(O)$OCH_3$, show a large extent of H transfer (>70%), while all the rest disulfide compounds shared a similar degree of H transfer in the range of 30-43% regardless R being an EWG or EDG group.

## 4.4 Conclusions

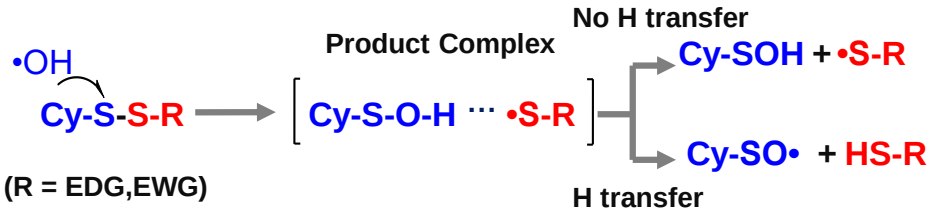


Scheme 4-3 Reaction mechanism for OH attack to the disulfide bond of Cy-S-S-R, using OH attack to the Cy-S for illustration purpose.

A two-step mechanism (Scheme 2) is proposed for the OH• reaction with Cy-S-S-R. The first step is a concerted process of •OH addition to one of the sulfur atoms within the disulfide bond and disulfide bond cleavage. This process is preferable from a backside attack to the electron-rich sulfur atom, leading to the formation of a product complex [Cy-S-O···H···•S-R] (only using OH attack to Cy-S as an example while OH attack to R-S also happens). Before the

product complex separates, hydrogen transfer could happen from Cy-SOH to •S-R, resulting in two products, Cy-SO• and R-SH. This process, however, is only more favorable when the R substituent contains a carbonyl or carboxyl group, which assists spin delocalization from the sulfur to the oxygen atom and therefore promotes H transfer. If product complex separates without H transfer, it leads to the formation of Cy-SOH and R-S•. The above findings are important since they clearly show that the reactivity of the cysteine disulfide bond could be tuned by changing the electronic property of the substituent group connecting to the disulfide bond. For instance, in order to increase the reactivity of cysteine disulfides, such as in the application of antioxidant, an electron donating group should be considered. For designing prodrugs consisting of cysteine disulfide linkage, connecting an electron withdrawing group can largely increase its resistance to •OH attack and therefore increase its circulating lifetime under physiological conditions.

## 4.5 References


1. Anfinsen, C. B., Principles that Govern the Folding of Protein Chains. *Science* **1973,** *181* (4096), 223-230.

2. Wedemeyer, W. J.; Welker, E.; Narayan, M.; Scheraga, H. A., Disulfide Bonds and Protein Folding. *Biochemistry* **2000,** *39* (15), 4207-4216.

3. Chari, R. V. J.; Miller, M. L.; Widdison, W. C., Antibody–Drug Conjugates: An Emerging Concept in Cancer Therapy. *Angew. Chem. Int. Ed.* **2014,** *53* (15), 3796-3827.

4. Dutton, R. J.; Wayman, A.; Wei, J.-R.; Rubin, E. J.; Beckwith, J.; Boyd, D., Inhibition of bacterial disulfide bond formation by the anticoagulant warfarin. *Proc. Natl. Acad. Sci. U.S.A.* **2010,** *107* (1), 297-301.

5. Hill, T. A.; Shepherd, N. E.; Diness, F.; Fairlie, D. P., Constraining Cyclic Peptides To Mimic Protein Structure Motifs. *Angew. Chem. Int. Ed.* **2014,** *53* (48), 13020-13041.

6. Kong, F.; Liang, Z.; Luan, D.; Liu, X.; Xu, K.; Tang, B., A Glutathione (GSH)-Responsive Near-Infrared (NIR) Theranostic Prodrug for Cancer Therapy and Imaging. *Anal. Chem.* **2016,** *88* (12), 6450-6456.

7. Bach, R. D.; Dmitrenko, O.; Thorpe, C., Mechanism of Thiolate−Disulfide Interchange Reactions in Biochemistry. *J. Org. Chem.* **2008,** *73* (1), 12-21.

8. Paranjothy, M.; Siebert, M. R.; Hase, W. L.; Bachrach, S. M., Mechanism of Thiolate-Disulfide Exchange: Addition-Elimination or Effectively SN2? Effect of a Shallow Intermediate in Gas-Phase Direct Dynamics Simulations. *J. Phys. Chem. A.* **2012,** *116* (47), 11492-11499.

9. Halliwell, B., The Chemistry of Free Radicals. *Toxicol. Ind. Health* **1993,** *9* (1-2), 1-21.

10. Nimse, S. B.; Pal, D., Free radicals, natural antioxidants, and their reaction mechanisms. *RSC Adv.* **2015,** *5* (35), 27986-28006.

11. Halliwell, B.; Gutteridge, J. M. C.; Cross, C. E., Free radicals, antioxidants, and human disease: Where are we now? *J. Lab. Clin. Med.* **1992,** *119* (6), 598-620.

12. Townsend, D. M.; Tew, K. D.; Tapiero, H., The importance of glutathione in human disease. *Biomed. Pharacother.* **2003,** *57* (3), 145-155.

13. Enami, S.; Hoffmann, M. R.; Colussi, A. J., OH-Radical Specific Addition to Glutathione S-Atom at the Air–Water Interface: Relevance to the Redox Balance of the Lung Epithelial Lining Fluid. *J. Phys. Chem. Lett.* **2015,** *6* (19), 3935-3943.

14. Wine, P. H.; Kreutter, N. M.; Gump, C. A.; Ravishankara, A. R., Kinetics of hydroxyl radical reactions with the atmospheric sulfur compounds hydrogen sulfide, methanethiol, ethanethiol, and dimethyl disulfide. *J. Phys. Chem.* **1981,** *85* (18), 2660-2665.

15. Wang, W.; Xin, J.; Zhang, Y.; Wang, W.; Lu, Y., Computational study on the mechanism for the gas-phase reaction of dimethyl disulfide with OH. *Int. J. Quantum Chem* **2011,** *111* (3), 644-651.

16. Butkovskaya, N. I.; Setser, D. W., Mechanism for the reaction of hydroxyl radicals with dimethyl disulfide. *Chem. Phys. Lett.* **1999,** *312* (1), 37-44.

17. Bil, A.; Grzechnik, K.; Mierzwicki, K.; Mielke, Z., OH-Induced Oxidative Cleavage of Dimethyl Disulfide in the Presence of NO. *J. Phys. Chem. A.* **2013,** *117* (34), 8263-8273.

18. Xia, Y.; Cooks, R. G., Plasma Induced Oxidative Cleavage of Disulfide Bonds in Polypeptides during Nanoelectrospray Ionization. *Anal. Chem.* **2010,** *82* (7), 2856-2864.

19. Tan, L.; Xia, Y., Gas-Phase Reactivity of Peptide Thiyl (RS•), Perthiyl (RSS•), and Sulfinyl (RSO•) Radical Ions Formed from Atmospheric Pressure Ion/Radical Reactions. *J. Am. Soc. Mass. Spectrom.* **2013,** *24* (4), 534-542.

20. Stinson, C. A.; Xia, Y., Reactions of Hydroxyalkyl Radicals with Cysteinyl Peptides in a NanoESI Plume. *J. Am. Soc. Mass Spectrom.* **2014,** *25* (7), 1192-1201.

21. Durand, K. L.; Tan, L.; Stinson, C. A.; Love-Nkansah, C. B.; Ma, X.; Xia, Y., Assigning Peptide Disulfide Linkage Pattern Among Regio-Isomers via Methoxy Addition to Disulfide and Tandem Mass Spectrometry. *J. Am. Soc. Mass. Spectrom.* **2017,** *28* (6), 1099-1108.

22. Rietman, B. H.; Peters, R. F. R.; Tesser, G. I., A Facile Method for the Preparation of S-(Alkylsulfenyl)cysteines. *Synth. Commun.* **1994,** *24* (9), 1323-1332.

23. Starkenmann, C.; Niclass, Y.; Troccaz, M., Nonvolatile S-Alk(en)ylthio-l-cysteine Derivatives in Fresh Onion (Allium cepa L. Cultivar). *J. Agric. Food. Chem.* **2011,** *59* (17), 9457-9465.

24. Love-Nkansah, C. B.; Tan, L.; Francisco, J. S.; Xia, Y., Gas-Phase Unimolecular Dissociation Reveals Dominant Base Property of Protonated Homocysteine Sulfinyl Radical Ions. *Chem. Eur. J.* **2016,** *22* (3), 934-940.

25. Hager, J. W., A new linear ion trap mass spectrometer. *Rapid Commun. Mass Spectrom.* **2002,** *16* (6), 512-526.

26. Tan, L.; Xia, Y., Gas-Phase Peptide Sulfinyl Radical Ions: Formation and Unimolecular Dissociation. *J. Am. Soc. Mass. Spectrom.* **2012,** *23* (11), 2011-2019.

# CHAPTER 5. ACETONE / ISOPROPANOL PHOTOINITIATING SYSTEM ENABLES TUNABLE DISULFIDE REDUCTION AND DISULFIDE MAPPING VIA TANDEM MASS SPECTROMETRY

(Adapted from publication in Analytical Chemistry)

## 5.1 Introduction

As mass spectrometry (MS) becomes the tool of choice for characterizing structural modifications in proteins, disulfide mapping still presents challenges for current proteomics analysis workflows.[1] The issue is directly linked to the nature of gas-phase fragmentation chemistry of protonated peptide ions under low energy collision-induced dissociation (CID), the most available tandem mass spectrometry (MS/MS) technique equipped on commercial mass spectrometers. As depicted by the mobile proton model,[2] disulfide bond does not dissociate readily as compared to the amide bonds under low energy CID, often leading to no detectable sequence fragment ions for the backbone region inside a disulfide loop.[3] This characteristics not only limits protein sequencing but also causes difficulty in disulfide mapping. To tackle this problem, disulfide bond reduction followed by alkylation[4] has been employed as a routine sample preparation procedure in bottom-up proteomics workflows.[5] Along this line, fast disulfide cleavage via chemical or electrochemical reduction has been developed which could be coupled with online liquid chromatography-mass spectrometry (LC-MS).[6,7] Besides, disulfide cleavage inside the ionization source region has been demonstrated using electrospray ionization (ESI),[8,9,10] matrix-assisted laser desorption ionization (MALDI),[11] and reactive electrospray-assisted laser desorption/ionization (ELDI)[12]. All above approaches when coupled with subsequent MS/MS (typically low energy CID) deliver rich sequence information due to opening the disulfide bridges; however, disulfide linkage information is lost if complete disulfide reduction is adopted.

Alternative ion activation methods have been explored aiming to induce disulfide cleavages in the gas phase so that intact disulfide bonds can be preserved before MS analysis. Disulfide bond can be preferentially cleaved by electrons (in electron capture dissociation (ECD)[13,14] and electron transfer dissociation (ETD)[15]), photons (in 157 nm,[16] 266 nm,[17,18] and 193 nm ultraviolet photodissociation (UVPD)[19]), radicals (radical initiated peptide sequencing (FRIPS) and TEMPO conjugated peptide ions),[20] and oxidants in ion/ion reactions[21]. These methods can each be used as a stand-alone MS/MS technique or to be combined with CID to improve sequence coverage.

Disulfide mapping strategies rely heavily on multi-enzymatic digestion and partial disulfide reduction, with a goal to produce peptide digests only consisting of inter-chain disulfides. This type of structures is preferred since sequence fragments around cysteine amino acid residues associated with a disulfide bond are more likely to be generated from MS/MS, which is necessary for confident disulfide assignment. Such disulfide mapping approach has been recently demonstrated for human serum albumin (17 disulfide bonds)[8] and serotransferrin (19 disulfide bonds).[19] Finding the right conditions for partial reduction and proteolytic cleavages while avoiding disulfide scrambling is critical for successful disulfide mapping.[16,22] The optimization process is typically achieved by trial-and-error and the conditions cannot be generalized for different protein systems. Obviously, new methods that could either improve digestion or partial disulfide reduction will greatly advance the overall process for disulfide mapping.

Disulfides are known to be highly reactive towards radicals and the dominant reaction channel is disulfide bond cleavage. Earlier efforts from our group have shown that radicals produced from gas discharge[23] or ultra-violet (UV) irradiation[9,10] can cleave disulfide bonds within peptides near or in an ESI emitter. However, disulfide cleavage efficiency is only moderate and

often accompanied by side reactions due to the lack of control of the reaction kinetics. In this work, we have developed a new photochemical reaction system for achieving efficient and tunable disulfide bond cleavage in the second-time scale. In this system, acetone was used as a clean and MS compatible photoinitiator upon 254 nm UV irradiation, while secondary hydroxyalkyl radicals resulting from alcohol co-solvent were responsible for cleaving the disulfide bond (Scheme 1). This photochemical reaction system was hyphenated with infusion ESI via a flow microreactor. Structural analysis capability of this photochemical system was demonstrated by coupling complete or partial disulfide cleavage with online ESI-MS/MS via CID for peptides containing one or multiple disulfide bonds.

**a) Radical Initiation**

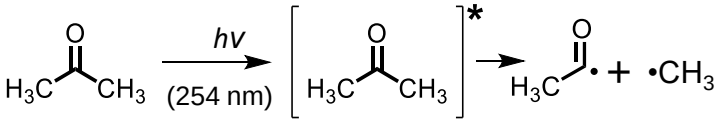


**b) Formation of Alkyl Hydroxyl Radical**

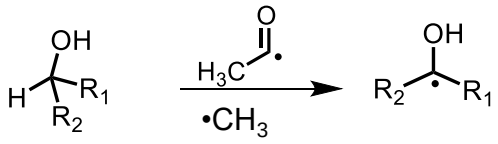


MeOH: $R_1$= $R_2$= H  EtOH: $R_1$= H, $R_2$= $CH_3$

IPA: $R_1$= $R_2$ = $CH_3$

**c) Cleavage of S-S**

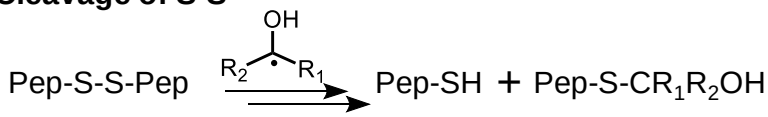


Scheme 5-1 Proposed reaction pathways for disulfide bond cleavage using the acetone/alkyl alcohol photoinitiating system.

## 5.2 Materials and Methods

### 5.2.1 Materials

Oxidized glutathione, reduced glutathione, methanol (MeOH), ethanol (EtOH), isopropyl alcohol (IPA), acetone, acetonitrile (ACN), TPCK treated trypsin, oxytocin, insulin from the porcine pancreas, and ribonuclease B were purchased from Sigma-Aldrich (St. Louis, MO, USA). Somatostatin-14 and selectin binding peptide were purchased from Aladdin® (Shanghai, China) and GL Biochem Ltd. (Shanghai, China), respectively. The single letter sequence and disulfide bond connecting pattern for each peptide are listed in Supporting Information, Table S-1. $d_3$-Methanol ($CD_3OH$, 99.5 atom % D) and $d_6$-acetone ($CD_3COCD_3$, 99.9 atom % D) were purchased from J&K Scientific Ltd. (Beijing, China). All commercially purchased chemicals were used without further purification. Deionized water was obtained from a water purification system at 0.03 μS·cm (Thermo Scientific; San Jose, CA, USA).

Table 5-1 List of model Cysteinyl Peptides Studied

| Label | Structure |
|---|---|
| P1 | γECG<br>\|<br>γECG |
| P2 | AGCK<br>\|<br>TFTSC |
| P3 | ⌜CIELLQARC⌝ |
| P4 | ⌜CYIQNCPLG⌝-$NH_2$ |
| P5 | ⌜AGCKNFFWKTFTSC⌝ |

The peptides are indicated by single letter sequence. The connection line between two “C” s (cysteine) within a peptide represents the disulfide linkage.

### 5.2.2 Peptide/Protein digestion and liquid chromatography

Trypsin digestion was conducted by mixing 10 µL of protein/peptide solution (10 µg/mL) with 15 µL of 20 mM ammonium acetate buffer, 5 µL acetonitrile, and 2 µL of trypsin (1 µg/µL), followed by incubation at 37 ºC for 3 hours. The trypsin digest was separated on a reversed phase LC (Shimadzu Corporation, Columbia, MD, USA). Column dimension was 4.6 mm x 150 mm with 5 µm C-18 packing material. Separation conditions for the digest are 0.1% formic acid in water (solvent A) and 0.1% formic acid in ACN (solvent B) with a linear gradient starting from 0% to 40% solvent B for 30 minutes at 0.5 mL/min flow rate.

### 5.2.3 Photochemical reactions in nanoESI emitter and flow microreactor

A low-pressure mercury (LP-Hg) lamp with an emission band around 254 nm (BHK, Inc., Ontario, CA) was utilized to initiate the photochemical reactions. For the nanoESI setup, the lamp was placed orthogonally to the tip and off-axis by approximately 2-4 cm of the borosilicate glass emitter, as reported previously.[9] The flow microreactor was made from UV-transparently coated fused silica capillary (100 µm i.d., 375 µm o.d.; Polymicro Technologies; Phoenix, AZ).[24,25] The lamp was placed in parallel to the capillary (~10 cm exposure length) at 0.5 cm distance. The peptide solution was pumped through the microreactor (1-10 µL/min), the end of which was connected to the inlet of an infusion ESI source. All photochemical reaction setups were enclosed in a cardboard box to prevent direct human exposure to UV light.

### 5.2.4 Mass Spectrometry

Experiments were performed on QTRAP 4000, 4500 hybrid triple quadrupole/linear ion trap, X500R QTOF (SCIEX, Concord, ON, Canada), and a TIMS-TOF mass spectrometer (Bruker, Germany). For the experiments performed on QTRAP 4000 and QTRAP 4500, MS mass analysis

was performed in linear ion trap mode in Q3, using the nanoESI source. For X500R QTOF and TIMS-TOF, mass analysis was performed using the equipped ESI source.

5.2.5 Procedure for isotopic deconvolution:

Since insulin has three disulfide bonds, the partially reduced insulin may exist as a mixture of three components: intact, one disulfide reduced, and two disulfides reduced insulin species. Multivariant linear regression (MLR) was used to deconvolute and quantify each component from experimentally measured insulin ion isotopes ($[M+5H]^{5+}$). The relative ion intensity of the n$^{th}$ isotope ($I'_{i,n}$, only counting the contribution form $^{13}C$ in the molecule) from the *i*th-reduced ($i$ =0, 1, 2) component can be expressed based on its theoretical isotope distribution ($I_{i,n}$),

$$I'_{i,n} = c_i \times I_{i,n} + b_i, \qquad i = 0, 1, 2$$

where $c_i$ is the fraction of the *i*th-reduced component in the mixture and $b_i$ is an associated constant.

The relative ion intensity of the n$^{th}$ isotope ($I'_n$) from the mixture is a sum of this isotope from all three components ($i$ =0, 1, 2),

$$I'_n = \sum_{i=0}^{2} I'_{i,n} = \sum_{i=0}^{2} c_i \times I_{i,n} + \sum_{i=0}^{2} b_i = \sum_{i=0}^{2} c_i \times I_{i,n} + b + \varepsilon_i$$

where $b = b_0 + b_1 + b_2$. All isotopes in the partially reduced mixture can be expressed as follows:

$$\begin{bmatrix} I'_1 \\ \vdots \\ I'_n \end{bmatrix} = \begin{bmatrix} 1 & I_{0,1} & I_{1,1} & I_{2,1} \\ \vdots & \vdots & \vdots & \vdots \\ 1 & I_{0,n} & I_{1,n} & I_{2,n} \end{bmatrix} \times \begin{bmatrix} \mathrm{b} \\ c_0 \\ c_1 \\ c_2 \end{bmatrix} + \begin{bmatrix} \varepsilon_1 \\ \vdots \\ \varepsilon_n \end{bmatrix}$$

MLR shows that the optimal solution can be calculated as

$$\begin{bmatrix} \mathrm{b} \\ c_0 \\ c_1 \\ c_2 \end{bmatrix} = \left( \begin{bmatrix} 1 & I_{0,1} & I_{1,1} & I_{2,1} \\ \vdots & \vdots & \vdots & \vdots \\ 1 & I_{0,n} & I_{1,n} & I_{2,n} \end{bmatrix}^T \begin{bmatrix} 1 & I_{0,1} & I_{1,1} & I_{2,1} \\ \vdots & \vdots & \vdots & \vdots \\ 1 & I_{0,n} & I_{1,n} & I_{2,n} \end{bmatrix} \right)^{-1} \begin{bmatrix} 1 & I_{0,1} & I_{1,1} & I_{2,1} \\ \vdots & \vdots & \vdots & \vdots \\ 1 & I_{0,n} & I_{1,n} & I_{2,n} \end{bmatrix}^T \begin{bmatrix} I'_1 \\ \vdots \\ I'_n \end{bmatrix}$$

the decisive factor of the result can be expressed as

$$r^2 = \frac{\sum_{i=1}^{n}\left(\sum_{j=0}^{2} c_j \times I_{j,i} + b - \bar{I}\right)^2}{\sum_{i=1}^{n}(I_i' - \bar{I})^2}$$

where $\bar{I} = \frac{1}{n}\sum_{i=1}^{n} I_i'$ is the average peak intensity.

## 5.3 Results

### 5.3.1 Acetone/alkyl alcohol photoinitiating system for disulfide cleavage

Previously, our lab reported the use of hydroxyl radicals (•OH) for initiating hydroxyalkyl radical formation inside a nanoESI emitter, where alcohol was used as a co-solvent for nanoESI of disulfide peptides.[9] Disulfide cleavage was the main reaction channel, however, the reaction yield was limited due to relatively low concentrations of primary radicals (•OH) formed from 185 nm UV photolysis of ambient air.[9,26] An obvious way to improve the reaction yield is to use more efficient radical initiators, such as 2,2-dimethoxy-2-phenylacetophenone (DMPA) and benzophenone, which are commonly used in organic synthesis and radical polymerization.[27] These compounds go through Norrish type I cleavage at the α-carbon of the carbonyl group and form primary radicals for radical initiation upon UV irradiation.[28,29] They, however, are not directly compatible with MS analysis due to non-volatile nature and relatively high concentrations (in mM) typically employed in the reaction system, which would cause severe interference to MS analysis. Acetone is the simplest ketone and it breaks down to acetyl radical and methyl radical upon UV irradiation (Scheme 5.1).[30,31] Considering that acetone has a relatively low boiling point, low

proton affinity, and it is miscible with most ESI solvent systems for peptide analysis, acetone should be well suited to be used as a photoinitiator.

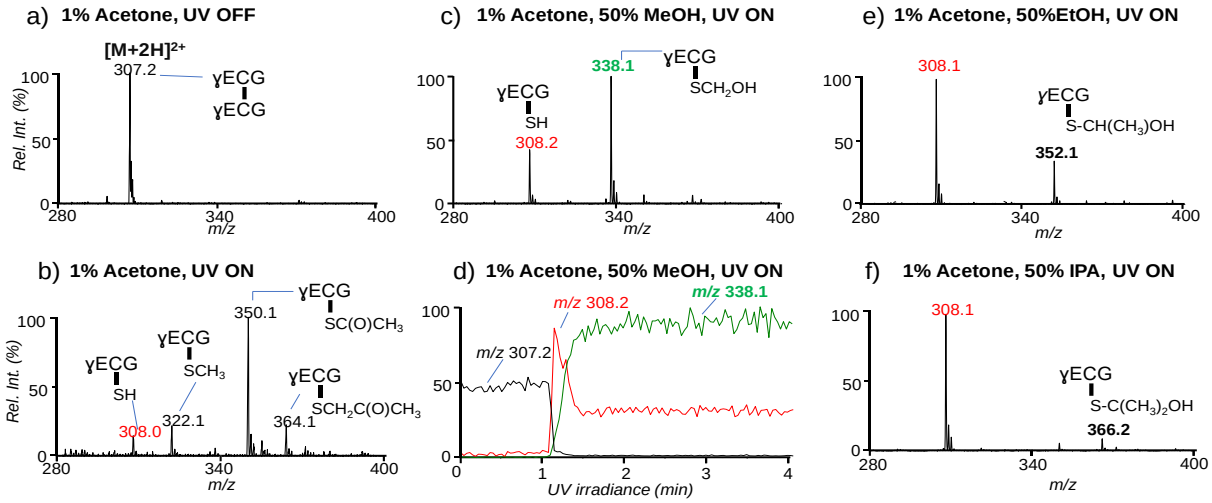


Figure 5-1 Positive ion mode MS spectra of oxidized glutathione (10 µM) prepared in solutions containing 1% acetone as a photoinitiator. a) Before and b) after UV exposure of the aqueous solution. c) UV irradiation of the peptide in $H_2O$:MeOH ((v/v) =1:1) and d) extracted ion chromatogram (XIC) for the reaction shown in c). UV irradiation of the peptide in e) $H_2O$:EtOH ((v/v) =1:1) and f) $H_2O$:IPA ((v/v) =1:1).

To test the idea, 1% acetone (volume%) was added to an aqueous solution of oxidized glutathione (10 µM) and loaded onto the nanoESI reaction setup. Before UV irradiation, only doubly protonated peptide ions ($[M+2H]^{2+}$) at *m/z* 307.2 was observed (Figure 5.1 (a)). After the lamp was turned on for about 2 minutes, intact peptide ions completely disappeared and new peaks resulting from disulfide bond cleavage dominated (Figure 5.1 (b)). The major products are reduced glutathione ($[\gamma ECG+H]^+$, *m/z* 308.0) and radical substitution products at cysteinyl sulfur, including methyl radical ($\bullet CH_3$, *m/z* 322.1), acetyl radical ($\bullet C(O)CH_3$, *m/z* 350.1), and acetonyl radical ($\bullet CH_2C(O)CH_3$, *m/z* 361.1), respectively. The identity of these products were verified by accurate mass measurements and MS/MS experiments. The same reaction was repeated without the addition of acetone. No reaction products associated with disulfide bond cleavage were observed, even with prolonged UV exposure (~5 min). Homolytic cleavage of disulfide bond can be induced

by 193-266 nm UV irradiation;[18,32] the absence of the disulfide cleavage without acetone addition in our study could be due to low photon flux of the UV lamp. The above set of experiments clearly suggests that Norrish Type I cleavage of acetone indeed happened for 1% of acetone upon 254 nm UV irradiation. Similar reaction phenomenon was observed with as low as 0.1% (v%) of acetone addition, albeit with longer UV irradiation time. Although disulfide bond cleavage was 100% by reacting with radicals derived from photolysis of acetone, the presence of multiple reaction channels points out the need to convert the first-generation radicals into less reactive secondary radical species. In this study, we focused on forming hydroxyalkyl radicals via using acetone as a photoinitiator.

Formation of hydroxyalkyl radicals was explored by adding alkyl alcohol precursor as co-solvent in the reaction system. Figure 5.1 (c) shows the nanoESI spectrum of oxidized glutathione in MeOH/$H_2O$ ((v/v) = 1:1, 1% acetone) solvent system upon UV irradiation. As a big contrast to Figure 5. 1 (b) where no methanol was added, only two distinct reaction products were observed, corresponding to the reduced (*m/z* 308.2) and *S*-hydroxymethyl modified glutathione ions (*m/z* 338.2). *S*-hydroxymethyl product was verified by detecting signature formaldehyde loss (30 Da) from low energy CID.[9] The extracted ion chromatogram (XIC) showed that the intact glutathione had a sharp drop from 100% to 0% within 30 seconds (UV irradiation 1.1-1.5 min), accompanied by steep increase of the reduced peptide (*m/z* 308), the ion signal of which maximized at 1.2 min UV irradiation and then dropped to reach a steady state within 20 s. During this time, the ion signal of the hydroxymethyl substitution product (*m/z* 338) increased rapidly and stayed constant afterwards. These kinetic data suggest that reduced thiol might be further converted to *S*-hydroxymethyl product after its initial formation. Indeed, almost identical spectrum to Figure 5.1 (c) was obtained when the oxidized glutathione was replaced by reduced glutathione for the

reaction (Figure 5.2). No definitive evidence could be obtained for tracing the singly protonated thiyl radical ions since they overlap with the doubly protonated glutathione ions at *m/z* 307.2.

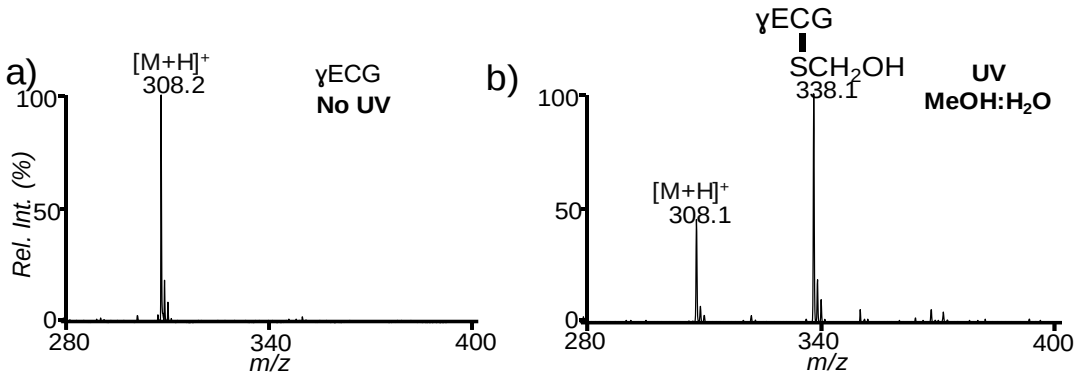


Figure 5-2 Reaction spectra of 10 μM reduced glutathione (γECG) subjected to radical reaction (spray condition: MeOH:$H_2O$ ((v/v)=1:1) with 1% acetone): (a) before UV and (b) after UV exposure.

The reaction phenomena for solvent systems involving larger alkyl alcohols, viz. EtOH and IPA, were similar to that observed in the MeOH solvent system. That is, 100% disulfide cleavage was achieved and only two reaction products were detected (Figure 5.1 (e) and 5.1 (f)). $MS^2$ CID of the substitution products, *m/z* 352 (Figure 5.3 (b)) and *m/z* 366 (Figure 5.3 (c)) showed abundant loss of 44 Da and 58 Da, confirming the formation of the respective *S*-hydroxyalkyl product. A distinct difference from the Acetone/MeOH system is that the yield of reduced thiol was increased significantly from 32% (MeOH) to 80% (EtOH) and 93% (IPA).

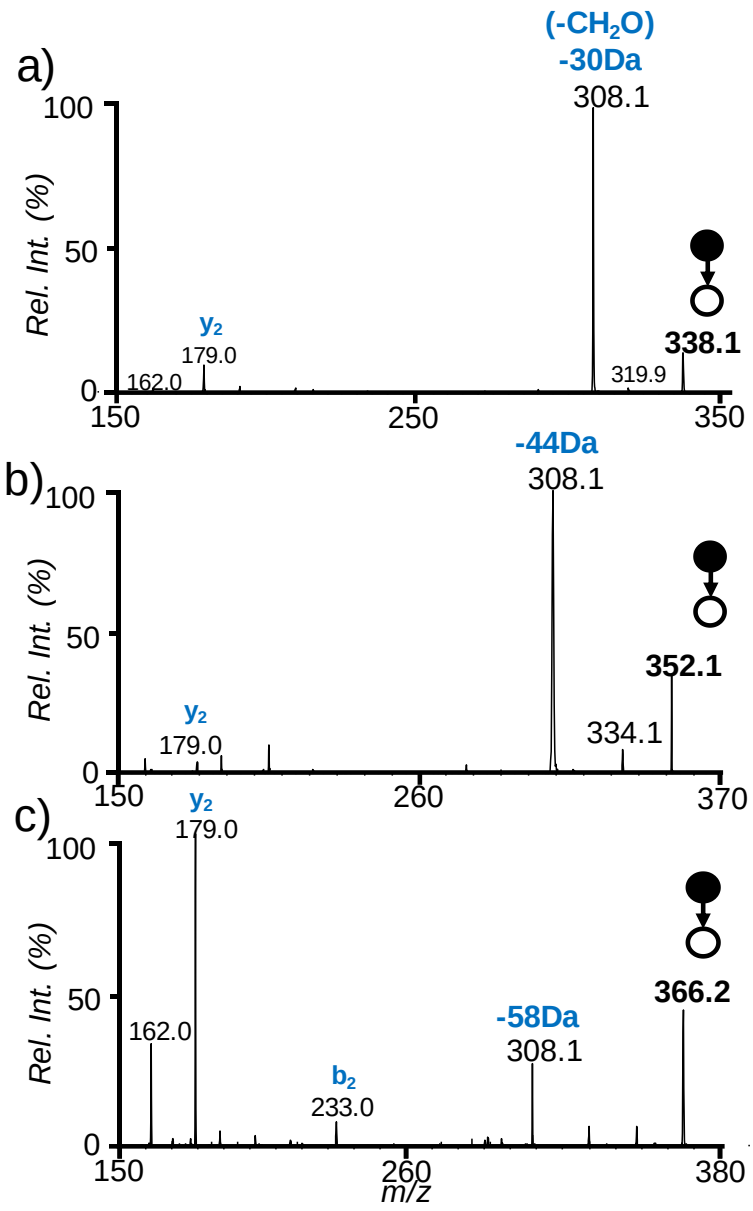


Figure 5-3 $MS^2$ CID of *S*-hydroxyalkyl addition product of oxidized glutathione, **P1**, using (a) methanol (detected at *m/z* 338.1) (b) ethanol (detected at *m/z* 352.1) and (c) isopropyl alcohol (detected at *m/z* 366.2), as co-solvents.

The possible reaction pathways accounting for disulfide cleavage using acetone/alcohol photoinitiating system are proposed in Scheme 5.1. Direct disulfide/photon interactions are considered negligible due to low photon flux and orders of magnitude lower concentration of the

peptide relative to acetone. The reaction pathway is likely to be initiated by photochemical decomposition of acetone into methyl/acetyl radicals.[30] In the presence of a large excess of alcohol, acetone should have little chance to interact with peptide directly, while reaction with alcohol solvent is the main reaction channel. In the case of methanol, the formation of hydroxymethyl radical (•$CH_2OH$) due to hydrogen abstraction from the C-H bond of methanol is supported by the $D_3COH$ experiments (Figure 5.4). For larger alcohols, hydrogen abstraction is generally preferred from the α-position due to its lower C-H bond dissociation energy.[33] For example, the BDE of $C_\alpha$-H in $(CH_3)_2C$-**H**OH is 380.7 kJ/mol, while that of the $C_\beta$-H is 394.6 kJ/mol.[34]

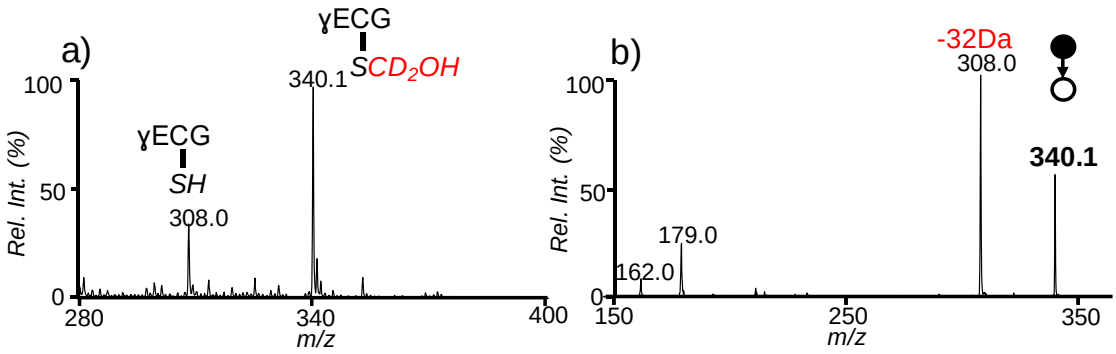


Figure 5-4 (a) Reaction spectra of 10 µM oxidized glutathione subjected to radical reaction (spray condition: $H_2O$:$CD_3OH$ ((v/v) = 1:1) with 1 % acetone). (b) $MS^2$ CID of *S*-hydroxyalkyl addition product detected at *m/z* 340.1.

Mechanistic studies involving reactions of hydroxyalkyl radicals with disulfides have been scarce.[33] Data generated from gas-phase reactions and theoretical calculations suggest that carbon-centered radicals cleave disulfide bond via a substitution mechanism.[35,36] Based on the observed products, we hypothesize that hydroxyalkyl radical attacks the disulfide bond, forming thiyl radical and S-hydroxyalkyl at the cleavage site. The thiyl radical can further abstract a hydrogen atom from hydroxyalkyl radical (BDE, ~150 kJ/mol for O-H in •$C(CH_3)_2OH$),[37] forming reduced thiol and ketone as stable products. Hydroxyalkyl radicals can also react with a reduced thiol to form *S*-

hydroxyalkyl product and the reactivity follows the order of $\bullet CH_2OH$ > $\bullet CH(CH_3)OH$ > $\bullet C(CH_3)_2OH$, as supported from reaction data of reduced glutathione. It is worth noting that the pathways described above are intended to describe the overall reaction phenomenon. Detailed mechanistic investigations are beyond the scope of the current report.

### 5.3.2 Disulfide reduction in a flow microreactor

Comparing the data for disulfide cleavage in Figure 5.1 using different alkyl alcohol as co-solvent, IPA solvent system stood out for producing reduced disulfide product with almost 100% conversion. Therefore, 1% acetone in 1:1 IPA/$H_2O$ was chosen as the optimal solvent system for peptide and protein analysis. Previously, our group has demonstrated that photochemical reactions can be greatly accelerated relative to bulk reactions when conducted in a flow microreactor due to significantly improved photon efficiency using flow path in μm-dimension.[24,25] Flow microreactor is also advantageous regarding precise control of reaction time so as to reduce detrimental side-reactions from prolonged UV exposure as found by using a static nanoESI setup. UV-transparently coated fused silica capillary was employed to construct the flow microreactor, which was connected directly to an infusion ESI source for online MS experiments as shown in Figure 5.5 (a). Such a reaction system was tested with a peptide containing an interchain disulfide bond (sequence shown the inset of Figure 5.5 (b)). Figure 5.5 (b) and 5.5 (c) compare the ESI-MS spectra before and after UV irradiation in positive ion mode. Clearly, after 3s UV irradiation, the intact peptide ions ($[M+2H]^{2+}$, *m/z* 467.2) were 100% consumed, while ions corresponding to the two reduced peptide chains, $[A+H]^+$ (*m/z* 378.2) and $[B+H]^+$ (*m/z* 558.2), dominated in the post-reaction spectrum. The progress of reduction was monitored as a function of the UV irradiation time. As shown in Figure 5.4 (d), the yield of disulfide reduction increases monotonically as UV irradiation time increases and it reaches 100% after 4 s. Above kinetic data demonstrate that the

degree of disulfide bond reduction could be tuned by adjusting the UV exposure time of the peptide in the flow microreactor, which is particularly useful for achieving partial disulfide reduction for peptides containing multiple disulfide bonds.

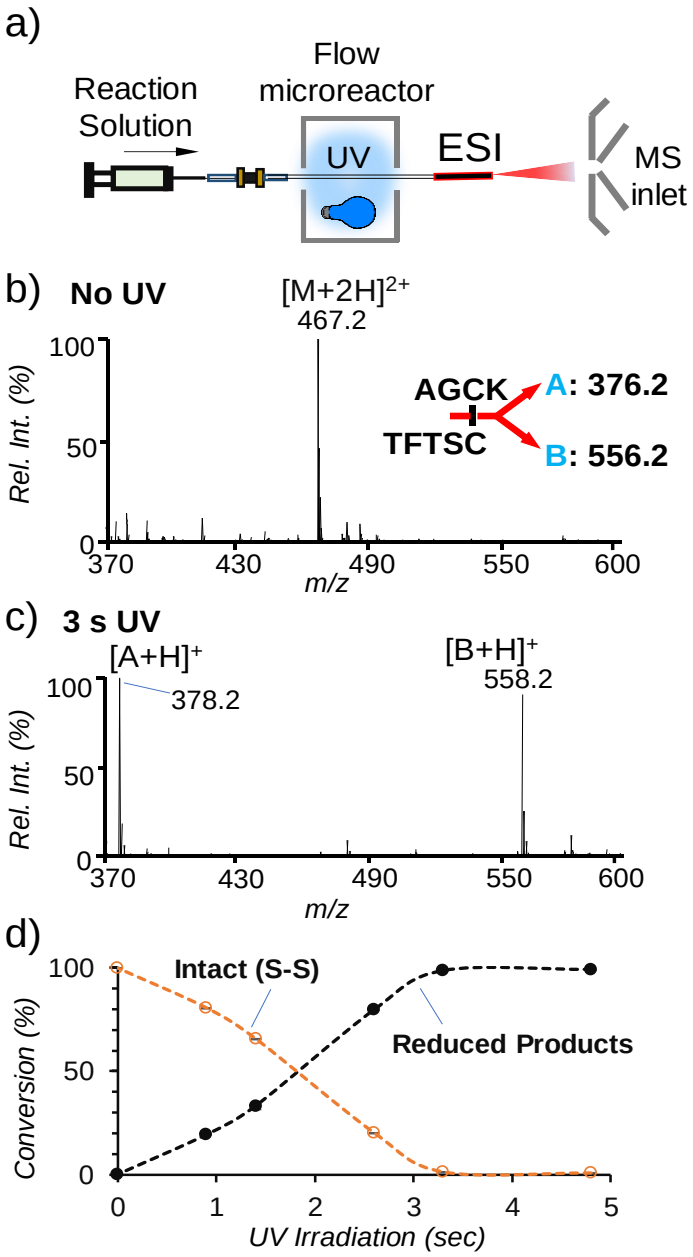


Figure 5-5 a) A flow microreactor setup for coupling acetone/IPA imitated disulfide bond reduction with ESI-MS. ESI-MS spectra of 10 µM of trypsin-digested somatostatin-14 in $H_2O$:IPA (1:1) with 1% acetone b) before UV and c) after 3 s UV irradiation in positive ion mode. d) Plot of *%conversion* of the intact peptide

### 5.3.3 Increasing sequence coverage for disulfide peptides from a complete reduction

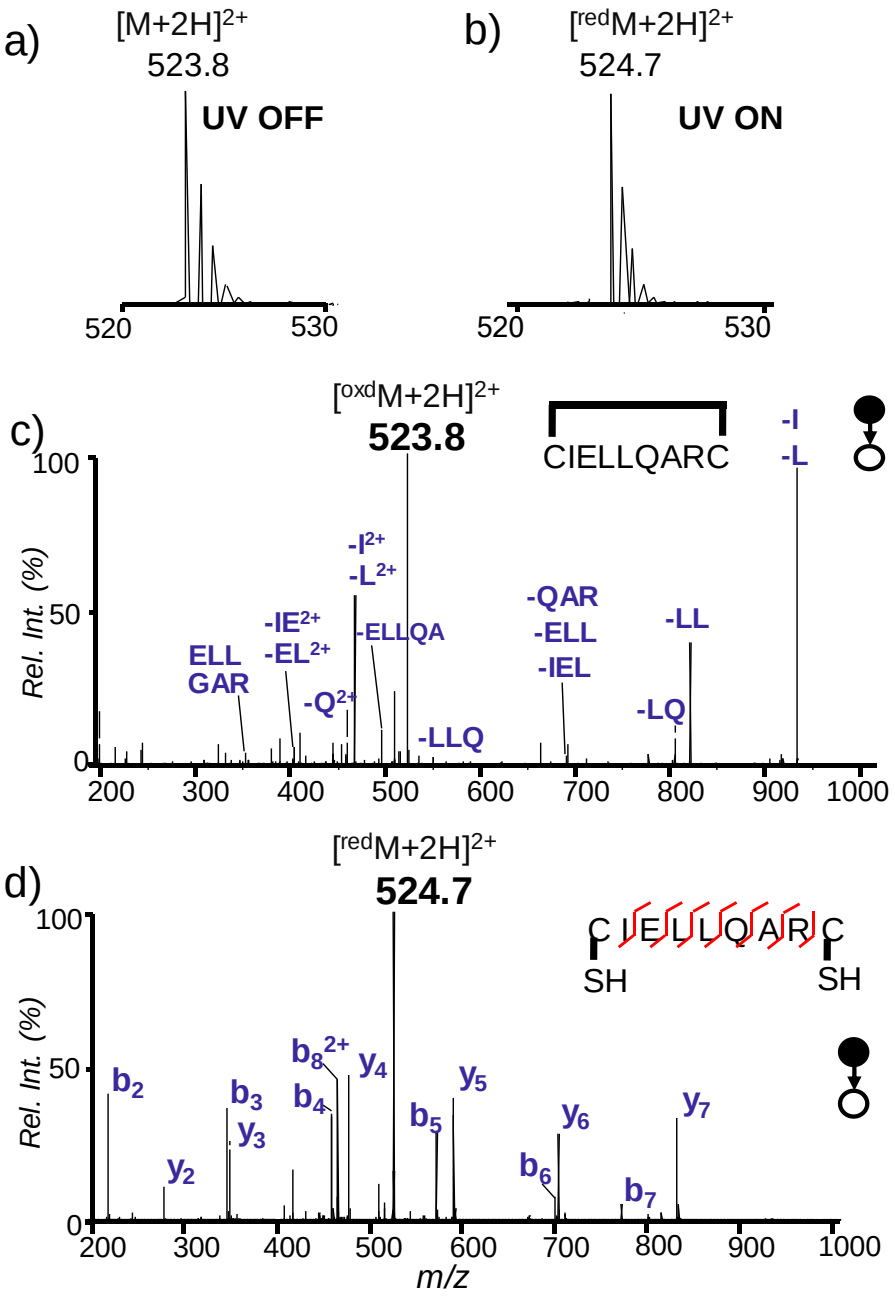


Figure 5-6 MS spectra of 10 µM of selectin binding peptide dissolved in $H_2O$:IPA (1:1) with 1% acetone: a) before UV, b) after 5 s UV irradiation, and $MS^2$ CID of (c) intact peptide ion at *m/z* 523.8 ($[^{oxd}M+2H]^{2+}$) and (d) reduced peptide ions at *m/z* 524.7 ($[^{red}M+2H]^{2+}$). The fragmentation map of the peptide is indicated in the inset.

Selectin binding peptide is a naturally existing circular peptide due to an intrachain disulfide bond between C1 and C9 residues (sequence shown in the inset of Figure 5.6). As expected, no sequence ions were obtained from $MS^2$ CID of doubly protonated intact peptide ions (Figure 5.6 (b)). After 5 s UV irradiation, 100% disulfide reduction was achieved for this peptide, as demonstrated by the complete disappearance of intact peptide ions ($[M+2H]^{2+}$, *m/z* 523.8, Figure 5.6 (a)) and appearance of ions at *m/z* 524.7 ($[red\text{-}M+2H]^{2+}$) ions (Figure 5.6 (b)). $MS^2$ CID of the reduced product at *m/z* 524.7 gave almost full series of *b*- and *y*-type fragment ions, allowing sequence identification of the peptide (Figure 5.6 (d)).

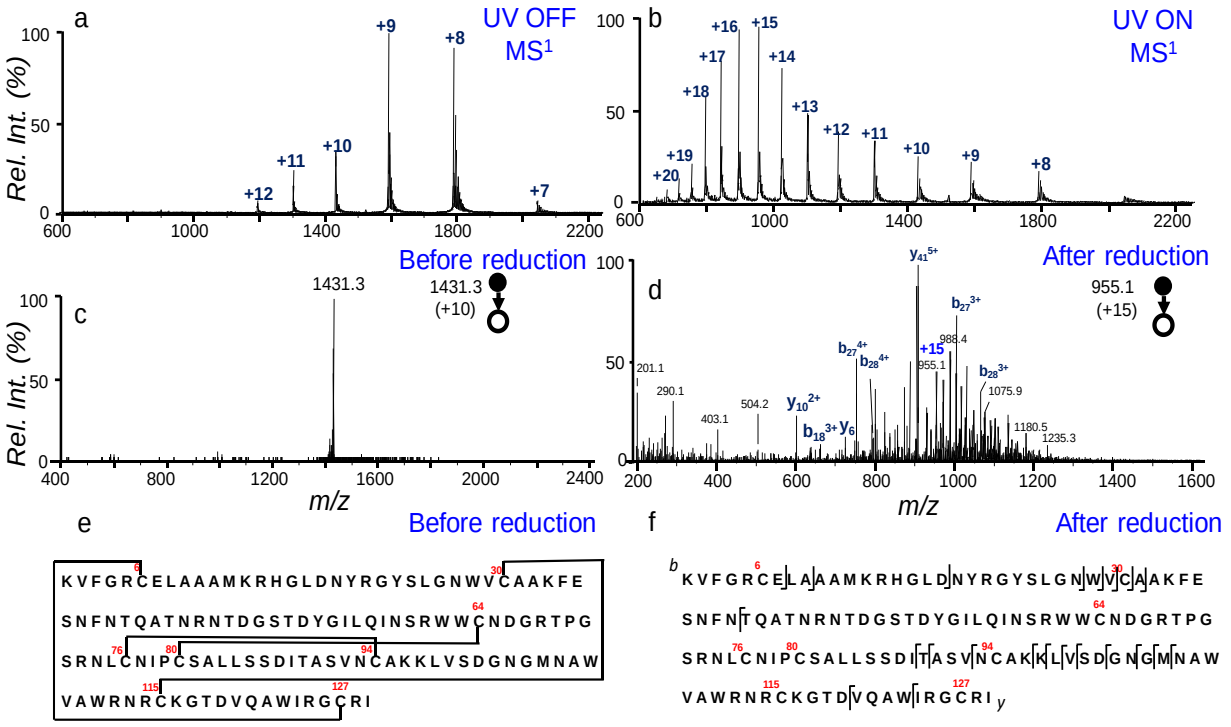


Figure 5-7 ESI-$MS^1$ spectra of 10 µM of lysozyme dissolved in $H_2O$: IPA (1:1) with 1% acetone: (a) before UV, (b) after 5 s UV irradiation. $MS^2$ CID of (c) intact lysozyme (+10, *m/z* 1431.3) and (d) reduced lysozyme (+15, *m/z* 955.1). Fragmentation map of lysozyme (e) intact and (f) reduced lysozyme.

Lysozyme (~14 kDa, 129 amino acids residues) was used to further test this methodology with larger proteins. Lysozyme has four disulfide bonds where $Cys_{64}$-$Cys_{80}$ and $Cys_{78}$-$Cys_{94}$ are intertwined and further enclosed by $Cys_{6}$-$Cys_{127}$ and $Cys_{30}$-$Cys_{115}$ (Figure 5-7). $MS^2$ CID of +10 ion of intact lysozyme (at *m/z* 1431.3) produced no distinct sequence ion under CID, as the four cross-linked disulfide bonds protect most of the protein (Figure 5-7 (c)). After 5 s of UV irradiation, the disulfide reduction was observed through a conformation change of protein ions. $MS^2$ CID of the lysozyme (at *m/z* 955.1) gave 22 distinct fragment ions (Figure 5-7 (d)). This represents a significant increase in the backbone cleavage.

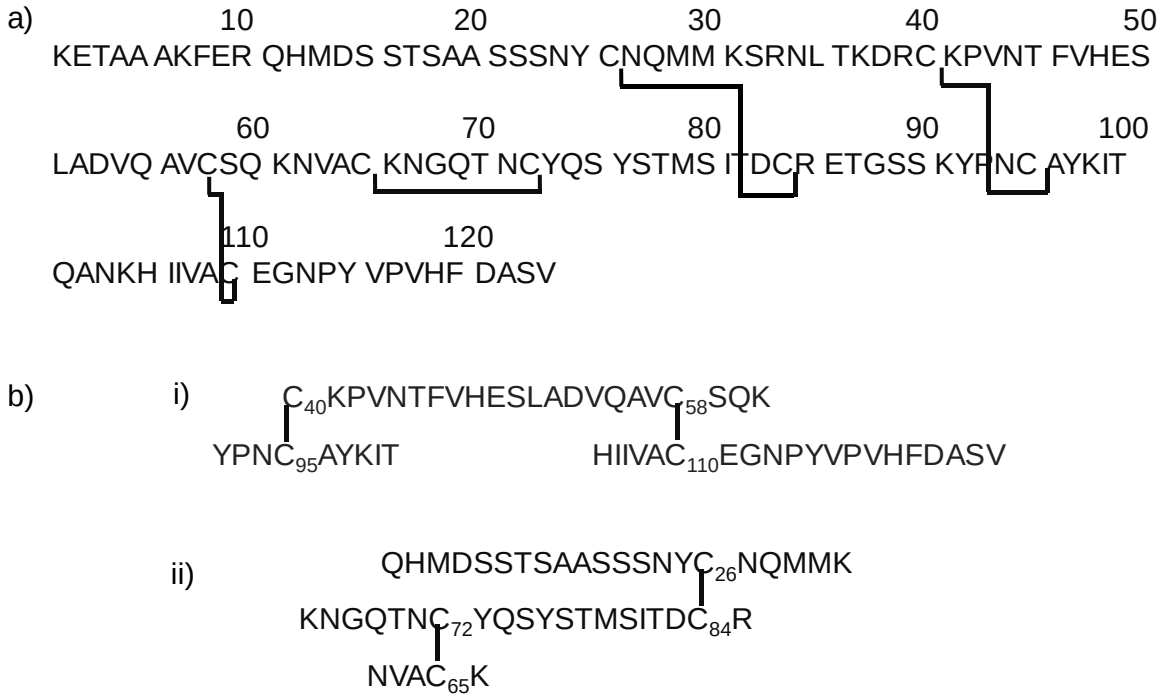


Figure 5-8 Sequence information of (a) intact ribonuclease B (b) disulfide-linked peptides i) and ii) from a tryptic digest of ribonuclease B. Only disulfide-linked peptide i) was observed.

We further applied complete disulfide reduction for the analysis of protein digests, mimicking the bottom-up proteomic approach. Ribonuclease-B, a small protein containing four

disulfide bonds (sequence shown in Figure 5.8) was subjected to trypsin digestion and LC separation before disulfide reduction and ESI-MS/MS analysis. One disulfide peptide was detected after digestion, which contained three peptide chains connected by two interchain disulfide bonds: $C_{40}$-$C_{95}$ and $C_{58}$-$C_{110}$ (sequence shown in Figure 5.8 (b) (i)). The other predicted peptide containing $C_{26}$-$C_{84}$ and $C_{65}$-$C_{72}$ disulfide bonds wasn't detected, possibly due to its resistance to proteolytic digestion.[38] Figure 5.9 (a) and 5.9 (b) compare the ESI-MS spectra of the peptide before and after UV irradiation (5 s). Clearly, the intact peptide ions ($[M+6H]^{6+}$, $[M+5H]^{5+}$, $[M+4H]^{3+}$) completely disappeared after UV irradiation. The presence of three separated peptide chains, viz. $[A+3H]^{3+}$ (*m/z* 802.1), $[B+H]^{+}$ (*m/z* 858.4), and $[C+2H]^{2+}$ (*m/z* 1084.5), confirmed the presence of two interchain disulfide bonds in this peptide.

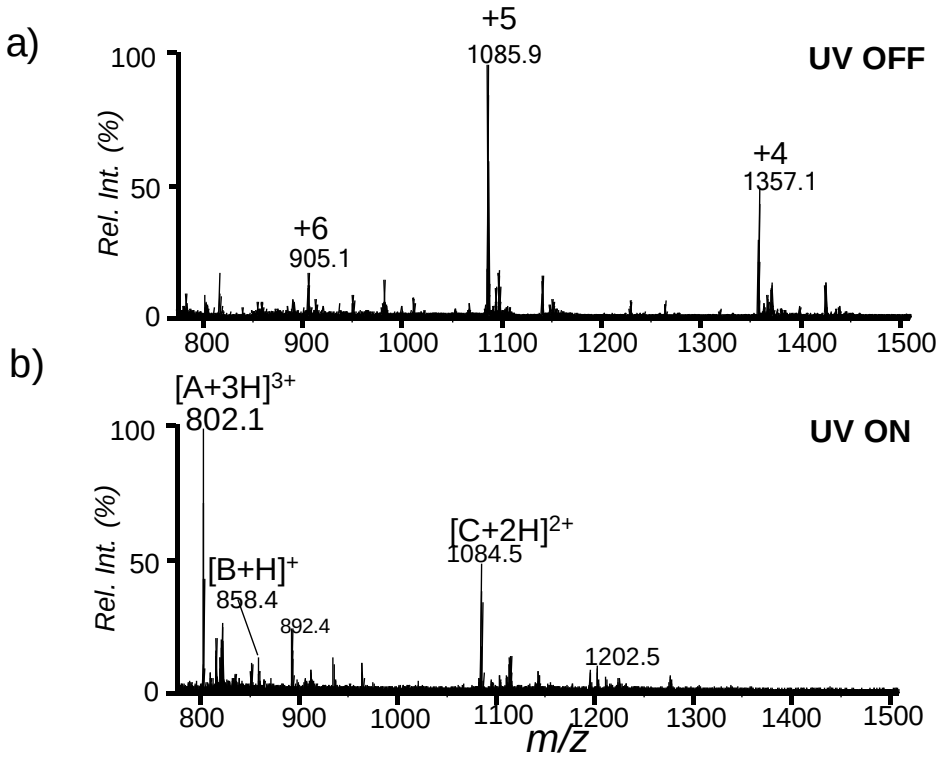


Figure 5-9 Reaction spectra of trypsin-digested ribonuclease-B subjected to the radical reaction: (a) before UV and (b) after 5 s UV irradiation.

The intact peptide ions ($[M+6H]^{6+}$) and the disulfide reduced A, B, and C chains ($[A+3H]^{3+}$, $[B+H]^{+}$, $[C+2H]^{2+}$) were each subjected to $MS^2$ CID for structural analysis (spectra shown in Figure 5.10). The fragmentation map of the intact and reduced peptide ions is summarized in Figure 5.10. $MS^2$ CID of the disulfide reduced chains led to almost 100% sequencing of the peptide, allowing determination of cysteine residues at $C_{40}$ and $C_{58}$ in A chain, $C_{95}$ in B chain, and $C_{110}$ in C chain. $MS^2$ CID of the intact peptide produced a series of sequence ions in A chain with intact B chain attached, i.e. $BAb_2$, $BAb_9$, $BAb_{10}$, $BAb_{11}$, $BAb_{14}$, $BAb_{15}$, $BAb_{16}$, and $BAb_{17}$, suggesting a disulfide linkage at $C_{40}$-$C_{95}$. Several fragment ions specific to the C chain were obtained, confirming its presence in the intact peptide, which could only be linked to A Chain through a disulfide linkage at $C_{58}$-$C_{110}$.

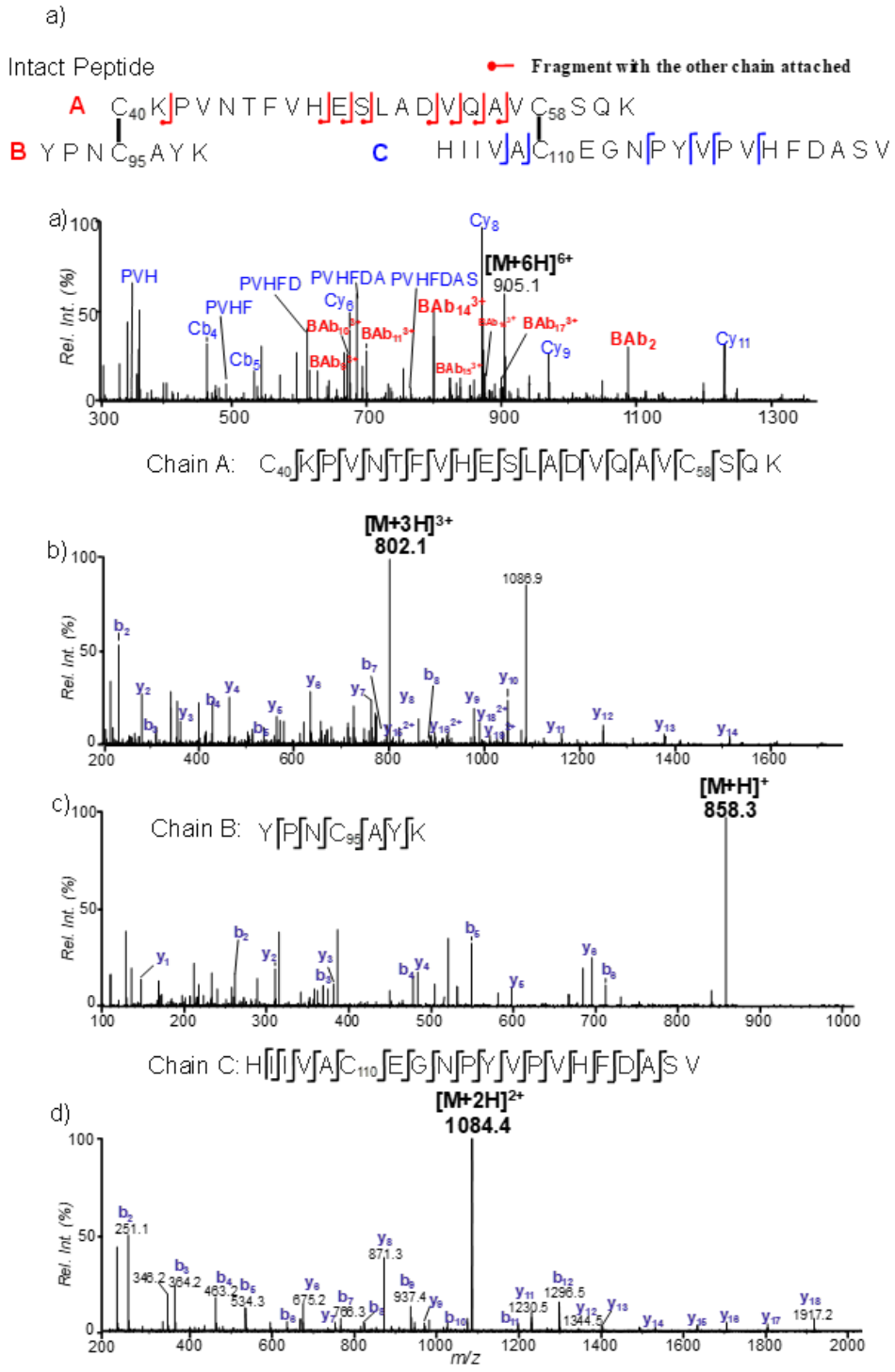


Figure 5-10 $MS^2$ CID of (a) intact peptide, and reduced chains of the peptide after UV induced radical reaction: (b) A chain – ($[M+3H]^{3+}$, detected at *m/z* 802.1), (c) B chain – ($[M+H]^{+}$, detected at *m/z* 858.3) and (d) C chain – ($[M+2H]^{2+}$, detected at *m/z* 1084.4). The inset shows the sequence for respective peptides and fragmentation channels are indicated in the inset.

### 5.3.4 Insulin from porcine pancreas

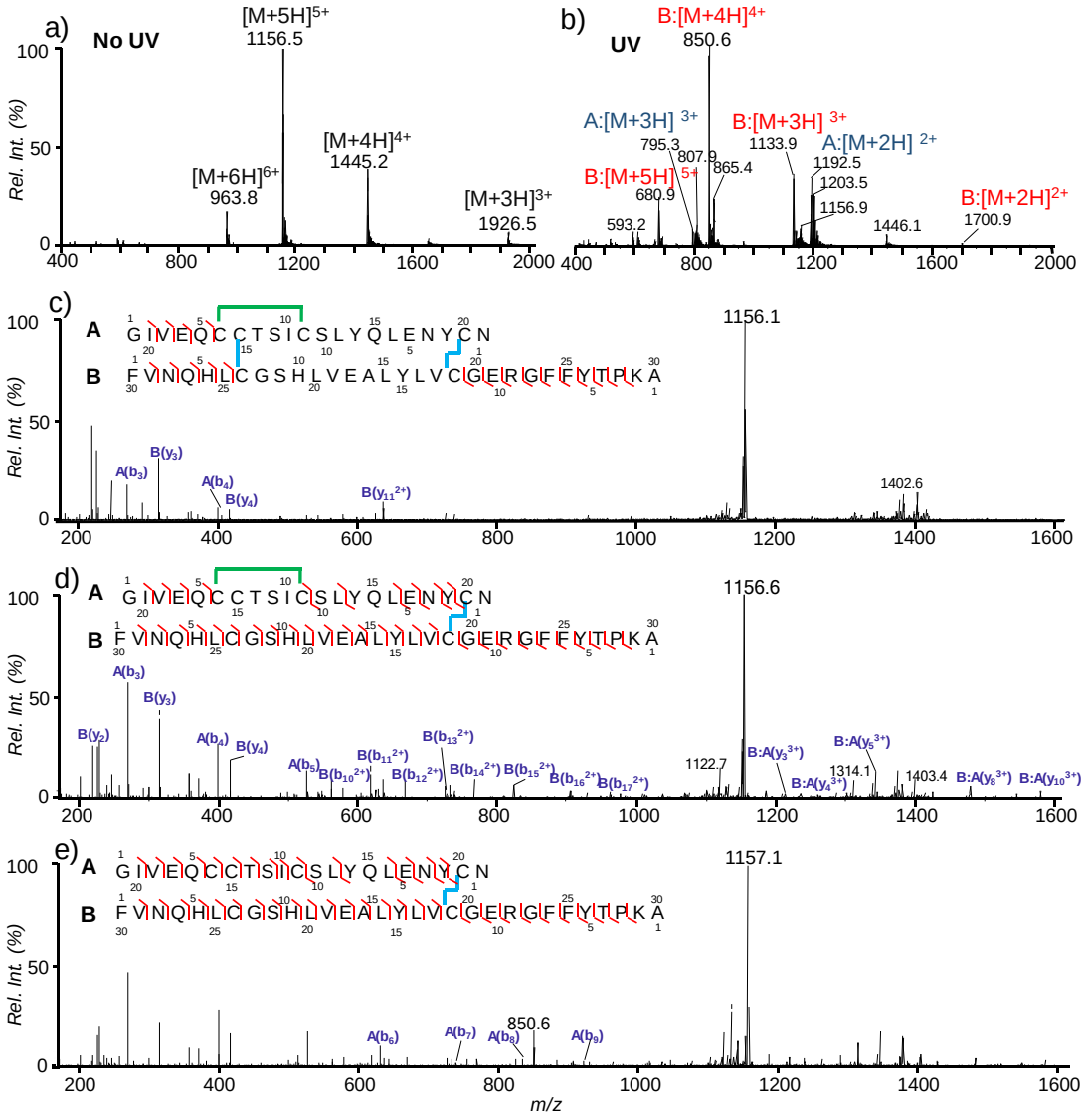


Figure 5-11 Reaction spectra of insulin from porcine pancreas in IPA: $H_2O$ ((v/v) = 1:1) with 1% acetone: (a) before UV and (b) after irradiation with UV light. CID fragmentation of (c) intact insulin ($[M+5H]^{5+}$) and partially reduced insulin (d) $[M+5]^{5+}$ + 2H detected at *m/z* 1156.6 (e) $[M+5]^{5+}$ + 4H detected at *m/z* 1157.1 Inset shows identified sequence and fragments for intact and partially reduced insulin.

#### 5.3.4.1 Sequence coverage in Insulin by near complete reduction

Insulin from porcine pancreas consists of two chains (A and B chain) consisting of three disulfide bonds: two interchain linked disulfide connecting chain A and B (A7 to B7 and A20 to

B19) and one intrachain linked disulfide formed within the chain A (A6 to A11) (Figure 5-11). Sequencing the structural information from the intact insulin is challenging since most of its structure is confined by the disulfide bonds, hence is not accessible by CID alone. Herein, we further demonstrate the capability of coupling radical induced disulfide cleavage of the disulfide bond and subsequent CID to obtain structural information from insulin. The mass spectrum of the native form of insulin (before reaction) is shown in Figure 5-11(a). $[M+3H]^{3+}$, $[M+4H]^{4+}$, $[M+5H]^{5+}$, $[M+6H]^{6+}$ ions for intact insulin were observed at *m/z* 963.8, 1156.5, 1445.2 and 1926.5, respectively. As expected, the radical reaction of insulin resulted in highly selective S-S bond cleavages of insulin, freeing the A- and B-chains from one another (Figure 5-11(b)). Ions corresponding to chain A were detected as $[M+2H]^{2+}$, $[M+3H]^{3+}$ at *m/z* 1192.5 and 795.3, respectively. Ions corresponding to chain B were detected as $[M+3H]^{3+}$, $[M+4H]^{4+}$, $[M+5H]^{5+}$ at *m/z* 1133.9, 850.6, and 680.9, respectively. The relatively low intensity of ions generated from chain A as compared to chain B is due to the presence of multiple acidic residues on chain A, hence the difficulty in detecting in positive ion mode. CID of these reduced disulfide free chains can be used to achieve full sequence coverage of insulin (Figure 5-12).

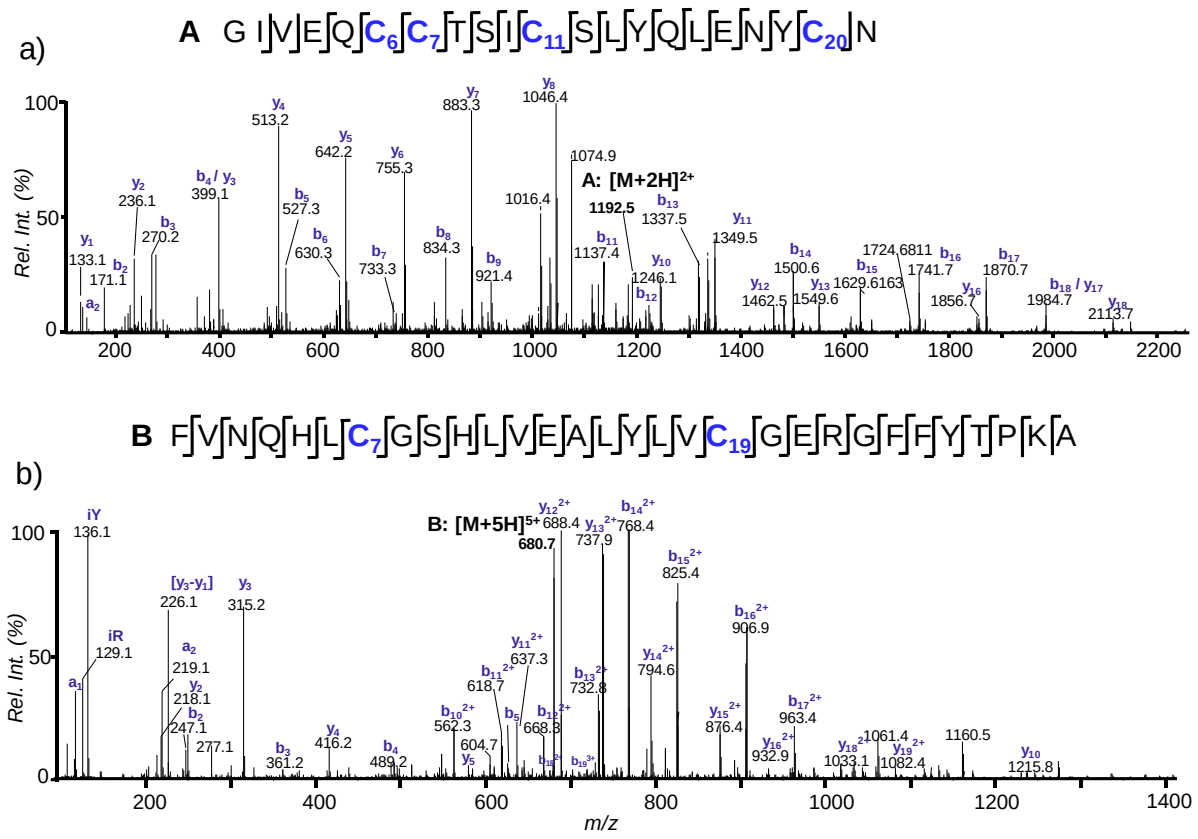


Figure 5-12 $MS^2$ CID of reduced chains of porcine insulin after UV induced radical reaction: (a) A chain – ($[M+2H]^{2+}$, detected at *m/z* 1192.5) and (b) B chain – ($[M+5H]^{5+}$, detected at *m/z* 680.7). The sequence for reduced chains of porcine insulin and fragmentation channels are indicated in the inset. Only the A-chain N-terminal glycine is not observed due to the *m/z* range (100-2200) used for the data acquisition.

### 5.3.4.2 Disulfide Linkage Assignment by Partial Reduction

For complete structural characterization of peptides/proteins, determining the complete sequence information as well as disulfide bond linkage site is necessary. However, characterization of disulfide connecting pattern by MS, directly from intact peptides and proteins remains a challenging task. We further attempted to demonstrate the disulfide linkage assignment in insulin by partial reduction approach. By optimizing the flow rate and UV irradiation, intact insulin was partially reduced. Figure 5-13 shows the slightly shifting of isotopic distribution for

$[M+5]^{5+}$ ion (*m/z* 1156.1) of intact insulin under partial reduction condition. With UV exposure of 3 sec, the reduction product corresponds to a mixture of isotopic peaks of intact insulin ($[M+5]^{5+}$) and partially reduced peak for $[M+5]^{5+}$ + 2H (corresponds to one disulfide bond reduction). Before UV irradiation, $MS^2$ CID of $[M+5]^{5+}$ of intact insulin at *m/z* 1156.1 mostly gave fragment ions from its exocyclic structure (Figure 5-10c). Most of its structure was confined by the three-disulfide bond. After UV irradiation, $MS^2$ CID of the $[M+5]^{5+}$ + 2H at *m/z* 1156.6 gave *b*- and *y*-fragment ions enclosed by A7-B7 disulfide bond, revealing the partial reduction of the disulfide (Figure 5-10(d)). Such specificity for selective reduction of disulfide of insulin could be due to the solvent accessibility for A7-B7 disulfide bond (Figure 5-14). With UV exposure of 4.5 sec, the isotopic distribution of intact insulin was further shifted corresponding to $[M+5]^{5+}$ + 4H (reduction of two disulfide bond). CID of the $[M+5]^{5+}$ + 4H at *m/z* 1157.1 revealed the reduction of A7-B7 and A6-A11 disulfide bonds to give the partially reduced product (Figure 5-11(d)). Such a sequential order of reduction of disulfide bonds could be the result of the opening of insulin after an initial reduction of A7-B7, allowing accessibility for reduction of the two remaining disulfide bonds.

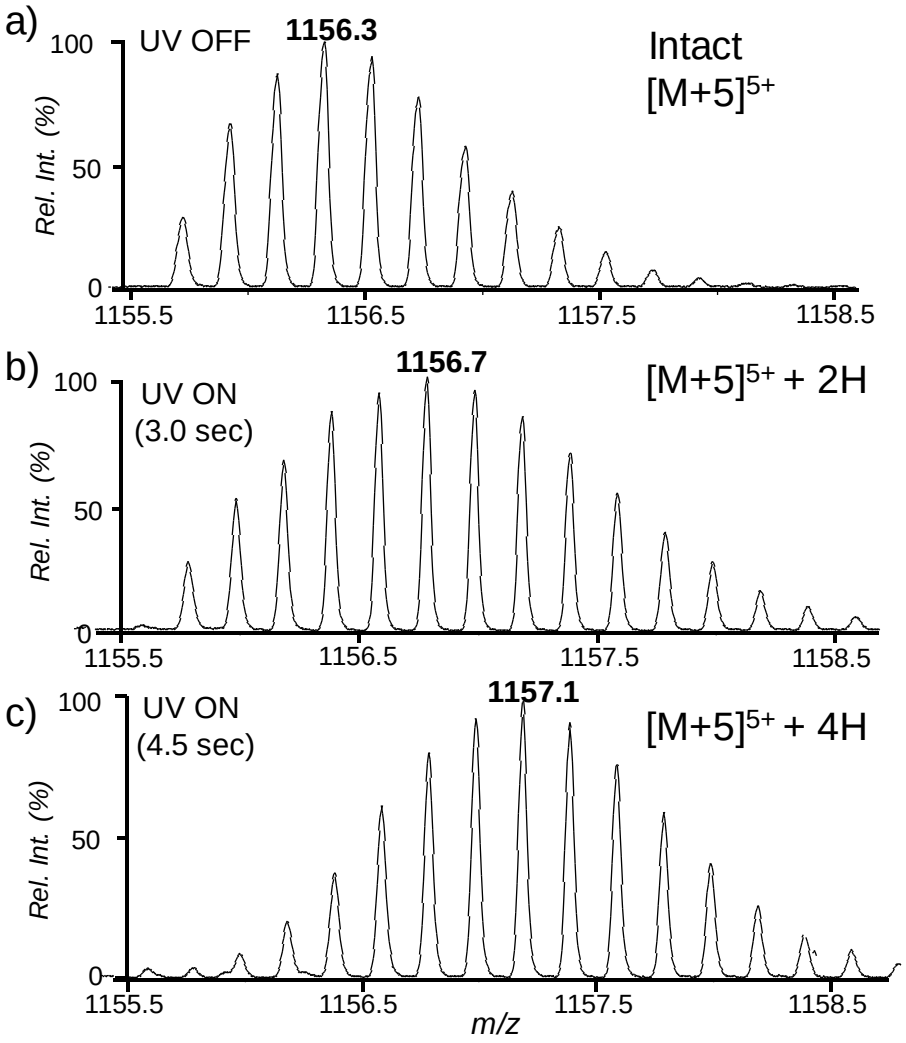


Figure 5-13 Difference in isotopic envelopes of (a) intact insulin, $[M+5]^{5+}$ detected at *m/z* 1156.3 (UV exposure: 0 sec) and partially reduced insulin (b) $[M+5]^{5+}$ + 2H detected at *m/z* 1156.7 (UV exposure: 3.0 sec) (c) $[M+5]^{5+}$ + 4H detected at *m/z* 1157.1 (UV exposure: 4.5 sec)

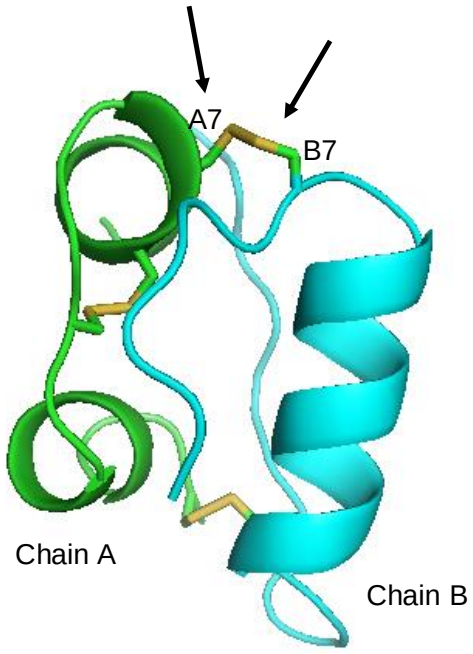


Figure 5-14 Structure of porcine insulin (PDB entry 4INS) (Disulfide bonds are displayed in yellow color). Disulfide A7-B7 bond is indicated by the black arrows.

## 5.4 Conclusions

A photochemical reaction system that allows for rapid and tunable disulfide reduction has been developed for characterizing peptides containing one or multiple disulfide bonds by ESI-MS/MS. Acetone/IPA was determined as the best photoinitiating system for disulfide bond reduction with almost 100% yield achieved within less than 5 s UV irradiation. The use of flow microreactor enabled precise control of the degree of disulfide reduction and online coupling with infusion ESI-MS/MS. By pairing complete disulfide reduction with subsequent low-energy CID, near complete sequence coverage was achieved for various peptides containing one or multiple disulfide bonds. Furthermore, different degrees of partial reduction could be achieved simply by adjusting the UV irradiation time, greatly facilitating disulfide linkage assignment, as demonstrated by mapping the three disulfide bonds in insulin. For the peptide systems studied

herein, no evidence for disulfide bond scrambling was obtained, likely benefited from the fast-online reaction and detection system. Compared to conventional disulfide mapping approach, the online photochemical system enjoys several distinct advantages, including full compatibility with ESI-MS without introducing any chemical matrix, significantly shortened reaction time (from hours to seconds), and flexibility in tuning the extent of disulfide reduction. These aspects are highly desirable for developing high throughput structural analysis capability for proteins consisting of multiple disulfide bonds. For future development, we plan to implement this photochemical reaction system with HPLC-MS and top-down protein analysis to expand its utility in proteomics applications.

## 5.5 References


1. Lakbub, J. C.; Shipman, J. T.; Desaire, H., Recent mass spectrometry-based techniques and considerations for disulfide bond characterization in proteins. *Anal. Bioanal. Chem.* **2018,** *410* (10), 2467-2484.

2. Wysocki, V. H.; Tsaprailis, G.; Smith, L. L.; Breci, L. A., Mobile and localized protons: a framework for understanding peptide dissociation. *J. Mass Spectrom.* **2000,** *35* (12), 1399-1406.

3. Lioe, H.; O'Hair, R. A., A novel salt bridge mechanism highlights the need for nonmobile proton conditions to promote disulfide bond cleavage in protonated peptides under low-energy collisional activation. *J. Am. Soc. Mass. Spectrom.* **2007,** *18* (6), 1109-1123.

4. Wall, J. S., Disulfide bonds. Determination, location, and influence on molecular properties of proteins. *J. Agric. Food. Chem.* **1971,** *19* (4), 619-625.

5. Zhang, Y.; Fonslow, B. R.; Shan, B.; Baek, M.-C.; Yates, J. R., Protein Analysis by Shotgun/Bottom-up Proteomics. *Chem. Rev.* **2013,** *113* (4), 2343-2394.

6. Zhang, Y.; Cui, W.; Zhang, H.; Dewald, H. D.; Chen, H., Electrochemistry-Assisted Top-Down Characterization of Disulfide-Containing Proteins. *Anal. Chem.* **2012,** *84* (8), 3838-3842.

7. Mysling, S.; Salbo, R.; Ploug, M.; Jørgensen, T. J. D., Electrochemical Reduction of Disulfide-Containing Proteins for Hydrogen/Deuterium Exchange Monitored by Mass Spectrometry. *Anal. Chem.* **2014,** *86* (1), 340-345.

8. Cramer, C. N.; Kelstrup, C. D.; Olsen, J. V.; Haselmann, K. F.; Nielsen, P. K., Complete Mapping of Complex Disulfide Patterns with Closely-Spaced Cysteines by In-Source Reduction and Data-Dependent Mass Spectrometry. *Anal. Chem.* **2017,** *89* (11), 5949-5957.

9. Stinson, C. A.; Xia, Y., Reactions of Hydroxyalkyl Radicals with Cysteinyl Peptides in a NanoESI Plume. *J. Am. Soc. Mass Spectrom.* **2014,** *25* (7), 1192-1201.

10. Durand, K. L.; Tan, L.; Stinson, C. A.; Love-Nkansah, C. B.; Ma, X.; Xia, Y., Assigning Peptide Disulfide Linkage Pattern Among Regio-Isomers via Methoxy Addition to Disulfide and Tandem Mass Spectrometry. *J. Am. Soc. Mass. Spectrom.* **2017,** *28* (6), 1099-1108.

11. Fukuyama, Y.; Iwamoto, S.; Tanaka, K., Rapid sequencing and disulfide mapping of peptides containing disulfide bonds by using 1,5-diaminonaphthalene as a reductive matrix. *J. Mass Spectrom.* **2006,** *41* (2), 191-201.

12. Peng, I. X.; Ogorzalek Loo, R. R.; Shiea, J.; Loo, J. A., Reactive-Electrospray-Assisted Laser Desorption/Ionization for Characterization of Peptides and Proteins. *Anal. Chem.* **2008,** *80* (18), 6995-7003.

13. Zubarev, R. A.; Kelleher, N. L.; McLafferty, F. W., Electron Capture Dissociation of Multiply Charged Protein Cations. A Nonergodic Process. *J. Am. Chem. Soc.* **1998,** *120* (13), 3265-3266.

14. Oh, H.; Breuker, K.; Sze, S. K.; Ge, Y.; Carpenter, B. K.; McLafferty, F. W., Secondary and tertiary structures of gaseous protein ions characterized by electron capture dissociation mass spectrometry and photofragment spectroscopy. *Proc. Natl. Acad. Sci. U.S.A.* **2002,** *99* (25), 15863-15868.

15. Syka, J. E. P.; Coon, J. J.; Schroeder, M. J.; Shabanowitz, J.; Hunt, D. F., Peptide and protein sequence analysis by electron transfer dissociation mass spectrometry. *Proc. Natl. Acad. Sci. U.S.A.* **2004,** *101* (26), 9528-9533.

16. Foley, S. F.; Sun, Y.; Zheng, T. S.; Wen, D., Picomole-level mapping of protein disulfides by mass spectrometry following partial reduction and alkylation. *Anal. Biochem.* **2008,** *377* (1), 95-104.

17. Fung, Y. M. E.; Kjeldsen, F.; Silivra, O. A.; Chan, T. W. D.; Zubarev, R. A., Facile Disulfide Bond Cleavage in Gaseous Peptide and Protein Cations by Ultraviolet Photodissociation at 157 nm. *Angew. Chem.* **2005,** *117* (39), 6557-6561.

18. Agarwal, A.; Diedrich, J. K.; Julian, R. R., Direct Elucidation of Disulfide Bond Partners Using Ultraviolet Photodissociation Mass Spectrometry. *Anal. Chem.* **2011,** *83* (17), 6455-6458.

19. Quick, M. M.; Crittenden, C. M.; Rosenberg, J. A.; Brodbelt, J. S., Characterization of Disulfide Linkages in Proteins by 193 nm Ultraviolet Photodissociation (UVPD) Mass Spectrometry. *Anal. Chem.* **2018**.

20. Lee, M.; Lee, Y.; Kang, M.; Park, H.; Seong, Y.; Sung, B. J.; Moon, B.; Oh, H. B., Disulfide bond cleavage in TEMPO-free radical initiated peptide sequencing mass spectrometry. *J. Mass Spectrom.* **2011,** *46* (8), 830-839.

21. Pilo, A. L.; McLuckey, S. A., Selective Gas-Phase Ion/Ion Reactions: Enabling Disulfide Mapping via Oxidation and Cleavage of Disulfide Bonds in Intermolecularly-Linked Polypeptide Ions. *Anal. Chem.* **2016,** *88* (18), 8972-8979.

22. Gray, W. R., Disulfide structures of highly bridged peptides: a new strategy for analysis. *Protein Sci.* **1993,** *2* (10), 1732-1748.

23. Xia, Y.; Cooks, R. G., Plasma induced oxidative cleavage of disulfide bonds in polypeptides during nanoelectrospray ionization. *Anal. Chem.* **2010,** *82* (7), 2856-2864.

24. Adhikari, S.; Xia, Y., Thiyl Radical-Based Charge Tagging Enables Sterol Quantitation via Mass Spectrometry. *Anal. Chem.* **2017,** *89* (23), 12631-12635.

25. Adhikari, S.; Zhang, W.; Xie, X.; Chen, Q.; Xia, Y., Shotgun Analysis of Diacylglycerols Enabled by Thiol–ene Click Chemistry. *Anal. Chem.* **2018,** *90* (8), 5239-5246.

26. Creasey, D. J.; Heard, D. E.; Lee, J. D., Absorption cross-section measurements of water vapour and oxygen at 185 nm. Implications for the calibration of field instruments to measure OH, HO2 and RO2 radicals. In *Geophys. Res. Lett.*, 2000; Vol. 27, pp 1651-1654.

27. Hoyle, C. E.; Bowman, C. N., Thiol–Ene Click Chemistry. *Angew. Chem. Int. Ed.* **2010,** *49* (9), 1540-1573.

28. Norrish, R. G. W.; Kirkbride, F. W., 204. Primary photochemical processes. Part I. The decomposition of formaldehyde. *J. Chem. Soc.* **1932,** (0), 1518-1530.

29. Norrish, R. G. W., Part II. Free radicals of short life: chemical aspects. A. General and inorganic. The primary photochemical production of some free radicals. *Trans. Faraday Soc.* **1934,** *30* (0), 103-113.

30. Norrish, R. G. W.; Crone, H. G.; Saltmarsh, O. D., Primary photochemical reactions. Part V. The spectroscopy and photochemical decomposition of acetone. *J. Chem. Soc.* **1934,** (0), 1456-1464.

31. Haas, Y., Photochemical [small alpha]-cleavage of ketones: revisiting acetone. *Photochem. Photobiol. Sci.* **2004,** *3* (1), 6-16.

32. Bookwalter, C. W.; Zoller, D. L.; Ross, P. L.; Johnston, M. V., Bond-selective photodissociation of aliphatic disulfides. *J. Am. Soc. Mass. Spectrom.* **1995,** *6* (9), 872-876.

33. Akhlaq, M. S.; Murthy, C. P.; Steenken, S.; Von Sonntag, C., Reaction of .alpha.-hydroxyalkyl radicals and their anions with oxidized dithiothreitol: a pulse radiolysis and product analysis study. *J. Phys. Chem.* **1989,** *93* (10), 4331-4334.

34. Luo, Y.-R., *Handbook of bond dissociation energies in organic compounds*. CRC Press: Boca Raton, FL, 2003.

35. Krenske, E. H.; Pryor, W. A.; Houk, K. N., Mechanism of SH2 Reactions of Disulfides: Frontside vs Backside, Stepwise vs Concerted. *J. Org. Chem.* **2009,** *74* (15), 5356-5360.

36. Anglada, J. M.; Crehuet, R.; Adhikari, S.; Francisco, J. S.; Xia, Y., Reactivity of hydropersulfides toward the hydroxyl radical unraveled: disulfide bond cleavage, hydrogen atom transfer, and proton-coupled electron transfer. *PCCP* **2018,** *20* (7), 4793-4804.

37. Internet Bond-energy Databank (pKa and BDE)-iBonD: . http://ibond.chem.tsinghua.edu.cn (accessed July 2018).

38. Bernard, B. A.; Newton, S. A.; Olden, K., Effect of size and location of the oligosaccharide chain on protease degradation of bovine pancreatic ribonuclease. *J. Biol. Chem.* **1983,** *258* (20), 12198-12202.

39. Cramer, C. N.; Haselmann, K. F.; Olsen, J. V.; Nielsen, P. K., Disulfide Linkage Characterization of Disulfide Bond-Containing Proteins and Peptides by Reducing Electrochemistry and Mass Spectrometry. *Anal. Chem.* **2016,** *88* (3), 1585-1592.

# VITA

Sarju Adhikari was born in Kathmandu, Nepal to Krishna Bahadur Adhikari and Sita Adhikari. After completing his high school from Universal College (Maitighar, Kathmandu), he went on to pursue his undergraduate's degree from Southeastern Louisiana University (Hammond, LA, USA). In Southeastern, he worked under Prof. Debra Dolliver on developing new synthetic pathways to oxime ethers where the geometric configuration (stereochemistry) of the group is controlled. He did his undergraduate research internship at University of Alabama (Tuscaloosa, AL) under the supervision of Prof. Kevin Shaughnessy (2012) and Prof. Timothy Snowden (2013). In Dec. 2013, Sarju completed his undergraduate's degree in Chemistry and Biology (dual major). He then enrolled in Purdue University (West Lafayette, IN) to seek a doctoral degree in Analytical Chemistry. He joined Prof. Yu Xia's research lab, where he worked on the analysis of biomolecules using photo-induced radical reactions and mass spectrometry. He also did part of his graduate research at Tsinghua University (Beijing, China) as a visiting researcher. Later, he joined Prof. Scott McLuckey's group and worked on top-down analysis of proteins using ET-DDC. In the next phase of his career, he hopes to work in an industrial setting where he can put his scientific skills into good use.

# PUBLICATIONS


1. **Adhikari, S**.; Dziekonski, E.T.; Londry, F.A.; and McLuckey, S.A. Dipolar DC Induced Collisional Activation of Non-Dissociated Electron-Transfer Products. *J. Mass Spectrom.*, 2019, DOI: 10.1002/jms.4352.

2. **Adhikari, S**.; Yang, X.; and Xia, Y. Acetone/Isopropanol Photoinitiating System Enables Tunable Disulfide Reduction and Disulfide Mapping via Tandem Mass Spectrometry. *Anal. Chem.*, 2018, 90, 13036-13043.

3. Porter, A.G.; Hu, H.; Liu, X.; Raghavan, A.; **Adhikari, S.**; Hall, D.R.; Thompson, D.J.; Liu, B.; Xia, Y.; and Ren, T. Heptamolybdate: A Highly Active Sulfide Oxygenation Catalyst. *Dalton Trans*., 2018, 47, 11882-11887.

4. **Adhikari, S.**; Wenpeng, Z.; Xie, X.; Chen, Q.; and Xia, Y. Shotgun Analysis of Diacylglycerols Enabled by Thiol-Ene Click Chemistry. *Anal. Chem.,* 2018, 90 (8), 5239-5246.

5. Ye, Z.; **Adhikari, S.**; Xia, Y.; and Dai, M. Expedient Syntheses of N-Heterocycles via Intermolecular Amphoteric Diamination of Allenes. *Nat. Commun.,* 2018, 9, 721.

6. Anglada, J.S.; Crehuet, R.; **Adhikari, S.**; Francisco, J.S.; and Xia, Y. Reactivity of Hydropersulfides Towards Hydroxyl Radical Unleased: Disulfide Bond Cleavage, Hydrogen Atom Transfer, and Proton-Coupled Electron Transfer. *PCCP*, 2018, 20, 4793-4804.

7. **Adhikari, S.**; and Xia, Y. Thiyl Radical-Based Charge Tagging Enables Sterol Quantitation via Mass Spectrometry. *Anal. Chem.,* 2017, 89 (23), 12631-12635.

8. Bhattarai, B.T.; **Adhikari, S.**; Kimball, E.A.; and Dolliver, D.D. Palladium-Catalyzed ortho-Halogenation of Diaryl Oxime Ethers. *Tetrahedron Lett.,* 2014, 55 (34), 4801-4806.

9. Dolliver, D.D.; Bhattarai, B.T.; Pandey, A.; Lanier, M.L.; Bordelon, A.S.; **Adhikari, S.**; Dinser, J.A.; Flowers, P.F.; Wills, V.S.; Schneider, C.L.; Shaughnessy, K.H.; Moore, J.N.; Raders, S.M.; Snowden, T.S.; McKim, A.S.; and Fronczek, F.R. Stereospecific Suzuki, Sonogashira, and Negishi Coupling Reactions of N-Alkoxyimidoyl Iodides and Bromides. *J. Org. Chem.*, 2013, 78 (8), 3676–3687.

analytical chemistry

Letter

pubs.acs.org/ac

# Thiyl Radical-Based Charge Tagging Enables Sterol Quantitation via Mass Spectrometry

Sarju Adhikari[†,‡] and Yu Xia*[,†,‡]

[†]Department of Chemistry, Purdue University, West Lafayette, Indiana 47906, United States

[‡]Department of Chemistry, Tsinghua University, Beijing 100084, China

Supporting Information

**ABSTRACT:** Inspired by the high reactivity and specificity of thiyl radicals toward alkenes, we have developed a new charge derivatization method to enable fast and quantitative analysis of sterols via electrospray ionization-mass spectrometry (ESI-MS). Thioglycolic acid (TGA), a commercially available compound, has been established as a highly efficient tagging reagent. Initiated from photochemical reactions, the thiyl radical derived from TGA abstracts an allylic hydrogen in the B ring of sterols, forming a radical intermediate which rapidly recombines with a second thiyl radical to produce the final tagged product. Because of the incorporation of a carboxylic acid group, TGA tagging not only improves the limit of detection (sub-nM) for sterols but also facilitates their quantitation via characteristic 44 Da neutral loss scan. This radical based derivatization is fast (1 min) and efficient (>90% yield) when conducted in a flow microreactor. The analytical utility of thiyl radical charge tagging method has been demonstrated by quantifying sterols from human plasma and vegetable oil.

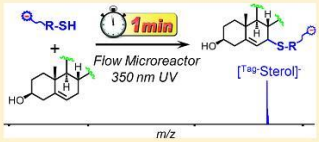




Sterols are naturally occurring and essential lipid molecules for animals (zoosterols), plants (phytosterols), and fungi. They commonly contain an unsaturated four-ring core structure (A, B, C, D rings), a 3$\beta$-hydroxyl (OH) group, and an aliphatic side chain attached to C17 (demonstrative structures shown in Scheme 1a). The major biological functions of sterols include regulating membrane fluidity and serving as precursors of steroids, vitamin D, hormones, and many other important mediator molecules.[1] Gas chromatography−mass spectrometry (GC−MS) and liquid chromatography−mass spectrometry (LC−MS) are the primary methods for the analysis of sterols from complex mixtures.[2,3] Since GC−MS suffers from lower sensitivity and throughput,[4] more recent development focuses on enhancing separation and throughput using high-performance liquid chromatography (HPLC)−MS platform, which typically employs an electrospray ionization (ESI)-MS interface.[5] Given the nonpolar nature of sterols, charge derivatization is a necessary and effective strategy to enhance the response of sterols via ESI. Established derivatization methods either target the hydroxyl function group via forming an ester bond with a charge tag (e.g., sulfate,[6] phosphonium,[7] picolinyl esters[8]) or convert the hydroxyl to ketone first and then use carbonyl chemistry to link a charge tag to sterols (e.g., forming Girard P hydrazones).[9,10] These methods significantly improved sterol analysis via ESI with the limit of detection (LOD) achieved at nanomolar to sub-nanomolar.[6−10] The derivatization reactions typically require several hours or even days to accomplish. Several derivatization reagents need to be synthesized in-house, further curbing wide accessibility to these methods.

Radical reactions, due to their fast reaction kinetics, are attractive candidates for chemical derivatization. Although only marginally explored, some notable examples of derivatization via radical chemistry include protein surface mapping via radical modification[11,12] and carbon−carbon double location determination in lipids via the Paternò−Büchi reactions.[13,14] Thiyl radicals are known to exhibit high reactivity toward alkenes, which has been harnessed as a type of "click chemistry" for forming a carbon−sulfur bond.[15,16] Inspired by the reactions of thiyl radicals toward alkenes, we aim to tailor thiyl radical chemistry into a highly efficient charge derivatization strategy to enhance the analysis of nonpolar molecules, which are poorly detected by ESI-MS. In this report, we choose sterols as the first-time demonstration of this concept.

The C5−C6 double bond in the B ring of sterols makes them susceptible to thiyl radical tagging (Scheme 1b). In the survey studies, cholesterol was used as a model compound to react with a series of thiol reagents each consisting of a readily charged functional group via ESI (cysteamine, thioglycolic acid (TGA), and sodium 2-mercaptoethanesulfonate). On the basis of the reaction conditions reported in thiol-ene coupling,[17] the thiol reagent (100 mM) and cholesterol (5 $\mu$M) were codissolved in dimethylformamide (DMF) with 1 mM 2,2-dimethoxy-2-phenylacetophenone (DMPA) added as a photoinitiator to effect thiyl radical formation. The reaction mixture was placed in a borosilicate glass vial and irradiated by a low-pressure mercury lamp with emission centered at 351 nm. After the completion of the reaction, 1 mL of sodium hydroxide (NaOH) solution (0.1 M) was added to the reaction mixture and the reaction product was extracted with ethyl acetate. The

**Received:** October 5, 2017
**Accepted:** November 20, 2017
**Published:** November 20, 2017

  

DOI: 10.1021/acs.analchem.7b04080
Anal. Chem. 2017, 89, 12631−12635

**Scheme 1. (a) Chemical Structures of Representative Sterols in Animals, Plants, and Fungi and (b) Proposed Reaction Pathways for Thiyl Radical-Based Charge Tagging of Sterols[a]**

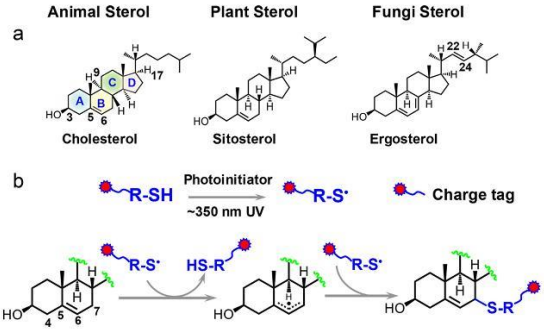


[a]Tagging can happen at C7 and C5 (structure not shown).

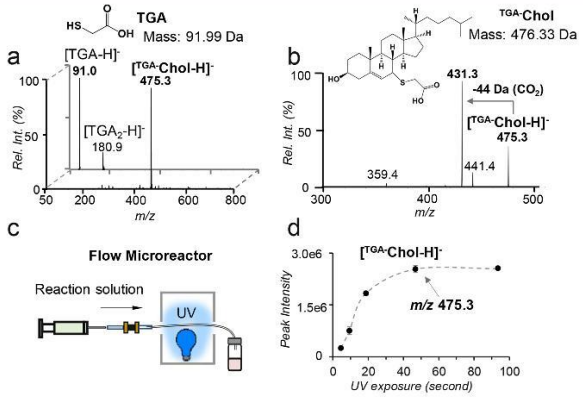


**Figure 1.** (a) Negative ion mode nanoESI MS spectra of cholesterol (5 $\mu$M) and TGA before reaction (back panel) and after reaction (front panel). TGA-tagged cholesterol appears at $m/z$ 475.3 ($[^{TGA}$-Chol-H$]^-$). (b) $MS^2$ CID of $[^{TGA}$-Chol-H$]^-$. (c) Schematic representation of a flow microreactor. (d) Plot of the peak intensity of $[^{TGA}$-Chol-H$]^-$ as a function of UV exposure time using the flow microreactor setup.

above procedure effectively removed remaining high concentration TGA, which could cause signal suppression upon subsequent nanoESI-MS analysis. The detailed experimental procedure can be found in the Supporting Information. Figure 1a compares nanoESI MS spectra of cholesterol before and after TGA tagging in the negative ion mode. Before reaction, only deprotonated TGA, $[TGA - H]^-$ ($m/z$ 91.0) and a small amount of its oxidized product, $[O\text{-}TGA_2 - H]^-$ ($m/z$ 180.9), were observed. As a big contrast, the postreaction spectrum is dominated by a single peak at $m/z$ 457.3 (front panel of Figure 1a). Accurate mass measurement proved that this product ($m/z$ 457.3253) had a mass increase of 89.9776 Da relative to cholesterol, corresponding to a net addition of $C_2H_2O_2S$, the elemental composition of deprotonated TGA (Figure S1a, Supporting Information). Collision-induced dissociation (CID) of the product ($[^{TGA}$-Chol $- H]^-$) produced a prominent loss of 44 Da ($CO_2$) from the carboxylic acid group of the TGA moiety (Figure 1b). The above data all supported that TGA addition to cholesterol was successful. The reaction progress, monitored via the ion intensity of $[^{TGA}$-Chol $- H]^-$, showed a rapid increase in the first 15 min and a plateau afterward (Figure S2, Supporting Information). Quantitative analysis of cholesterol via GC–MS showed that the derivatization yield was above 90% after 20 min UV exposure (Figure S3, Supporting Information). TGA outperformed the rest thiol reagents tested in this study in terms of speed of reaction, product yield, and the easiness of sample cleanup for MS analysis; therefore, it was chosen for further method development.

Compared to bulk reactions, photochemical reactions in flow microreactors (micrometer ($\mu$m)-size inner dimensions) have been demonstrated to proceed more rapidly due to higher photon absorption efficiency.[18] To further speed up TGA derivatization and make this reaction compatible with small



DOI: 10.1021/acs.analchem.7b04080
Anal. Chem. 2017, 89, 12631−12635

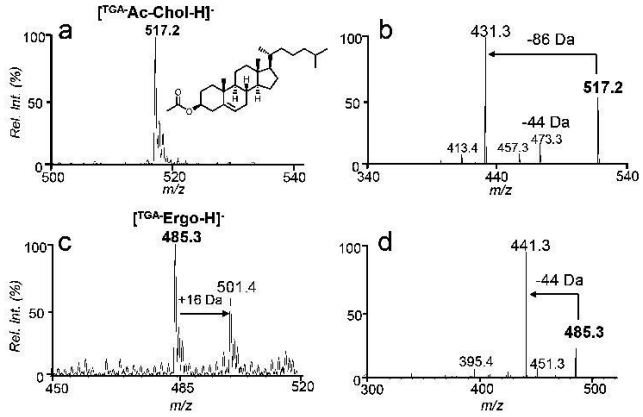


**Figure 2.** Negative ion mode nanoESI-MS of TGA derivatized (a) cholesterol acetate (1 $\mu$M, $m/z$ 517.2) and (b) $MS^2$ CID of $[^{TGA-}$Ac-Chol − H$]^-$, (c) ergosterol (1 $\mu$M, $m/z$ 485.3), and (d) $MS^2$ CID of $[^{TGA-}$Ergo − H$]^-$.

sample size handling which is typically encountered in bioanalysis, a flow microreactor employing a fused silica capillary (100 $\mu$m i.d., 375 $\mu$m o.d.) has been developed (Figure 1c). The reaction kinetic curve was obtained by monitoring the ion intensity of $[^{TGA-}$Chol − H$]^-$ (Figure 1d). Clearly, the reaction proceeded to a steady state within 50 s. GC−MS analysis of the remaining cholesterol suggested 94% conversion yield after 1 min UV irradiation, which was comparable to that obtained from the 20 min bulk reaction. The vastly accelerated reaction rate in the flow microreactor can be attributed to the large surface area to volume ratio of the microreactor, allowing maximal light transmission and thus significantly improving irradiation efficiency of the reaction mixture.

Initially, we expected to detect the thiol-ene coupling product, resulting from thiyl radical addition to the C5−C6 double bond followed by H atom abstraction from another thiol. This product should appear at $m/z$ 477.3; however, the observed product (peak at $m/z$ 475.3) is two Da less than the thiol-ene coupling product, suggesting the preservation of the C=C. This result can be rationalized from the reverse nature of thiyl radical addition to a C=C and the structure of cholesterol. The rate of thiyl radical addition to a ring C=C is several orders of magnitude smaller than the product dissociation rate,[19] leading to ineffective thiol-ene coupling. This explains why the thiol-ene coupling product was not observed for cholesterol. On the other hand, although alkyl thiyl radicals cannot abstract alkyl hydrogen due to the relatively small S−H bond dissociation energies (BDEs, ~87 kcal/mol),[20] they can abstract the allylic hydrogen at the C7 position (C7−H BDE = 83.2 kcal/mol).[21] We hypothesize that the TGA thiyl radical abstracts the C7−H, forming a delocalized three-carbon allylic radical intermediate, which recombines with another thiyl radical at either C5 or C7 position, leading to the observed TGA-tagged cholesterol. It is worth noting that TGA thiyl radical is unlikely to abstract C4−H, the BDE of which is 89.0 kcal/mol,[21] higher than the BDE of the alkyl thiol reagent. The proposed reaction pathway (Scheme 1b), however, needs to be further verified, e.g., using C7−D cholesterol, to provide more evidence on the C7−H abstraction process.

Established derivatization techniques target the free −OH functionality of sterols and thus have a limitation in analyzing the esterified form of sterols. As a contrast, the TGA tagging method can be readily applied to cholesterol ester (CE) analysis. Figure 2a shows the post-tagging spectrum using cholesterol acetate ($[^{TGA-}$Ac-Chol − H$]^-$, $m/z$ 517.2) as a demonstration. $MS^2$ CID of the tagged product (Figure 2b) produced 44 Da loss and 86 Da loss. The latter fragment resulted from sequential losses of $CO_2$ (from TGA) and $CH_2CO$ (from the acetyl moiety).

Ergosterol serves as a structural component of fungi cell membrane and thus it is a frequently used target for developing antifungal drugs.[22] Ergosterol consists of three C=Cs, the diene structure in the B ring and a C22−C23 double bond in the aliphatic chain (structure shown in Scheme 1a). Since the aliphatic allylic hydrogen has a higher BDE than that of C9−H (about 10 kcal/mol higher),[20] we expect that TGA tagging would be more competitive at the B ring. Indeed, only one TGA tagging product (the peak at $m/z$ 485.3, Figure 2c) was observed from the reaction of TGA and ergosterol for an extended reaction period and no competing thiol-ene coupling product was observed (should appear at $m/z$ 487.5, if formed). $MS^2$ CID of tagged product produced abundant 44 Da loss (Figure 2d), characteristic to the TGA tag. Because of the presence of diene in the B ring, minor sequential oxidation of the TGA-tagged ergosterol was detected (the peak at $m/z$ 501.4 in Figure 2c).

We further applied the TGA tagging to several other frequently encountered sterols from mammalian cells and plants (e.g., 7-dehydrocholesterol, Figure S4, Supporting Information). We found that single TGA tagging could be accomplished within 1 min for different sterol standards consisting at least one C=C in the B ring, likely resulting from the overwhelming excess of TGA (100 mM) relative to sterols ($\mu$M or lower) in the reaction system. TGA tagging, however, was not successful for steroids having a conjugated enone structure (e.g., progesterone) due to competitive photo-



DOI: 10.1021/acs.analchem.7b04080
Anal. Chem. 2017, 89, 12631−12635

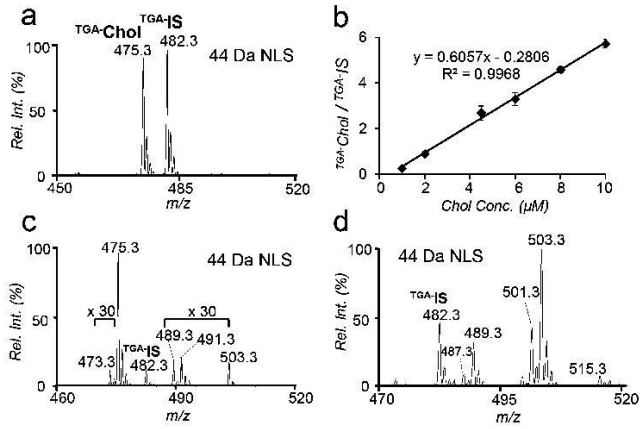


**Figure 3.** (a) 44 Da NLS of TGA tagged cholesterol (1 $\mu$M) and cholesterol-$d_7$ (Chol-$d_7$, IS, 5 $\mu$M). (b) Calibration curve obtained for cholesterol based on 44 Da NLS. Error bars stand for standard deviation ($n$ = 3). 44 Da NLS profile of TGA tagged sterols from (c) 20 $\mu$L human plasma and (d) soybean oil with 5 $\mu$M Chol-$d_7$ added as IS.

**Table 1. Free, Esterified, and Total (Free and Esterified) Sterols from Commercially Bought Soybean Oil**[a]

| | | | concentration [mg/100 g] | | |
|---|---|---|---|---|---|
| sterol | MW [Da] | detection $m/z$ | free | esterified | total |
| brassicasterol | 398.67 | 487.3 | 0.52 ± 0.07 | 0.41 ± 0.01 | 1.4 ± 0.1 |
| campesterol | 400.69 | 489.3 | 64 ± 5 | 17 ± 0.3 | 75 ± 4 |
| stigmasterol | 412.70 | 501.3 | 69 ± 8 | 23 ± 0.3 | 84 ± 5 |
| $\beta$-sitosterol | 414.70 | 503.3 | 135 ± 1 | 67 ± 1 | 190 ± 6 |

[a]Chol-$d_7$ (5 $\mu$M) was used as IS.

chemical rearrangement reactions.[23] These results demonstrate that thiyl radical tagging of sterols exhibits selectivity to unsaturated B ring, which is an attractive feature for mixture analysis.

Tandem mass spectrometry (MS/MS) analysis of TGA-tagged sterols all showed abundant loss of $CO_2$, due to the presence of deprotonated carboxylic acid moiety. On the basis of this characteristic fragmentation channel, 44 Da neutral loss scan (NLS) was evaluated for the quantitation of TGA-tagged sterols. Figure 3a shows a representative 44 Da NLS spectrum of 1 $\mu$M cholesterol with 5 $\mu$M cholesterol-$d_7$ (Chol-$d_7$) added as internal standard (IS). The calibration curve obtained by plotting the peak area ratios of $[^{TGA}\text{–Chol} - H]^-$ and $[^{TGA}\text{–IS} - H]^-$ against cholesterol concentration showed good linear regression ($R^2$ = 0.9968). LOD was achieved at 0.5 nM (S/N ratio > 3, Figure S5, Supporting Information), comparable to those reported by other charge derivatization approaches, such as sulfation (0.2 nM),[6] phosphonium labeling (0.05 nM),[7] *N*-alkylpyridinium quaternization (54 nM),[24] and Girard P reagent (0.1 nM).[10] Most importantly, the whole process of TGA tagging and subsequent MS analysis is significantly shortened to less than 2 min per run. Although $CO_2$ loss is a facile fragmentation channel for unsaturated fatty acids,[25] their potential interference for sterol analysis via 44 Da NLS should be limited due to their appearance at lower $m/z$ range than the commonly observed sterols.

Because of the selectivity and sensitivity of TGA tagging toward sterols, this method is well suited for small sample volume analysis without a prior lipid extraction. As a demonstration, 20 $\mu$L of human plasma was dissolved in DMF at a final volume of 200 $\mu$L for TGA derivatization (1 min UV irradiation). Figure 3c shows the 44 Da NLS spectrum. Besides the TGA-tagged cholesterol peak ($m/z$ 475.4), less abundant sterols such as dehydrocholesterol ($m/z$ 473.4; intact mass, 384.6 Da), campesterol ($m/z$ 489.3; intact mass, 400.37 Da), and sitosterol ($m/z$ 503.3; intact mass, 414.4 Da) were also detected. The peak at $m/z$ 491.4 corresponds to hydroxycholesterols (intact mass, 402.6 Da), which have been reported to be a mixture of multiple structural isomers in human plasma (Tables S1–S3, Supporting Information) and they typically exist in the sub-micromolar to nanomolar concentration range.[26] Using Chol-$d_7$ as the IS, quantitation of cholesterol in plasma was performed for cholesterol (procedure shown in the Supporting Information). The concentration of free cholesterol was found to be 1.4 ± 0.3 $\mu$mol/mL, while the concentrations of total and esterified cholesterol were 3.1 ± 0.1 $\mu$mol/mL and 2.0 ± 0.1 $\mu$mol/mL, respectively. These values fall within the range of reported cholesterol levels from human plasma using GC/LC–MS methods.[26]

Phytosterols typically exist at low concentrations (ppm) in vegetable oil and their quantitation demands laborious sample processing. To test the applicability the TGA tagging method,



DOI: 10.1021/acs.analchem.7b04080
Anal. Chem. 2017, 89, 12631–12635

we performed quantitative analysis of phytosterols in soybean oil purchased from a local grocery store (detailed procedures shown in the Supporting Information). A variety of TGA derived sterols including brassicasterol ($m/z$ 487.3), campesterol ($m/z$ 489.3), stigmasterol ($m/z$ 501.3), $\beta$-sitosterol ($m/z$ 503.3), and cycloartenol ($m/z$ 515.3) were clearly observed from 44 Da NLS spectrum (Figure 3d, 5 $\mu$M Chol-$d_7$ added as IS). Table 1 summarizes the quantitative information on the free, esterified, and total phytosterols, expressed in mg/100 g of soybean oil. A significant portion of the sterols existed in their free form rather than in esterified form. $\beta$-Sitosterol was found to be the most abundant species in all sterol fraction (both free and esterified form) followed by stigmasterol and campesterol.

In summary, a rapid and simple charge derivatization method via thiyl radical tagging was developed for quantitative analysis of sterols from complex mixtures. The reaction allows linking the charged thiol group to the allylic position of the double bond in the B ring of a sterol. Thioglycolic acid (TGA), a commercially available compound, stands out as a highly efficient reagent. The carboxylic acid group in TGA allows tagged sterols to be detected by negative ion mode nanoESI-MS with high sensitivity. The deployment of a flow microreactor setup for this photochemical reaction further shortens the reaction time to less than 1 min with a yield higher than 90%, a significant improvement over conventional tagging methods which require several hours or even days to accomplish. Taking advantage of the dominant $CO_2$ loss from CID of TGA-tagged sterols, 44 Da NLS has been established as a sensitive and quantitative method for sterol analysis from mixtures (e.g., total, free, and esterified sterols in human plasma and vegetable oil). Because of the fast reaction stemmed from radical chemistry, the TGA derivatization method shows potential to be incorporated into high-throughput workflows for applications in lipidomics and biomedical research. In this study, we noticed that structural isomers of several oxysterols cannot be distinguished using thiyl radical tagging. The same issue also exists for other conventional charge derivatization methods and has been resolved by adding an LC separation component in the workflow. In future studies, we plan to couple thiyl radical tagging with HPLC–MS/MS to further expand its capability in mixture analysis.

## ■ ASSOCIATED CONTENT

### Supporting Information

The Supporting Information is available free of charge on the ACS Publications website at DOI: 10.1021/acs.analchem.7b04080.

Details for chemicals and materials, lipid extraction, derivatization procedures of sterols in bulk and in the photochemical microreactor, and analysis of sterols in human plasma and vegetable oil (PDF)

## ■ AUTHOR INFORMATION


### Corresponding Author

*E-mail: xiayu@mail.tsinghua.edu.cn.

### ORCID

Yu Xia: 0000-0001-8694-9900


### Notes

The authors declare no competing financial interest.

## ■ ACKNOWLEDGMENTS

Financial support from NIHGM Grant R01GM118484 is greatly appreciated.

## ■ REFERENCES


(1) Bloch, K. *New Compr. Biochem.* **1991**, *20*, 363–381.
(2) McDonald, J. G.; Smith, D. D.; Stiles, A. R.; Russell, D. W. *J. Lipid Res.* **2012**, *53*, 1399.
(3) Murphy, R. C. *Tandem Mass Spectrometry of Lipids Molecular Analysis of Complex Lipids*; Royal Society of Chemistry: Cambridge, U.K., 2014.
(4) Hübschmann, H.-J. In *Handbook of GC/MS*; Wiley-VCH Verlag GmbH & Co. KGaA, 2008; pp 7–292.
(5) Liebisch, G.; Binder, M.; Schifferer, R.; Langmann, T.; Schulz, B.; Schmitz, G. *Biochim. Biophys. Acta, Mol. Cell Biol. Lipids* **2006**, *1761*, 121–128.
(6) Chatman, K.; Hollenbeck, T.; Hagey, L.; Vallee, M.; Purdy, R.; Weiss, F.; Siuzdak, G. *Anal. Chem.* **1999**, *71*, 2358–2363.
(7) Woo, H. K.; Go, E. P.; Hoang, L.; Trauger, S. A.; Bowen, B.; Siuzdak, G.; Northen, T. R. *Rapid Commun. Mass Spectrom.* **2009**, *23*, 1849–1855.
(8) Honda, A.; Miyazaki, T.; Ikegami, T.; Iwamoto, J.; Yamashita, K.; Numazawa, M.; Matsuzaki, Y. *J. Steroid Biochem. Mol. Biol.* **2010**, *121*, 556–564.
(9) Griffiths, W.; Wang, Y.; Alvelius, G.; Liu, S.; Bodin, K.; Sjövall, J. *J. Am. Soc. Mass Spectrom.* **2006**, *17*, 341–362.
(10) Crick, P. J.; William Bentley, T.; Abdel-Khalik, J.; Matthews, I.; Clayton, P. T.; Morris, A. A.; Bigger, B. W.; Zerbinati, C.; Tritapepe, L.; Iuliano, L.; Wang, Y.; Griffiths, W. J. *Clin. Chem.* **2015**, *61*, 400–411.
(11) Hambly, D. M.; Gross, M. L. *J. Am. Soc. Mass Spectrom.* **2005**, *16*, 2057–2063.
(12) Chen, J.; Rempel, D. L.; Gau, B. C.; Gross, M. L. *J. Am. Chem. Soc.* **2012**, *134*, 18724–18731.
(13) Ma, X.; Xia, Y. *Angew. Chem., Int. Ed.* **2014**, *53*, 2592–2596.
(14) Ma, X.; Chong, L.; Tian, R.; Shi, R.; Hu, T. Y.; Ouyang, Z.; Xia, Y. *Proc. Natl. Acad. Sci. U. S. A.* **2016**, *113*, 2573–2578.
(15) Tasdelen, M. A.; Yagci, Y. *Angew. Chem., Int. Ed.* **2013**, *52*, 5930–5938.
(16) Dénès, F.; Pichowicz, M.; Povie, G.; Renaud, P. *Chem. Rev.* **2014**, *114*, 2587–2693.
(17) Jackson, J. A.; Turner, J. D.; Rentoul, L.; Faulkner, H.; Behnke, J. M.; Hoyle, M.; Grencis, R. K.; Else, K. J.; Kamgno, J.; Bradley, J. E.; Boussinesq, M. *Int. J. Parasitol.* **2004**, *34*, 1237–1244.
(18) Su, Y.; Straathof, N. J. W.; Hessel, V.; Noël, T. *Chem. - Eur. J.* **2014**, *20*, 10562–10589.
(19) Chatgilialoglu, C.; Ferreri, C. *Acc. Chem. Res.* **2005**, *38*, 441–448.
(20) Luo, Y.-R. *Handbook of Bond Dissociation Energies in Organic Compounds*; CRC Press: Boca Raton, FL, 2003.
(21) Zielinski, Z. A.; Pratt, D. A. *J. Am. Chem. Soc.* **2016**, *138*, 6932–6935.
(22) Muller, C.; Binder, U.; Bracher, F.; Giera, M. *Nat. Protoc.* **2017**, *12*, 947–963.
(23) Asher, J. D. M.; Sim, G. A. *J. Chem. Soc.* **1965**, *0*, 1584–1594.
(24) Wang, H.; Wang, H.; Zhang, L.; Zhang, J.; Leng, J.; Cai, T.; Guo, Y. *J. Mass Spectrom.* **2013**, *48*, 1101–1108.
(25) Yang, K.; Zhao, Z.; Gross, R. W.; Han, X. *Anal. Chem.* **2011**, *83*, 4243–4250.
(26) Quehenberger, O.; Armando, A. M.; Brown, A. H.; Milne, S. B.; Myers, D. S.; Merrill, A. H.; Bandyopadhyay, S.; Jones, K. N.; Kelly, S.; Shaner, R. L.; Sullards, C. M.; Wang, E.; Murphy, R. C.; Barkley, R. M.; Leiker, T. J.; Raetz, C. R.; Guan, Z.; Laird, G. M.; Six, D. A.; Russell, D. W.; et al. *J. Lipid Res.* **2010**, *51*, 3299–3305.




DOI: 10.1021/acs.analchem.7b04080
*Anal. Chem.* 2017, 89, 12631–12635

analytical chemistry

Article

Cite This: Anal. Chem. 2018, 90, 5239−5246

pubs.acs.org/ac

# Shotgun Analysis of Diacylglycerols Enabled by Thiol−ene Click Chemistry

Sarju Adhikari,[†,‡] Wenpeng Zhang,[†,‡] Xiaobo Xie,[†] Qinhua Chen,[§] and Yu Xia*[,†,‡]

[†]Department of Chemistry, MOE Key Laboratory of Bioorganic Phosphorus Chemistry & Chemical Biology, Tsinghua University, Beijing 100084, China

[‡]Department of Chemistry, Purdue University, West Lafayette, Indiana 47906, United States of America

[§]Affiliated Dongfeng Hospital, Hubei University of Medicine, Shiyan, Hubei Province 442000, China

Supporting Information

**ABSTRACT:** Diacylglycerols (DAGs) are a subclass of neutral lipids actively involved in cell signaling and metabolism. Alteration in DAG metabolism has been associated with onset and progression of several human-related diseases. The structural diversity of DAGs and their low concentrations in biological samples call for the development of methods that are capable of sensitive identification and quantitation of each DAG species as well as rapid profiling when a biochemical pathway is perturbed. In this work, the thiol−ene click chemistry has been employed to introduce a charge-tag, namely, cysteamine (CA), at a carbon−carbon double bond (C=C) of unsaturated DAGs. This one-pot photochemical derivatization is fast (within 1 min), universal (monotagging) for DAGs varying in fatty acyl chain lengths and the number of C=Cs, and suitable for small sample volume (e.g., 1−50 μL plasma). Because of the presence of the amine group in CA, tagged DAGs showed at least 10 times increase in response to electrospray ionization as compared to conventional ammonium adduct formation. Low-energy collision-induced dissociation of CA tagged DAGs allowed confident assignment of fatty acyl composition. A neutral loss scan based on characteristic 95 Da loss (a combined loss of CA and $H_2O$) of tagged DAGs has been established as a sensitive means for unsaturated DAG detection (limit of detection = 100 pM) and quantitation from mixtures. The analytical utility of CA tagging was demonstrated by shotgun analysis of unsaturated DAGs in human plasma, including samples from type 2 diabetes mellitus patients.

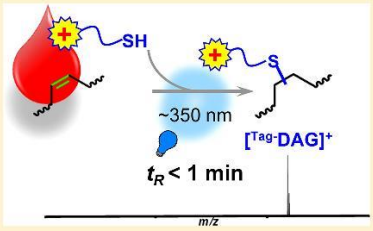


Neutral lipids, including sterol lipids and glycerol lipids, are important components of cellular lipidomes, performing distinct biological functions as compared to polar lipids. As a subclass of glycerol lipids, diacylglycerols (DAGs) share a generic structure, in which two hydroxyl groups in the glycerol backbone are substituted by fatty acyls through ester bonds. DAGs play a variety of roles inside cells; they are produced as metabolites of triacylglycerols (TAGs), while they can be precursors or intermediates in the biosynthesis of TAGs, glycerophospholipids, and glyceroglycolipids.[1] DAGs also serve as signaling molecules.[2] For example, DAG accumulation is associated with activation of protein kinase C in skeletal muscle and liver cells, which ultimately influences downstream insulin signaling.[3] Abnormal accumulation of DAGs has been reported in disease states associated with insulin resistance, such as cardiac hypertrophy,[4] diabetes,[5] and cardiac lipotoxicity.[6] Recently, plasma DAG composition has been used as a biomarker of metabolic syndrome onset in rhesus monkeys.[7]

In terms of DAG profiling, gas chromatography−mass spectrometry (GC-MS) is a traditionally used technique.[8] In this workflow, DAGs need to be separated from other lipid classes and subsequently derivatized (e.g., trimethylsilyl ethers) to increase their volatility.[9] The overall process requires relatively large sample amount and long analysis time. More recently, high-performance liquid chromatography (HPLC)-MS has been increasingly applied to DAG analysis. DAGs together with other neutral lipids can be well-separated on the column, allowing quantitation of 1,2-DAG and 1,3-DAG *sn*-isomers from complex mixtures.[10] The advancement of electrospray ionization-tandem mass spectrometry (ESI-MS/MS) of lipids has facilitated global lipid analysis without the need of a prior lipid class separation, coined as "shotgun lipid analysis" by Han and Gross.[11] Shotgun analysis has the advantages of fast analysis speed and the capability of detecting a broad range of lipid classes, which has found increasing applications in biomedical discoveries.[12] Per the nonpolar nature, DAGs are detected as adduct ions, viz. $[DAG + X]^+$ (X = $Li^+$, $Na^+$, $NH_4^+$) by ESI.[13,14] Collision-induced dissociation (CID) of the ammonium adduct ions forms abundant fatty acyl specific fragment ions (as combined loss of $NH_3$ and free fatty acid), allowing the assignment of DAG structures.[13] An obvious drawback of using adduct ion formation in DAG analysis is that

Received: January 2, 2018
Accepted: March 23, 2018
Published: March 23, 2018

the ionization efficiency is not high, which also varies according to the fatty acyl chain lengths and the degree of unsaturation.[15,16] These variations require the use of multiple DAG internal standards for quantitation.[13]

Charge derivatization is an effective approach to boost ionization efficiency of neutral lipids via ESI-MS.[17] Established derivatization methods target the free hydroxyl group in DAGs through ester bond formation with a charge reagent. This strategy also blocks potential fatty acyl migration in DAGs.[18] *N*-Chlorobetainyl chloride,[19] *N*,*N*-dimethylglycine (DMG),[18] and DMG imidazolide[20] have been demonstrated as efficient charge derivatization reagents, enhancing the ion signal of DAGs by at least 2 orders of magnitude than forming their adduct ions.[19] CID of charge derivatized DAGs typically produces tag specific fragment in high abundance, facilitating the development of MS/MS transitions for sensitive quantitation (limit of quantitation (LOQ), 100 pM via DMG derivitization).[18] Because fatty acyl chain specific fragment ions are absent from direct CID of the charge tagged DAGs, adduct formation of the derivatized DAGs with $Li^+$ or $NH_4^+$ is still needed for structural elucidation. This approach although requires the addition of salt into ESI solution, the Han group demonstrated that it provided a distinct benefit of quantifying the *sn*-1,2- and 1,3-isomers based on CID of lithiated DMG-DAG ions.[18]

In biological systems, a substantial proportion of DAGs consists of unsaturated fatty acyls. As an example, the concentration of unsaturated DAGs was found to be ~0.81 $\mu$M out of ~0.88 $\mu$M, the total DAG concentration in human plasma; that is, 92% of DAGs are unsaturated.[21] Given the prevalence of unsaturated DAGs in lipidomes, we are interested in exploring alternative charge derivatization methods that target the carbon−carbon double bond (C=C) as a site for the introduction of a charge tag. Recently, we have demonstrated thiyl radical tagging for sterol lipid analysis by linking an ionizable thiol reagent (thioglycolic acid, TGA) to the unsaturated B ring in sterols.[22] This derivatization when coupled with ESI-MS/MS via low energy CID provided rapid (in minutes) and sensitive quantitation (limit of detection (LOD) in nM) of sterols from complex mixtures.

Thiol−ene coupling reaction, involving thiyl radical addition to an alkene function group, is a widely adopted methodology for the formation of carbon−sulfur bonds.[23] It fulfills the "click-chemistry" paradigm of high reaction rates, quantitative conversion in mild condition, and simple workup procedures (i.e., removal of byproducts by nonchromatographic methods).[24] Thiol−ene chemistry has found broad applications in polymer and material synthesis,[25] surface functionalization,[26] and drug delivery.[27]

Taking advantage of its high specificity for C=C transformation, herein we explored a charge derivatization strategy based on thiol−ene chemistry to tag the C=C in unsaturated DAGs as illustrated in Scheme 1a. The success of the tagging would allow enhanced sensitivity of the DAGs via ESI-MS. Moreover, the newly formed C−S bond in the derivatized DAG species is less likely to be a facile dissociation site under charge driven fragmentation conditions due to the relatively nonpolar nature of the C−S bond. This property should facilitate the formation of structural informative fragment ions, that is, fatty acyl chain related fragments. In this work, synthetic DAG standards with varying chain lengths and degrees of unsaturation were used for method development, including optimizing reaction conditions, screening for suitable thiol compounds as charge tags, and developing MS/MS methods

**Scheme 1. (a) Charge Tagging of Unsaturated Lipid via Thiol−ene Click Chemistry[a] and (b) Chemical Structures of the Three Thiol Reagents**

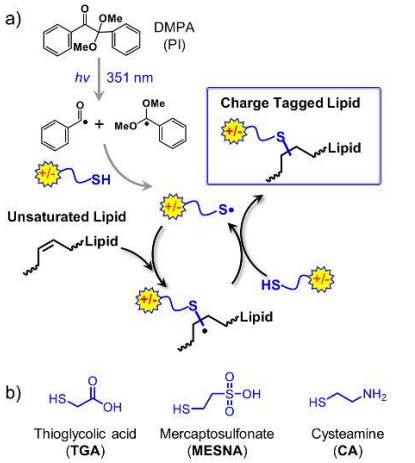


[a]DMPA is a commonly used photoinitiator (PI) for thiyl radical formation upon 351 nm wavelength UV irradiation

for identification and quantitation. The analytical capability of the established method was demonstrated by performing analysis of DAGs from human plasma samples of type 2 diabetes mellitus (DM) patients using a shotgun lipidomic approach.

## EXPERIMENTAL SECTION

**Lipid Nomenclature.** Shorthand notations for glycerolipids are based on the guidelines provided by LIPID MAPS.[28] For synthetic lipid standards with known *sn* positions, "/" separator is used such as in DAG 16:0/18:1/0:0 to represent DAG consisting of C16 and C18 fatty acyls at *sn*-1 and *sn*-2 positions, respectively. DAG 16:0/0:0/18:1 stands for a DAG with C16 and C18 fatty acyls at *sn*-1 and *sn*-3 positions, respectively. 0:0 represents no fatty acyl chain is linked. The "0" and "1" after the carbon number represents the degree of unsaturation. The interchangeable "_" notation, such as in DAG 16:0_18:1, is adopted for DAG with unidentified *sn* positions.

**Materials.** All the chemical reagents and solvents were purchased from commercial sources and were used without further purification. DAGs 16:0/18:1(9Z)/0:0, 15:0/18:1-$d_7$(9Z)/0:0, 18:0/20:4(5Z,8Z,11Z,14Z)/0:0, 18:1(9Z)/18:1(9Z)/0:0, and 18:1(9Z)/0:0/18:1(9Z) were purchased from Avanti Polar Lipids Inc. (Alabaster, AL, USA). DAGs 14:1(9Z)/14:1(9Z)//0:0, 16:1(9Z)//16:1(9Z)//0:0, 17:1(9Z)/17:1(9Z)/0:0, 18:1(6Z)/18:1(6Z)/0:0, 18:2-(9Z,12Z)/18:2(9Z,12Z)/0:0, 18:3(9Z,12Z,15Z)/18:3-(9Z,12Z,15Z)/0:0, 20:1(9Z)/20:1(9Z)/0:0, 22:1(9Z)/22:1(9Z)/0:0, and 24:1(9Z)/24:1(9Z)/0:0 were purchased from Nu-Check Prep, Inc. (Elysian, MN, USA). Thioglycolic acid (TGA), sodium-2-mercaptoethanesulfonate (MESNA), cysteamine (CA) hydrochloride, dimethylformamide (DMF),



DOI: 10.1021/acs.analchem.8b00012
*Anal. Chem.* 2018, 90, 5239−5246

2,2-dimethoxy-2-phenylacetophenone (DMPA), hydrochloric acid, and ethyl acetate were purchased from Sigma-Aldrich (St. Louis, MO, USA). Deionized water was obtained from a purification system at 0.03 $\mu$S·cm (model: Micropure UV; Thermo Scientific; San Jose, CA, USA). Pooled human plasma (Li Heparin used as anticoagulant) was purchased from Innovative Research (Novi, MI, USA).

**Human Plasma Sample Collection.** Six human plasma samples, including 3 healthy normal controls and 3 type 2 DM patients were collected from Affiliated Dongfeng Hospital, Hubei University of Medicine (Shyian, Hubei Province, China).

**Lipid Extraction.** The procedure for total lipid extraction from plasma (Section 1, Supporting Information) was based on established protocols.[29,30] Briefly, 50 $\mu$L of plasma, 0.3 mL of 0.67 M phosphate buffer solution, and 2.0 mL of chloroform−methanol (3:1, v/v) were combined in 100 mm × 13 mm glass test tubes. The mixture was vortex-mixed for 2 min and then was centrifuged at 1200 g for 5 min for phase separation. The aqueous layer was removed using a glass Pasteur pipet, while the remaining organic layer was transferred to another glass test tube and was dried under a stream of nitrogen gas. For quantitative analysis, DAGs were fractioned from other classes of lipids using a 100-mg Isolute silica cartridge (Biotage, Charlotte, NC, USA). The lipid extracts were stored at −20 °C until further analysis.

**Derivatization of DAG Standards, Plasma Lipid Extract, and Plasma.** DAG (0.01−200 $\mu$M), thiol reagent (100 mM), and DMPA (photoinitiator, 0.5 mM), were dissolved in DMF and degassed with nitrogen gas before photochemical reactions. The solution was pumped through a flow microreactor (in $\mu$L/min flow rate range), made from UV transparently coated fused silica capillary (100 $\mu$m i.d., 375 $\mu$m o.d.; Polymicro Technologies; Phoenix, AZ, USA). A low-pressure mercury lamp with an emission band at 351 nm (model number: 80−1057−01/351; BHK, Inc.; Ontario, CA, USA) was placed in parallel to the capillary at a distance of 0.5 cm. This whole setup was enclosed in a cardboard box to prevent stray light. At the exit of the microflow reactor, the reaction solution (100 $\mu$L) was collected in a glass vial and added with ethyl acetate (200 $\mu$L). The mixture was washed twice with 0.1 M aq. HCl (400 $\mu$L) to remove excess thiol reagent (e.g., CA) before MS analysis. The same procedure was applied to direct derivatization of lipids in plasma (1−20 $\mu$L) without a prior lipid extraction step.

**MS Analysis of Neutral Lipid Standards and Lipid Extracts.** MS analysis of charge derivatized DAG standards and lipid extracts were performed on a 4000 QTRAP and a 4500 QTRAP mass spectrometer (SCIEX, Toronto, ON, CA) equipped with a home-built nanoESI source (pulled borosilicate glass emitters). Optimized MS parameters were as follows: nanoESI spray voltage: ± (1400−1800) V; curtain gas: 10 psi; declustering potential: ± 20 V; a scan rate of 1000 Da/s for 4000 QTRAP and 10 000 Da/s for 4500 QTRAP. The instrument was used in a linear ion trap MS analysis mode or in triple quadrupole linked scan mode (precursor ion scan (PIS) or neutral loss scan (NLS)).[31]

## ■ RESULTS AND DISCUSSION

**Charge Tagging via Thiol−ene Chemistry.** Scheme 1a shows a classic view of thiol−ene reaction with an unsaturated lipid depicted for the conventional alkene.[24] Briefly, upon exposure to 351 nm UV irradiation, DMPA (the photoinitiator, PI) undergoes Norrish Type I cleavage to generate benzoyl radical and 1,1-dimethoxy-1-phenylmethyl radical. These carbon-centered radicals abstract the sulfur−hydrogen in the thiol reagent, forming alkylthiyl radical. The thiyl radical then adds to the C=C to form a carbon-centered radical, which subsequently abstracts a hydrogen atom from another thiol molecule to produce the derivatized product, while the newly formed thiyl radical propagates in the radical chain process. Thiol−ene reactions are not regioselective for internal double bonds; so two regio-isomers resulting from the addition to either carbon in the original C=C are formed.[32]

Using DAG 16:0/18:1/0:0 as a model compound, three thiol reagents, TGA, MESNA, and CA (structures shown in Scheme 1b), were tested for thiol−ene charge tagging. These thiols were selected based on the presence of readily ionizable functional group either for protonation or deprotonation under typical ESI conditions, reasonable solubility, and commercial availability. Moreover, it was preferred that the charge tagged DAG ions could generate structurally informative fragment ions upon CID. DMPA, a commonly used photoinitiator for thiol−ene reactions was adopted here, while DMF was used as the reaction solvent.[23] Prior to MS analysis, a simple wash procedure was performed to reduce signal suppression from remaining thiol reagent. The reaction progress was monitored through the intensity of tagged DAG ions via nanoESI-MS.

Figure 1a−c summarizes the postreaction nanoESI-MS spectra of DAG 16:0/18:1/0:0 (1 $\mu$M) resulting from three individual thiol reagents after reaching equilibrium. A single reaction product was detected at high ion intensities (counts per second, cps) from each reagent, that is, $m/z$ 685.5 ($[^{TGA}DAG - H]^-$), $m/z$ 735.4 ($[^{MESNA}DAG - H]^-$), $m/z$ 672.5 ($[^{CA}DAG + H]^+$) from TGA and MESNA in negative ion mode, and CA in positive ion mode, respectively. The mass differences (insets in Figure 1) between the detected products and the DAG molecule (594.2 Da) match well with the mass of the corresponding thiol reagent, suggesting successful thiol−ene coupling. Moreover, all three thiol reagents significantly improved ionization of DAG in nanoESI. Using CA as an example, the ion intensity of CA tagged DAG was 10 times higher than its ammonium adduct (Figure S1).

The data in Figure 1d represent typical $MS^2$ beam-type CID (CE = 35 V) of TGA derivatized DAG anions ($m/z$ 685.5) in negative ion mode. Different from CID of TGA derivatized sterols,[22] 44 Da loss ($-CO_2$) from TGA carboxylic group was not observed; neither was the tag loss. Instead, the fatty acyl anions, including $[C16:0\text{-}H]^-$ ($m/z$ 255.3) and $[^{TGA}C18:1\text{-}CO_2-H]^-$ ($m/z$ 329.2, a sequential loss of $CO_2$ from the TGA tag) were quite abundant. Beam-type CID of MESNA derivatized DAG anions (CE = 60 eV, Figure 1e) produced three major fragments, neutral loss of C16:0 ($m/z$ 479.2), thiol tagged C18:1 anions ($[^{MESNA}C18:1\text{-}CO_2-H]^-$, $m/z$ 423.2), and $[C16:0\text{-}H]^-$ ($m/z$ 255.3). Clearly, CID of TGA and MESNA tagged DAG anions readily allow identification of fatty acyl composition in DAG.

Beam-type CID spectrum of protonated $^{CA}$DAG (Figure 1 f, CE = 32 V) is rather simple with three fragment peaks produced present at almost equal abundance. The fragment peak at $m/z$ 577.5 resulted from sequential loss of CA tag (77 Da) and $H_2O$ (18 Da), leading to a characteristic neutral loss of 95 Da. The fragment ions at $m/z$ 339.5 and 313.5 derived from sequential loss of CA tag and the fatty acyl chains, C18:1 and C16:0, respectively. The above sequences of fragmentation were supported by accurate mass measurement and $MS^3$ CID experiments (Figures S2 and S3). The possible structures for



DOI: 10.1021/acs.analchem.8b00012
Anal. Chem. 2018, 90, 5239−5246

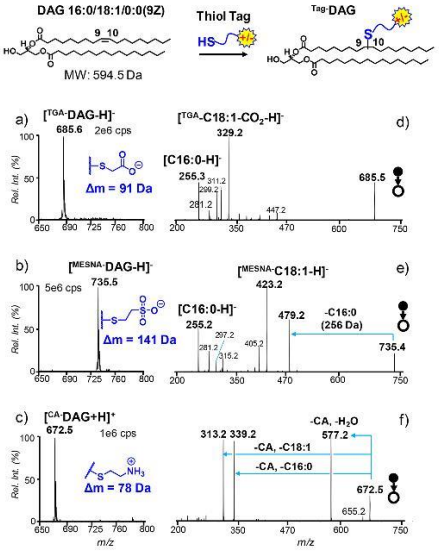


**Figure 1.** Charge tagging of DAG 16:0/18:1(9Z)/0:0 (1 $\mu$M) using thiol−ene chemistry. The inset at the top shows a generic reaction scheme for charge tagging. Post reaction nanoESI MS spectra after derivatization with (a) TGA and (b) MESNA in negative ion mode, and (c) CA in positive ion mode. $MS^2$ beam-type CID of (d) $^{TGA}$DAG at $m/z$ 685.5 (CE = 35 V) in negative ion mode, (e) $^{MESNA}$DAG at $m/z$ 735.4 (CE = 60 V) in negative ion mode, and (f) $^{CA}$DAG at $m/z$ 672.5 (CE = 32 V) in positive ion mode.

the observed major fragments are presented in Scheme 2, while possible fragmentation pathways are proposed in Schemes S1−S5.

Although the three thiol reagents all delivered improved ionization and useful structural information (fatty acyl chain composition) upon CID, we decided to choose CA for further method development. This is because, besides the fatty acyl information, the distinct 95 Da neutral loss associated with the CA tag facilitates the development of NLS for detection and quantitation of DAGs from mixtures.

**Scheme 2. Proposed Structures for Fragments at $m/z$ 577, 339, and 313 Resulting from CID of $[^{CA}$DAG 16:0/18:1/0:0 + H$]^+$**

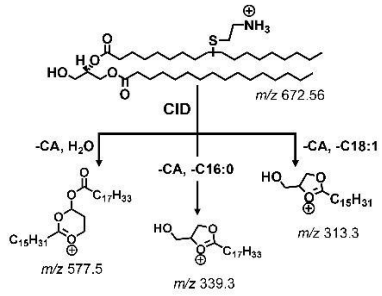


**Optimization of CA Thiol−ene Coupling.** In synthetic settings, the thiol reagent is typically placed in stoichiometric relationship to the alkenes in thiol−ene reactions.[23] Although the concentrations of DAGs in biological samples are typically at sub-$\mu$M level or lower, it is necessary to use high concentrations of PI and thiol reagent (both in mM) to maintain adequate steady-state concentrations of the thiyl radical so as to sustain radical chain reactions depicted in Scheme 1a. For instance, reactions involving 10 mM CA, 0.5 mM DMPA, and 5 $\mu$M DAG 16:0/18:1/0:0 produced a major product at $m/z$ 670.5, two Da less than the expected thiol−ene coupling product (Figure S4). This type of product has been observed in polymer synthesis and identified by NMR to have a shifted C=C in the structure.[33] By increasing the concentration of CA to 100 mM or higher, this side product could be effectively reduced to less than 2% of the thiol−ene coupling product. Although higher concentrations of CA led to faster and cleaner reactions, there was no significant benefit to increase CA concentrations over 100 mM. With the use of a flow microreactor, CA tagging could be accomplished within 40 s for a variety of DAGs consisting of different lengths of fatty acyls and different numbers of C=Cs. The representative kinetic curves can be found in Figures S5 and S6, Supporting Information.

**Polyunsaturated DAGs.** For DAGs consisting of polyunsaturated fatty acyls, we wondered if multiple tagging could happen. Figure 2 summarizes the postreaction spectra of DAG 15:0/18:1-$d_7$/0:0, DAG 18:3/18:3/0:0 and DAG 18:0/20:4/0:0, which were derivatized separately but under identical reaction conditions using the flow microreactor setup. The production of mono-CA tagging products reached steady state

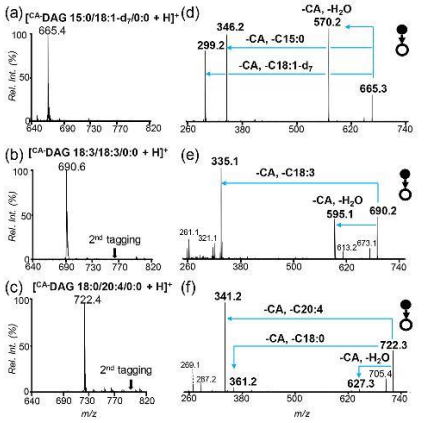


**Figure 2.** Post-CA tagging nanoESI MS spectra of (a) DAG 15:0/18:1-$d_7$/0:0, (b) DAG 18:3/18:3/0:0, and (c) DAG 18:0/20:4/0:0. $MS^2$ beam type CID (CE 32 V) of (d) $^{CA}$DAG 15:0/18:1-$d_7$/0:0 ($m/z$ 665.3), (e) $^{CA}$DAG 18:3/18:3/0:0 ($m/z$ 690.2), and (f) $^{CA}$DAG 18:0/20:4/0:0 ($m/z$ 722.3).



DOI: 10.1021/acs.analchem.8b00012
Anal. Chem. 2018, 90, 5239−5246

within 1 min of UV exposure. Despite the presence of multiple C═Cs in the latter two DAGs, only single CA tagging products were observed ($m/z$ 690.3 and 722.3), same as the tagging of DAG 15:0/18:1-$d_7$ /0:0 ($m/z$ 665.3), which has one C═C in the molecule. It is worth noting that no doubly charged ions corresponding to sequential tagging were present in the lower mass range (Figure S7). Irradiation of reaction mixture with UV for 1 h in bulk processes, led to <10% of second tagging (Figure S8). Under the same reaction condition, derivatization using TGA produced >35% of second tagging products of DAG 18:1/18:1/0:0 (Figure S9). Such difference can be attributed to the higher reactivity of TGA than CA.[34] Although the preferred formation of mono-CA tagging products in the polyunsaturated system is not fully understood at this moment, the phenomenon nonetheless is advantageous for sensitive detection and quantitation in subsequent MS/MS experiments.

The CA derivatized DAG species was further analyzed by MS/MS via beam-type CID (Figure 2d–f). Upon CID (CE = 32 V), fragments corresponding to sequential loss of CA and fatty acyl chains are consistently observed with high intensities.

However, the relative intensity of the 95 Da loss (the combined loss of CA and $H_2O$) decreases as the degree of unsaturation in a fatty acyl chain increases, for example, C20:4 < C18:3 < C18:2 < C18:1. This aspect suggests that the application of 95 Da NLS to the polyunsaturated system may have a lower sensitivity than the ones consisting lower degree of unsaturation in the fatty acyl chains. In this case, NLS targeted for a specific polyunsaturated fatty acyl chain, for example, 381 Da NLS for the combined losses of CA (77 Da) and C20:4 (304 Da), can be used to get around this problem and achieve sensitive detection. Table S2 summarizes the combined loss of CA and various fatty acyl chains present in DAGs.

**DAG *sn*- and C═C Positional Isomers.** We also explored the potential of differentiating *sn*- and C═C positional isomers of DAGs via CA tagging and subsequent CID. For instance, *sn*-1,2- and 1,3-DAG 18:1(9Z)/18:1(9Z) were derivatized by CA and analyzed. Unfortunately, the MS/MS spectra for the two *sn*-isomers were identical and thus, did not provide any distinction (Figure S10). CID of CA tagged DAG 18:1(6Z)/18:1(6Z) /0:0 showed similar fragmentation pattern to DAG 18:1(9Z)/18:1(9Z)/0:0 (data not shown). Therefore, no distinction on the C═C location was achieved from CA tagging and CID.

**Quantitative Analysis.** It has been shown that the ionization response of DAGs in alkali metal adduct forms are highly dependent on chain lengths and the degrees of unsaturation of fatty acyls.[13] Here we examined if such bias also existed for DAGs after CA tagging. Nine unsaturated DAGs (equal molar, 1 $\mu$M each) with fatty acyls varying from C28 to C48 and degrees of unsaturation in the range of 1 to 4 were mixed together, while 0.5 $\mu$M DAG 15:0/18:1-$d_7$/0:0 was added as the internal standard (IS). This mixture was then subjected to CA derivatization for 1 min using the flow microreactor setup. Figure 3a shows the postreaction nanoESI-MS spectrum. The derivatized DAG species yielded similar ion response regardless of the change of fatty acyl chain length and unsaturation. The relative standard deviation (16%, $n$ = 3) of the DAG signals are within the expected errors arising from sample handling. The above results suggest that CA tagging can successfully minimize ionization bias for DAGs in ESI due to variations in fatty acyl composition. Moreover, signal suppression among DAGs during mixture analysis is very limited.

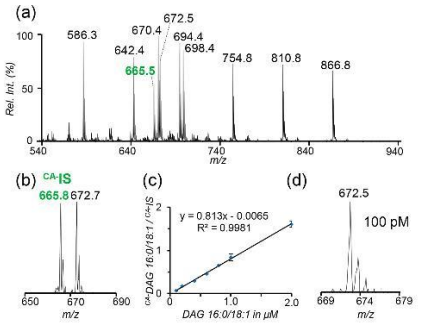


**Figure 3.** (a) Post-CA tagging nanoESI MS spectrum of equimolar (1 $\mu$M each) mixture of DAG 14:1/14:1/0:0 ($m/z$ 586.3), 16:1/16:1/0:0 ($m/z$ 642.4), 17:1/17:1/0:0 ($m/z$ 670.4), 16:0/18:1/0:0 ($m/z$ 672.5), 18:2/18:2/0:0 ($m/z$ 694.4), 18:1/18:1/0:0 ($m/z$ 698.4), 20:1/20:1/0:0 ($m/z$ 754.8), 22:1/22:1/0:0 ($m/z$ 810.8), and 24:1/24:1/0:0 ($m/z$ 866.8), with 0.5 $\mu$M of IS (15:0/18:1-$d_7$/0:0, $m/z$ 665.5). (b) 95 Da NLS of $^{CA}$DAG 16:0/18:1/0:0 (1 $\mu$M) and IS (1 $\mu$M). (c) A linear plot resulted from 95 NLS for DAG 16:0/18:1/0:0 ($R^2$ = 0.9981). Error bars represent standard deviation; $n$ = 3. (d) 95 Da NLS of 100 pM DAG 16:0/18:1/0:0 after CA tagging.

We further assessed the performance of 95 Da NLS for DAG quantitation. A good linear correlation ($R^2$ = 0.9981) was achieved between MS response and concentration (DAG 16:0/18:1/0:0, 0.1–2 $\mu$M) by employing 1.0 $\mu$M DAG 15:0/18:1-$d_7$/0:0 as IS (Figure 3b and c). Since monotagging was dominant for DAGs consisting of multiple C═Cs, 95 Da NLS also provided good linear correlations for their quantitation (Table S1). The LOD for DAG 16:0/18:1/0:0 could be achieved at 100 pM from 95 Da NLS (S/N 3:1, Figure 3d). Such level of LOD is comparable to values reported from other charge derivatization approaches, for example, LOQ of 100 pM using DMG via ESI-MS/MS[18] and LOD of 10 nM using *N*-chlorobetainyl chloride via ESI-MS.[19] Overall, CA tagging of DAG followed by ESI-MS/MS enjoys the benefits of fast analysis (less than 2 min per run) and sensitive detection.

**Analysis of DAGs from Human Plasma.** The analysis of DAGs from crude mixture is often hindered from their relatively low abundance (~0.88 $\mu$M) and ion suppression from other neutral lipids, such as CEs (~3.5 mM) and TAGs (~1.0 mM).[21] Conventional analytical methods typically involve multistep liquid–liquid extraction, enrichment and/or chromatographic separation before MS. Herein, we tried to achieve rapid and sensitive analysis of DAGs by thiol–ene derivatization without resorting to chromatographic separation on clinical human plasma samples. As a demonstration, 1 $\mu$L of human plasma was directly subjected to CA derivatization (1 $\mu$M of DAG 15:0/18:1-$d_7$/0:0 added as IS). Figure 4a shows the postreaction nanoESI-MS spectrum. Three classes of neutral lipids were detected, representing CA tagged CEs, DAGs, and TAGs. These assignments were based on the detected monoisotopic $m/z$ values and corresponding MS/MS data. For instance, the peak at $m/z$ 726.9 was identified as $^{CA}$CE 18:2. CID of this peak produced a dominant fragment peak at $m/z$ 369 (cholestene cations) due to sequential loss of CA and C18:2 from the tagged CE. Similarly, ions at $m/z$ 962.8



DOI: 10.1021/acs.analchem.8b00012
Anal. Chem. 2018, 90, 5239–5246

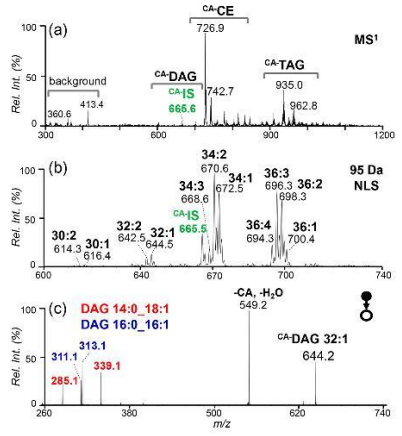


**Figure 4.** (a) Post-CA tagging nanoESI mass spectrum of 1 $\mu$L pooled human plasma with 1 $\mu$M DAG 15:0/18:1-$d_7$/0:0 added as the IS. The $m/z$ regions correspond to tagged neutral lipid classes are indicated. (b) 95 Da NLS for unsaturated DAGs (mass range $m/z$ 600−740). (c) $MS^2$ CID of $m/z$ 644.2 ($[^{CA}DAG\ 32:1 + H]^+$) reveals two fatty acyl composition isomers, DAG 14:0_18:1 and DAG 16:0_16:1.

were identified as $^{CA}$TAG 18:1/18:1/18:1 based on the detection of sequential loss of CA and C18:1 (Figure S12).

As expected, CA tagged DAGs were detected at low intensities as compared to CEs and DAGs in the $MS^1$ spectrum (Figure 4a). However, by using 95 Da NLS, 7 distinct DAG molecular species were observed (Figure S12). The above data clearly demonstrate the capability of CA tagging followed by 95 Da NLS for selective detection of DAGs even at the presence of other more abundant neutral lipids. We further examined if unsaturated phosphocholines (PCs) would be tagged by CA given their relatively high abundance in plasma. It turned out that PC had very low reactivity toward CA; CID of the CA tagged PC ions presented different fragmentation pattern from that of $^{CA}$DAG ions (Figure S13). Therefore, the presence of unsaturated PCs would not interfere with DAG detection.

For quantitative analysis DAGs were extracted and purified from 50 $\mu$L of human plasma (recovery rate = 94 ± 3%). Eleven peaks of $^{CA}$DAGs were detected from 95 Da NLS (Figure 4b). MS/MS analysis proved that many DAGs consisted of fatty acyl compositional isomers. For example, CID of ions at $m/z$ 644.2, $^{CA}$DAG 32:1, showed abundant losses of 359 Da (CA + C18:1), 333 Da (CA + C16:0), 331 (CA + C16:1), and 305 Da (CA + C14:0), corresponding to product ions at $m/z$ 285, 311, 313, and 339, respectively (Figure 5c). Based on the number of fatty acyl carbon atoms and double bonds, DAG 32:1 was assigned to contain two fatty acyl compositional isomers: DAG 14:0_18:1 and DAG 16:0_16:1. Similarly, DAG 34:2 (the peak at $m/z$ 670.2 in Figure 4b) contained DAG 16:1_18:1 and DAG 16:0_18:2 ( Figure S15). In order to assess the relative change of the distinct DAG species within the parent ion, fatty acyl chain specific NLS and PIS can also be employed (Figure S16). PIS of 339 and 337 Da revealed the existence of DAGs containing C18:1 and C18:2, respectively. Overall, 18 distinct DAG

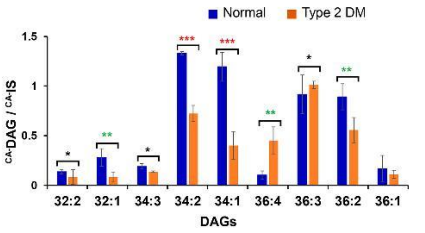


**Figure 5.** Comparison of relative amount of major unsaturated DAGs in human plasma samples from normal control and type 2 DM patient. One $\mu$M of the internal standard (DAG 15:0/18:1-$d_7$/0:0) was added before the derivatization step. Error bars represent standard deviation; $n$ = 3, *$p$ < 0.05, **$p$ < 0.01, ***$p$ < 0.001 ($t$ test).

species were identified to the level of fatty acyl composition as summarized in Table 1. Quantitative analysis of DAGs from the

**Table 1. Identified DAG Species in Pooled Human Plasma**

| DAG | MW (Da) | detection ($m/z$) | acyl chain composition | conc. ($\mu$M) |
|---|---|---|---|---|
| 30:1 | 538.5 | 616.4 | 14:0_16:1 | 0.1 ± 0.01 |
| 30:2 | 536.5 | 614.3 | 14:1_16:1 | 0.08 ± 0.01 |
| 32:1 | 566.5 | 644.5 | 16:0_16:1/14:0_18:1 | 1.1 ± 0.1 |
| 32:2 | 564.5 | 642.5 | 16:1_16:1/14:0_18:2 | 0.7 ± 0.2 |
| 34:1 | 594.5 | 672.5 | 16:0_18:1/16:1_18:0 | 6.4 ± 1.0 |
| 34:2 | 592.5 | 670.6 | 16:0_18:2/16:1_18:1 | 7.7 ± 1.1 |
| 34:3 | 590.5 | 668.6 | 16:1_18:2/16:0_18:3 | 1.4 ± 0.3 |
| 36:1 | 622.5 | 700.4 | 18:0_18:1 | 1.3 ± 0.4 |
| 36:2 | 620.5 | 698.3 | 18:1_18:1/18:0_18:2 | 5.3 ± 0.6 |
| 36:3 | 618.5 | 696.3 | 18:1_18:2 | 6.0 ± 1.0 |
| 36:4 | 616.5 | 694.3 | 18:2_18:2/18:1_18:3 | 1.6 ± 0.6 |

pooled human plasma was performed using 95 Da NLS. Calibration curves for each individual DAG species were obtained using DAG 15:0/18:1-$d_7$/0:0 (1 $\mu$M) as IS (Table S1). These values fall within the range of reported unsaturated DAGs measured from human plasma using HPLC-MS/MS.[21] However, since CA tagging is specific for unsaturated DAGs, saturated DAGs (e.g., DAG 16:0/16:0) could not be detected. Besides, CA tagging followed by CID cannot differentiate *sn*-isomers.

**DAG Analysis of Type 2 Diabetes Mellitus Human Plasma.** Various studies have shown the correlation of increased intracellular DAG content in liver and muscle in type 2 DM.[35] Recently, Shaw et al. have demonstrated aberration of plasma lipidome occurs prior to the onset of type 2 DM.[36] We were interested to test if CA tagging followed by 95 Da NLS was capable in providing quick profiling of DAGs in plasma for type 2 DM patients. Figure 5 summarizes the relative intensity changes of unsaturated DAGs relative to IS (DAG 15:0/18:1-$d_7$/0:0, 1 $\mu$M) from two sets of samples (normal controls, $N$ = 3; DM patients, $N$ = 3). Representative 95 Da NLS spectra can be found in Figure S14. The major DAG species include DAG 34:2, 34:1, 36:3, and 36:2. The relative intensities of DAG 34:2, 34:1, and 36:2 decreased by 2.5 ± 0.7, 2.8 ± 1.1, and 1.6 ± 0.4 times in DM patients as compared to the control, respectively. However, DAG 36:4 in the DM patients increased by 5 ± 2 times relative to the control. In terms of the change of fatty acyl compositional



DOI: 10.1021/acs.analchem.8b00012
Anal. Chem. 2018, 90, 5239−5246

isomers, CID of $^{CA}$DAG 36:2 revealed a reduction of DAG 16:0_18:1 relative to isomer DAG 16:0_18:2 in DM patients (Figure S17). Further studies are required with the use of a larger sampling size and controlled medication of the type 2 DM patients.

## CONCLUSIONS

In this study, we have utilized thiol−ene click chemistry as an effective charge derivatization method to enable fast analysis of unsaturated DAGs by nanoESI-MS. Cysteamine (CA) was identified as a proper derivatization reagent, which allowed fast charge tagging (in 1 min) and enhanced ionization (by 10 times) of a variety of unsaturated DAGs as compared to conventional adduct ion formation. Low-energy CID of CA tagged DAGs led to simple product ion spectrum, yet rich in structural information. Specifically, the combined neutral loss of the tag (CA) and fatty acyls (RCOOH) readily allowed the assignment of fatty acyl chains, leading to confident identification of multiple fatty acyl compositional isomer of DAGs in biological samples. The other major fragmentation channel was the combined loss of CA and $H_2O$ (95 Da). On the basis of this characteristic loss, 95 Da NLS was established as a sensitive means for detection (LOD of 100 pM) and quantitation of unsaturated DAGs. The above method was further applied to DAG analysis of pooled human plasma and plasma samples from type 2 DM patients. In comparison with methods based on GC-MS and HPLC-MS for DAG analysis, CA tagging followed by ESI-MS/MS has several advantages, such as fast analysis speed (2 min vs up to 60 min for analysis) and the potential of direct analysis of small quantity of clinical sample (e.g., 1 $\mu$L plasma). In terms of limitations, this method cannot analyze saturated DAGs and it is not capable to provide *sn*-position information. Preliminary LC-MS data showed multiple or broadened elution peaks resulting from mono-CA tagging of DAGs having more than one C=C, likely due to formation of multiple regio-isomers (Figure S19). This phenomenon suggests that CA tagging could increase the complexity for mixture analysis when coupled with LC-MS. CA tagging for DAG analysis is just one example of applying thiol−ene click chemistry to solve a specific analytical problem, viz. DAG analysis. As shown in the example of direct analysis of human plasma, other classes of unsaturated neutral lipids (CEs and TAGs) were also detected. In future studies, we plan to expand the thiol−ene derivatization toolbox and develop methods to enhance analysis of other important neutral lipids.

## ASSOCIATED CONTENT

### Supporting Information

The Supporting Information is available free of charge on the ACS Publications website at DOI: 10.1021/acs.analchem.8b00012.

Additional information on extraction protocols for DAGs from human plasma, optimization of experimental parameters, and MS data on analysis of DAGs from human plasma (PDF)

## AUTHOR INFORMATION


### Corresponding Author

*E-mail: xiayu@mail.tsinghua.edu.cn.

### ORCID

Yu Xia: 0000-0001-8694-9900


### Author Contributions

All authors have given approval to the final version of the manuscript.

### Notes

The authors declare no competing financial interest.

## ACKNOWLEDGMENTS

Financial support from National Natural Science Foundation of China (No. 21722506, No. 21621003) and NIH R01GM118484 is greatly appreciated.

## REFERENCES


(1) Goñi, F. M.; Alonso, A. *Prog. Lipid Res.* **1999**, *38*, 1−48.
(2) Colón-González, F.; Kazanietz, M. G. *Biochim. Biophys. Acta, Mol. Cell Biol. Lipids* **2006**, *1761*, 827−837.
(3) Erion, D. M.; Shulman, G. I. *Nat. Med.* **2010**, *16*, 400−402.
(4) Arimoto, T.; Takeishi, Y.; Takahashi, H.; Shishido, T.; Niizeki, T.; Koyama, Y.; Shiga, R.; Nozaki, N.; Nakajima, O.; Nishimaru, K. *Circulation* **2006**, *113*, 60−66.
(5) Eichmann, T. O.; Lass, A. *Cell. Mol. Life Sci.* **2015**, *72*, 3931−3952.
(6) Drosatos, K.; Schulze, P. C. *Curr. Heart Failure Rep.* **2013**, *10*, 109−121.
(7) Polewski, M. A.; Burhans, M. S.; Zhao, M.; Colman, R. J.; Shanmuganayagam, D.; Lindstrom, M. J.; Ntambi, J. M.; Anderson, R. M. *J. Lipid Res.* **2015**, *56*, 1461−1470.
(8) Murphy, R. C.; Fiedler, J.; Hevko, J. *Chem. Rev.* **2001**, *101*, 479−526.
(9) Tserng, K.-Y.; Griffin, R. *Anal. Biochem.* **2003**, *323*, 84−93.
(10) Leiker, T. J.; Barkley, R. M.; Murphy, R. C. *Int. J. Mass Spectrom.* **2011**, *305*, 103−108.
(11) Han, X. *Lipidomics Comprehensive Mass Spectrometry of Lipids*; John Wiley & Son, Inc.: Hoboken, NJ, 2016.
(12) Han, X. *Biochim. Biophys. Acta, Mol. Cell Biol. Lipids* **2017**, *1862*, 804−807.
(13) Murphy, R. C.; James, P. F.; McAnoy, A. M.; Krank, J.; Duchoslav, E.; Barkley, R. M. *Anal. Biochem.* **2007**, *366*, 59−70.
(14) Bowden, J. A.; Albert, C. J.; Barnaby, O. S.; Ford, D. A. *Anal. Biochem.* **2011**, *417*, 202−210.
(15) Li, X.; Evans, J. J. *Rapid Commun. Mass Spectrom.* **2005**, *19*, 2528−2538.
(16) Li, X.; Collins, E. J.; Evans, J. J. *Rapid Commun. Mass Spectrom.* **2006**, *20*, 171−177.
(17) Wang, M.; Wang, C.; Han, R. H.; Han, X. *Prog. Lipid Res.* **2016**, *61*, 83−108.
(18) Wang, M.; Hayakawa, J.; Yang, K.; Han, X. *Anal. Chem.* **2014**, *86*, 2146−2155.
(19) Li, Y. L.; Su, X.; Stahl, P. D.; Gross, M. L. *Anal. Chem.* **2007**, *79*, 1569−1574.
(20) Johnson, D. W. *J. Mass Spectrom.* **2001**, *36*, 277−283.
(21) Quehenberger, O.; Armando, A. M.; Brown, A. H.; Milne, S. B.; Myers, D. S.; Merrill, A. H.; Bandyopadhyay, S.; Jones, K. N.; Kelly, S.; Shaner, R. L.; Sullards, C. M.; Wang, E.; Murphy, R. C.; Barkley, R. M.; Leiker, T. J.; Raetz, C. R.; Guan, Z.; Laird, G. M.; Six, D. A.; Russell, D. W.; et al. *J. Lipid Res.* **2010**, *51*, 3299−3305.
(22) Adhikari, S.; Xia, Y. *Anal. Chem.* **2017**, *89*, 12631−12635.
(23) Hoyle, C. E.; Bowman, C. N. *Angew. Chem., Int. Ed.* **2010**, *49*, 1540−1573.
(24) Hoyle, C. E.; Lee, T. Y.; Roper, T. *J. Polym. Sci., Part A: Polym. Chem.* **2004**, *42*, 5301−5338.
(25) Lowe, A. B. *Polym. Chem.* **2014**, *5*, 4820−4870.
(26) Resetco, C.; Hendriks, B.; Badi, N.; Du Prez, F. *Mater. Horiz.* **2017**, *4*, 1041−1053.
(27) Meghani, N. M.; Amin, H. H.; Lee, B.-J. *Drug Discovery Today* **2017**, *22*, 1604−1619.




DOI: 10.1021/acs.analchem.8b00012
*Anal. Chem.* 2018, 90, 5239−5246

(28) Liebisch, G.; Vizcaíno, J. A.; Köfeler, H.; Trötzmüller, M.; Griffiths, W. J.; Schmitz, G.; Spener, F.; Wakelam, M. J. O. *J. Lipid Res.* **2013**, *54*, 1523−1530.
(29) Folch, J.; Lees, M.; Stanley, G. H. S. *J. Biol. Chem.* **1957**, *226*, 497−509.
(30) Ingalls, S. T.; Kriaris, M. S.; Xu, Y.; Dewulf, D. W.; Tserng, K. Y.; Hoppel, C. L. *J. Chromatogr., Biomed. Appl.* **1993**, *619*, 9−19.
(31) Hager, J. W. *Rapid Commun. Mass Spectrom.* **2002**, *16*, 512−526.
(32) Turunc, O.; Firdaus, M.; Klein, G.; Meier, M. A. R. *Green Chem.* **2012**, *14*, 2577−2583.
(33) Mutlu, H.; Parvulescu, A. N.; Bruijnincx, P. C. A.; Weckhuysen, B. M.; Meier, M. A. R. *Macromolecules* **2012**, *45*, 1866−9297.
(34) Hong, M.; et al. *J. Polym. Sci., Part A: Polym. Chem.* **2012**, *50*, 2499−2506.
(35) Szendroedi, J.; Yoshimura, T.; Phielix, E.; Koliaki, C.; Marcucci, M.; Zhang, D.; Jelenik, T.; Müller, J.; Herder, C.; Nowotny, P.; Shulman, G. I.; Roden, M. *Proc. Natl. Acad. Sci. U. S. A.* **2014**, *111*, 9597−9602.
(36) Meikle, P. J.; Wong, G.; Barlow, C. K.; Weir, J. M.; Greeve, M. A.; MacIntosh, G. L.; Almasy, L.; Comuzzie, A. G.; Mahaney, M. C.; Kowalczyk, A.; Haviv, I.; Grantham, N.; Magliano, D. J.; Jowett, J. B. M.; Zimmet, P.; Curran, J. E.; Blangero, J.; Shaw, J. *PLoS One* **2013**, *8*, e74341.



DOI: 10.1021/acs.analchem.8b00012
*Anal. Chem.* 2018, 90, 5239−5246

analytical chemistry

Article

Cite This: Anal. Chem. XXXX, XXX, XXX−XXX

pubs.acs.org/ac

# Acetone/Isopropanol Photoinitiating System Enables Tunable Disulfide Reduction and Disulfide Mapping via Tandem Mass Spectrometry

Sarju Adhikari,[†,‡] Xiaoyue Yang,[†] and Yu Xia*[,†,‡]

[†]Department of Chemistry, MOE Key Laboratory of Bioorganic Phosphorus Chemistry and Chemical Biology, Tsinghua University, Beijing 100084, China

[‡]Department of Chemistry, Purdue University, West Lafayette, Indiana 47906, United States

Supporting Information

**ABSTRACT:** Herein, we report the development of a new photochemical system which enables rapid and tunable disulfide bond reduction and its application in disulfide mapping via online coupling with mass spectrometry (MS). Acetone, a clean and electrospray ionization (ESI) compatible solvent, is used as the photoinitiator (1% volume) in the solvent system consisting of 1:1 alkyl alcohol and water. Under ultraviolet (UV) irradiation (~254 nm), the acetone/alcohol system produces hydroxyalkyl radicals, which are responsible for disulfide bond cleavage in peptides. Acetone/isopropanol is most suitable for optimizing the disulfide reduction products, leading to almost complete conversion in less than 5 s when the reaction is conducted in a flow microreactor. The flow microreactor device not only facilitates direct coupling with ESI-MS but also allows fine-tuning of the extent of disulfide reduction by varying the UV exposure time. Near full sequence coverage for peptides consisting of intra- or interchain disulfide bonds has been achieved from complete disulfide reduction and online tandem mass spectrometry (MS/MS) via low energy collision-induced dissociation. Coupling different degrees of partial disulfide reduction with ESI-MS/MS allows disulfide mapping as demonstrated for characterizing the three disulfide bonds in insulin.

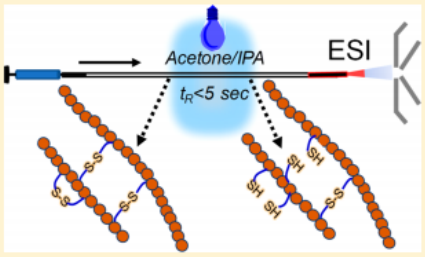


As mass spectrometry (MS) becomes the tool of choice for characterizing structural modifications in proteins, disulfide mapping still presents a challenge for current proteomics analysis workflows.[1] The issue is directly linked to the nature of gas-phase fragmentation chemistry of protonated peptide ions under low-energy collision-induced dissociation (CID), the most available tandem mass spectrometry (MS/MS) technique equipped on commercial mass spectrometers. As depicted by the mobile proton model,[2] disulfide bond does not dissociate readily as compared to the amide bonds under low-energy CID, often leading to no detectable sequence fragment ions for the backbone region inside a disulfide loop.[3] This aspect not only limits protein sequencing but also causes difficulty in disulfide mapping. To tackle this problem, disulfide bond reduction followed by alkylation[4] has been employed as a routine sample preparation procedure in bottom-up proteomics workflows.[5] Along this line, fast disulfide cleavage via chemical or electrochemical reduction has been developed which could be coupled with online liquid chromatography−mass spectrometry (LC−MS).[6,7] Besides, disulfide cleavage inside—the ionization source region has been demonstrated using electrospray ionization (ESI),[8−10] matrix-assisted laser desorption ionization (MALDI),[11] and reactive electrospray-assisted laser desorption/ionization (ELDI).[12] All above approaches when coupled with subsequent MS/MS (typically low-energy CID) deliver rich sequence information due to opening the disulfide bridges; however, disulfide linkage information is lost if complete disulfide reduction is adopted.

Alternative ion activation methods have been explored aiming to induce disulfide cleavages in the gas phase so that intact disulfide bonds can be preserved before MS analysis. Disulfide bond can be preferentially cleaved by electrons (in electron capture dissociation (ECD)[13,14] and electron transfer dissociation (ETD)[15]), photons (in 157 nm,[16] 266 nm,[17,18] and 193 nm ultraviolet photodissociation (UVPD)[19]), radicals (radical initiated peptide sequencing (FRIPS) and TEMPO conjugated peptide ions),[20] and oxidants in ion/ion reactions.[21] These methods can each be used as a stand-alone MS/MS technique or to be combined with CID to improve sequence coverage.

Disulfide mapping strategies rely heavily on multi-enzymatic digestion and partial disulfide reduction, with a goal to produce peptide digests only consisting of interchain disulfides. This

Received: September 1, 2018
Accepted: October 15, 2018
Published: October 15, 2018





DOI: 10.1021/acs.analchem.8b04019
Anal. Chem. XXXX, XXX, XXX−XXX

type of structures is preferred since sequence fragments around cysteine amino acid residues associated with a disulfide bond are more likely to be generated from MS/MS, which is necessary for confident disulfide assignment. Such disulfide mapping approach has been recently demonstrated for human serum albumin (17 disulfide bonds)[8] and serotransferrin (19 disulfide bonds).[19] Finding the right conditions for partial reduction and proteolytic cleavages while avoiding disulfide scrambling is critical for successful disulfide mapping.[16,22] The optimization process is typically achieved by trial-and-error and the conditions cannot be generalized for different protein systems. Obviously, new methods that could either improve digestion or partial disulfide reduction will greatly advance the overall process for disulfide mapping.

Disulfides are known to be highly reactive toward radicals and the dominant reaction channel is disulfide bond cleavage. Earlier efforts from our group have shown that radicals produced from gas discharge[23] or ultraviolet (UV) irradiation[9,10] can cleave disulfide bonds within peptides near or in an ESI emitter. However, disulfide cleavage efficiency is only moderate and often accompanied by side reactions due to the lack of control of the reaction kinetics. In this work, we have developed a new photochemical reaction system for achieving efficient and tunable disulfide bond cleavage at the second-time scale. In this system, acetone was used as a clean and MS compatible photoinitiator upon 254 nm UV irradiation, while secondary hydroxyalkyl radicals resulting from alcohol cosolvent were responsible for cleaving the disulfide bond (Scheme 1). This photochemical reaction system was

**Scheme 1. Proposed Reaction Pathways for Disulfide Bond Cleavage from Using Acetone/Alkyl Alcohol Photoinitiating System**

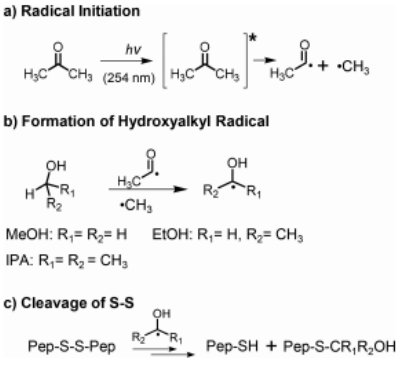


hyphenated with infusion ESI via a flow microreactor. Structural analysis capability of this photochemical system was demonstrated by coupling complete or partial disulfide cleavage with online ESI-MS/MS via CID for peptides containing one or multiple disulfide bonds.

## EXPERIMENTAL SECTION

**Materials.** Oxidized glutathione, reduced glutathione, methanol (MeOH), ethanol (EtOH), isopropyl alcohol (IPA), acetone, acetonitrile (ACN), TPCK treated trypsin, oxytocin, insulin from the porcine pancreas, and ribonuclease B were purchased from Sigma-Aldrich (St. Louis, MO, USA). Somatostatin-14 and selectin binding peptide were purchased from Aladdin (Shanghai, China) and GL Biochem Ltd. (Shanghai, China), respectively. The single letter sequence and disulfide bond connecting pattern for each peptide are listed in Supporting Information, Table S-1. $d_3$-Methanol ($CD_3OH$, 99.5 atom % D) and $d_6$-acetone ($CD_3COCD_3$, 99.9 atom % D) were purchased from J&K Scientific Ltd. (Beijing, China). All commercially purchased chemicals were used without further purification. Deionized water was obtained from a water purification system at 0.03 $\mu$S cm (Thermo Scientific; San Jose, CA, USA).

**Peptide/Protein Digestion and Liquid Chromatography.** Trypsin digestion was conducted by mixing 10 $\mu$L of protein/peptide solution (10 $\mu$g/mL) with 15 $\mu$L of 20 mM ammonium acetate buffer, 5 $\mu$L acetonitrile, and 2 $\mu$L of trypsin (1 $\mu$g/$\mu$L), followed by incubation at 37 °C for 3 h. The trypsin digest was separated on a reversed phase LC (Shimadzu Corporation, Columbia, MD, USA). Column dimension was 4.6 mm × 150 mm with 5 $\mu$m C-18 packing material. Separation conditions for the digest are 0.1% formic acid in water (solvent A) and 0.1% formic acid in ACN (solvent B) with a linear gradient starting from 0% to 40% solvent B for 30 min at 0.5 mL/min flow rate.

**Photochemical Reactions in NanoESI Emitter and in Flow Microreactor.** A low-pressure mercury (LP-Hg) lamp with an emission band around 254 nm (BHK, Inc., Ontario, CA) was utilized to initiate the photochemical reactions. For the nanoESI setup, the lamp was placed orthogonally to the tip and off-axis by approximately 2−4 cm of the borosilicate glass emitter, as reported previously.[9] The flow microreactor was made from UV-transparently coated fused silica capillary (100 $\mu$m i.d., 375 $\mu$m o.d.; Polymicro Technologies; Phoenix, AZ).[24,25] The lamp was placed in parallel to the capillary (~10 cm exposure length) at 0.5 cm distance. The peptide solution was pumped through the microreactor (1−10 $\mu$L/min), the end of which was connected to the inlet of an infusion ESI source. All photochemical reaction setups were enclosed in a cardboard box to prevent direct human exposure to UV light.

**Mass Spectrometry.** QTRAP 4000 and 4500 hybrid triple quadrupole/linear ion trap MS (SCIEX, Concord, ON, Canada) were used to perform preliminary studies with nanoESI emitter reaction setup. For the online coupling of the flow microreactor with infusion ESI-MS/MS, X500R TOF (SCIEX) was used. TIMS TOF (Bruker, Germany) was used to study partially disulfide reduced insulin products.

## RESULTS AND DISCUSSION

**Acetone/Alkyl Alcohol Photoinitiating System for Disulfide Cleavage.** Previously, our lab reported the use of hydroxyl radicals (•OH) for initiating hydroxyalkyl radical formation inside a nanoESI emitter, where alcohol was used as a cosolvent for nanoESI of disulfide peptides.[9] Disulfide cleavage was the main reaction channel; however, the reaction yield was limited due to relatively low concentrations of primary radicals (•OH) formed from 185 nm UV photolysis of ambient air.[9,26] An obvious way to improve the reaction yield is to use more efficient radical initiators, such as 2,2-dimethoxy-2-phenylacetophenone (DMPA) and benzophenone, which are commonly used in organic synthesis and radical polymerization.[27] These compounds go through Norrish type I cleavage at the $\alpha$-carbon of the carbonyl group and form



DOI: 10.1021/acs.analchem.8b04019
Anal. Chem. XXXX, XXX, XXX−XXX

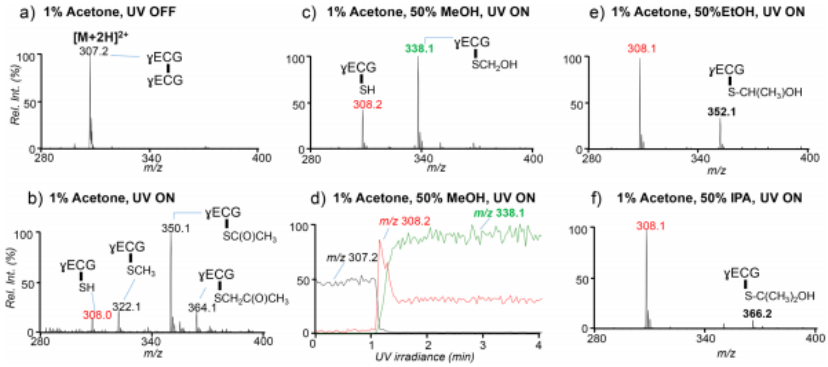


**Figure 1.** Positive ion mode MS spectra of oxidized glutathione (10 $\mu$M) prepared in solutions containing 1% acetone as a photoinitiator. (a) Before and (b) after UV exposure of the aqueous solution in nanoESI emitter. (c) UV irradiation of the peptide in $H_2O$/MeOH ((v/v) = 1:1) and (d) extracted ion chromatogram (XIC) for the reaction shown in part c. UV irradiation of the peptide in (e) $H_2O$/EtOH ((v/v) = 1:1) and (f) $H_2O$/IPA ((v/v) = 1:1).

primary radicals for radical initiation upon UV irradiation.[28,29] They, however, are not directly compatible with MS analysis due to nonvolatile nature and relatively high concentrations (in millimolar) typically employed in the reaction system, which would cause severe interference to MS analysis. Acetone is the simplest ketone and it breaks down to acetyl radical and methyl radical upon UV irradiation (Scheme 1).[30,31] Considering that acetone has relatively low boiling point, low proton affinity, and it is miscible with most ESI solvent systems for peptide analysis, acetone should be well suited to be used as a photoinitiator.

To test the idea, 1% acetone (volume%) was added to an aqueous solution of oxidized glutathione (10 $\mu$M) and loaded onto the nanoESI reaction setup (Figure S1, Supporting Information). Before UV irradiation, only doubly protonated peptide ions ($[M + 2H]^{2+}$) at $m/z$ 307.2 was observed (Figure 1a). After the lamp was turned on for about 2 min, intact peptide ions completely disappeared and new peaks resulting from disulfide bond cleavage dominated (Figure 1b). The major products are reduced glutathione ($[\gamma ECG + H]^+$, $m/z$ 308.0) and radical substitution products at cysteinyl sulfur, including methyl radical ($^{\bullet}CH_3$, $m/z$ 322.1), acetyl radical ($^{\bullet}C(O)CH_3$, $m/z$ 350.1), and acetonyl radical ($^{\bullet}CH_2C(O)$-$CH_3$, $m/z$ 361.1), respectively. The identity of these products were verified by accurate mass measurements and MS/MS experiments. The same reaction was repeated without addition of acetone. No reaction products associated with disulfide bond cleavage were observed, even with prolonged UV exposure (~5 min). Homolytic cleavage of disulfide bond can be induced by 193−266 nm UV irradiation;[18,32] the absence of the disulfide cleavage without acetone addition in our study could be due to low photon flux of the UV lamp. The above set of experiments clearly suggests that Norrish Type I cleavage of acetone indeed happens for 1% of acetone upon 254 nm UV irradiation. Similar reaction phenomenon was observed with as low as 0.1% (v%) of acetone addition, albeit with longer UV irradiation time. Although disulfide bond cleavage is 100% by reacting with radicals derived from photolysis of acetone, the presence of multiple reaction channels points out the need to convert the first-generation radicals into less reactive secondary radical species. In this study, we focused on forming hydroxyalkyl radicals via using acetone as a photoinitiator.

Formation of hydroxyalkyl radicals was explored by adding alkyl alcohol precursor as cosolvent in the reaction system. Figure 1c shows the nanoESI spectrum of oxidized glutathione in MeOH/$H_2O$ ((v/v) = 1:1, 1% acetone) solvent system upon UV irradiation. As a big contrast to Figure 1b where no methanol was added, only two distinct reaction products were observed, corresponding to the reduced ($m/z$ 308.2) and *S*-hydroxymethyl modified glutathione ions ($m/z$ 338.2). *S*-hydroxymethyl product was verified by detecting signature formaldehyde loss (30 Da) from low energy CID (Figure S2, Supporting Information).[9] The extracted ion chromatogram (XIC) showed that the intact glutathione had a sharp drop from 100% to 0% within 30 s (UV irradiation 1.1−1.5 min), accompanied by steep increase of the reduced peptide ($m/z$ 308), the ion signal of which maximized at 1.2 min UV irradiation and then dropped to reach a steady state within 20 s. During this time, the ion signal of the hydroxymethyl substitution product ($m/z$ 338) increased rapidly and stayed constant afterward. These kinetic data suggest that reduced thiol might be further converted to *S*-hydroxymethyl product after its initial formation. Indeed, almost identical spectrum to Figure 1c was obtained when the oxidized glutathione was replaced by reduced glutathione for the reaction (Figure S3, Supporting Information). No definitive evidence could be obtained for tracing the singly protonated thiyl radical ions since they overlap with the doubly protonated glutathione ions at $m/z$ 307.2.

The reaction phenomena for solvent systems involving larger alkyl alcohols, viz. EtOH and IPA, were similar to that observed in the MeOH solvent system. That is, 100% disulfide cleavage was achieved and only two reaction products were detected (Figure 1e,f). $MS^2$ CID of the substitution products, $m/z$ 352 (Figure 1e) and $m/z$ 366 (Figure 1f) showed abundant loss of 44 and 58 Da, confirming the formation of the respective S-hydroxyalkyl product (Figure S2, Supporting Information). A distinct difference from the acetone/MeOH system is that the yield of reduced thiol was increased



DOI: 10.1021/acs.analchem.8b04019
Anal. Chem. XXXX, XXX, XXX−XXX

significantly from 32% (MeOH) to 80% (EtOH) and 93% (IPA).

The possible reaction pathways accounting for disulfide cleavage using acetone/alcohol photoinitiating system are proposed in Scheme 1. Direct disulfide/photon interactions are considered negligible due to low photon flux and orders of magnitude lower concentration of the peptide relative to acetone. The reaction pathway is likely to be initiated by photochemical decomposition of acetone into methyl/acetyl radicals.[30] In the presence of a large excess of alcohol, acetone should have little chance to interact with peptide directly, while reaction with alcohol solvent is the main reaction channel. In the case of methanol, the formation of hydroxymethyl radical ($^{\bullet}CH_2OH$) due to hydrogen abstraction from the C−H bond of methanol is supported by the $D_3COH$ experiments (Figure S4, Supporting Information). For larger alcohols, hydrogen abstraction is generally preferred from the $\alpha$-position due to its lower C−H bond dissociation energy.[33] For example, the BDE of $C_\alpha$−H in $(CH_3)_2C$−**H**OH is 380.7 kJ/mol, while that of the $C_\beta$−H is 394.6 kJ/mol.[34]

Mechanistic studies involving reactions of hydroxyalkyl radicals with disulfides have been scarce.[33] Data generated from gas-phase reactions and theoretical calculations suggest that carbon-centered radicals cleave disulfide bond via a substitution mechanism.[35,36] Based on the observed products, we hypothesize that hydroxyalkyl radical attacks the disulfide bond, forming thiyl radical and S-hydroxyalkyl at the cleavage site. The thiyl radical can further abstract a hydrogen atom from hydroxyalkyl radical (BDE, ~150 kJ/mol for O−H in $^{\bullet}C(CH_3)_2OH$),[37] forming reduced thiol and aldehyde/ketone as stable products. Hydroxyalkyl radicals can also react with a reduced thiol to form S-hydroxyalkyl product and the reactivity follows the order of $^{\bullet}CH_2OH$ > $^{\bullet}CH(CH_3)OH$ > $^{\bullet}C(CH_3)_2OH$, as supported from reaction data of reduced glutathione. It is worth noting that the pathways described above are intended to describe the overall reaction phenomenon. Detailed mechanistic investigations are beyond the scope of the current report.

**Disulfide Reduction in a Flow Microreactor.** Comparing the data for disulfide cleavage in Figure 1 using different alkyl alcohol as cosolvent, IPA solvent system stood out for producing reduced disulfide product with almost 100% conversion. Therefore, 1% acetone in 1:1 IPA/$H_2O$ was chosen as the optimal solvent system for peptide and protein analysis. Previously, our group has demonstrated that photochemical reactions can be greatly accelerated relative to bulk reactions when conducted in a flow microreactor due to significantly improved photon efficiency using flow path in micrometer-dimension.[24,25] Flow microreactor is also advantageous regarding precise control of reaction time so as to reduce detrimental side-reactions from prolonged UV exposure as found by using a static nanoESI setup. UV-transparently coated fused silica capillary was employed to construct the flow microreactor, which was connected directly to an infusion ESI source for online MS experiments as shown in Figure 2a.

Such a reaction system was tested with a peptide containing an interchain disulfide bond (sequence shown the inset of Figure 2b). Figure 2b,c compares the ESI-MS spectra before and after UV irradiation in positive ion mode. Clearly, after 3 s UV irradiation, the intact peptide ions ($[M + 2H]^{2+}$, $m/z$ 467.2) were 100% consumed, while ions corresponding to the two reduced peptide chains, $[A + H]^+$ ($m/z$ 378.2) and $[B + H]^+$ ($m/z$ 558.2), dominated in the postreaction spectrum.

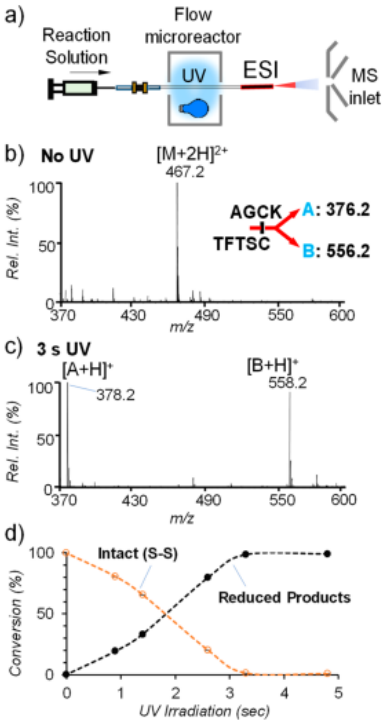


**Figure 2.** (a) Flow microreactor setup for coupling acetone/IPA imitated disulfide bond reduction with ESI-MS. ESI-MS spectra of 10 $\mu$M of trypsin-digested somatostatin-14 in $H_2O$/IPA (1:1) with 1% acetone (b) before UV and (c) after 3 s UV irradiation in positive ion mode. d) Plot of % conversion of the intact peptide to disulfide reduced species as a function of UV irradiation time.

The progress of reduction was monitored as a function of the UV irradiation time. As shown in Figure 2d, the yield of disulfide reduction increases monotonically as UV irradiation time increases and it reaches 100% after 4 s. Above kinetic data demonstrate that the degree of disulfide bond reduction could be tuned by adjusting the UV exposure time of the peptide in the flow microreactor, which is particularly useful for achieving partial disulfide reduction for peptides containing multiple disulfide bonds.

**Increasing Sequence Coverage for Disulfide Peptides and Proteins from Complete Reduction.** Selectin binding peptide is a naturally existing circular peptide due to an intrachain disulfide bond between C1 and C9 residues (sequence shown in the inset of Figure 3). As expected, no sequence ions were obtained from $MS^2$ CID of doubly protonated intact peptide ions (Figure S5, Supporting Information). After 5 s UV irradiation, 100% disulfide reduction was achieved for this peptide, as demonstrated by the complete disappearance of intact peptide ions ($[M + 2H]^{2+}$, $m/z$ 523.8, Figure 3a) and appearance of ions at $m/z$



DOI: 10.1021/acs.analchem.8b04019
Anal. Chem. XXXX, XXX, XXX−XXX

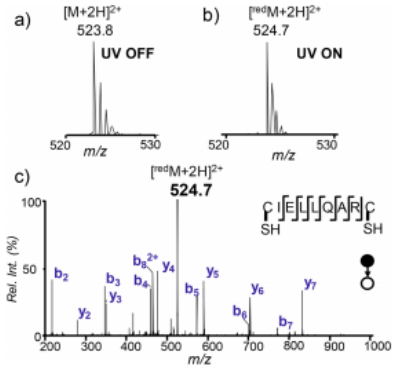


**Figure 3.** MS spectra of 10 $\mu$M of selectin binding peptide dissolved in $H_2O$/IPA (1:1) with 1% acetone: (a) before UV, (b) after 5 s UV irradiation in flow microreactor, and (c) $MS^2$ CID of reduced peptide ions at $m/z$ 524.7 ($[^{red}M + 2H]^{2+}$). The fragmentation map of the peptide is indicated in the inset.

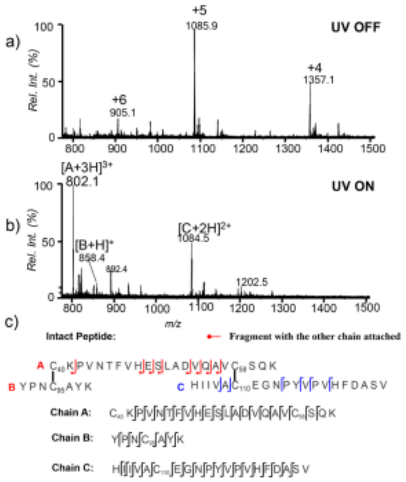


**Figure 4.** MS spectra of trypsin-digested ribonuclease-B subjected to the radical reaction: (a) before UV and (b) after 5 s UV irradiation in flow microreactor. (c) Sequence and fragmentation maps of intact peptide and reduced A, B, and C chains.

524.7 ($[^{red}M + 2H]^{2+}$) ions (Figure 3b). $MS^2$ CID of the reduced product at $m/z$ 524.7 gave almost full series of b- and y-type fragment ions, allowing sequence identification of the peptide (Figure 3c). Similar reaction phenomenon was observed with another peptide containing intrachain disulfide bond (oxytocin, Figure S6, Supporting Information).

Lysozyme (four disulfide bonds, 129 amino acid residues) was tested as a model for larger proteins. Complete disulfide reduction of all four disulfide bonds were achieved within 5 s UV irradiation as compared to 3 h reduction using DTT. $MS^2$ CID of the reduced lysozyme ions (+15, $m/z$ 955.1) produced rich backbone fragmentation for sequence identification (Figure S7, Supporting Information,).

We further applied complete disulfide reduction for the analysis of protein digests, mimicking the bottom-up proteomic approach. Ribonuclease-B, a small protein containing four disulfide bonds (sequence shown in Figure S8, Supporting Information) was subjected to trypsin digestion and LC separation before disulfide reduction and ESI-MS/MS analysis. One disulfide peptide was detected after digestion, which contained three peptide chains connected by two interchain disulfide bonds: $C_{40}$–$C_{95}$ and $C_{58}$–$C_{110}$ (sequence shown in Figure 4). The other predicted peptide containing $C_{26}$–$C_{84}$ and $C_{65}$–$C_{72}$ disulfide bonds was not detected, possibly due to its resistance to proteolytic digestion.[38] Figure 4a and 4b compare the ESI-MS spectra of the peptide before and after UV irradiation (5 s). Clearly, the intact peptide ions ($[M + 6H]^{6+}$, $[M + 5H]^{5+}$, $[M + 4H]^{3+}$) completely disappeared after UV irradiation. The presence of three separated peptide chains, viz. $[A + 3H]^{3+}$($m/z$ 802.1), $[B + H]^{+}$ ($m/z$ 858.4), and $[C + 2H]^{2+}$ ($m/z$ 1084.5), confirmed the presence of two interchain disulfide bonds in this peptide. The intact peptide ions ($[M + 6H]^{6+}$) and the disulfide reduced A, B, and C chains ($[A + 3H]^{3+}$, $[B + H]^{+}$, $[C + 2H]^{2+}$) were each subjected to $MS^2$ CID for structural analysis (spectra shown in Figure S9). The fragmentation map of the intact and reduced peptide ions is summarized in Figure 4c. $MS^2$ CID of the disulfide reduced chains led to almost 100% sequencing of the peptide, allowing determination of cysteine residues at $C_{40}$ and $C_{58}$ in A chain, $C_{95}$ in B chain, and $C_{110}$ in C chain. $MS^2$ CID of the intact peptide produced a series of sequence ions in A chain with intact B chain attached, i.e., $BAb_2$, $BAb_9$, $BAb_{10}$, $BAb_{11}$, $BAb_{14}$, $BAb_{15}$, $BAb_{16}$, and $BAb_{17}$, suggesting a disulfide linkage at $C_{40}$–$C_{95}$. Several fragment ions specific to the C chain were obtained, confirming its presence in the intact peptide, which could only be linked to A chain through a disulfide linkage at $C_{58}$–$C_{110}$.

**Mapping Disulfide Bonds in Insulin from Tunable Partial Reduction.** A distinct advantage of the photochemical reaction system is the capability of tuning the degree of disulfide reduction simply by adjusting the UV irradiation time (in seconds). This tunability is critical in analyzing disulfide connecting patterns for intact proteins or peptides which contain multiple disulfide bonds. Such aspect is demonstrated by disulfide mapping of porcine insulin, which consists of two interchain disulfide linkages between chain A and chain B ($AC_7$–$BC_7$ and $AC_{20}$–$BC_{19}$) and one intrachain linkage within chain A ($AC_6$ –$AC_{11}$). Data in Figure 5 compare the ESI-MS spectra of insulin before UV and after different periods of UV irradiation. Before UV irradiation, the protonated insulin ions, 5+ and 4+ ($m/z$ 1156.3 and 1145.3), dominated in the spectrum (Figure 5a). After 1.8 s UV irradiation, ions of A chain (3+ at $m/z$ 795.3 and 2+ at $m/z$ 1192.0) and B chain (4+ at $m/z$ 850.9 and 3+ at $m/z$ 1133.9) appeared as abundant species (Figure 5b). Deconvolution of the isotope cluster of the remaining insulin 5+ ions showed that it contained 53% intact, 31% and 16% one disulfide and two disulfide reduced species, respectively (Figure 5e, deconvolution procedure in Supporting Information). When the UV irradiation time was extended to 3.1 s, the remaining 5+ ion population only contained 12% intact insulin ions, while the one and two disulfides reduced species was 28% and 60%, respectively (Figure 5f). It is worth noting that partial disulfide reduction



DOI: 10.1021/acs.analchem.8b04019
Anal. Chem. XXXX, XXX, XXX−XXX

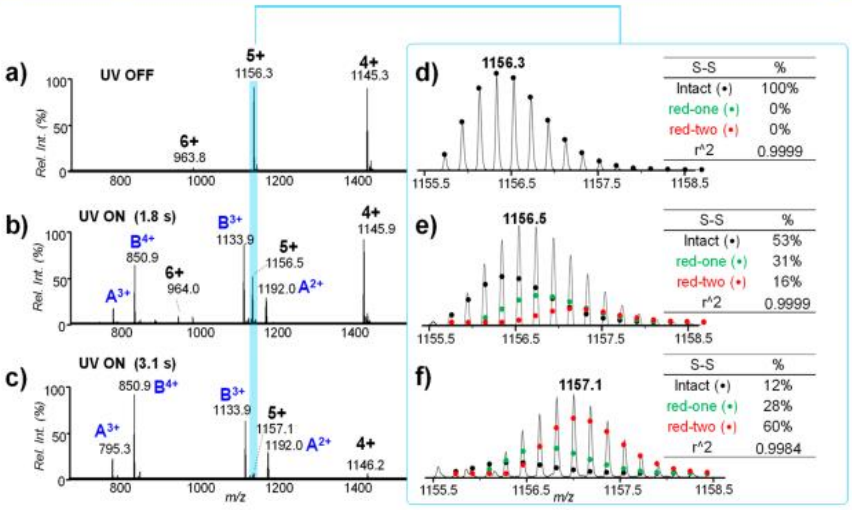


**Figure 5.** Positive ion mode ESI MS spectra of porcine insulin in 1% acetone, IPA/$H_2O$ ((v/v) = 1:1). (a) Before UV, (b) after 1.8 s, and (c) 3.1 s UV irradiation in flow microreactor. (d–f) The zoomed-in region of 5+ insulin ions from parts a–c. Deconvoluted isotopic distributions of the intact (black dots), one disulfide reduced (green dots), and two disulfide reduced (red dots) species are overlaid with the experimental data and their relative contributions are listed in the insets.

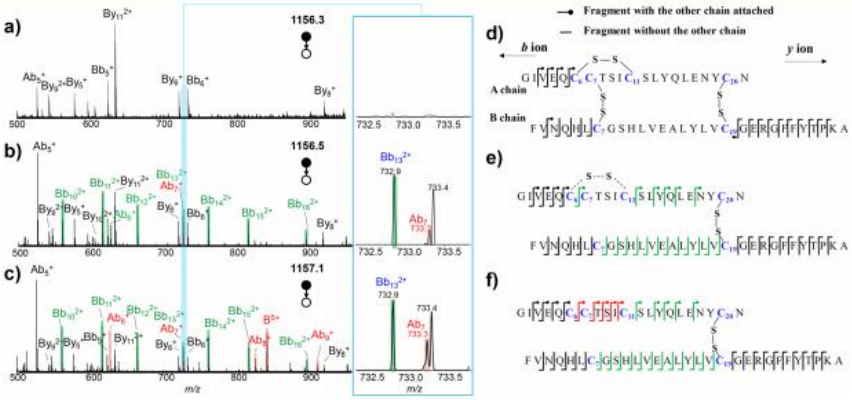


**Figure 6.** $MS^2$ CID of 5+ insulin ion populations derived from (a) intact, (b) 31% one disulfide reduced and 16% two disulfide reduced species, and (c) 28% one disulfide reduced and 60% two disulfide reduced species. The corresponding fragmentation maps are shown in parts d–f.

typically produced a mixture of different degrees of disulfide reduction; however, due to the capability of online reaction monitoring the optimized condition for a certain reduced population could be achieved rapidly. The intact 5+ insulin ions and those resulting from different degrees of reduction (1.8 and 3.1 s UV irradiation) were each subjected to $MS^2$ CID for disulfide mapping. The lower $m/z$ region (500–900) of the CID data are summarized in Figure 6a–c and the corresponding fragmentation maps derived from detected b- and y-type ions are summarized in Figure 6d–f. CID data in the higher $m/z$ region are supplied in the Figure S10, Supporting Information. As expected, $MS^2$ CID of the intact insulin ions (5+, $m/z$ 1156.1, Figure 6a) only produced sequence fragment ions in the exocyclic backbone regions and no specific information regarding disulfide linkage can be obtained. However, $MS^2$CID of the fully reduced $A^{2+}$ and $B^{5+}$ ions produced full sequence coverage of each chain, allowing



DOI: 10.1021/acs.analchem.8b04019
Anal. Chem. XXXX, XXX, XXX−XXX

pinpointing the positions of the six cysteine residues (Figure S11, Supporting Information).

Figure 6b shows $MS^2$ CID of the 5+ ions ($m/z$ 1156.5) containing 31% one disulfide reduced and 16% two disulfide reduced species. The presence of $Bb_{7-18}$ ions suggests an interchain disulfide had been cleaved before CID and this bond should involve $C_7$ residue in chain B. On the other hand, the detection of $BAy_{4,\ 6-8}$ ions allow for locating an interchain disulfide bond between $AC_{20}$ and $BC_{19}$. Two sequence ions were detected between $AC_6$ and $AC_{11}$, viz. $Ab_6$ and $Ab_7$, albeit at relatively low intensities (inset of Figure 6b). This phenomenon is suggestive for an intrachain disulfide in this sequence region. $MS^2$ CID of the 5+ insulin ions containing 60% two disulfides reduced species is shown in Figure 6c with unique ions highlighted in red. The presence of abundant $Ab_{6-9}$ and $BAy_{11-15}$ ions clearly suggests that this ion population contains structures with the intrachain disulfide bond in chain A and an interchain disulfide bond ($AC_7$−$BC_7$) had been reduced. It is worth mentioning that the relative ion intensities of $Ab_6$ and $Ab_7$ are significantly increased as the two disulfide reduced species increased from 16% to 60% (insets of Figure 6b,c), supporting that they are likely derived from the two-disulfide bond reduced population. Interestingly, no fragment ion relating to structures containing reduced $AC_{20}$−$BC_{19}$ disulfide was observed. If this disulfide bond had been cleaved, sequence ions such as $By_{12-23}$, $ABb_{7-17}$, $Ay_{1-10}$, or $BAb_{11-20}$ should be present. The above data clearly demonstrate that disulfide reduction was slowest for the disulfide bond between $AC_{20}$−$BC_{19}$. The difference in the disulfide reduction kinetics could be attributed to the different solvent accessibility of the three disulfide bonds, in which the $AC_{20}$−$BC_{19}$ has been reported to be least accessible in insulin under electrochemical reduction.[39]

Although the two interchain disulfide bonds have been pinpointed from $MS^2$ CID of the partially reduced insulin ions, the intrachain disulfide bond in chain A still needs to be determined. To acquire such information, ions of partially reduced chain A (2+, $m/z$ 1191.0) which consisted of an intact intrachain disulfide bond but with two other interchain disulfide bonds being cleaved, were subjected to $MS^2$ CID. It is worth pointing out that a small portion of the fully reduced A chain ions was inevitably mixed in the precursor ion population and underwent beam-type CID together with the partially reduced A chain ions even from using the narrowest isolation window available on the instrument. Nevertheless, comparisons of the CID data between the partially reduced and the fully reduced A chain ions showed that the relative ion intensities of $b_{6-10}$ were significantly reduced from the partially reduced A chain ion population while those of exocyclic sequence ions were quite comparable, i.e., $b_{4,5}$ and $b_{11-17}$ (data shown in Figure S12, Supporting Information). Consequently, the disulfide linkage between $C_6$ and $C_{10}$ in chain A was determined.

## CONCLUSIONS

A photochemical reaction system that allows for rapid and tunable disulfide reduction has been developed for characterizing peptides containing one or multiple disulfide bonds by ESI-MS/MS. Acetone/IPA is determined as the best photoinitiating system for disulfide bond reduction with almost 100% yield achieved within less than 5 s UV irradiation. The use of flow microreactor enables precise control of the degree of disulfide reduction and online coupling with infusion ESI-MS/MS. By pairing complete disulfide reduction with subsequent low-energy CID, near complete sequence coverage is achieved for various peptides containing one or multiple disulfide bonds. Furthermore, different degrees of partial reduction can be achieved simply by adjusting the UV irradiation time, greatly facilitating the disulfide linkage assignment, as demonstrated by mapping the three disulfide bonds in insulin. For the peptide systems studied herein, no evidence for disulfide bond scrambling has been obtained, likely benefited from the fast reaction and online detection system. Compared to conventional disulfide mapping approach, the online photochemical system enjoys several distinct advantages, including full compatibility with ESI-MS without introducing any chemical matrix, significantly shortened reaction time (from hours to seconds) and flexibility in tuning the extent of disulfide reduction. These aspects are highly desirable for developing high-throughput structural analysis capability for proteins consisting of multiple disulfide bonds. As a preliminary test, disulfide reduction in the microflow reactor was online-coupled with reversed phase LC−MS. Disulfide linkage analysis was successful for peptide digest of a model protein. Detailed characterization of this system for bottom-up protein analysis is currently undergoing and will be reported separately.

## ASSOCIATED CONTENT

### Supporting Information

The Supporting Information is available free of charge on the ACS Publications website at DOI: 10.1021/acs.analchem.8b04019.

Procedure for isotopic deconvolution and mass spectra data on disulfide bond cleavage using acetone/alcohol photoinitiating system (PDF)

## AUTHOR INFORMATION


### Corresponding Author

*E-mail: xiayu@mail.tsinghua.edu.cn.

### ORCID

Yu Xia: 0000-0001-8694-9900


### Author Contributions

All authors have given approval to the final version of the manuscript

### Notes

The authors declare no competing financial interest.

## ACKNOWLEDGMENTS

Financial support from National Natural Science Foundation of China (Grant No. 21722506, Grant No. 21621003) and Grant NIH R01GM118484 is greatly appreciated. We acknowledge assistance from D. Zhang for isotope deconvolution.

## REFERENCES


(1) Lakbub, J. C.; Shipman, J. T.; Desaire, H. *Anal. Bioanal. Chem.* **2018**, *410*, 2467−2484.

(2) Wysocki, V. H.; Tsaprailis, G.; Smith, L. L.; Breci, L. A. *J. Mass Spectrom.* **2000**, *35*, 1399−1406.

(3) Lioe, H.; O'Hair, R. A. *J. Am. Soc. Mass Spectrom.* **2007**, *18*, 1109−1123.

(4) Wall, J. S. *J. Agric. Food Chem.* **1971**, *19*, 619−625.

(5) Zhang, Y.; Fonslow, B. R.; Shan, B.; Baek, M.-C.; Yates, J. R. *Chem. Rev.* **2013**, *113*, 2343−2394.




DOI: 10.1021/acs.analchem.8b04019
*Anal. Chem.* XXXX, XXX, XXX−XXX

(6) Zhang, Y.; Cui, W.; Zhang, H.; Dewald, H. D.; Chen, H. *Anal. Chem.* **2012**, *84*, 3838−3842.
(7) Mysling, S.; Salbo, R.; Ploug, M.; Jørgensen, T. J. D. *Anal. Chem.* **2014**, *86*, 340−345.
(8) Cramer, C. N.; Kelstrup, C. D.; Olsen, J. V.; Haselmann, K. F.; Nielsen, P. K. *Anal. Chem.* **2017**, *89*, 5949−5957.
(9) Stinson, C. A.; Xia, Y. *J. Am. Soc. Mass Spectrom.* **2014**, *25*, 1192−1201.
(10) Durand, K. L.; Tan, L.; Stinson, C. A.; Love-Nkansah, C. B.; Ma, X.; Xia, Y. *J. Am. Soc. Mass Spectrom.* **2017**, *28*, 1099−1108.
(11) Fukuyama, Y.; Iwamoto, S.; Tanaka, K. *J. Mass Spectrom.* **2006**, *41*, 191−201.
(12) Peng, I. X.; Ogorzalek Loo, R. R.; Shiea, J.; Loo, J. A. *Anal. Chem.* **2008**, *80*, 6995−7003.
(13) Zubarev, R. A.; Kelleher, N. L.; McLafferty, F. W. *J. Am. Chem. Soc.* **1998**, *120*, 3265−3266.
(14) Oh, H.; Breuker, K.; Sze, S. K.; Ge, Y.; Carpenter, B. K.; McLafferty, F. W. *Proc. Natl. Acad. Sci. U. S. A.* **2002**, *99*, 15863−15868.
(15) Syka, J. E. P.; Coon, J. J.; Schroeder, M. J.; Shabanowitz, J.; Hunt, D. F. *Proc. Natl. Acad. Sci. U. S. A.* **2004**, *101*, 9528−9533.
(16) Foley, S. F.; Sun, Y.; Zheng, T. S.; Wen, D. *Anal. Biochem.* **2008**, *377*, 95−104.
(17) Fung, Y. M. E.; Kjeldsen, F.; Silivra, O. A.; Chan, T. W. D.; Zubarev, R. A. *Angew. Chem.* **2005**, *117*, 6557−6561.
(18) Agarwal, A.; Diedrich, J. K.; Julian, R. R. *Anal. Chem.* **2011**, *83*, 6455−6458.
(19) Quick, M. M.; Crittenden, C. M.; Rosenberg, J. A.; Brodbelt, J. S. *Anal. Chem.* **2018**, *90*, 8523−8530.
(20) Lee, M.; Lee, Y.; Kang, M.; Park, H.; Seong, Y.; Sung, B. J.; Moon, B.; Oh, H. B. *J. Mass Spectrom.* **2011**, *46*, 830−839.
(21) Pilo, A. L.; McLuckey, S. A. *Anal. Chem.* **2016**, *88*, 8972−8979.
(22) Gray, W. R. *Protein Sci.* **1993**, *2*, 1732−1748.
(23) Xia, Y.; Cooks, R. G. *Anal. Chem.* **2010**, *82*, 2856−2864.
(24) Adhikari, S.; Xia, Y. *Anal. Chem.* **2017**, *89*, 12631−12635.
(25) Adhikari, S.; Zhang, W.; Xie, X.; Chen, Q.; Xia, Y. *Anal. Chem.* **2018**, *90*, 5239−5246.
(26) Creasey, D. J.; Heard, D. E.; Lee, J. D. *Geophys. Res. Lett.* **2000**, *27*, 1651−1654.
(27) Hoyle, C. E.; Bowman, C. N. *Angew. Chem., Int. Ed.* **2010**, *49*, 1540−1573.
(28) Norrish, R. G. W.; Kirkbride, F. W. *J. Chem. Soc.* **1932**, 1518−1530.
(29) Norrish, R. G. W. *Trans. Faraday Soc.* **1934**, *30*, 103−113.
(30) Norrish, R. G. W.; Crone, H. G.; Saltmarsh, O. D. *J. Chem. Soc.* **1934**, 1456−1464.
(31) Haas, Y. *Photochem. Photobiol. Sci.* **2004**, *3*, 6−16.
(32) Bookwalter, C. W.; Zoller, D. L.; Ross, P. L.; Johnston, M. V. *J. Am. Soc. Mass Spectrom.* **1995**, *6*, 872−876.
(33) Akhlaq, M. S.; Murthy, C. P.; Steenken, S.; Von Sonntag, C. *J. Phys. Chem.* **1989**, *93*, 4331−4334.
(34) Luo, Y.-R. *Handbook of Bond Dissociation Energies in Organic Compounds*; CRC Press: Boca Raton, FL, 2003.
(35) Krenske, E. H.; Pryor, W. A.; Houk, K. N. *J. Org. Chem.* **2009**, *74*, 5356−5360.
(36) Anglada, J. M.; Crehuet, R.; Adhikari, S.; Francisco, J. S.; Xia, Y. *Phys. Chem. Chem. Phys.* **2018**, *20*, 4793−4804.
(37) *Internet Bond-energy Databank (pKa and BDE)-iBonD*, http://ibond.chem.tsinghua.edu.cn, accessed July 2018.
(38) Bernard, B. A.; Newton, S. A.; Olden, K. *J. Biol. Chem.* **1983**, *258*, 12198−12202.
(39) Cramer, C. N.; Haselmann, K. F.; Olsen, J. V.; Nielsen, P. K. *Anal. Chem.* **2016**, *88*, 1585−1592.



DOI: 10.1021/acs.analchem.8b04019
*Anal. Chem.* XXXX, XXX, XXX−XXX